

ABSTRACT

MEHRABAN, NAHID. Design and Synthesis of Phthalocyanine Macrocycles for Photodynamic Therapy; A Combined Study using Molecular Modeling and Drug Delivery. (Under the direction of Dr. Harold S. Freeman).

Photodynamic therapy (PDT) is a medical application of dye chemistry that requires the presence of light, a photosensitizer, and molecular oxygen, which in tandem form the highly reactive singlet oxygen (${}^1\text{O}_2$) species that can destroy cancer cells. New developments in this field are possible via different approaches, including the design and synthesis of more efficient sensitizer dyes based on molecular modeling studies and increased photosensitizer uptake and selectivity for cancer cells utilizing drug delivery systems. Use of these specific approaches comprised the key goal of the present research. While many interesting photosensitizers are under investigation for possible PDT use, zinc phthalocyanine was chosen as the prototype for this study.

To achieve the project goal, three types of studies have been conducted, the details of which are outlined in the chapters that follow. In the first chapter, the synthesis and molecular characterization of a new zinc phthalocyanine analog containing 4-methoxybenzyloxy groups in the periphery of the parent structure are presented along with its biological and excited state properties. To assess the PDT potential of this hydrophobic chromogen, it was encapsulated in polymeric micelles derived from PLGA-b-PEG and its cytotoxicity and cell uptake properties were evaluated using human lung cancer cell line A549. Results showed higher cytotoxic effect for encapsulated sensitizer dye compare to the free form. Computational studies involving the new dye sensitizer showed a correlation between the singlet and triplet state energy level and (${}^1\text{O}_2$) production, leading to the extension of these calculations reported in chapter 4.

Second chapter involves the synthesis and evaluation of photophysical and photochemical properties of new zinc phthalocyanines containing a tetrazole group, bearing in mind the use of this moiety in pharmaceutical drug development as well as the convenience of their synthesis. A bathochromic shift was observed for the visible spectrum of ZnPc derivatives with tetrazole moiety was observed. The dark and cytotoxicity and cell uptake of these dyes and other known zinc phthalocyanines were evaluated on A549 cells. It was found that zinc phthalocyanine with tetrazole derivatives have no dark toxicity and localize both in cytoplasm and nucleus compared to ZnPc that only localizes in cytoplasm.

In the third chapter, the choice of metals and substituents in the alpha or beta position of the parent structure was evaluated using molecular modeling. The goal was to optimize a computational model using density functional theory (DFT) to find the optimum phthalocyanine structure needed to increase the $^1\text{O}_2$ efficiency and lambda max. Based on the calculations, removal of the four fused rings, addition of substituents with a triple bond, and changing metal have a significant impact on the singlet oxygen production.

© Copyright 2016 by Nahid Mehraban

All Rights Reserved

Design and Synthesis of Phthalocyanine Macrocycles for Photodynamic Therapy: A
Combined Study using Molecular Modeling and Drug Delivery

by
Nahid Mehraban

A dissertation submitted to the Graduate Faculty of
North Carolina State University
in partial fulfillment of the
requirements for the Degree of
Doctor of Philosophy

Fiber and Polymer Science

Raleigh, North Carolina

2015

APPROVED BY:

Dr. Alan Tonelli

Dr. Ahmed El-Shafei

Dr. Lucian A. Lucia

Dr. Phillip R. Musich

Dr. Harold S. Freeman
Committee Chair

DEDICATION

I dedicate this work to my dear parents, Fahimeh and Morteza, my supportive brother, Arash, with their endless love and in loving memory of my brother Siavash.

BIOGRAPHY

Nahid Mehraban was born in Tehran, Iran. Her interests in genetics, biochemistry and molecular biology drove her to pursue her undergraduate study in the fields of molecular and cell biology with emphasis on biochemistry. She received Bachelors of Science degrees from Tarbiat Moallem Tehran University and East Tennessee State University (ETSU). To further her understanding of biochemistry, Nahid decided to pursue graduate studies in chemistry and received her Masters of Science degree in chemistry from ETSU. During her graduate studies, she was introduced to the field of Photodynamic Therapy (PDT) which she found challenging, yet rewarding. When the opportunity arose for her to continue her studies in PDT under supervision of Dr. Freeman at NCSU, she took it with great enthusiasm. Nahid received her PhD in May 2016.

ACKNOWLEDGMENTS

I would like to express my deepest gratitude to my adviser, Dr. Harold S. Freeman for his guidance, support, patience and encouragement. He truly set an example of excellence as a researcher, mentor, instructor, and role model. This work could have not been completed without his support and guidance.

I would also like to extend my heartfelt appreciation to my committee member, Dr. Phillip R. Musich from Quillen college of Medicine at East Tennessee State University for his invaluable support and guidance through the years and helping me to complete the biological aspect of my research and providing the necessary supplies.

I would also like to extend my heartfelt thanks to my other thesis committee members, Drs Ahmed El-Shafei, Alan Tonelli from College of Textiles, and Dr. Lucian Lucia from the department of Forest Biomaterials at North Carolina State University (NCSU) for all of their guidance throughout this process.

My extended gratitude to Dr. John Rust, Dr. David Hinks from college of textiles, Dr. Luciano Da Silva, our visiting scholar from Brazil and Dr. Mehran Eslaminia.

My gratitude extended to Drs. Felix Castellano, Elena Jakubikova, Reza Ghiladi, Jonathan Lindsey, and Daniel Comins from department of chemistry at NCSU for their support and feedback.

I also would like to thank my family and friends Fahimeh, Morteza, and Arash Mehraban, Sharoc and Shahram Peykamian for their support and encouragement which gave me the impetus to further my education to earn a PhD.

TABLE OF CONTENTS

Chapter 1	1
1.1 Introduction.....	1
1.1.1 PDT Mechanism	4
1.1.2 Singlet Oxygen.....	5
1.1.3 Singlet oxygen formation.....	7
1.1.4 Mechanisms of cell death.....	10
1.1.5 Therapeutic irradiation.....	11
1.2 PS uptake and selectivity	14
1.2.1 Effect of hydrophobicity (lipophilicity) and hydrophilicity on cell uptake and selectivity	15
1.2.2 Effect of intracellular pH on PS uptake	17
1.2.3 Use of nanoparticles.....	18
1.2.4 Polymeric Micelle/micelles	19
1.3 Increased $^1\text{O}_2$ Production	32
1.3.1 Incorporation of heavy atoms	32
1.3.2 Isosteric replacements.....	36
1.3.3 Two photon systems	42
1.3.4 Triplet PSs.....	44
1.4 Phthalocyanine	49
1.4.1 Phthalocyanine/Organic pigment.....	51
1.4.2 Synthesis of phthalocyanine	52
1.4.3 Problems with current phthalocyanines	56
1.5 Laser light source	58
1.5.1 Non-Laser light source.....	59
1.5.2 Light dose.....	60
Chapter 2	63
2.1 Introduction.....	63
2.2 Materials and Methods.....	67
2.2.1 Synthesis	68

2.2.2 DFT Calculations	70
2.2.3 Singlet oxygen quantum yield	70
2.2.4 Steady-State and life-time fluorescence.....	71
2.2.5 Polymeric micelle preparation	72
2.2.6 TEM measurements	72
2.2.7 Dynamic light scattering and zeta potential	72
2.2.8 Sensitizer Drug load and Entrapment Efficiency.....	72
2.2.9 Qualitative analysis of hydrophilicity	73
2.2.10 Cellular uptake of encapsulated dyes into polymeric micelles	73
2.2.11 MTT and CTB Dark toxicity Assays	74
2.2.12 MTT and CTB Cytotoxicity Assays	75
2.3 Results and discussion	75
2.3.1 Synthesis	75
2.3.2 Computation analysis.....	76
2.3.3 Singlet oxygen quantum yields.....	80
2.3.4 Photophysical properties	80
2.3.5 Characterization of nanoparticles	82
2.3.6 Study the lipophilicity of ZnPcBCH ₃ with ZnPc	86
2.3.7 Cell localization of ZnPc and ZnPcBCH ₃ in A549 cells	87
2.3.8 Cell Uptake:	89
2.3.9 <i>In vitro</i> Dark and Cytotoxicity Assay on A549 cells	90
2.4 Conclusion	93
2.5 Supporting Documents.....	93
Chapter 3	96
3.1 Introduction.....	96
3.2 Material and Method.....	97
3.3 Synthesis	99
3.4 Singlet oxygen quantum yield	103
3.4.1 Steady-State and life-time fluorescence.....	104
3.4.2 MTT and CTB Dark toxicity Assays	105
3.4.3 MTT and CTB Cytotoxicity Assays	106
3.4.4 Cell Uptake Assay.....	106

3.5 Results.....	106
3.5.1 Synthesis	106
3.5.2 Singlet oxygen quantum yield:	108
3.6 Conclusion	121
3.7 Supporting Documents.....	122
Chapter 4.....	125
4.1 Introduction.....	125
4.2 Material and Methods:	127
4.2.1 Modeling:	127
4.2.2 Singlet oxygen quantum yield	128
4.2.3 Steady-State and life-time fluorescence.....	128
4.3 Results and discussion	129
4.3.1 Evaluation of energy efficiency (ΔE_{S0-T1})	129
4.3.2 Impact of the presence of metal and the number of substituents	130
4.3.3 Impact of the addition of substituents that can do energy transfer with ZnPc	135
4.3.4 Impact of the addition and subtraction of the number of fused rings on ΔE_{s-t}	137
4.3.5 Evaluation of UV/VIS Spectra.....	139
4.3.6 HUMO-LUMO gap	142
4.4 Conclusion	154
4.5 Supporting Documents.....	155
Chapter 5	158
5.1 Supporting Document	160
Chapter 6	162
6.1 PDT Dye Design	162
6.2 <i>In vitro</i> studies.....	164
References.....	166
Appendix A	183
Appendix B	185

LIST OF TABLES

Table 1-1. Examples of PSs targeting lysosome and mitochondria.....	13
Table 1-2. Examples of polymeric micelles/micelles tested <i>in vitro</i> and <i>in vivo</i> for PDT	28
Table 1-3. Laser sources	59
Table 1-4. Non-laser Sources.....	60
Table 1-5. Summary of some of the light source and the phthalocyanine that are recently been studied.	61
Table 2-1. Bond angles and lengths that are obtained from crystal structure vs the calculated ones.	77
Table 2-2. Calculated values for the energy gap between the ground state singlet and the first triplet state.....	79
Table 2-3. Experimental data for photophysical properties of ZnPc and ZnPcBCH ₃ in DMSO that was obtained in plate reader with correction factor of 0.32.....	82
Table 2-4. Reported molar extinction coefficient in DMF.	82
Table 2-5. Reported zeta potential and average diameter values.....	84
Table 2-6. Reported nanoparticle yield, sensitizer drug load and entrapment efficiency obtained from nanoprecipitation with THF.	86
Table 3-1. Measured singlet oxygen and fluorescence quantum yields in DMF.....	108
Table 3-2. Measured absorption lambda max $\lambda(\max)$, fluorescence emission f_e , excited state lifetime τ , fluorescence quantum yield Φ_f and Stokes shift in DMF.....	111
Table 3-3. Measure molar extinction coefficient DMF using a Cary 300.	111
Table 3-4. Molar absorptivity measured in 96-well plate with correction factor of 0.32 in DMSO.	112
Table 4-1. Comparing the singlet oxygen production with energy difference between singlet and triplet states.	130
Table 4-2. Calculated ΔE_{s-t} (eV) value for the phthalocyanines with one substituents.	134
Table 4-3. Calculated ΔE_{s-t} (eV) value for the free phthalocyanine vs ZnPc, MgPc and RuPc.	134
Table 4-4. Calculated ΔE_{s-t} (eV) value for ZnPc dimer and ZnPccarbazole.....	137
Table 4-5. Calculated ΔE_{s-t} (eV) value for ZnPc with plus and minus fused rings.....	138
Table 4-6. Calculated and experimental lambda max values.	139
Table 4-7. Comparing the calculated and experimental differences between the singlet energies.	140
Table 4-8. Reported calculated and experimental lambda max.....	142
Table 4-9. Calculated HOMO and LUMO gap values for phthalocyanine with different metals.	144
Table 4-10. Measured HOMO –LUMO gap values for ZnPc derivative with 4 substituents.	145
Table 4-11. HOMO-LUMO gap values for ZnPc derivatives with one substituents.	146

LIST OF FIGURES

Figure 1-1. Examples of porphyrin (1-4) and non-porphyrin (5-9) PSs	3
Figure 1-2. Formation of PDT reactive species through type I and type II photochemistry (modified from [10])......	5
Figure 1-3. Two unpaired π electrons in two degenerate orbitals of triplet oxygen ground state (paramagnetic behavior) give rise to the singlet excited state.....	7
Figure 1-4. Reaction of $^1\text{O}_2$ with double bonds	9
Figure 1-5. Possible intermediates form during [2+2] addition reactions with $^1\text{O}_2$	10
Figure 1-6. Illustration of the therapeutic window for PDT treatment.....	12
Figure 1-7. Structure of Zn(II) N-alkylpyridylporphyrins designed for mitochondria targeting.....	14
Figure 1-8. Examples of pH responsive Ir(III) complexes.....	18
Figure 1-9. Examples of nanoparticle structures developed for PDT treatments.....	19
Figure 1-10. Schematic representation for spherical polymeric micelle formation via different methods. Co-solvent evaporation [67], dialysis [68], oil/water emulsion.....	20
Figure 1-11. Example of a tri-block copolymers used to form polymeric micelles.....	21
Figure 1-12. Structure of PEG-b-PCL.....	23
Figure 1-13. Structure of a surfactant-like tetra-tail amphiphilic peptide.....	24
Figure 1-14. Conjugation of protoporphyrin IX to PEG-PLA.....	25
Figure 1-15. A pH sensitive MPEG poly(β -amino ester) structure for micelle formation....	26
Figure 1-16. Examples of structural units reported in Table 2	26
Figure 1-17. A dendrimer-based phthalocyanine structure for sensitizer delivery.....	27
Figure 1-18. Eosin and dibromorhodamine structures containing heavy atoms.....	33
Figure 1-19. Halogenated Zn-Pc structures for enhanced $^1\text{O}_2$ formation efficiency	33
Figure 1-20. Properties of N-confused porphyrin ($\text{H}_2\text{N}_2\text{CP}$) with and without metal atoms.	34
Figure 1-21. Pd- and Pt-complexed 5,10,15,20-tetrakis (pentafluorophenyl) porphyrin structures.....	35
Figure 1-22. A Mg tetrabenzoporphyrin having high $^1\text{O}_2$ quantum efficiency	36
Figure 1-23. Modification of the squaraine system to increase $^1\text{O}_2$ quantum efficiency.	36
Figure 1-24. $^1\text{O}_2$ quantum efficiency values for various tetraphenylporphyrins.....	37
Figure 1-25. Brominated porphycene macrocycles and their $^1\text{O}_2$ quantum efficiency.....	38
Figure 1-26. Iodinated squaraine giving enhanced $^1\text{O}_2$ quantum efficiency	39
Figure 1-27. Poly(amidoamine) Ir(III) complex as a new $^1\text{O}_2$ sensitizer.	40
Figure 1-28. Ir(III) PEG complexes as new $^1\text{O}_2$ sensitizer.	41
Figure 1-29. A light harvesting dendrimer having fluorescence resonance energy transfer ..	43
Figure 1-30. Structure of $[\text{Ru}(\text{LP1})_3][\text{PF}_6]_2$	44
Figure 1-31. Structure of cyclometalated Ir(III) complex	45
Figure 1-32. Example of resonance energy transfer (RET) and ISC for a BODIPY/aza-BODIPY based PS	46

Figure 1-33. Energy level diagram showing Ru(II) complex having a light-harvesting coumarin ligand.	47
Figure 1-34. Example Ru(II) based phen complexes having close $^3\text{MLCT}$ and ^3IL states	48
Figure 1-35. Energy diagram for a Ru(II) complex having BODIPY as a visible light harvesting ligand, showing energy transfer is unlikely	49
Figure 1-36. Metal free phthalocyanine (1) and metallophthalocyanine.....	51
Figure 1-37. Pathways to phthalocyanine system.....	53
Figure 1-38. Mechanism of zinc phthalocyanine formation.....	54
Figure 1-39. Examples of water soluble phthalocyanines.....	55
Figure 1-40. Comparing the amount of singlet oxygen production by changing symmetry..	56
Figure 1-41. Change in singlet oxygen formation by changing S1 and S2 energy states.....	57
Figure 2-1. Summary of Type I and Type II photoreactions where P is the photosensitizer, S_0 is the singlet ground state, S_1 is the first excited singlet state, T_1 is the first excited triplet state, ISC is intersystem crossing, and $^1\text{O}_2$ is singlet oxygen.	64
Figure 2-2. Structure of PLGA-b-PEG.	67
Figure 2-3. A. General structure of ZnPc to demonstrate α , β , γ , and δ positions. B. Optimized structure of ZnPc. C. Optimized structure of ZnPcBCH ₃	78
Figure 2-4. Absorption and emission spectra of ZnPc and ZnPcBCH ₃ in DMSO.	81
Figure 2-5. A, B and C are the size distribution obtained from DLS using THF(A), acetone (B) and acetonitrile (C, D) in nanoprecipitation process.	85
Figure 2-6. Monitoring the lipophilicity of the ZnPc vs ZnPcBCH ₃ through absorptivity of the visible spectra in DMSO, DMEM and FBS media.	87
Figure 2-7. Localization of ZnPc and ZnPcBCH ₃ in A549 cells were using Texas Red light cube for ZnPc and Cy5 for ZnPcBCH ₃	89
Figure 2-8. Comparing the fluorescence intensity of and cell uptake of encapsulated ZnPcBCH ₃ at different incubation time and concentration.	90
Figure 2-9. Dark toxicity analysis of ZnPc and ZnPcBCH ₃	91
Figure 2-10. CTB toxicity assay for encapsulated vs free dyes.....	92
Figure 2-11. FTIR spectrum of compound 3.	93
Figure 2-12. ^1H NMR spectrum of compound 3.....	94
Figure 2-13. ESI mass spctrum of compound 3.....	94
Figure 2-14. FTIR spectrum of compound 4.	95
Figure 2-15. ESI mass spectrum of compoound 4.....	95
Figure 3-1. Profile decay of ZnPcBCH ₃ which is the same as the one for ZnPc, ZnPcCH ₃ , ZnPcNO ₂ , ZnPc-M-Tet, ZnPc-B-Tet.	110
Figure 3-2. Normalized emission spectrum of ZnPc, ZnPcBCH ₃ , ZnPc-M-Tet, ZnPc-B-Tet, ZnPcCH ₃ , and ZnPcNO ₂	113
Figure 3-3. Normalized visible spectra for ZnPc, ZnPc-M-Tet, ZnPcCH ₃ , ZnPc-B-Tet, ZnPcNO ₂	114
Figure 3-4. Fluorescence imaging of A549 cells showing the main localization of ZnPc, ZnPcBCH ₃ , and ZnPcCH ₃ in cytoplasm. ZnPc-M-Tet and ZnPc-B-Tet are localized both in the cytoplasm and in the nucleus.	114
Figure 3-5. Dark toxicity results for tested dyes.....	116

Figure 3-6. Addition of DMSO has impact on absorbance.	118
Figure 3-7. Addition of DMSO has no impact on fluorescence measurement.	118
Figure 3-8. Measured cytotoxicity of ZnPc, ZnPc-M-Tet, ZnPc-NO ₂ , ZnPcCH ₃ and ZnPcBCH ₃ using CTB assay.	119
Figure 3-9. Measured cell uptake of all dyes against A549 cells.	120
Figure 3-10. Measured cell uptake of encapsulated ZnPc-M-tetrazole.	121
Figure 3-11. ¹ H NMR spectrum for compound 3.	122
Figure 3-12. ESI mass spectrum of compound 3.	123
Figure 3-13. FTIR spectrum of compound 3.	123
Figure 3-14. mass spectrum of compound 4.	124
Figure 3-15. FTIR of compound 4.	124
Figure 4-1. ZnPc4BCH ₃ and ZnPc1BCH ₃ structures.	131
Figure 4-2. Phthalocyanines with one to four substituent in the peripheral position.	132
Figure 4-3. Phthalocyanine with a Zn, Mg and Ru metal.	133
Figure 4-4. Proposed ZnPc derivatives with carbazole and another ZnPc as a substituents.	136
Figure 4-5. Changing the Symmetry of the phthalocyanine through changing the number of fused rings.	138
Figure 4-6. Two possible structures for ZnPc with a substituent in the alpha positions.	141
Figure 4-7. Electron configuration of ZnPc with four electron donating and withdrawing substituents.	143
Figure 4-8. Electron configuration of ZnPc with an electron donating or an electron withdrawing substituent.	143
Figure 4-9. Electron configuration of phthalocyanine with and without metals.	144
Figure 4-10. Localization of HOMO and LUMO of ZnPc derivatives studied in chapter 4.	146
Figure 4-11. ¹ H NMR spectrum of compound 1.	155
Figure 4-12. ESI mass spectrum of compound 6.	156
Figure 4-13. ¹ H NMR spectrum of compound 7.	156
Figure 4-14. ESI mass spectrum of ZnPcNO ₂	157
Figure 4-15. ESI mass spectrum of ZnPcCH ₃	157
Figure 5-1. ¹ H NMR spectrum of compound 3.	160
Figure 5-2. ESI mass spectrum of compound 3.	160
Figure 5-3. FTIR spectrum of compound 3.	161

Chapter 1

BACKGROUND AND LITERATURE REVIEW

1.1 Introduction

Dyes and pigments absorb and reflect certain wavelengths of light, which leads to the perception of color. Electronically, the difference between photosensitizer (PS) molecules and other dye types is the ability of PSs to transfer the energy of absorbed light to molecules in the vicinity or be utilized for photochemical reactions [1]. PSs are either porphyrin or non-porphyrin based. Examples of porphyrin-based PSs include phthalocyanines, chlorins, bacteriochlorin, and purpurins [2, 3]. Protoporphyrin IX is a porphyrin based photosensitizers obtained from δ -aminolevulinic acid (ALA) through a biosynthesis mechanism [4].

Non-porphyrin based PSs include psoralens, anthracyclines, hypericin, hypocrellins, cyanines, phenothiazinium compounds such as methylene blue, nile blue analogs, toluidine blue, rhodamines, triarylmethanes, and acridines [5]. Two of the most recent developed PSs are bodipy [6] and squarines [7]. Examples of the porphyrin and non-porphyrin based PS types are shown in Figure 1-1. Examples of porphyrin (1-4) and non-porphyrin (5-9) PSs. Figure 1-1.

Key target criteria for PDT PSs include:

1. High selectivity toward cancer cells

2. Production of toxic reactive oxygen species (e.g. ${}^1\text{O}_2$) or free radicals
3. Optimal ADME (absorption, distribution, metabolism, excretion) [8].
4. Near IR light absorption
5. Absence of dark toxicity
6. High molar extinction coefficient

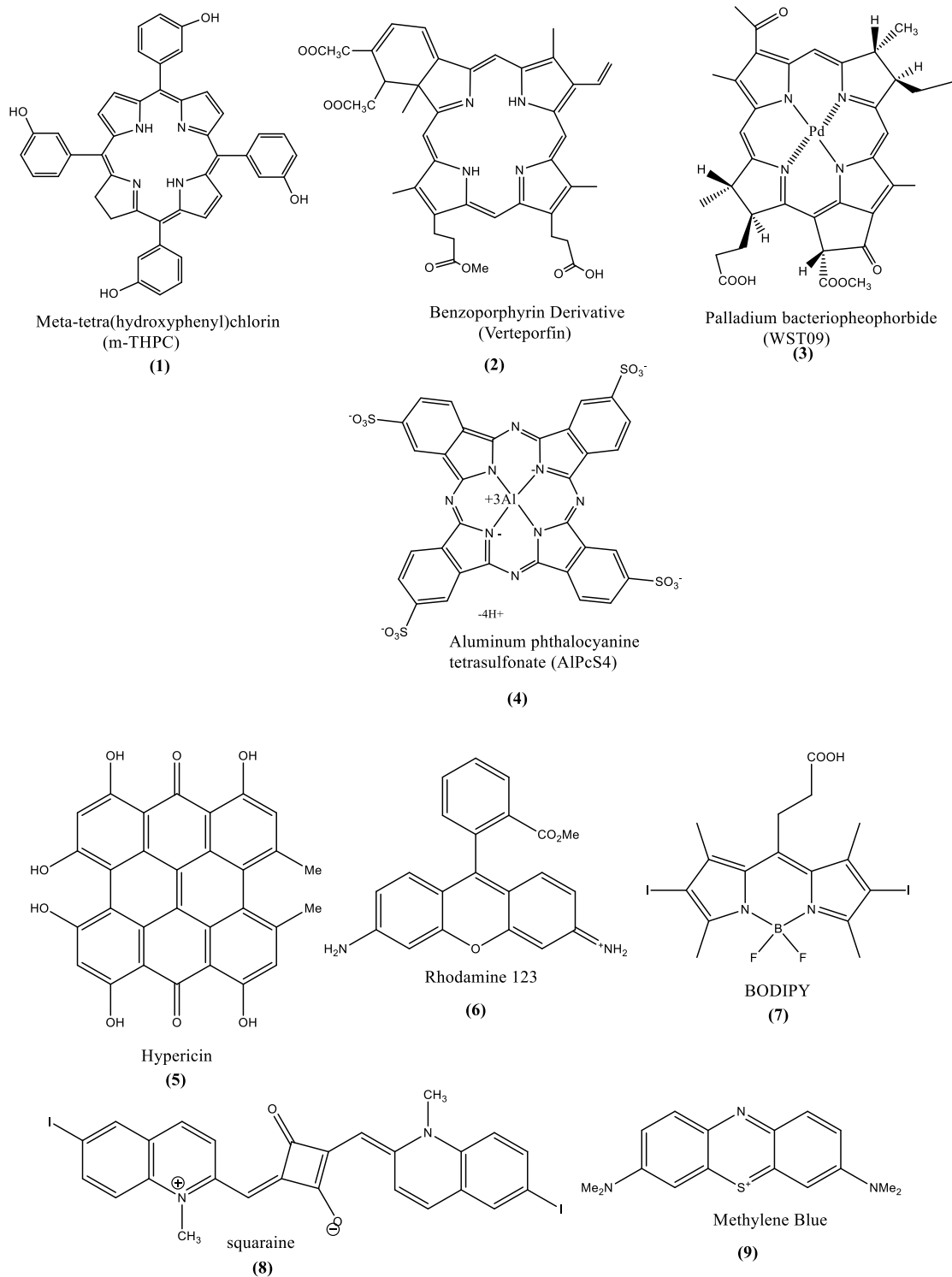


Figure 1-1. Examples of porphyrin (1-4) and non-porphyrin (5-9) PSs.

1.1.1 PDT Mechanism

Photodynamic Therapy (PDT) is based on the use of a PS, which efficiently populates an excited triplet state upon interaction with visible and NIR light. The triplet state of a PS (${}^3\text{PS}^*$) can produce toxic reactive oxygen species (ROS), such as ${}^1\text{O}_2$ or free radicals, by two different pathways. ${}^3\text{PS}^*$ can react with molecules to generate intermediate free radicals that in turn generate ROS (type I photochemistry). Alternatively, it can directly interact with molecular oxygen in its ground triplet state (${}^3\text{O}_2$) to produce “*in situ*” cytotoxic ${}^1\text{O}_2$ through an energy transfer process. This type II photochemistry Figure 1-2 is the most relevant PDT mechanism in cells, because most PSs are effective ${}^1\text{O}_2$ producers [9]. The ROS generated are capable of causing irreversible damage if generated inside cells, particularly inside specific subcellular organelles (e.g. mitochondria) where PSs can localize and accumulate [9]. PDT would therefore be able to selectively kill diseased cells, provided that selective delivery of the PS to the target could be assured.

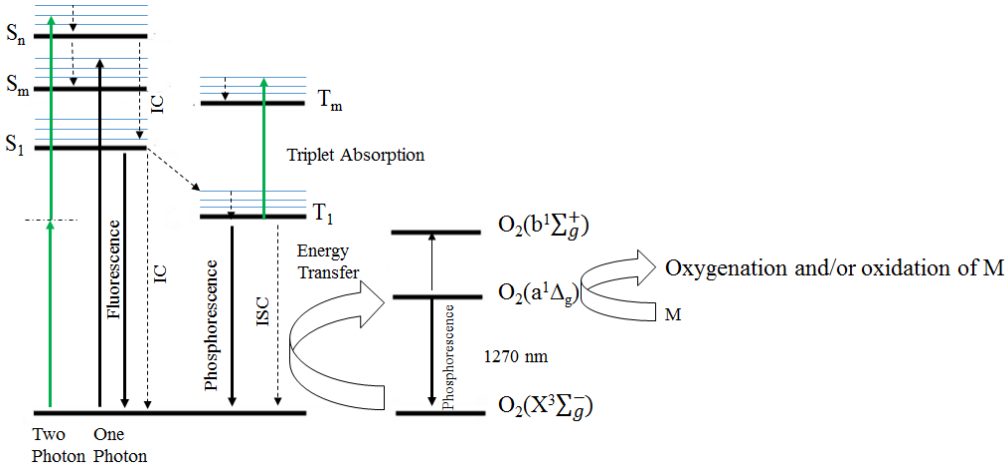


Figure 1-2. Formation of PDT reactive species through type I and type II photochemistry (modified from [10]).

1.1.2 Singlet Oxygen

Lewis in 1924 proposed that the paramagnetic oxygen is a biracial species. In 1931, H. Kautsky claimed that the photooxygenation of dyes is because of the sensitized formation of a short lived, highly active and diffusive form of a molecular oxygen. The MO diagram of the molecular oxygen shown in Figure 1-3 represents the highest molecular orbital is a twofold degenerate that allocates two electrons in total. Thus, in accordance with Hund's rule, the ground state of the molecular oxygen is a triplet state, $3\Sigma_g^-$. The energy of the two low-lying singlet states, $1\Delta_g$ and $1\Sigma_g^+$, are 95 and 158 KJ mol⁻¹ respectively are above the triplet ground state. In solution the upper excited $1\Sigma_g^+$ rapidly deactivates into a longer lived $1\Delta_g$ which is called singlet oxygen and it is a very cytotoxic species. Singlet oxygen can be detected at 1270nm through relaxation of the lower excited state to the ground state. Triplet oxygen is an efficient quencher of excited state because of having two low-

lying excited singlet states. An excited sensitizer $^1S^*$ can produce two molecules of singlet oxygen that are shown in sequences in equation 1, 2 and 3.



According to the first equation, formation of the singlet oxygen is an exothermic reaction only if the energy gap between the singlet and triplet state is sufficient for energy transfer which is 95 KJmol^{-1} .

$$E_s - E_t \geq 95 \text{ KJ mol}^{-1} \quad (4)$$

The second reaction however is always possible and it is called oxygen-catalysed intersystem crossing (ISC).

Formation of singlet oxygen can reach to 2 maximum if the $E_s - E_t \geq 95 \text{ KJ mol}^{-1}$ takes place. Otherwise, formation of the singlet oxygen is less than 1. The energy gap between E_s and E_t will be used in chapter 4 to predict singlet oxygen production.

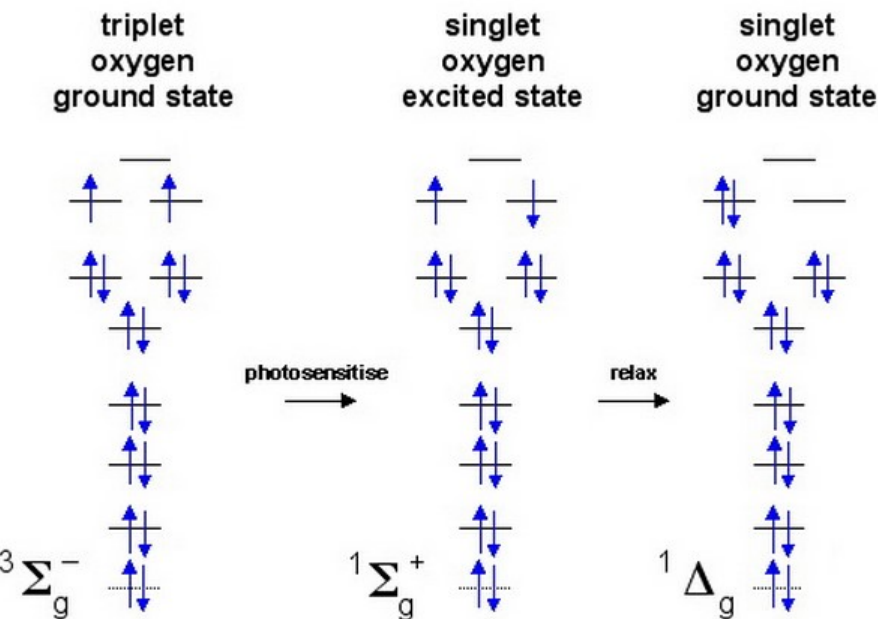


Figure 1-3. Two unpaired π electrons in two degenerate orbitals of triplet oxygen ground state (paramagnetic behavior) give rise to the singlet excited state.

1.1.3 Singlet oxygen formation

The term singlet oxygen ($^1\text{O}_2$) refers to the two lowest energy excited electronic states of oxygen, O_2 ($a^1\Delta_g$ and $\text{O}_2(b^1\Sigma_g^+)$), as shown in Figure 2. $\text{O}_2(b^1\Sigma_g^+)$ is unstable in aqueous media, decaying rapidly to $a^1\Delta_g$ [11]. One way to form $^1\text{O}_2$ involves energy transfer from an excited PS to ground state oxygen $\text{O}_2(X^3\Sigma_g^-)$. Energy transfer can also result in the production of $\text{O}_2(b^1\Sigma_g^+)$ which quickly decays to $\text{O}_2(a^1\Delta_g)$ in solution. $^1\text{O}_2$ can form upon oxygen quenching of the S_1 or T_1 state of the PS but the most efficient $^1\text{O}_2$ precursor is T_1 , which has a longer lifetime than S_1 [10]. In general, the quantum yield of photosensitized singlet oxygen can be stated as:

$$\Phi_\Delta = S_1 \text{ quenching} + T_1 \text{ quenching} \quad (5)$$

where S_1 quenching reflects the amount of $^1\text{O}_2$ produced by ground state oxygen quenching of the PS S_1 state and T_1 quenching reflects the amount of $^1\text{O}_2$ produced by quenching of the PS T_1 state [12].

A detailed and excellent discussion of the lifetime of intracellular $^1\text{O}_2$ is given in the review of Ogilby [10]. A critical point is that data from single cell and ensemble studies indicate that $^1\text{O}_2$ lifetime in a cell is significantly longer than long believed. Early on, time-resolved or photobleaching experiments were used to estimate intracellular $^1\text{O}_2$ levels and gave values of 10-300ns [9, 13-15]. Since then, the development of methods for monitoring $^1\text{O}_2$ from laser-induced phosphorescence, in time-resolved solution-phase experiments, led to lifetimes in H_2O and D_2O -incubated cells of $\sim 3.5 \mu\text{s}$ and $\sim 15-20 \mu\text{s}$, respectively [15-17]. Clearly these values are much longer than long presumed.

Diffusion of $^1\text{O}_2$ through surrounding medium can take place once $^1\text{O}_2$ forms at sites where PS is localized. The distance, d , that $^1\text{O}_2$ subsequently travels has been estimated from the following equation:

$$d = \sqrt{6tD} \quad (6)$$

Thus, d depends on $^1\text{O}_2$ lifetime τ_Δ , the magnitude of diffusion coefficient D and time period t . Bearing in mind that $^1\text{O}_2$ lifetimes of $2 - 3.5 \mu\text{s}$ in H_2O and H_2O incubated cells, $t = 5\tau_\Delta$ ($10 \mu\text{s}$) and a value of $4 \times 10^{-6} \text{cm}^2\text{s}^{-1}$ for D were used to estimate the radial diffusion distance [10]. This led to $d = 155\text{nm}$. At $\tau_\Delta \sim 25 \mu\text{s}$, $d = 550\text{nm}$ was obtained. These results indicate that the long accepted diffusion limit of 10-20nm from the site of $^1\text{O}_2$ formation is no longer appropriate.

Some of the possible reactions that can take place between ${}^1\text{O}_2$ and carbon-carbon double bonds are listed in Figure 1-4. Possible intermediates that can form in [2+2] reactions are represented in Figure 1-5.

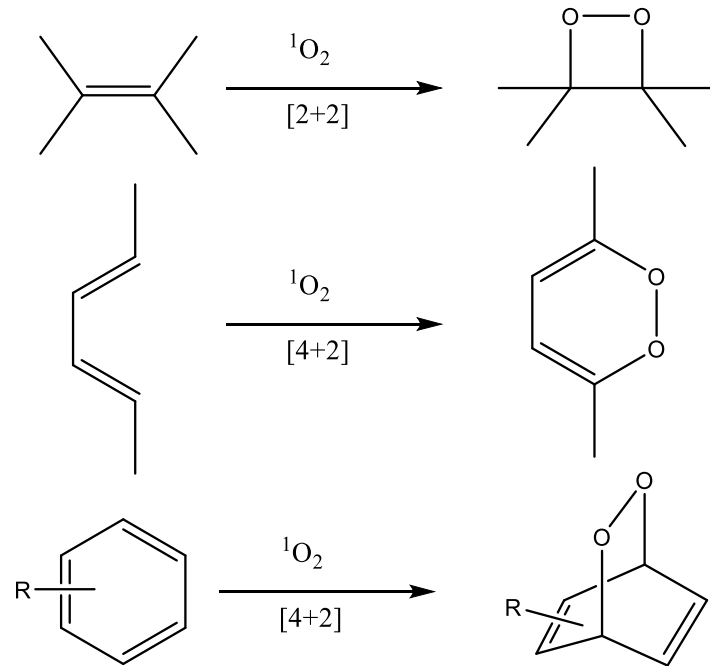


Figure 1-4. Reaction of ${}^1\text{O}_2$ with double bonds

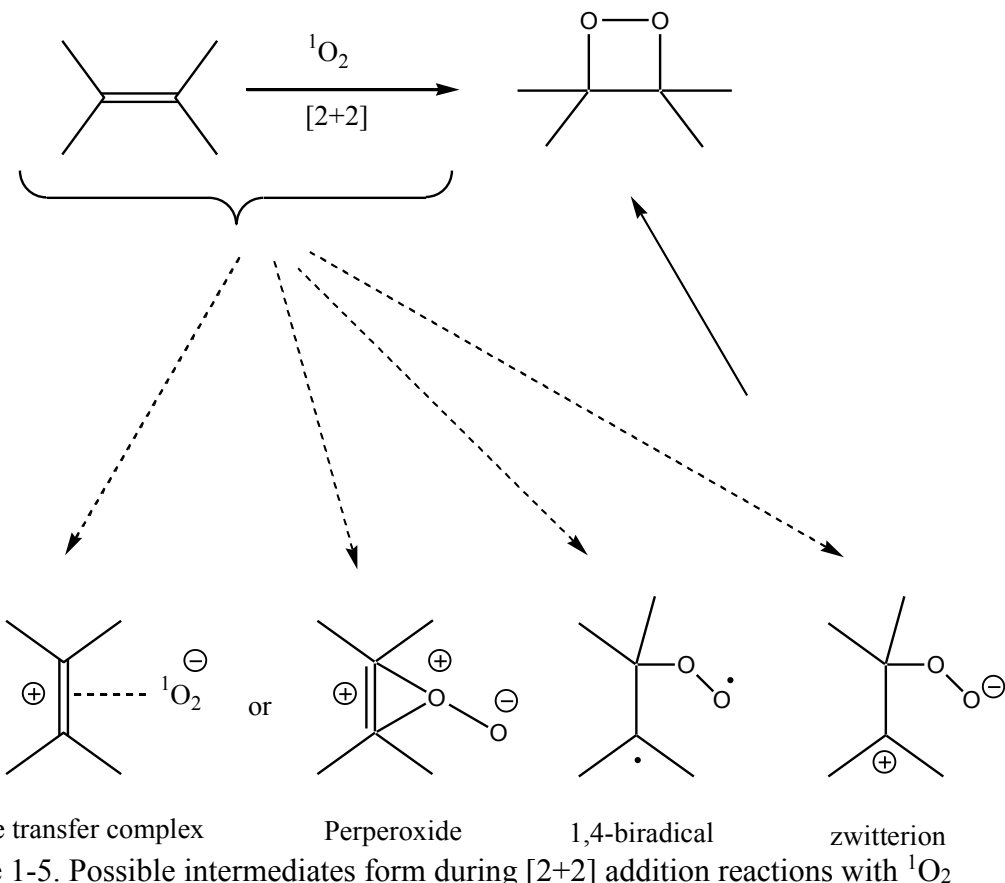


Figure 1-5. Possible intermediates form during [2+2] addition reactions with $^1\text{O}_2$

1.1.4 Mechanisms of cell death

While dependent on many factors, with the subcellular location of the PS being only one, PDT treatment can cause cell death by pathways involving apoptosis and necrosis. Necrosis is an un-programmed cell death that is caused by chemical and physical damage [18]. It is a quick method of degradation that can affect widespread cell populations and can be characterized by cytoplasm swelling, damage to organelles, and disruption of the cell membrane. As a result of necrosis, intracellular contents will be released which leads to inflammation *in vivo*. Necrosis is more likely to happen when high doses of light are being used. Apoptosis is a programmed cell death that can be identified in single cells that are

surrounded by other normal-looking cells and is characterized by cell shrinkage. Apoptotic cells tend to fragment into multiple membrane enclosed spherical vesicles, *in vitro*. These vesicles can be scavenged by phagocytes *in vivo*, and inflammation can be prevented in case of apoptosis and cells die in an immunologically controlled way. [18]. Recent studies have shown that autophagy plays a role in PDT [19]. Autophagy is a process involving the transportation of cellular organelles and proteins through lysosomal degradation pathways and is related to cell survival, development, and differentiation. When proteins undergo irreversible ROS damage forming toxic oxidized protein, autophagy will be stimulated to remove these toxic species. Failure in these mechanisms leads to accumulation of oxidized macromolecules beyond the capacity of the cell to be repaired. In this case, the vital functions of the cells will be compromised which leads to cell death [20].

PSs differ in terms of pharmacokinetics and biodistribution. After their injection into the blood stream, they can bind to endothelial cells, the adventitia of the vessels, then accumulate within the tumor cells or bind to the extracellular matrix. The cytotoxicity induced by the absorbed light is restricted to the area of irradiation [21]. The effectiveness of PDT depends on the stage at which light has been delivered [22]. PDT can also lead to tumor death by deprivation of oxygen and nutrition arising from anti-vascular effects such as hemorrhage or thrombosis in tumor blood vessels [22].

1.1.5 Therapeutic irradiation

To avoid undesired light absorption by biological chromogens instead of the PSs, the λ_{max} of the target PS should be >650nm. Excitation at wavelengths in the near IR region also

leads to deeper light penetration. This range of wavelengths is called the therapeutic irradiation window and is illustrated in Figure 1-6 [23]. Bearing in mind that the energy of the light decreases as wavelength increases, the preferred λ_{max} has been reported to be 630-800nm by some [14] and 650-950nm by others [24]. The molar absorptivity (ϵ_{max}) of a PS should be $>20,000$ to minimize the required dose of the PS for PDT treatment [25].

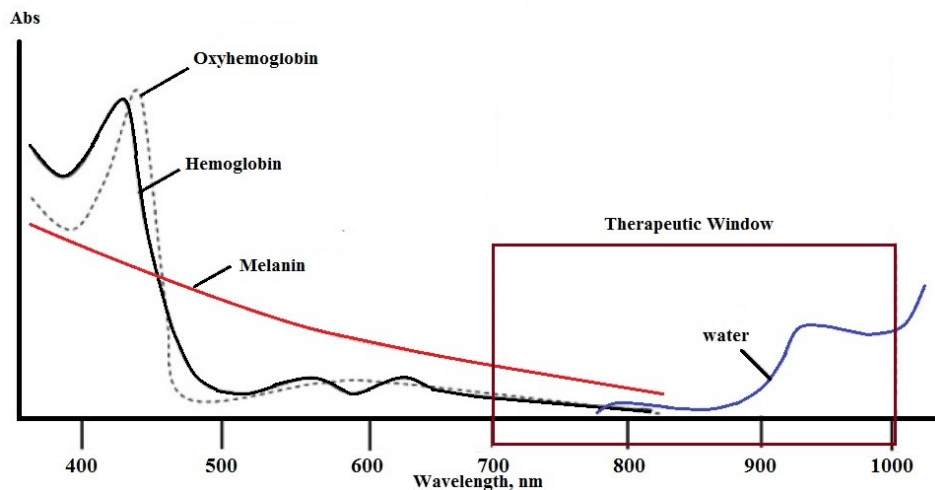


Figure 1-6. Illustration of the therapeutic window for PDT treatment.

1.1.5.1 Importance of subcellular localization.

Controlling the subcellular localization of PS in cells is important because this has an impact on both PDT efficiency and the potential for cytotoxic affects. In this regard, it has been reported that even low levels of singlet oxygen generated in or near the mitochondria is far more efficacious than a large amount generated in the cell nucleus [26]. This opens the door to a pro-drug approach, i.e. forming the PDT-active species at the target site, as an ideal way to minimized unwanted cytotoxic activity. An example is the formation of PpIX from ALA (5-aminolevulinic acid) in the mitochondria. It should be noted, however, that

localization of PS in a subcellular structure does not guarantee that it will remain there. Depending on PS solubility and local concentration gradients it can diffuse out to the cytoplasm. Consequently, the design of PSs capable of bonding to the target site has been suggested [22].

It is also reported that low-level lysosomal photodamage can increase PDT efficiency due to subsequent mitochondrial photodamage. This phenomenon is not related to the amount of ROS formation, but appears to involve an increase in apoptotic signals arising from mitochondrial photodamage [27]. Localization of PS in mitochondria can be observed by using fluorescence imaging to monitor the coincidence of the PS and Rhodamine-123, taking advantage of the utility of Rhodamine-123 as a mitochondria specific stain. Examples of PSs targeting lysosome and mitochondria are listed in Table 1.

Table 1-1. Examples of PSs targeting lysosome and mitochondria.

Photosensitizer Type	Sub-cellular Localization	Reference
N-aspartyl chlorin E6 (NPe6)	Lysosome	[27]
(Benzoporphyrin derivative) (BPD)	Mitochondria	[27]
5-Ethylamino-9-diethylaminobenzo[a]phenothiazinium chloride (EtBNS)	Lysosome	[27]
Galactose conjugate of 3-(1-hexyloxyethyl)-3-devinyl pyropheophorbide-a (HPPHgal)	Lysosome	[27]
Porphyrin-rhodamine B cation	Mitochondria	[28]
Porphyrin-mono-triphenyl phoosphonium cation	Mitochondria	[28]
Triphenylphosphonium (TPP) cation	Mitochondria	[29]
(E)-N-alkyl-4-[2-(ferrocenyl) vinyl]pyridinium cations	Mitochondria	[29]

Relatively new PS compounds targeting mitochondria include Zn(II) N-alkylpyridylporphyrins Figure 1-4. The presence of n-hexyl groups in these cationic compounds increased mitochondrial uptake and distribution. Localization in the vicinity of cytochrome c oxidase caused its inactivation during illumination. Light-induced inactivation accounts for the resultant mitochondrial photodamage and suppressed respiration and cell death [30].

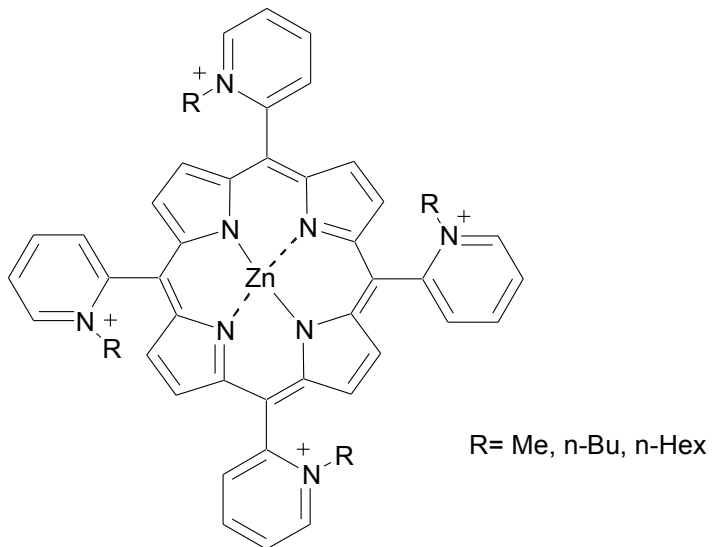


Figure 1-7. Structure of Zn(II) N-alkylpyridylporphyrins designed for mitochondria targeting.

1.2 PS uptake and selectivity

While the formation of ${}^1\text{O}_2$ in the right subcellular location is essential to optimizing PDT efficiency, the proficient delivery of PSs to the right location is the essential starting point. Key considerations associated with achieving this goal are covered in this section.

1.2.1 Effect of hydrophobicity (lipophilicity) and hydrophilicity on cell uptake and selectivity

Arguably, one of the most critical issues in PDT sensitizer design is selectivity. The higher the selectivity, the higher the accumulation of the PS in cancer cells and the less side effects for patients. PS selectivity is influenced by its hydrophobicity/hydrophilicity and can be expressed as the logarithm of the octanol/water partition coefficient ($\log P$) as well as the degree of asymmetry that is present in the PS. Typically, a molecule with average size of the porphyrin, 2,3-dihydroxy-5,10,15,20-tetrakis(3-hydroxyphenyl)porphyrin, with $\log P$ of 9.3 can enter the cells upon diffusion through the phospholipid bilayer [31].

Most of the relatively hydrophobic PSs show sufficient affinity to bind to membranes. Even water soluble PSs such as N-aspartyl Chlorin e6(NPe6), sulfonated porphyrins/phthalocyanines bind to the membrane because they also contain a large hydrophobic ring [32]. An example of an amphiphilic PS that accumulates in lysosomes and endosome *in vitro* and *in vivo* is AlPcS2a [13] and an example of a lysosomal PS is N-aspartyl chlorin e6 (NPe6). It has been demonstrated that PDT using lysosomal NPe6 on living human cell lung adenocarcinoma cell (ASTC-a-1), initiated a mitochondrial apoptotic pathway [33]. Temopofin, known by brand name of Foscan[®], is a lipophilic sensitizer with $\log P$ of 5.5 that tends to aggregate and interact with plasma proteins [8] and cell membranes [34].

Hydrophilic as well as aggregated PSs will be taken up through pinocytosis and/or endocytosis and they will accumulate mostly in the lysosome and endosome. As a consequence of light exposures, lysosomes become permeabilized and the sensitizers and

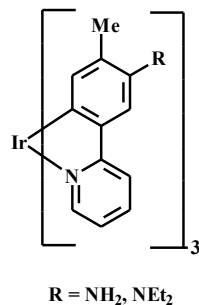
enzymes can be released into the cytosol. As a result, tubulin forms which leads to accumulation of cells in mitosis and causes cell death in some cases [35]. Accumulation of cationic PSs takes place mostly in mitochondria because of the transmembrane potential of the inner mitochondrial membrane [36]. Cationic PSs with a delocalized positive charge tend to localize in mitochondria with a high negative membrane potential of 150-170 mV [29].

One advantage of hydrophilic PSs is their low tendency to aggregate in aqueous media. Aggregation facilitates internal conversion to the ground state which suppresses ISC [37]. Another advantage of hydrophilic PSs is that they decompose or disappear from the body faster, which results in fewer side effects. Consequently, water solubility can increase bioavailability and *in vivo* distribution [38]. The disadvantage of hydrophilic PSs is the low penetration of these compounds through cell membranes compared to hydrophobic PSs. AlPcS is an example of a hydrophilic PS having low cell internalization efficiency [39]. Water soluble phenothiazinium compounds such as methylene blue not only have poor cell/tissue penetration, they also have low stability under reductive biological conditions [40].

Although hydrophobic (lipophilic) PSs have a higher tendency to permeate cell membranes, their tendency to undergo aggregation in aqueous media makes them non-ideal without using a suitable delivery system. Hydrophobic PSs also tend to remain longer in the patient's body compared to hydrophilic PSs. These observations have caused PSs with amphiphilic properties through conjugation with water soluble, amphiphilic polymers and colloidal administrations to become attractive in PDT studies [41-45].

1.2.2 Effect of intracellular pH on PS uptake

PS uptake into various organelles is also affected by internal pH. It is known that the pH of organelles such as the Golgi apparatus, endosomes, and lysosomes are 6.7, 6.5, and 5.5, values that are lower than the pH of the cytosol and mitochondria (7.2–7.5) in normal cells. In addition, it has been reported that the pH of some types of cancer tissues are in the slightly acidic range, viz. < 7.3 . Interestingly, there are few examples of reversible on/off pH-probes that respond to changes in intracellular pH. Regarding pH probes that are sensitive to a change in intracellular pH, Ir-tolylpyridine complexes have been used to selectively stain lysosomes. For instance, a new pH-sensitive Ir(III) complex was developed that contains three N,N-diethylamino groups Figure 1-8. The luminescence emission of the complex produced a band at 554 nm in DMSO, which was ~ 60 nm shorter than the analog having R = NH₂. Protonation of the three NEt₂ groups induced a considerable enhancement in the band at 497 nm. In aqueous media, the emission intensity of this complex at 494 nm was very weak at pH > 7.4 but was considerably enhanced at pH < 7 . In a subsequent study, new pH-responsive Ir(III) complexes were developed, leading to ¹O₂ generation upon irradiation. The induction of necrosis-like cell death of HeLa-S3 cells upon irradiation of at 465 nm was reported [46, 47].



$\mathbf{R} = \mathbf{NH}_2, \mathbf{NEt}_2$

Figure 1-8. Examples of pH responsive Ir(III) complexes.

1.2.3 Use of nanoparticles

One approach to increasing PS selectivity involves using a molecule having high affinity toward cancer cells, such as folic acid [48, 49] or antibodies [50], peptides, LDLs, and polymers [51]. This approach is employed for third-generation PSs wherein the affinity for cancer cells increases by targeting subcellular compartments such as mitochondria [52]. Therefore, third-generation PSs are often second-generation PSs bound to carriers for selective accumulation in tumors [53].

The second approach involves using nanoparticle-based drug delivery methods in PDT. Although amphiphilic PSs or third-generation PSs can enhance selectivity, employing nanoparticles in PDT studies has become very attractive for the following reasons: 1) lower levels of the PSs can be used for PDT treatment; 2) PSs can be used in monomeric form within some of the nanoparticles; 3) most of the FDA approved PDT agents are hydrophobic and nanoparticles can increase the selectivity of these compounds to reduce side effects after treatment as well as aggregation problems; 4) dark toxicity would be less of a problem [54]; 5) exploiting strategies such as pH sensitivity, thermal sensitivity, peptide or antibody tags in nanoparticle system can increase selectivity more efficiently; 6) having control on making

nano particles with a diameter of less than 200nm for better passive targeting through enhanced permeability retention (EPR); 8) increase in cell uptake [36, 44]. Examples of some of the nanoparticles that have been used in PDT studies so far include liposomes [55, 56], micelles, polymeric micelles, carbon nanodots [57], quantum dots, catanionic vesicles [58], gold nanoparticles [59, 60], hydrogels [61], and dendrimer nano particles [62], TiO₂ [63], examples of which are shown in Figure 1-9.

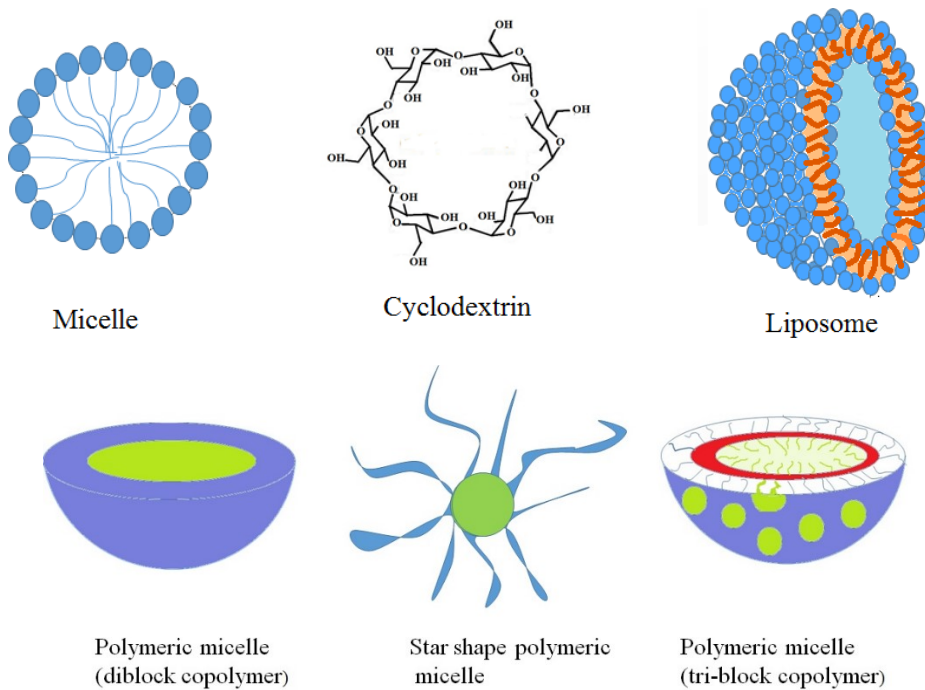


Figure 1-9. Examples of nanoparticle structures developed for PDT treatments.

1.2.4 Polymeric Micelle/micelles

Polymeric micelles are made of amphiphilic block or graft copolymers that form spontaneously in aqueous media due to thermodynamically favored aggregation above the

critical micelle concentration (CMC) [64]. Micelles with lower CMC levels have higher thermodynamic stability, which can be obtained by increasing the hydrophobic section of the amphiphiles [64, 65]. Below the CMC level polymer chains tend to remain in the monomolecular state. As their concentration in water increases, however, the hydrophobic component tries to escape water and forms the inner core. Subsequently, the hydrophilic head interacts with water on the surface of the spherical micelle and forms the corona. Formation of the micelle core is due mainly to hydrophobic interactions as well as hydrogen bonding of constituted block copolymer, metal complexation and electrostatic interactions [66]. A feature of polymeric micelle is illustrated in Figure 1-10.

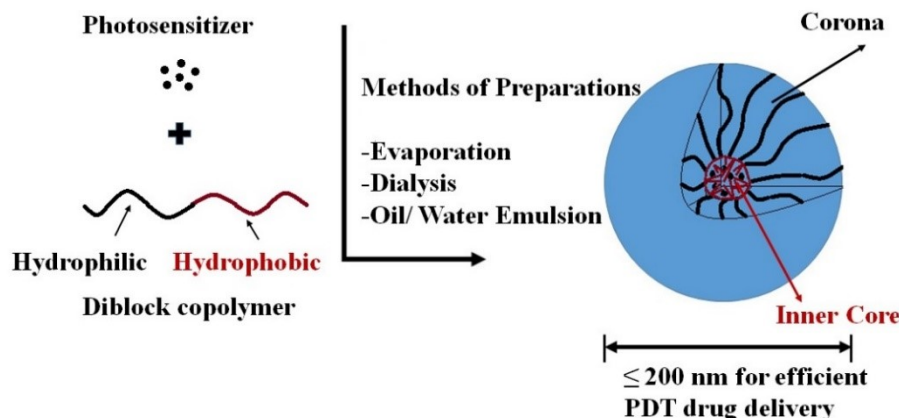
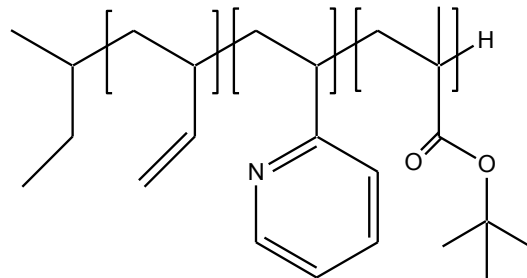


Figure 1-10. Schematic representation for spherical polymeric micelle formation via different methods. Co-solvent evaporation [67], dialysis [68], oil/water emulsion.

Having the hydrophobic core enable micelles to entrap hydrophobic PSs via secondary valency forces or electrostatic interactions. The use of nanoparticles such as polymeric micelles provides the framework for next generation PSs [69]. In addition to

diblock copolymers, tri-block copolymers, Figure 1-11 [70], star-shaped polymers [67, 71] can be used to form micelles. In some cases the polymer component is a polypeptide [72].



polybutadiene-block-poly(1-methyl-2-vinyl pyridinium methyl sulfate)-block-poly(methacrylic acid) (BVqMAA) triblock terpolymers

Figure 1-11. Example of a tri-block copolymers used to form polymeric micelles.

Studies in this area have taken into consideration that the PS employed may concentrate in the tumor cells via active and passive-targeting strategies [73]. Using artificial carriers such as cationic liposomes, silica nanoparticles and polymeric conjugates can prolong the plasma circulation half-lives of the PS and increase its accumulation in tumors through enhanced permeability and retention effects [73, 74].

The passive targeting mechanism takes advantage of an “enhanced permeation and retention” (EPR) process. EPR allows preferential extravasation of drugs though leaky vasculatures, due to having an incomplete endothelial barrier and poor lymphatic drainage in most of the tumor structure [75, 76]. Stimuli-responsive polymeric micelles giving controlled release upon pH and temperature changes can be used to increase PS delivery to the specific target [77]. Salt concentration, magnetic fields, light [70], chemical auxiliaries and enzymes

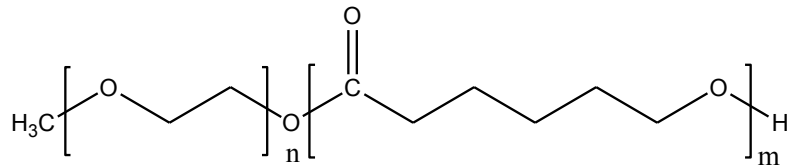
[78, 79] are types of stimuli than can be used. In addition to the EPR mechanism, active targeting facilitates penetration of the PS carrier into the cancer cells via surface functionalization of the nanocarrier with a specific molecular motif such as an antibody or peptide. EGFR-targeting peptide ligand GE11 has been used to target head and neck squamous cell carcinoma H&N SCC cells *in vivo* and *in vitro* [75]. Active targeting prevents one of the problems associated with passive targeting, which is nanoparticles accumulated in the tumor stroma passively can be redistributed into the blood stream, which reduces selectivity [80].

One of the advantages of polymeric micelles over standard micelles made from compounds such as polysorbate 80 (Tween 80[®]) is their higher stability in solution. Also, polymeric micelles can solubilize a larger amount of the PDT agent and they are suitable for parenteral administration [64]. Micelles can be made of amphiphilic peptides. These amphiphiles can form spherical to nanofiber structures due to hydrogen bonding and hydrophilic interactions. Using lysine as a sub-unit, the hydrophilic component will be ionized at acidic pH levels and the micelles become destabilized due to electrostatic repulsion interactions [79].

Other advantages of polymeric micelles include ease of preparation, efficient drug loading, controlled drug release, and extended blood circulation that allows efficient targeting through the EPR effect. This also reduces the undesirable bio-distribution of hydrophobic compounds [81]. Polymeric micelles are one of the nanocarriers that can resolve the hydrophobicity and/or toxicity drawbacks of many PSs [72]. Polymeric micelles with diameter size of 10-200 nm can be used for drug delivery because they are large enough

to escape rapid renal clearance and small enough to avoid removal by reticuloendothelial clearance (RES). Therefore, permeability and retention (EPR) in tumor tissue will take place more effectively in vascular architecture that is leaky or defective around tumor cells [69, 77]. Usually the hydrophilic end of the molecule is PEG and this forms small size micelles (10-100 nm) [82].

One drawback of having long circulating polymeric micelles is unwanted photoactivity in normal cells. Li and co-workers showed that PEG-b-PCL, Figure 1-12, containing a generator and scavenger of ${}^1\text{O}_2$ combination can reduce phototoxicity in normal cells [81].



Poly(ethylene glycol)-b-poly(caprolactone) (PEG-b-PCL)

Figure 1-12. Structure of PEG-b-PCL.

To increase the inherent biocompatibility and bioactivity of micelles, peptides can also be used. The problem with these types of micelles is a low hydrophobic tail interaction that decreases the stability of the micelles. This problem can be resolved by increasing the number of hydrophobic tails. Formation of a stable micelle is achieved by utilizing a surfactant-like amphiphilic peptide, Figure 1-13, with four hydrophobic tails [83].

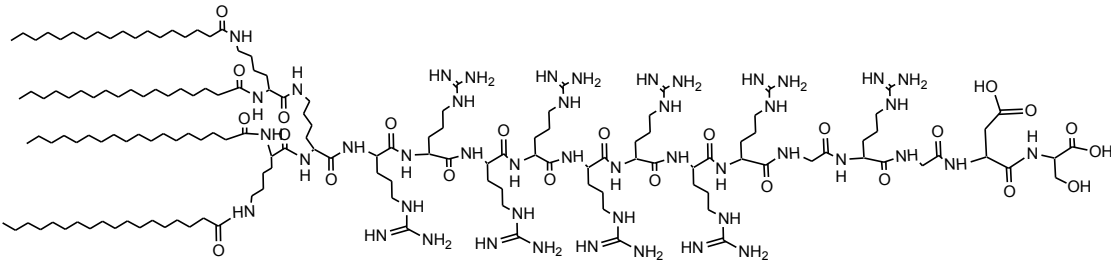


Figure 1-13. Structure of a surfactant-like tetra-tail amphiphilic peptide.

Another advantage to using polymeric micelles is the ability to protect unstable PSs such as 5-ALA in aqueous media at neutral to basic pH. 5-ALA is a pro-drug that can be converted into protoporphyrin IX (PpIX) in proliferating cancer cells versus normal cells. 5-ALA is also very polar which limits its diffusion through membranes. Conjugation of PpIX to PEG-PLA, Figure 1-14, increases PDT efficiency [84]. Hydrophobic PS conjugated to hydrophilic polymers can self-assemble into nanoparticles [85].

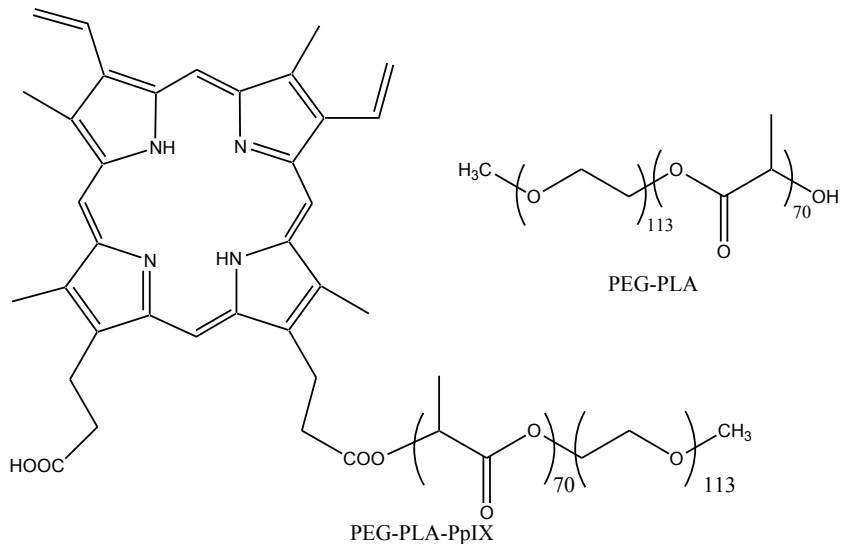


Figure 1-14. Conjugation of protoporphyrin IX to PEG-PLA.

Controllable release is another advantage of using polymeric micelles. Trigger-controllable release of the PDT sensitizer by L-phenylalanine was reported for biodegradable supramolecular polymer micelles (SMPMs). In response to an additional L-phenylalanine molecule, SMPMs disassemble due to interactions between L-phenylalanine and sensitizer-loaded SMPMs [86]. To increase the stability of the polymeric micelles nanoparticle, it can be mineralized using calcium phosphate [72].

One way to influence sensitizer release from polymeric micelles is to take advantage of the pH difference between the extracellular of normal cells vs tumor tissue. The extracellular pH of tumor tissue is typically 6.4-6.8, due to accumulation of lactic acid [87], while the extracellular pH is 7.4 for normal cells. However, only a few pH sensitive polymers are responsive to the extracellular pH of tumor tissue and others are sensitive to endosomal or lysosomal pH. PH-Responsive MPEG poly(β -amino ester) polymeric micelles

are responsive to extracellular tumors. This type polymer micelle is pH responsive due to its tertiary amines [77], an example of which is shown in Figure 1-15.

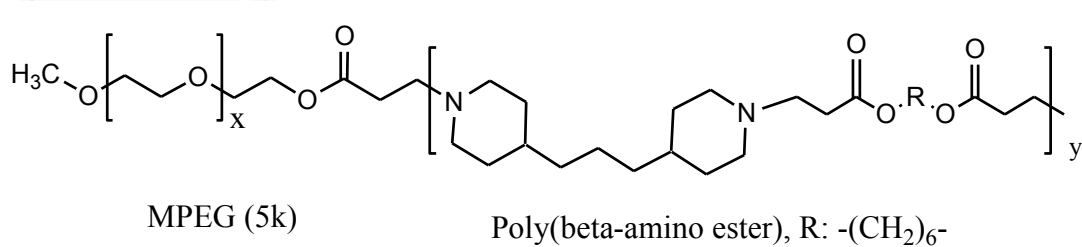


Figure 1-15. A pH sensitive MPEG poly(β -amino ester) structure for micelle formation.

Some of the recent studies involving the use of polymeric micelles are summarized in Table 2, and examples of polymer structures are shown in Figure 1-16.

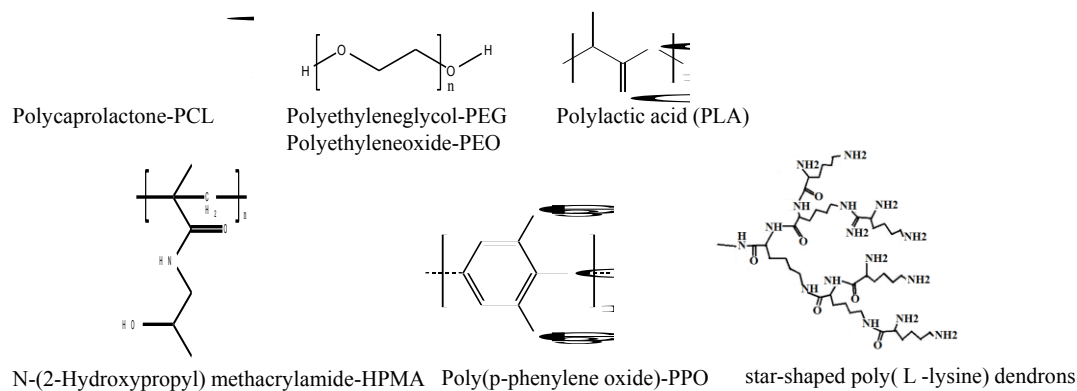


Figure 1-16. Examples of structural units reported in Table 2.

Utilizing DSPE-mPEG₂₀₀₀ micelles, 89% of hypericin was encapsulated and sub-localization into mitochondria occurred. Phototoxicity increased 2.5-fold compared to the case involving PEGylated PSs [88]. Drug loading efficiency for MPEG-poly(β -amino ester) block copolymer of 70-80% was reported for PpIX [77]. Using PEO₇₅₀-b-PCL₅ polymer

increased the cell uptake by 60% for phenophobide [69]. Loading capacity of encapsulated PpIX will increase from 0.2 to 4% by conjugation of the PpIX with PEG-PLA [84]. Highest loading capacity was observed using micelles containing benzoyl and naphthoyl end groups. The loading capacity for these micelles was 30% w/w [82]. Phototoxicity of dendrimer phthalocyanine encapsulated in PEG-PLL increased by 100-fold compared to the dendrimer phthalocyanine itself, Figure 1-17 [89].

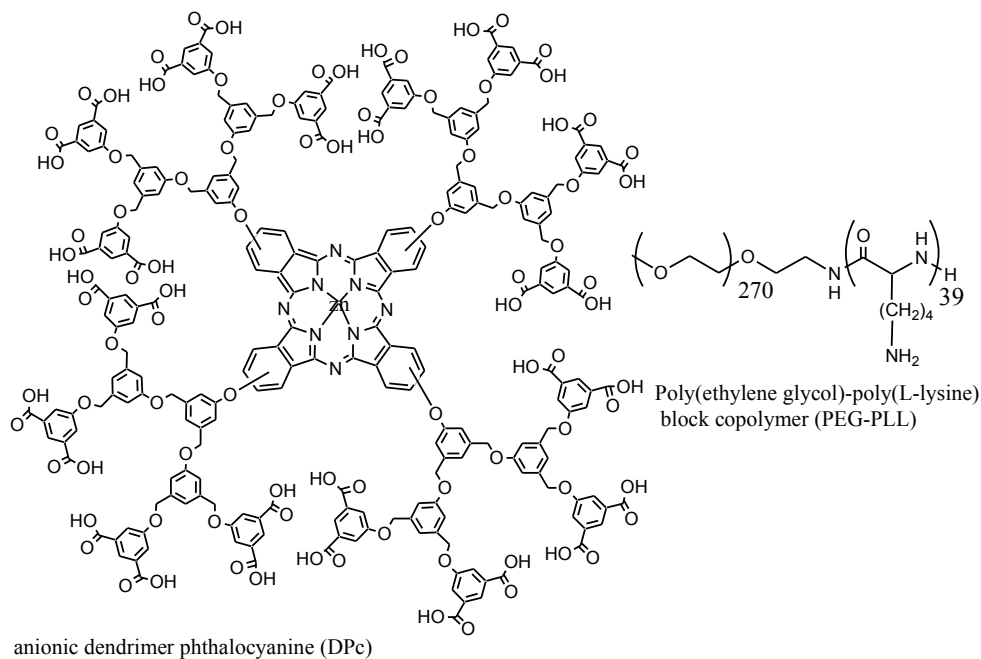


Figure 1-17. A dendrimer-based phthalocyanine structure for sensitizer delivery.

Many studies using nanomedicine technologies have been conducted. However, translating these studies into clinical application will not be possible if the parameters needed to maximize cell killing were not reported. As an example, optimized or maximum cell internalization is reported as $\leq 2\text{h}$ for A431 cells and takes place when a 10 mol% EGFR-PEG-PCL-GE11 component is used in micelle formulation [90].

Table 1-2. Examples of polymeric micelles/micelles tested *in vitro* and *in vivo* for PDT.

Strategy for Targeting & Drug Release	Sensitizer	Polymer/monomer	Loaded particle size(nm)	<i>In vitro/In vivo</i>	Ref
Active targeting	Silicon phthalocyanine	PEG-PCL-GE11 Peptide (YHWYGYTPQN VI)		Human epidermoid carcinoma and head & neck cancer	[75, 80]
Active targeting Folate amino acid and overexpressed folate receptor	THPC	Poly (2-ethyl-2-oxazoline)- <i>b</i> -poly(d, l-lactide) (PEOz-PLA) (m-THPC-PM) (folate-m-THPC-PM)	103.8	<i>In vitro</i> on epidermoid cell line (KB); <i>In vivo</i> on KB xenograft mice	[77, 91]
Active Galactosyl moiety for increased selectivity toward ASGP receptors on HepG2 cells	Porphyrin (conjugated to polymer)	APP-PAEMA_PCL Gal-APP-PAEMA-PCL	60	Human laryngeal carcinoma (HEp2); Human hepatocellular liver carcinoma (HepG2)	[68]
Passive Cellular endocytosis	Doxorubicin (DOX)	Star shaped poly(L-lysine) dendrons porphyrin polymer (PP-PLLD)	150-192.5	Human nasopharyngeal carcinoma (CNE2)	[71]
Passive targeting; Dual chemo-photodynamic therapy	Paclitaxel Synthetic chlorin	Star-shaped di-block copolymer (CSBC-58)	103.2	Breast cancer (MCF7)	[67]

Table 1-2 continued

Passive targeting	Pheophorbide a (phA) & β -carotene(CAR)	Poly(ethylene glycol)-b-poly(caprolactone) PEG-b-PCL	100	Human breast and cervical cancer cell line	[81]
Passive targeting	Chlorin e6	Poly(ethylene glycol)-b-poly(l-aspartic acid)-b-poly(l-phenylalanine) (PEG-PAsp-PPhe)	74.6	<i>In vitro</i> assay on MCF7	[72]
Passive targeting (endocytosis); Dual chemo-PDT	<i>m</i> -THPC SN-38	Chlorinated core star shape block copolymer (CSBC)	115.7-163.7	Human colon cancer (HT-29); <i>In vivo</i> xenograft	[76]
Passive targeting Dual photothermal (PTT) and PDT	IR825 Chlorin e6	C18PMH-PEG-Ce6-Gd	100-200	<i>In vitro</i> and <i>in vivo</i> assay on 4T1 Cell line	[92]
Passive endocytosis	Dendrimer phthalocyanine DPc	DPc+(PEG-PLL) \rightarrow (DPc/m)	50	A549 cells in mice	[89]
Passive targeting Accumulate in mitochondria	Hypericin	DSPE-mPEG ₂₀₀₀ micelle	12	Malignant brain tumor (MBTs)	[88]

Table 1-2 Continued

Enzyme control release (in presence of L-phenylalanine)	THPP	Ethyl cellulose-graft-poly(ϵ -Caprolactone) and alpha cyclodextrin → EC-g-PCL and α -CD	205	85% THPP release in 6 h; MCF-7	[86]
Passive pH responsive polymeric micelles	PpIX	MPEG-Poly(β -amino ester) block copolymer (PpIx-pH-PMs)	122	<i>In vivo</i> on live SCC7 tumor-bearing mice; <i>In vitro</i> on SCC7 cells	[77]
Passive targeting	Pheophorbide	PEO ₇₅₀ -b-PCL5 polymer	20	Human breast cell line (MCF-7)	[69]
Passive targeting	Porphyrazine	Polybutadiene-block-poly(1-ethyl-2-vinyl pyridinium methyl sulfate)-block-poly(methacrylic acid) (BVqMAA) triblock terpolymers	256	<i>In vitro</i> assay on A549 cells; Diameter size 6-12% loading; <i>In vivo</i> assay	[70]
Passive targeting	Chlorin e6/Fe ₃ O ₄	Multimeric grain-marked micelles with Fe ₃ O ₄ inner core and outer multi grain micelle PLLA-b-PEG-Ma	98	KB tumor-bearing nude mice <i>in vivo</i> ; KB cells line <i>In vitro</i>	[93]
Passive targeting	PpIX	PEG-PLA	30	H2009 lung cancer cells	[84]

Table 1-2 Continued

Polymer degrades at site of action due to presence of lipase	<i>m</i> -THPC	mPEG750-b-oligo(ϵ -caprolactone)5 (mPEG750-b-OCL5) with a hydroxyl, benzoyl or naphthoyl end group		<i>In vivo</i> ; <i>In vitro</i> on head & neck squamous carcinoma cell line UM-SCC-14C	[82]
Study the effect of the length of hydrophobic units, PPO, on phototoxicity and solubility	ZnPc	Poloxamine polymers: T304 (15-PEO unit, 17.1-PPOunit) T904 (60.9-PEO unit, 69.3-PPO unit) T1107 (238.6-PEO unit, 77.6-PPO unit) T1307 (286.4-PEO unit, 93.1-PPO unit)	2.7 4.9 13.9 47.6	KB cells; Increase in phototoxicity and ZnPc solubility by increasing PPO unit	[64]
Passive targeting	Xanthene dye erythrosine B (ERY)	CTAB (cationic) micelle SDS (anionic) micelle		logP of 0.46 (hydrophilic dye)	[94]
Tri-block copolymer	Gn-DPcZn	Polyion micelle; Amphiphilic triblock copolymer; PLL-b-PEG-b-PLL		High stability <i>in vivo</i>	[95]
Passive targeting	Pheophorbide	PEO(2000)-b-PCL(2800) PEO(5000)-b-PCL(4000) PEO(2400)-b-PDLLA(2000) PEO(3100)-b-PS(2300)	20-30	HCT-116 human colorectal carcinoma	[96]

1.3 Increased $^1\text{O}_2$ Production

1.3.1 Incorporation of heavy atoms

The ability to produce satisfactory levels of $^1\text{O}_2$ is a critical characteristic of PDT sensitizers and correlates with increasing the triplet excited state lifetime of a PS [97, 98]. Increased triplet state lifetime can occur by increasing ISC efficiency. One way to increase ISC is by incorporating heavy atoms into the sensitizer structure, as illustrated for eosin and rhodamine in Figure 1-18 [99-101]. A closed-shelled diamagnetic metal is better suited than an open-shelled paramagnetic metal because the latter shortens the triplet lifetime and makes certain chromogens photo-inactive. Halogenation of the rings in the phthalocyanine (Pc) system, Figure 1-19, also increases the $^1\text{O}_2$ quantum yield, which can be explained using the principles of spin-orbit coupling. In this regard a bathochromic shift in absorption maxima as well as an slight increase in $^1\text{O}_2$ production was observed by substituent of H with halogens and follows the order of Cl < Br < I. Temperature, media viscosity and oxygen concentration can also influence $^1\text{O}_2$ production [37]. The development of complexes contain Ir is another approach to increasing $^1\text{O}_2$ levels. For instance, cyclometalated Ir(III) complexes such as fac-Ir(ppy)₃ 1 (ppy = 2-phenylpyridine) and fac-Ir(tpy)₃ 2 (tpy = 2-(4'- tolylpyridine)) have unique photophysical properties as phosphorescence materials, since they possess high luminescent quantum yields and have relatively long phosphorescent lifetimes ($\tau \sim \mu\text{s}$) [47]. The highly efficient spin-orbit coupling of Ir(III) metal ion in the complexes promotes ISC to the triplet state. Consequently, these complexes exhibit strong phosphorescence even at room temperature. The authors also used DFT calculations to show that protonation of the

pyridyl groups narrows the HOMO–LUMO energy gap and induces a red-shift in the emission wavelength [47].

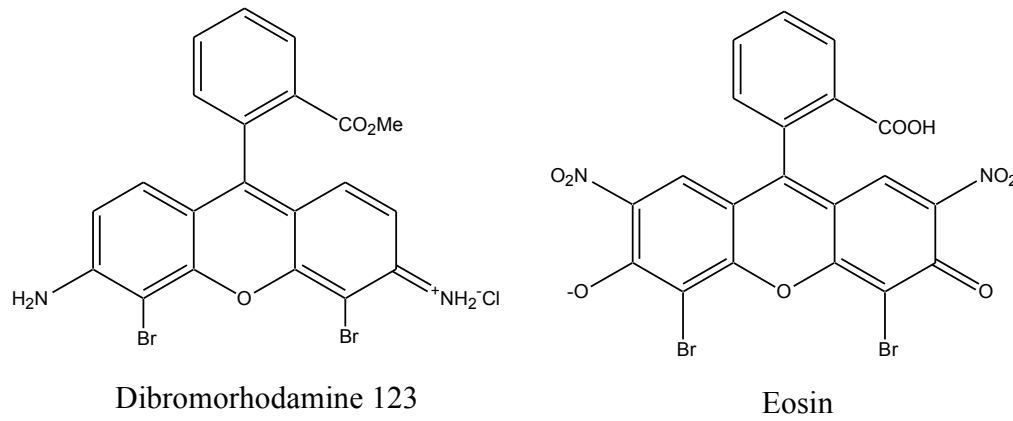


Figure 1-18. Eosin and dibromorhodamine structures containing heavy atoms.

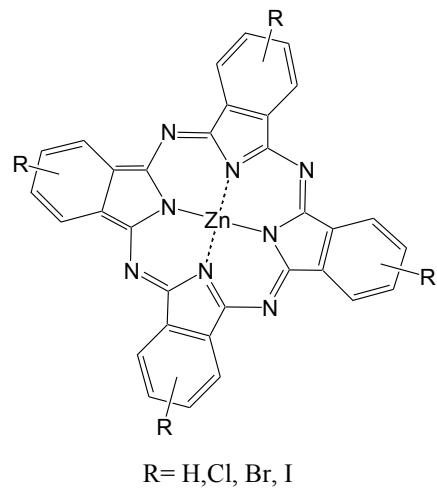


Figure 1-19. Halogenated Zn-Pc structures for enhanced ${}^1\text{O}_2$ formation efficiency.

Incorporation of Ag (III) into N-confused porphyrin (H_2N_2CP) can also increase the efficiency of 1O_2 generation, Figure 1-20, by increasing ISC efficiency to the triplet state

[102]. Incorporating heavy metals in 5,10,15,20-tetrakis(pentafluorophenyl) porphyrin, Figure 18, increased $^1\text{O}_2$ quantum yield from 0.28 to 0.89 and 0.92 for Pd(II) and Pt(III), respectively [103].

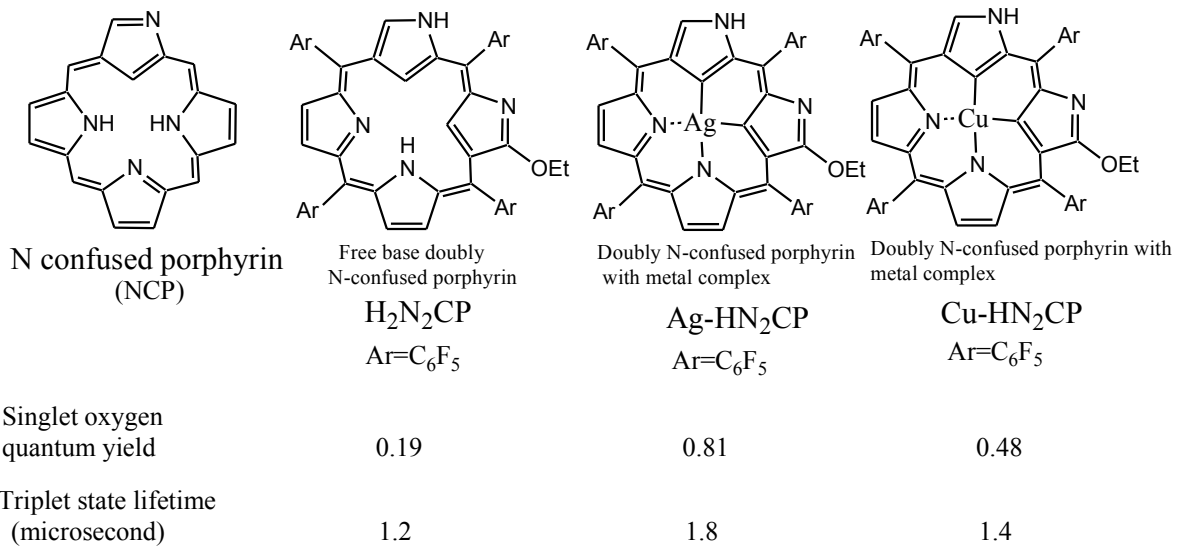


Figure 1-20. Properties of N-confused porphyrin ($\text{H}_2\text{N}_2\text{CP}$) with and without metal atoms.

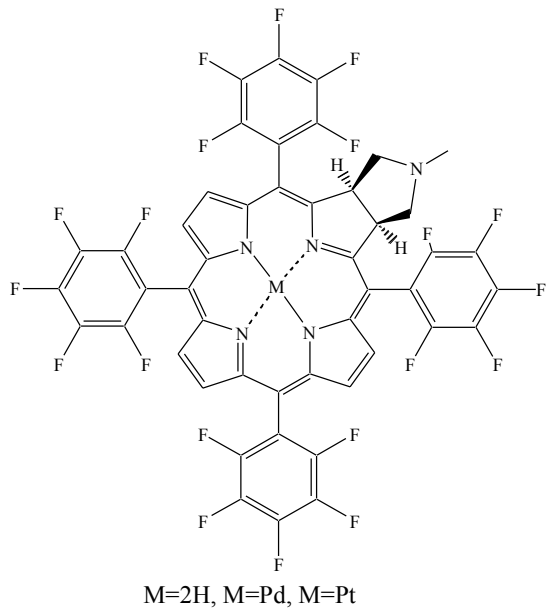


Figure 1-21. Pd- and Pt-complexed 5,10,15,20-tetrakis (pentafluorophenyl) porphyrin structures.

Up to a 70% increase in $^1\text{O}_2$ quantum efficiency was reported for Mg tetrabenzoporphyrin containing a pyridine ligand, Figure 1-22 [104]. Placing one or five Zn atoms into a picolylamine-based porphyrin raised the $^1\text{O}_2$ quantum yield from the 0.5 to 0.82 and 0.92, respectively [105].

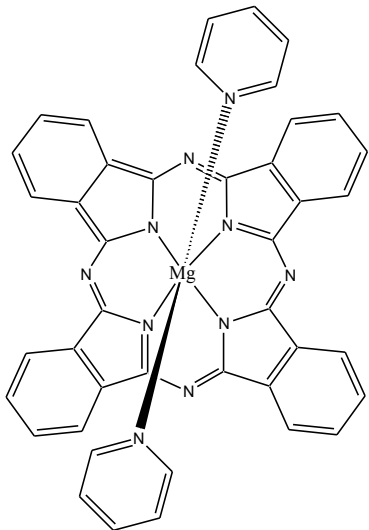


Figure 1-22. A Mg tetrabenzoporphyrin having high ${}^1\text{O}_2$ quantum efficiency.

1.3.2 Isosteric replacements

Structures for enhancing intersystem crossing in polymethine-like molecules were developed, by replacement of oxygen atoms by sulfur in the squaraine system, as illustrated in the Figure 1-23. This replacement facilitates $\text{S}_1(\text{n}\pi^*) \rightarrow \text{T}_1(\pi\pi^*)$ and the magnitude of the resultant ISC rate constant increased ${}^1\text{O}_2$ quantum efficiency [106, 107].

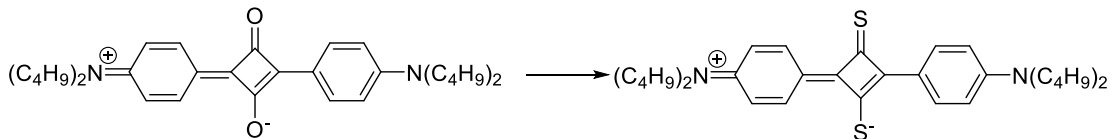


Figure 1-23. Modification of the squaraine system to increase ${}^1\text{O}_2$ quantum efficiency.

In the case of porphyrin and phthalocyanine systems, the conformation and the symmetry of these molecules also affects ${}^1\text{O}_2$ production [108]. In a study by Roder and coworkers, it was shown that the addition and the number of ethyl groups in

tetraphenylporphyrins effected a gradual change in properties such as $^1\text{O}_2$ production and ISC. The ISC and $^1\text{O}_2$ quantum yield values for tetraphenylporphyrins with and without Zn are summarized in Figure 21. These measurements were conducted in DMF [109].

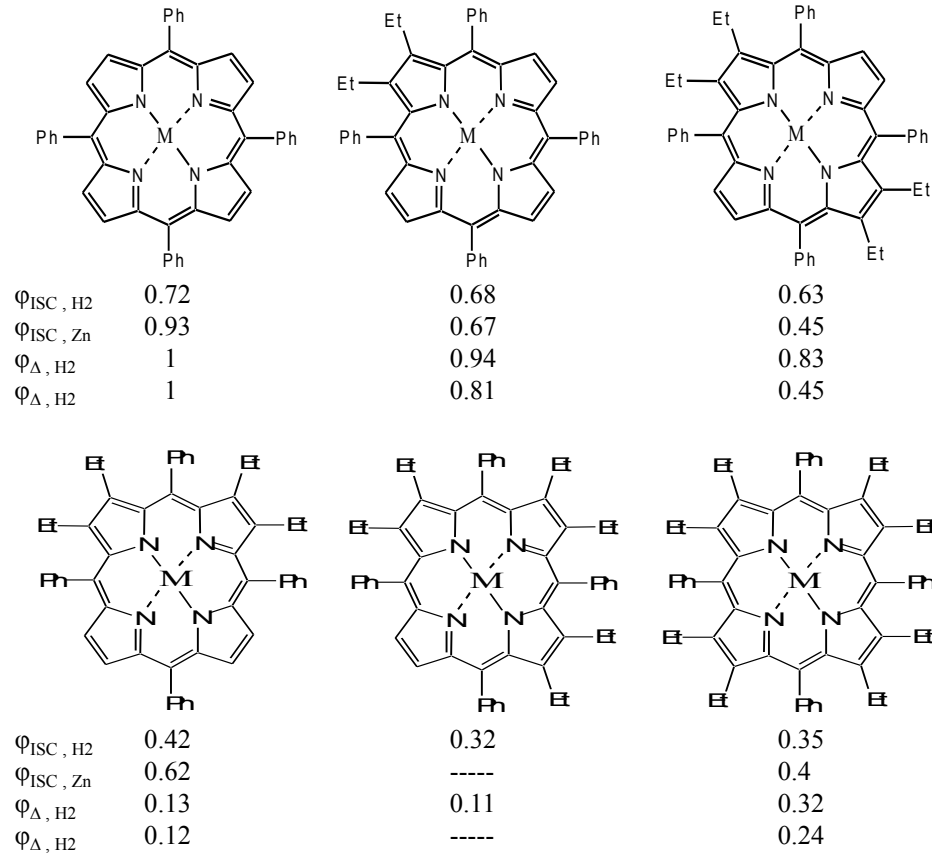


Figure 1-24. $^1\text{O}_2$ quantum efficiency values for various tetraphenylporphyrins.

Incorporation of 1-4 bromine atoms into the porphycene macrocycle, Figure 1-25, changed $^1\text{O}_2$ efficiency from 0.36 to 0.9, 0.95, 0.71, and 0.49. It was also found that the symmetry and geometry of the molecules affected $^1\text{O}_2$ production [110]. Unsymmetrical halogenated aniline-based squaraines, Figure 1-26, include an iodinated derivative giving increased $^1\text{O}_2$ production [111]. Molecules with higher symmetry have a similar singlet and

ground state geometry. This similarity in geometry led to increased fluorescent quantum yield and reduced ISC efficiency.

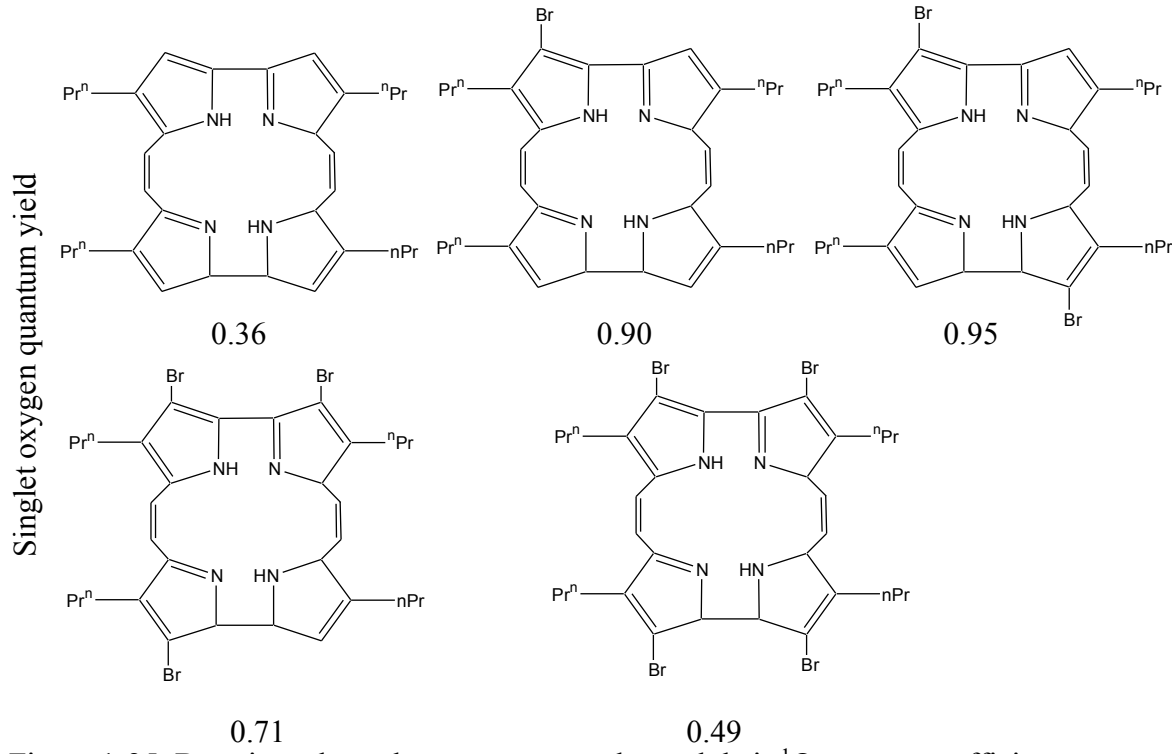


Figure 1-25. Brominated porphycene macrocycles and their ${}^1\text{O}_2$ quantum efficiency.

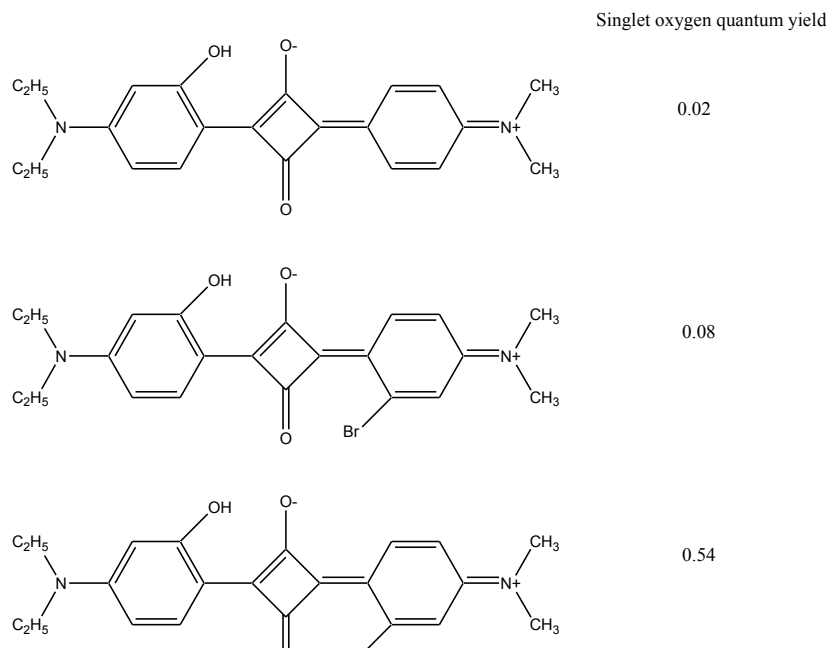


Figure 1-26. Iodinated squaraine giving enhanced $^1\text{O}_2$ quantum efficiency

It is believed that the use of heavy atoms to encapsulate a PS enhances ISC and thus $^1\text{O}_2$ quantum efficiency. With this in mind, Pt(IV)- and Au-modified silica nanoparticles were developed as a delivery system for enhancing the PDT effectiveness of hypocrellin A (HA). Comparing $^1\text{O}_2$ efficiency results from encapsulating HA with and without Pt- and Au- modification, indicated that including one of these heavy atoms as a dopant increases $^1\text{O}_2$ generation [112].

Cyclometalated Ir complexes have grown in interest as PSs, due to recognition of their high quantum yields of triplet formation, long lifetimes of the excited triplet state (typically in the μs range), and triplet energy high enough to allow for the energy transfer process. Further, it has been shown that they are usually resistant to attack by $^3\text{O}_2$. However,

disadvantages such as low H₂O solubility hinder biomedical applications of these complexes. To address this concern, the synthesis and photochemical characterization of a water-soluble Ir–PhenISA conjugate was undertaken, the results of which showed that binding to a suitable polymer improved the photophysical properties of the Ir emitters. In this regard, bis - (cyclometalated) Ir complexes appended to the polymer afforded triplet metal-to-ligand charge transfer excited states that can either radiatively decay or react with ³O₂ and can then be exploited for either imaging or PDT applications. It has been found that photoluminescence can be triggered by two-photon excitation, which offers advantages over traditional one-photon excitation in terms of less cellular damage and deeper light penetration *in vivo*. Specifically, binding an Ir(III) complex (triplet emitter) to a poly(amidoamine) gave the Figure 1-27conjugate [9], doubling the luminescent quantum yield and demonstrating their potential use as both cell imaging agents and PSs for ¹O₂ generation.

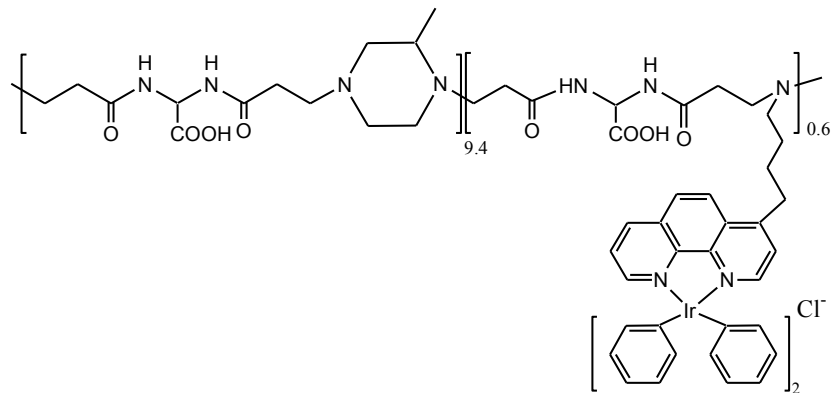


Figure 1-27. Poly(amidoamine) Ir(III) complex as a new ¹O₂ sensitizer.

A group of water-soluble IR-bipyridyl complexes Figure 1-27 displayed significantly reduced cytotoxicity, with half maximal inhibitory concentration (IC₅₀) values being up to

10^2 μM after a 48-h incubation, which were ~ 90 times larger than values from their PEG-free counterparts. It is believed that the reduced cytotoxicity originates from the PEG pendants, which prevent the complexes from interacting with intracellular DNA, proteins, and organelles [9, 73, 113]. The authors studied the photophysical and photochemical properties of their Ir(III) PEG complexes and their PEG-free counterparts and found that ${}^1\text{O}_2$ production efficiency was closely related to the emission lifetimes of the complexes, which can be systematically controlled by changing the cyclometalating ligands. The cellular uptake efficiency of the PEG complexes was lower than their PEG-free counterparts. Since all these PEG complexes were noncytotoxic in the dark, but exhibited considerable light-induced cytotoxic activity, they have potential to serve as efficient PS for PDT. It was also confirmed that the PEG complexes were localized in the mitochondrial region, facilitating efficient oxidative damage of this cellular organelle and causing necrotic cell death upon light excitation [73].

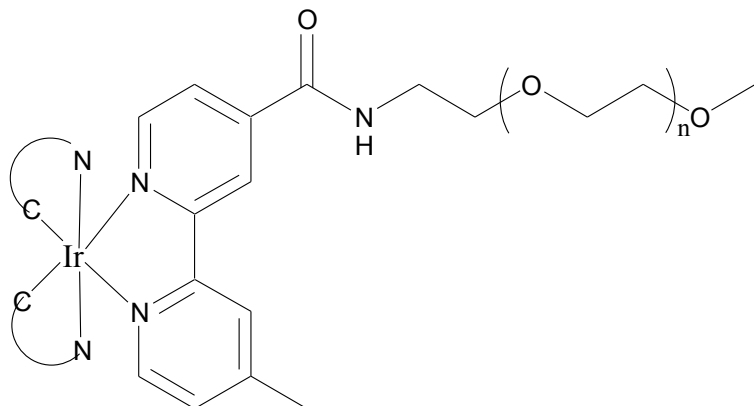


Figure 1-28. Ir(III) PEG complexes as new ${}^1\text{O}_2$ sensitizer.

1.3.3 Two photon systems

Approaches to increasing triplet state efficiency by designing molecules capable of absorbing two photons simultaneously in the same quantum event. The associated electron donor (D) acceptor (A) combinations are linked through a conjugated linker (π -bridge) and are symmetrical or asymmetrical, forming (D- π -D) or (A- π -A), (D- π -A)[114], (A- π -D- π -A) and (D- π -A- π -D) structures [115]. Two photon absorption (TPA) is very attractive for biological application which require NIR absorbing systems [116]. One approach to increasing TPA efficiency is to incorporate a light harvesting dendrimer (antenna) containing chromophores that funnel the excited-state energy of the PS without changing the desired photochemical and photophysical properties of the porphyrin, Figure 1-29[116].

Two-photo activated PDT (2- γ PDT) provides the potential for treating deeper tumors and/or enhancing tumor targeting. Pyropheophorbide-a methyl ester (MPPa) has been used to study one- and two-photon activated PDT and it was found that femtosecond laser pulses at 674nm provides 1- γ PDT efficacy against cervical, lung, and ovarian cancer cells. It was also shown that MPPa can be activated by a 120 fs laser at 800nm at a light dose causing no detectable phototoxicity [117].

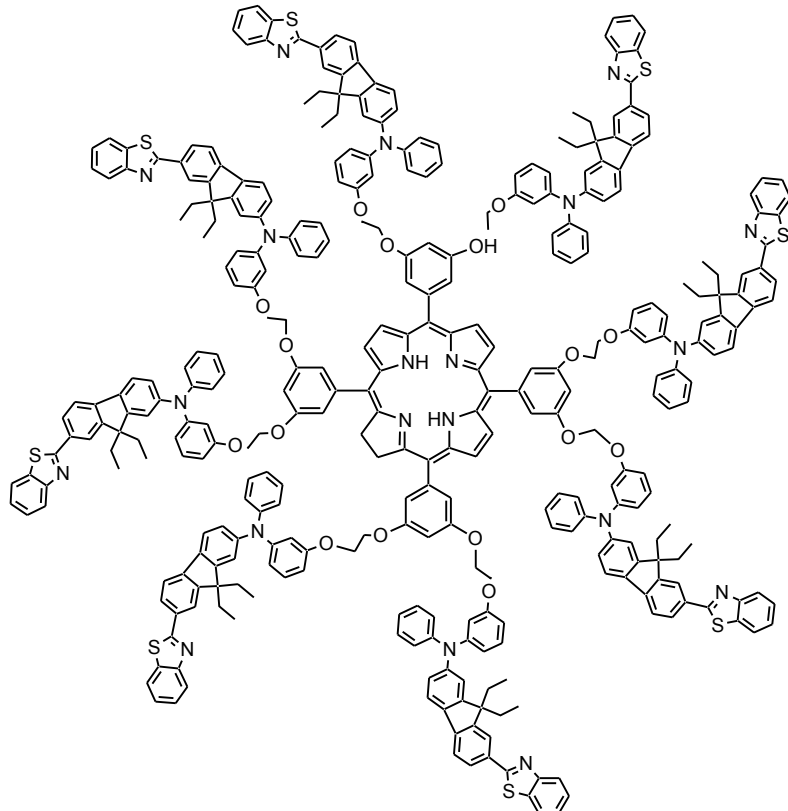


Figure 1-29. A light harvesting dendrimer having fluorescence resonance energy transfer

The addition of π -conjugation to Ru(II)-based PSs has been studied. The sensitizing ability of the complex increased by addition of one or two pyridine-quinoline hybrid systems to an anthracene unit. While the addition of two heteroaromatic ligands had a beneficial effect, adding a third group to the complex reduced photosensitization which is due to the bulkiness of the whole system, Figure 1-30[118].

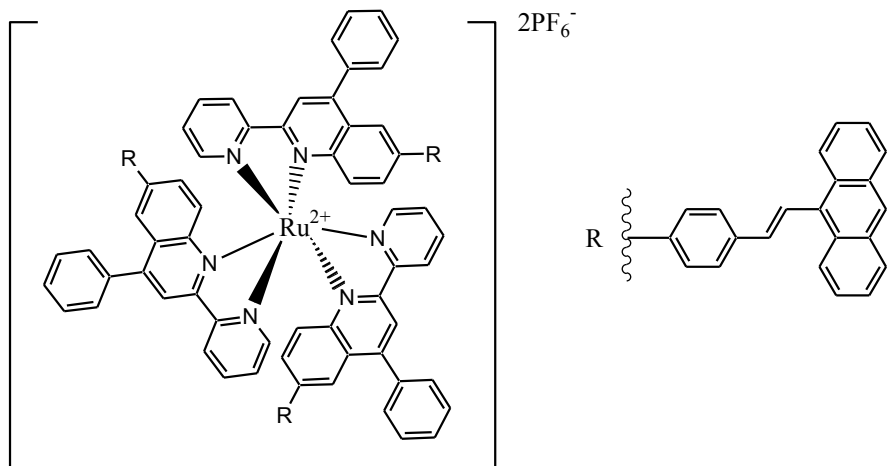


Figure 1-30. Structure of $[\text{Ru}(\text{LP1})_3]\text{[PF}_6\text{]}_2$.

1.3.4 Triplet PSs

Another approach to increasing ${}^1\text{O}_2$ production involves the use of triplet PSs. Triplet PSs have applications in catalysis of organic reactions, light-induced hydrogen production, and PDT [119]. To produce a triplet PS, population of the first triplet excited state is required which can be done by ISC.

Cyclometalated Ir(III) complexes with styrylBODIPY ligands and showing NIR absorptions/emissions have been reported. The complexes were used as triplet PSs for ${}^1\text{O}_2$ mediated photooxidations. In general, cyclometalated Ir(III) complexes having short absorption wavelength, weak absorption of visible light and short-lived triplet excited states, are not suitable for PDT application PDT because strong absorption of visible light and long-lived triplet excited states are preferred [120] [120]. Consequently, a key goal has been to develop new complexes that show strong fluorescence as well as satisfactory ISC. To develop transition metal complexes showing strong visible light absorption and long-lived triplet excited states bulky organic fluorophores have been attached to the coordination center

using a C–C triple bond as the p-conjugation linker. In this way, the heavy atom effect of Ir(III) can be maximized and the excitation energy can be efficiently channeled to the triplet excited states thus enhancing the PDT applicability of Ir(III) complexes. More importantly, the absorption as well as the emission wavelengths can be extended to the NIR spectral region (644–729 nm). This approach led to heteroleptic cyclometalated Ir(III) complexes containing BODIPY Figure 1-31 exhibiting strong NIR absorption, strong NIR fluorescence (700–800 nm), and long-lived triplet excited states (92–156 ms). The photophysical properties of the complexes and the NIR light-harvesting ligands were studied using steady state and time-resolved absorption/emission spectroscopy, as well as DFT calculations [121].

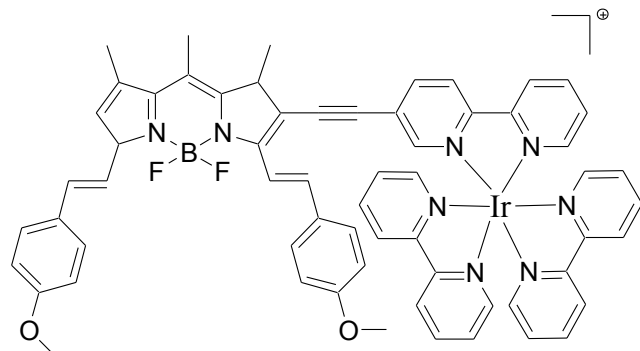


Figure 1-31. Structure of cyclometalated Ir(III) complex

It has been reported that photooxidation enhancement can be accomplished through intramolecular resonance energy transfer (RET). In a study by Zhao and coworkers, Bodipy triad triplet PSs Figure 1-32 were developed by connecting an unsubstituted styryl-BODIPY (energy donor), with λ_{max} of 409, to bisiodo aza-BODIPY (intramolecular energy acceptor) through click chemistry. The presence of additional absorption bands in the visible regions

enhanced light absorption in the visible region. Therefore the energy of the donor can be transferred to the acceptor via ISC. Aza-BODIPY with a much larger absorption band functions as a spin convertor to produce the triplet excited state [122].

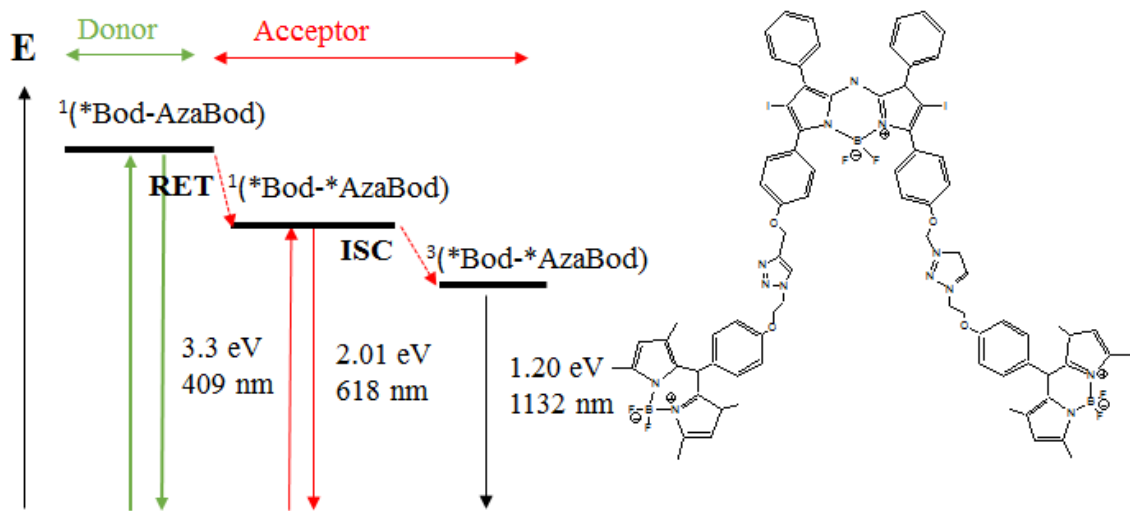


Figure 1-32. Example of resonance energy transfer (RET) and ISC for a BODIPY/aza-BODIPY based PS

In a closely related report, Zhao and coworkers summarized the literature pertaining to design approaches for triplet PSs [119]. An example was the design of complexes having large molecular absorptivity values (ϵ_{max}) in the visible spectrum and long-lived triplet excited states. Energy funneling based triplet PSs that show broadband absorptions in the visible spectrum were discussed, as a way to enhance triplet PS performance. A key goal was to develop new triplet PSs by establishing correlations between ISC and molecular structures. This report included Ru(II) polyimine triplet PSs structures such as the coumarin-based Ru(II) complex in Figure 1-33, which gave an absorption at 341 nm having $\epsilon_{\text{max}} \sim$

79,000 versus an $\epsilon_{\text{max}} = 14,000$ when the coumarin moiety was replaced by N-acetyl group. It was shown that the energy level of the ligand localized excited state (^1IL) was higher than the $^1\text{MLCT}$ (metal to ligand charge transfer) state, providing efficient energy transfer or internal conversion from the coumarin moiety to the coordination center. In addition, the energy level of the ^3IL of coumarin is significantly higher than the $^3\text{MLCT}$; consequently the phosphorescence lifetime and the quantum yield were not adversely affected by the ligand.

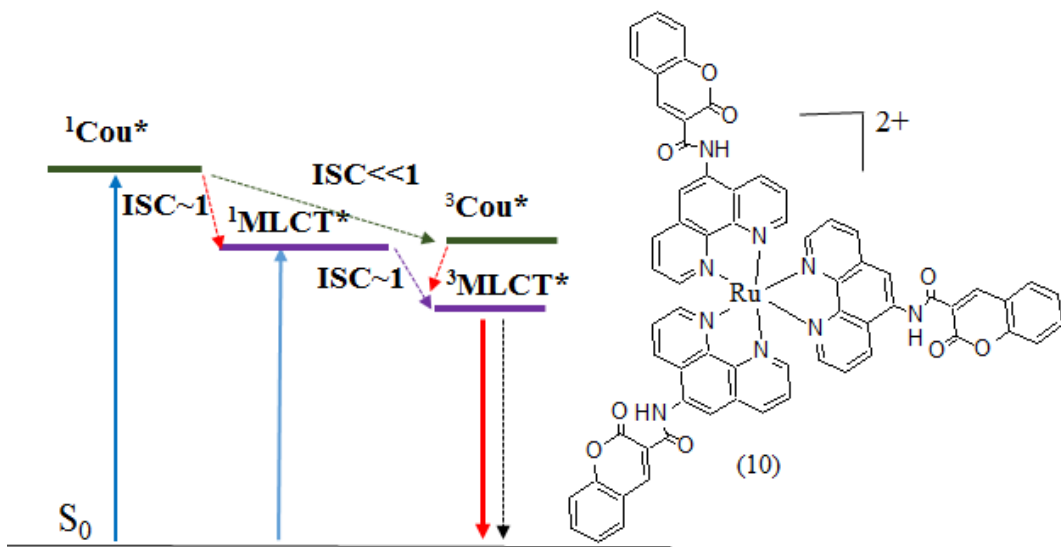


Figure 1-33. Energy level diagram showing Ru(II) complex having a light-harvesting coumarin ligand.

Ru(II) complexes having pyrene and naphthalimide appendages were also reported [119, 123, 124]. Attachment of pyrene groups to the phenanthroline (Phen) ligand led to enhancement of the absorption in the 300-350 nm region. In this case, the ^3IL energy level is close to the $^3\text{MLCT}$ and the triplet state lifetime is enhanced. Similarly, a long lived triplet

state was observed for the Ru(II) polyimine complex having a 4-piperidinyl-1,8-naphthalimide group attached to the Phen ligand Figure 1-34.

Another approach to increasing the triplet lifetime involved having the ligand and coordination center connected through π conjugation such as a C≡C moiety [119, 121]. The properly chosen ligand can also enhance λ_{\max} but the ligand cannot be very bulky since this would decrease ISC efficiency.

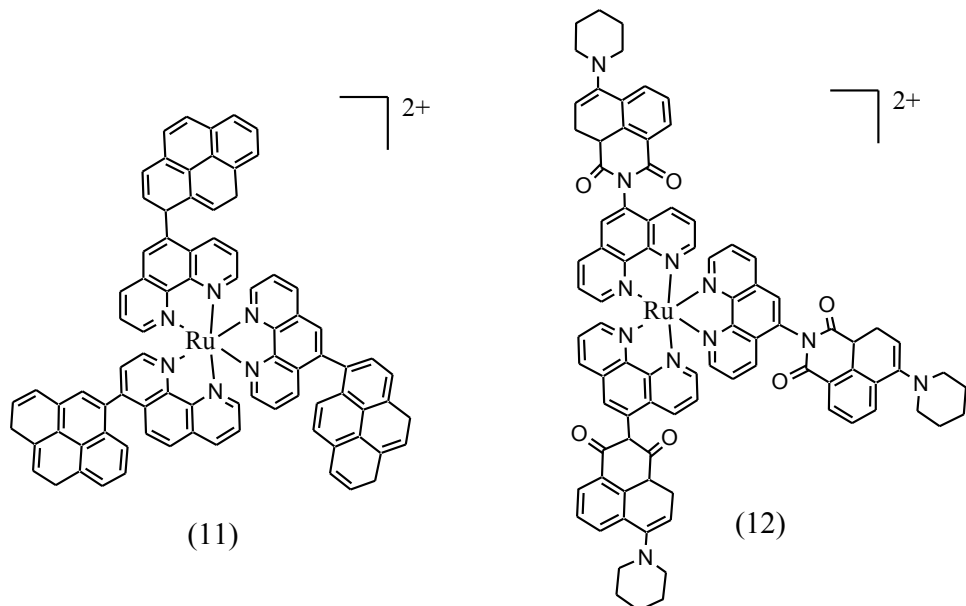


Figure 1-34. Example Ru(II) based phen complexes having close ${}^3\text{MLCT}$ and ${}^3\text{IL}$ states

Figure 1-35 shows that the ${}^3\text{MLCT}$ state of the coordination center (1.94 eV) is higher than the ${}^3\text{IL}$ state energy level of Bodipy (1.72 eV). Therefore the phosphorescence of the ${}^3\text{MLCT}$ state is quenched by ${}^3\text{MLCT} \rightarrow {}^3\text{IL}$ and the triplet state is mostly localized on the Bodipy unit. In this case, energy transfer from ${}^1\text{IL} \rightarrow {}^1\text{MLCT}$ is not likely to happen since the

^1IL is located below $^1\text{MLCT}$. Therefore the strong visible absorptions of the Bodipy (523 nm) and ϵ_{max} (66,000) do not aid triplet excited state production.

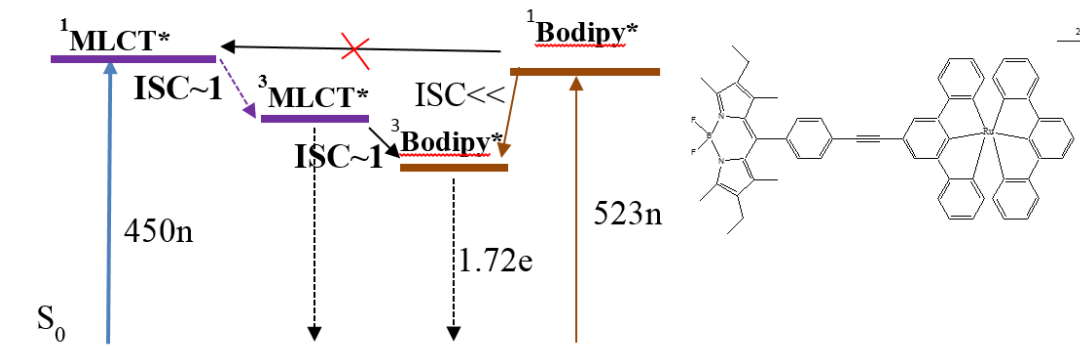


Figure 1-35. Energy diagram for a Ru(II) complex having BODIPY as a visible light harvesting ligand, showing energy transfer is unlikely

It is known that charge transfer can decrease $^1\text{O}_2$ production by quenching of the excited state [125]. However, complexes such as Ru(II) bipyridine and related compounds are good PSs of singlet oxygen in spite of the charge transfer (CT) nature of the lowest excited state of these compounds. This is because of the relatively long lifetime of the triplet metal-to-ligand charge transfer states, $^3\text{MLCT}$, of many Ru(II) coordination compounds that make these excited states susceptible to quenching by oxygen. It is been reported that the MLCT absorption mainly produces $^1\text{MLCT}$ that undergo ISC and populate $^3\text{MLCT}$ [126].

1.4 Phthalocyanine

Phthalocyanine is one of the second generation photosensitizers that was discovered by Braun and Tcherniac in 1907. It was obtained by heating an alcoholic solution of o-

cyanobenzamide to give a blue precipitate after cooling down the solution [127].

Phthalocyanines are synthetic porphyrins (azoporphyrin derivatives with four pyrrole substituent that are fused with nitrogen atoms) with the lambda max range of 675 to 700 that can be chelated with various diamagnetic metals such as zinc, aluminum to enhance the photo toxicity [128, 129].

Phthalocyanine as a functional colorant has become the major interest for different industrial and medical applications such as nonlinear optical devices, chemical sensors, liquid crystals, semiconductors, photocatalysis, gas sensors, solar cells, and photodynamic therapy. Phthalocyanine can be metalized with most of the metals in the periodic table. The common metallophthalocyanine that are being used for PDT are Zn^{2+} , Al^{+3} and Ga^{+3} , Si^{+4} because of having a long triplet lifetime as well as having high efficiency in singlet oxygen production [130, 131]. Shifting the absorption maxima called Q-band to the near infrared region makes this group of dyes more interesting in different applications [132]. Many different types of Phthalocyanines are available for PDT. These groups are likely to be used in PDT because of the useful properties such as near infrared absorption in therapeutically useful range. Compare to porphyrins, phthalocyanines retain their photochemical stability better [133]. Figure 1-36, the general structure of phthalocyanine and its numbering system.

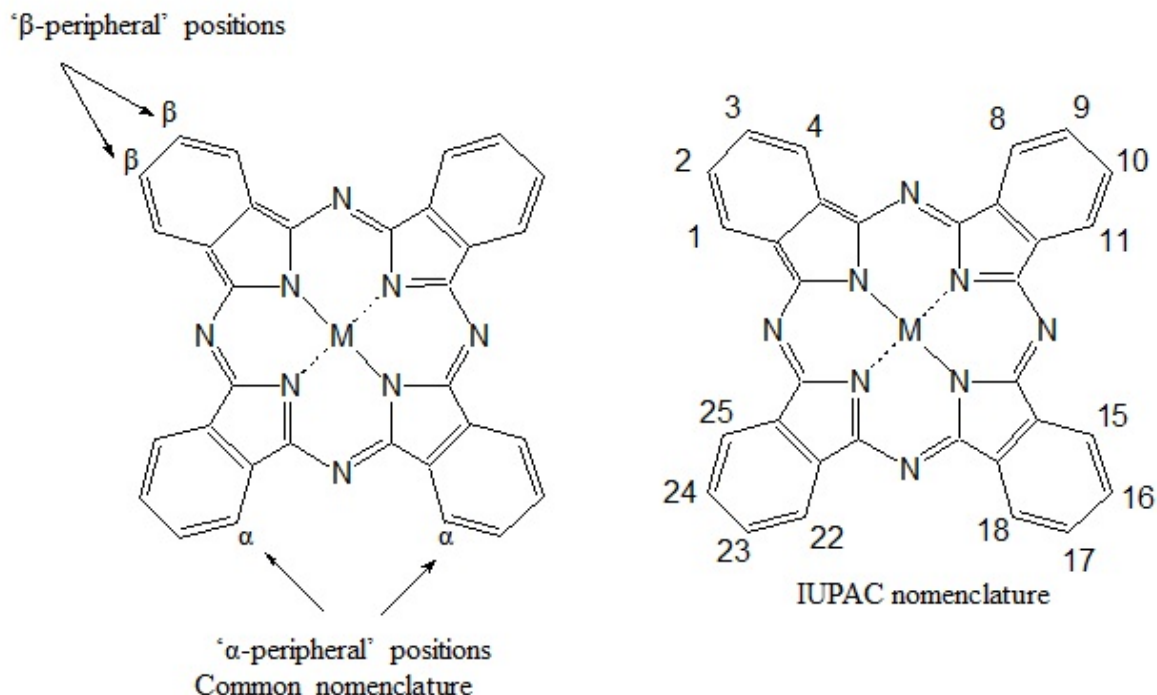


Figure 1-36. Metal free phthalocyanine (1) and metallophthalocyanine

1.4.1 Phthalocyanine/Organic pigment

The structure of phthalocyanine is derived from aza-[18]-annulene series. This is a conjugated heteroatom comprise of 18 π bonds. Initially phthalocyanine were produced as pigments. Later on processes such as chlorination, chlorosulfonation, chloromethylation made it possible to form these pigments into dyes [134]. Phthalocyanine is a planar aromatic macrocycle consisting of four indol unit that are linked together by nitrogen. The unique properties of phthalocyanine dye make it interesting in different application such as optical disks, liquid crystals, catalysts, optoelectronics, electron sensors, synthetic metals, solar cells, electro-chromic devices, organic electronic devices, pigments or dyestuff, thin-film, and photodynamic therapy [135].

Coordination Complexes of phthalocyanine with zinc, cobalt, and platinum, iron and copper show similar stabilities and they are stable to non-oxidizing concentrated acid and bases [134].

Addition of substituents in peripheral position (β and α) can increase the solubility in various solvents and also affect the electronic spectra depends on the nature of the substituent. Subsequently, photochemical and photophysical properties of phthalocyanine may also change [136].

1.4.2 Synthesis of phthalocyanine

Synthesis of phthalocyanine can be employed using different 1, 2 substituted benzene precursors. Conditions and catalysts are different depends on what precursor is been used.

Formation of alkoxide anion takes place in presence of strong organic bases such as DBU, DBN or NH_3 or addition of alkali metal such as lithium and sodium. A summary of the possible routes for phthalocyanine synthesis has been illustrated in Figure 1-37.

The main significance of phthalocyanine spectra are two bands, one stronger band presents in visible region, Q-band, and one in UV region called B or soret band. Q-band manifest transition of electron from the highest occupied molecular orbital (HOMO) or a_{1u} (π) to lowest unoccupied molecular orbital (LUMO) or $e_g(\pi^*)$. On the other hand a_{2u} to e_g transitions reveal soret or B band formation.

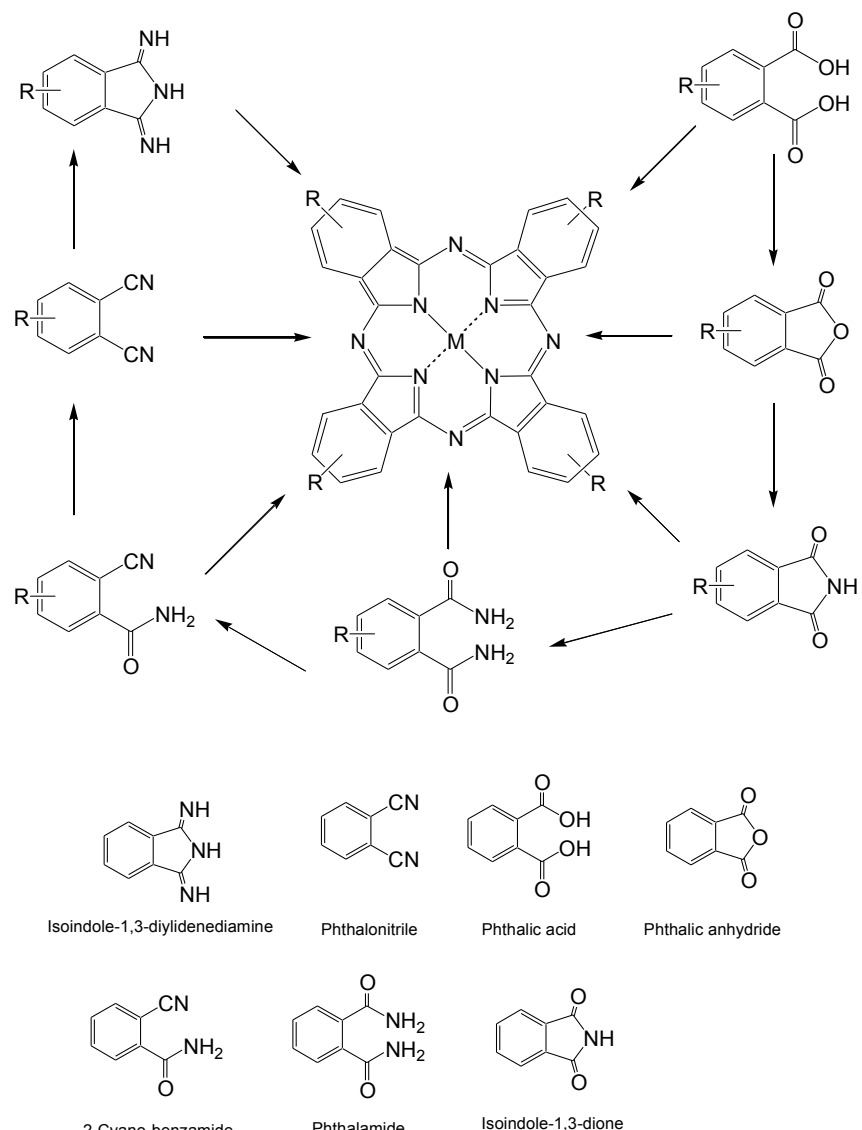


Figure 1-37. Pathways to phthalocyanine system.

The mechanism of synthesis of phthalocyanine using phthalonitrile is represented pictorially in Figure 1-38.

Some of the examples of the phthalocyanine that are prepared for PDT are listed in Figure 1-39

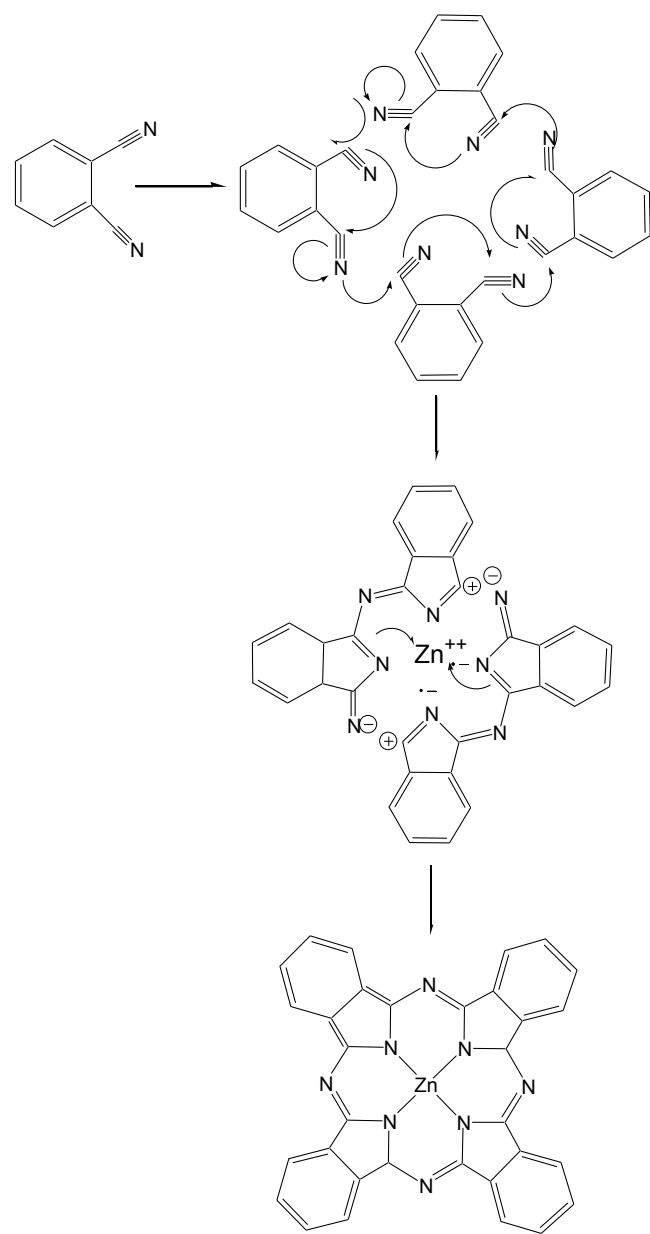


Figure 1-38. Mechanism of zinc phthalocyanine formation.

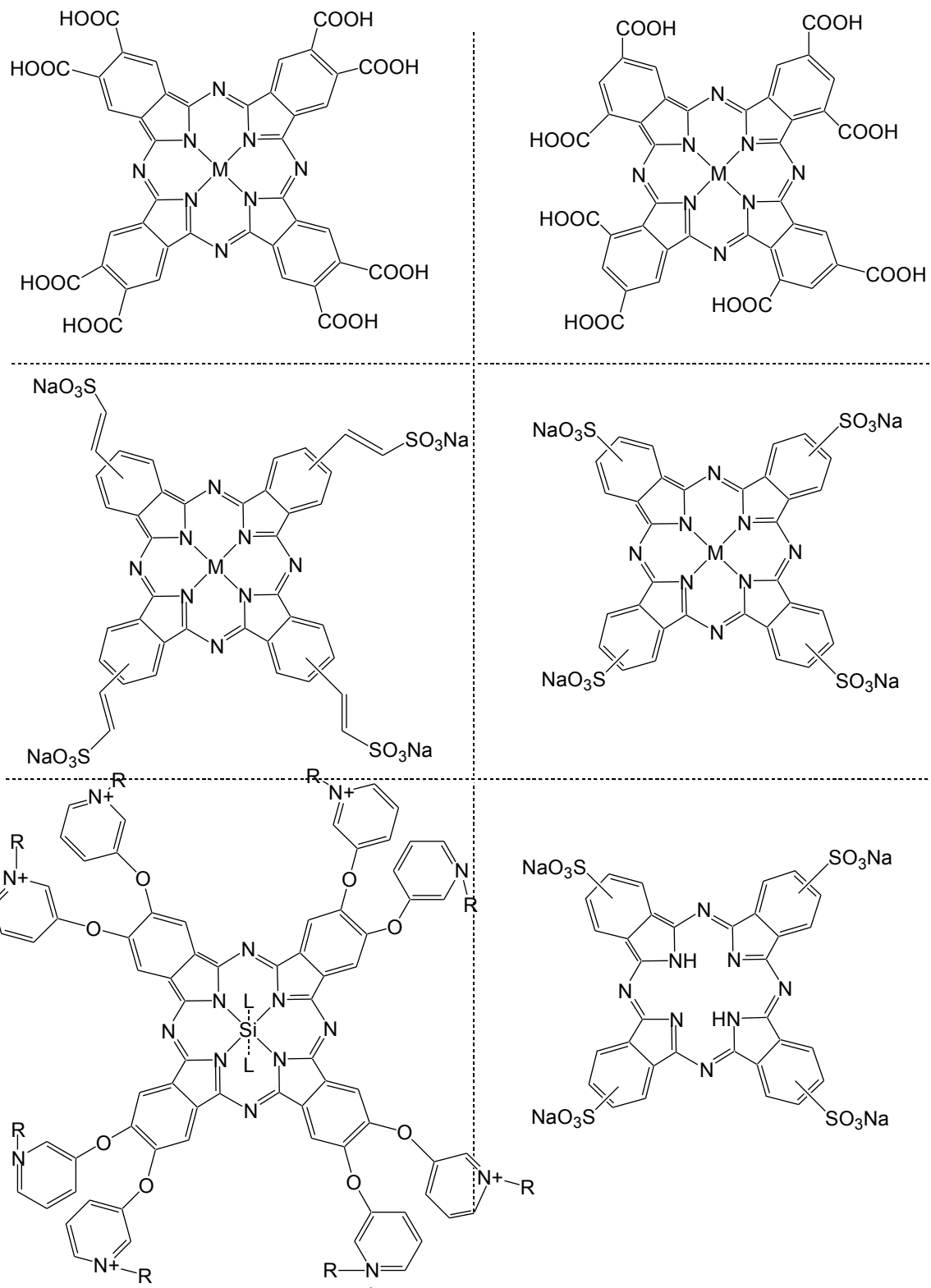


Figure 1-39. Examples of water soluble phthalocyanines.

1.4.3 Problems with current phthalocyanines

Studies show that change in the symmetry of the phthalocyanine can increase the amount of singlet oxygen production, Figure 1-40. The problem with changing the symmetry of the phthalocyanine is the harder characterization and the low yield that usually obtained [137].

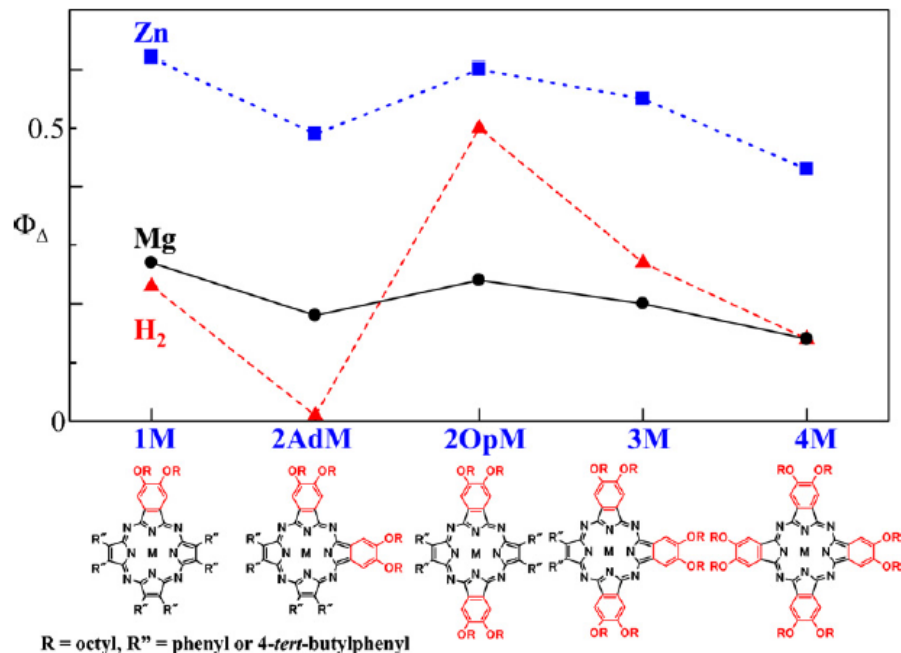


Figure 1-40. Comparing the amount of singlet oxygen production by changing symmetry.

Figure 1-41, represent the molecular structure relationship between formation of singlet oxygen and $S1 \rightarrow T1$ ISC by changing the symmetry of the structure. As the distance between $T1x$ and $T1y$ gets bigger, more efficient ISC takes place and we will observe an increase in the singlet oxygen formation. Also a bathochromic shift can be observed in the lambda max [137].

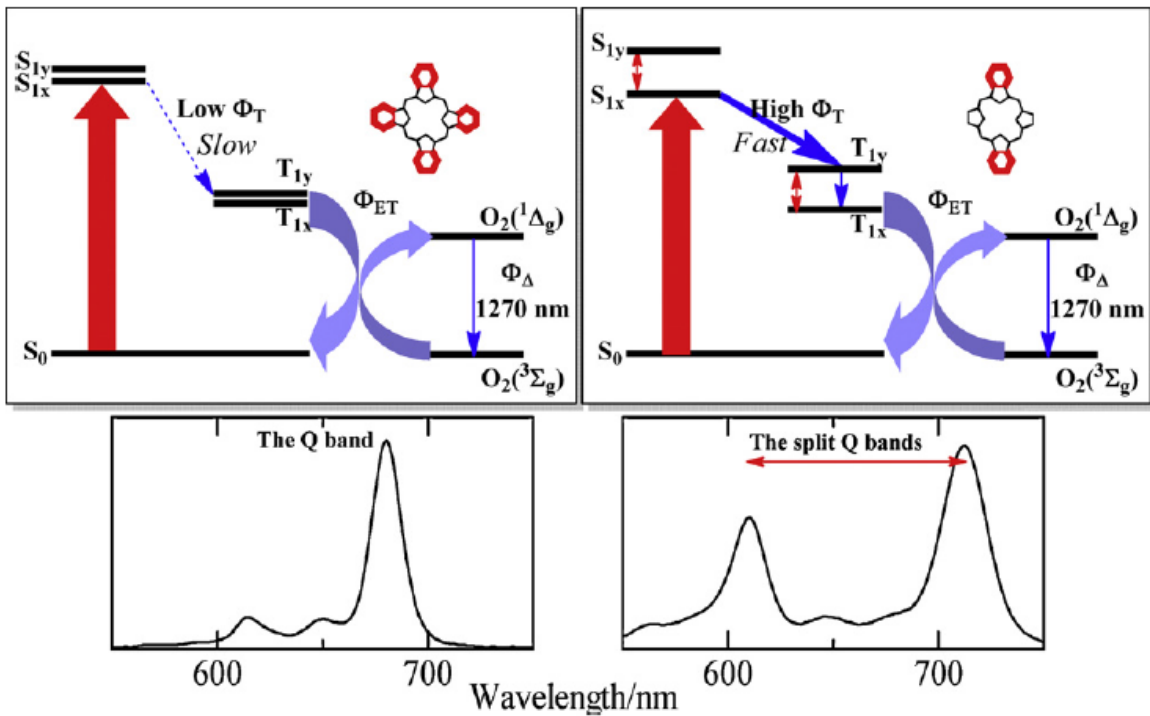


Figure 1-41. Change in singlet oxygen formation by changing S1 and S2 energy states.

Another problem with phthalocyanine is the low solubility in most of the solvents as well as aggregation in aqueous media. About 7000 phthalocyanine have been synthesized, among which around 4000 of them are non-water soluble. The water soluble phthalocyanines are more attractive for PDT application since they could be removed from the body through renal excretion. They also do no aggregate in the aqueous media. However, some recent studies show that using nanoparticles can increase the potential of using hydrophobic phthalocyanines for PDT studies as well. One example is encapsulation of zinc phthalocyanine in PLGA [138]. It is important to know that many of the photosensitizers with important properties are not water soluble and addition of water soluble groups may

change the desired photophysical properties. In this case using a proper nanoparticle to load the photosensitizer could be more useful to increase the efficiency of PDT.

Although many phthalocyanine have been synthesized, the number of phthalocyanines with ability to produce singlet oxygen under two photon absorption (TPA) are very limited. There are some advantages and disadvantages for using these types of dyes which will be discussed further later.

1.5 Laser light source

PDT light source can be lasers or incandescent light that are show similar efficiencies. The choice of light source for photodynamic therapy is different depends on the absorption and fluorescent excitation, the tissue characteristic as well as the cost and size [139].

One of the standard widely used laser light source in clinical trial for PDT is argon/dye laser. Spectra Physics (Mountain view, CA) and Coherent (Santa Clara, CA) are two manufactures that produced these lasers. This laser has ability to deliver a continuous wave (CW) of 630 nm from 1 to 7 W depends on the model. Another variation of Argon/dye laser are metal vapor lasers such as gold or copper vapor lasers. The wavelength that gold vapor laser generates is 627.8 nm. One of the disadvantages of metal vapor lasers is the period of time is required for these lasers to be warmed up or cooled down. KTP:YAG/dye lasers made by Laserscope (San Jonse, CA) is another laser type that can operate at 1064nm and it has some advantages compare to the other two lasers: one is the portability(limitation because of the size and water cooling requirement) and the other is tenability(it is not done easily with the user). 630 nm diode lasers for activation of Photofrin made by Diomed Inc.

(Andover, MA) are semiconductor light sources utilizing 120 v power and air-cooling system. The 652 nm diode was produced by Biolitec (East Longmeadow, MA) was used for activation of Foscan [140].

Laser dyes can be coupled to fiber-optic cables to avoid energy loss to a tip that is cleaved (for forward light projection), bulbous (for isotropic spherical distribution), or coated with cylindrical scattering material (to yield light perpendicular to the midpoint of the fiber axis [128]. Some examples of laser are shown in Table 1-3[141].

The amount of the light does and its duration has effect on cell toxicity. Cells may escape cell death at low light dose rate because of their ability to repair toxic oxidative products as well as sublethal damage [128].

Table 1-3. Laser sources.

Laser source	Wavelength	Power/power density
Argon/dye	630	Up to 3-4 W
Gold vapor	627.8	Pulsed: 3W mean power
(1-5) HeNe	632.8	25-300 mW
N ₂ /dye	630	Pulsed: 50 mW mean power

1.5.1 Non-Laser light source

Summary of the non-laser light sources that are used for clinical PDT are represented in Table 1-4[141].

LEDs have the output powers up to 150 mW/cm² over a 3x3 cm area. LEDs are manufactured at three different wavelength of 630 nm, 670nm, and 690 nm sold by Quantum Device (Barn-veld, WI) and EXFO (Mississauga, ON, Canada).

Table 1-4. Non-laser Sources.

Non-laser Souce	Wavelength(nm)	Power density
Filtered sunlight	>600	
250 W quartz halogen	620-640	40mW/cm ⁻²
1000 W quartz	620-720	9 W equivalent at 630 nm
500 W tungsten filament(slide projector)	>600	7-10 mW/cm ⁻²
1-5 kW xenon arc	600-700	Up to 150 mW/cm ⁻²
(14) fluorescent tubes	600-650	40mW/cm ⁻²
(4) 1 kW high-pressure sodium	>600	4 mW/cm ⁻²

1.5.2 Light dose

It is required to minimize the doses of light exposure to reduce the damage to the surrounding area of interest. Obtaining this goal requires both theoretical and experimental techniques. By 1986, the theoretical techniques were not developed as much as the experimental technique because there was a poor understanding of how light propagate in tissue. Light exposure are mostly empirical and mostly being described as the incident areal power density in mW cm^{-2} or areal energy density in Jcm^{-2} .

In vivo studies has shown that the response of the tumor growth to the same drug dose and light is different by changing the rate of the light delivery to the neoplasm [142].

A summary of some of the experimental methods for different light does and light source are summarized in Table 1-5.

Table 1-5. Summary of some of the light source and the phthalocyanine that are recently been studied.

sensitizer	With/ without nano-particle	Light source	Light Dose mW/cm ²	Period (min)	Lambda max nm	μM	Cell line	Ref
	PEG-PEI-MSNS	lamp	10			10		
m-THPC	-----	10 W copper vapor-pumped tunable dye laser	400			10	RIF-1 2x10 ⁴ /35 mm petri dish	⁹⁰
ZnPc		LED	4	10	650 ± 20	5x10-8 M	Hella	⁹¹
PcF	Cyclo-dextrin	Red light source		20-40	400-800	0-1		⁹²
ZnPc	Liposome	LED	4	10	640 ± 20		A-549	⁹³
ZnPcBr ₈		LED (640 nm, 70 mW)	4.5 J/cm ²	2 min and 13 s	640 ± 20	1	HE _p -2	⁹⁴
ZnPcBr ₈		Diode semiconductor laser(660nm,30 mW)	4.5 J/cm ²	5	660 ± 10	1	HE _p -2	⁹⁴
ZnPc	PLA	Photon Lase I, DMC	20 J/cm ² (166.6 mW/cm ²)	2	675	1,2, 4 μg /ml	MCF-7	⁹⁵
ZnS ₃ Pc		Laser diode	120		672	1-10 $\mu\text{g}/\text{mL}$	MCF-7	⁹⁶

Table 1-5 Continued

ZnPcS _{mix}		680 nm diode laser	5.73	29min & 5s			MCF-7	⁹⁷
----------------------	--	--------------------------	------	---------------	--	--	-------	---------------

Chapter 2

INCREASING THE EFFICIENCY OF PDT USING POLYMERIC MICELLES

2.1 Introduction

Photodynamic therapy (PDT) is a noninvasive modality that can be used for treatment of cancer and certain oral and infection diseases [143, 144]. PDT involves two alternative mechanisms of type I and II that are summarized in Figure 2-1. One mechanism involves photooxygenation of a sensitizer in the T₁ excited state through electron transfer to ${}^3\text{O}_2$ to form radical cations ($\text{P}^{+\cdot}$) and superoxide ion radicals($\text{O}_2^{-\cdot}$). An alternative mechanism of type I photochemistry is formation of photosensitizer anion or radical anion ($\text{P}^{-\cdot}$) [145-147]. Non-reactive superoxide anions formed can lead to formation of hydrogen peroxide (H_2O_2). H_2O_2 is destructive and also can pass through cell membranes. Through the Haber-Weiss reaction, H_2O_2 reacts with superoxide anions($\text{O}_2^{-\cdot}$) to form hydroxyl radicals that can oxidize molecules in the cell [148]. It is important to note that recent studies have shown that the type I mechanism plays an important role in PDT activity depends on the type of photosensitizer [145].

In type II photochemistry which is a dominant type of photochemistry in PDT, upon excitation, photosensitizer promotes to the excited singlet state that can decay to the triplet

state though ISC. Formation of $^1\text{O}_2$ takes place followed by quenching of excited triplet P(T_1) through triplet-triplet energy transfer energy transfer from P(T_1) to ($^3\text{O}_2$)[146].

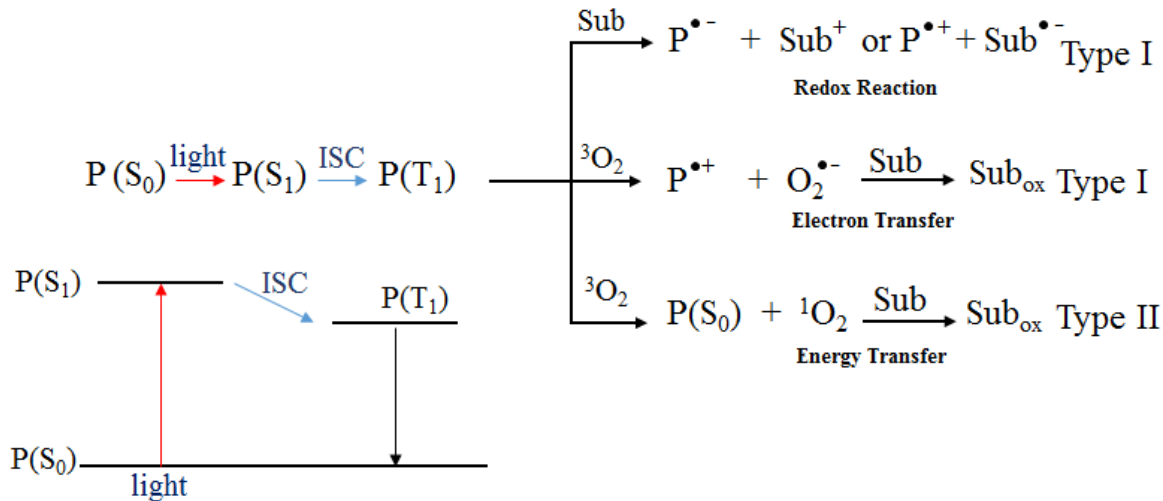


Figure 2-1. Summary of Type I and Type II photoreactions where P is the photosensitizer, S_0 is the singlet ground state, S_1 is the first excited singlet state, T_1 is the first excited triplet state, ISC is intersystem crossing, and $^1\text{O}_2$ is singlet oxygen.

Studies have shown that the energy gap between T_1 and S_0 have impact on the efficiency of the photosensitizer in PDT. The higher the energy difference, the more efficient the energy transfer and the more efficient sensitizer for PDT. A minimum energy difference between two states is needed to consider a fluorescent dye as a sensitizer for PDT and that minimum energy is 0.98 eV ($\Delta E_{\text{S}0-\text{T}1} > 0.98 \text{ eV}$) [149]. To screen potential PS for PDT use, this energy can be calculated using molecular modeling.

One way to increase $^1\text{O}_2$ production is to incorporate metals and or heavy atoms into the structure of the molecule. Incorporation of heavy these metals can increase intersystem crossing through spin-orbit perturbation. In this work, closed shell zinc was the choice of

metal for the phthalocyanine ligand because of the important properties the resulting dye has, Figure 2-3. This complex is a photostable sensitizer from the porphyrin family that has a heteroatomic system comprising 18π bonds. Properties that make this photosensitizer unique include its low dark toxicity, resistance to chemical and photochemical degradation, selective retention in tumor tissues, relatively long triplet state lifetime [150]. Compared to other porphyrin-type structures such as protoporphyrin IX, Figure 1-14, zinc phthalocyanine has a higher molar extinction coefficient which is important to reduce the required drug doses and subsequently their side effects [150]. The main shortcoming of zinc phthalocyanine is the low solubility and selectivity of this dye that can be overcome by suitable modification of this compound in the peripheral positions, Figure 1-38. To enhance the solubility, several attempts have been made to encapsulate ZnPc into a liposome or a polymeric micelle. In a previous work by Mariana Sorares and et al, they used PLGA to encapsulate ZnPc into a polymeric micelle. Utilizing emulsion evaporation method they could obtain a micelle with diameter size of 227 to 450 nm [151] is PLGA which is a biodegradable polymer. Another group attempted to encapsulate ZnPc into PCL using solvent emulsification-evaporation method. The mean diameter size of the polymeric micelles were reported as 187.4 nm [152]. Some of the studies have shown that the polymeric micelles are more robust than liposome.

Solubility issue can also be resolved by addition of a suitable ligands in either of ZnPc peripheral positions. Many studies have been done to specifically improve water solubility of these compounds [153]. One of the groups that can improve the solubility of this dye is Alkyl group. It is known that the incorporation of the alkyl group can improve the lipophilicity. Higher lipophilicity increases tissue distribution that leads to increase in volume

distribution. More or larger alkyl group often reduce down the water solubility but occasionally it can increase the water solubility through lowering the crystal lattice energy. Comparing the branched vs unbranched alkyl group, unbranched alkyl group with higher lipophilic surface area can lead to a large lipophilic surface area [154]. In this work, eight alkyl groups were incorporated in the peripheral positions of the ZnPc to increase lipophilicity and perhaps selectivity of this sensitizer for tumor cells. Also, four arene groups in the form of benzyloxy groups were incorporated into the base structure to increase the polarizability of the structural element of drugs.

Other than increasing the lipophilicity of ZnPc, it is also necessary for these compounds to have water solubility properties for the purpose of intravenous injection. Adding a measure of water solubility can be accomplished either through modification of the dye itself or by using biodegradable nanoparticles as a vehicle for delivery of the sensitizers to the target cells. The advantage of using nanoparticles is a small size particles that can be obtained and it can enhance passive targeting and can affect the bio-distribution of dye nanoparticles in cancer cells. For more information about passive targeting refer to chapter 1.2.4. The use of nanoparticles is also advantageous since a lower dosage of the dye will be needed. Subsequently using a lower dosage can eventually reduce the phototoxic side effect of this dye.

The goals of this aspect of the present study were:

1. To determine how the addition of four benzyloxy groups in peripheral position of ZnPc impacts the properties of the new dye, ZnPcBCH₃, such as solubility, encapsulation, singlet

oxygen, lambda max and cell uptake. Based on the above discussion, it was expected that the lipophilicity, solubility and cell uptake would increase compared to ZnPc.

2. To determine whether a correlation exists between calculated ($\Delta E_{S_0-T_1} > 0.98$ eV) and (1O_2) production. So, the energy difference between the singlet ground state (S_0) and first excited triplet state (T_1) was calculated for ZnPc and ZnPcBCH₃ and compared to the experimental (1O_2) quantum yield.

3. To determine whether encapsulation of ZnPcBCH₃ into PLGA-b-PEG, shown in Figure 2-2, increases the cytotoxicity of this sensitizer toward cancer cells and gives a smaller size nanoparticle.

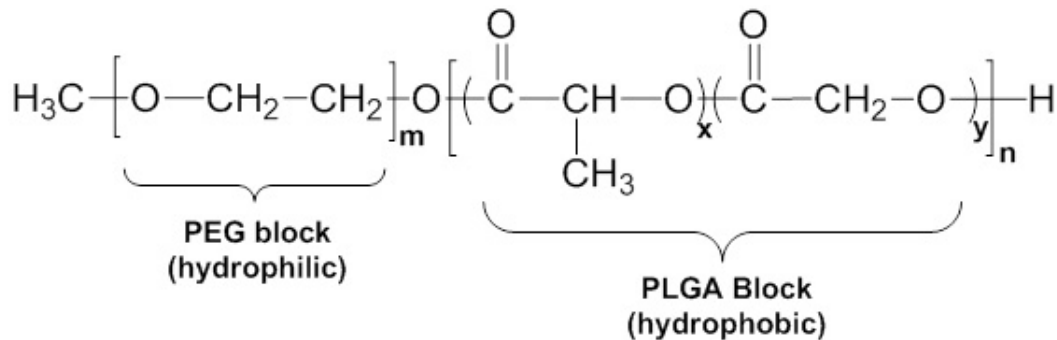


Figure 2-2. Structure of PLGA-b-PEG.

2.2 Materials and Methods

Chemicals. Zinc phthalocyanine (ZnPc), 4-hydroxybenzoic acid, poly (ethylene glycol) methyl ether-block-poly (lactide-co-glycolide) known as PEG-b-PLGA with PEG average M_n 2000 and PLGA average M_n 11,500 and MTT (3-(4,5-dimethylthiazol-2-yl)-2,5-diphenyl-2H-tetrazolium bromide) were purchased from Sigma Aldrich. Dimethyl sulfoxide

(DMSO) was purchased from Alfa Aesar, while dimethylformamide and acetonitrile were purchased from Fisher Scientific.

Biological supplies. DMEM/High Glucose (SH30243.02) was purchased from Fisher. CellTiter-Blue® Cell Viability Assay (CTB), to measure the cell viability of the cells were purchased from Promega. NucBlue, as a molecular probe was purchased from Thermo-Fisher to stain nucleus. Human A549 lung carcinoma cells cultured in DMEM contain 10% v/v FBS. Cells were incubated at 5% CO₂ at 37°C. Phototoxicity of the encapsulated dye was evaluated using scope light 2000 and a 599±29 long pass filter was used.

Instrumentations. ¹H NMR spectra was recorded on a Varian 400 MHz spectrometer. Fluorescence decay was recorded on a Fluorolog-3 spectrofluorometer (HORIBA Jobin Yvon Inc) and nanoled-625. FTIR spectra were recorded on a Nicolet Nexus 470 FTIR spectrophotometer (Thermos Scientific, USA). UV-VIS measurements were recorded on a Cary 300 spectrophotometer. Plate readers were a Molecular Devices Spectramax Gemini XS fluorescent Plate reader and a Molecular Devices SpectraMax UV/Visible spectrophotometric plate reader. Singlet oxygen quantum yields were measured using an Edinburgh Analytical Instrument (FS920) and NIR PMT from HAMAMATSU (H10330A series).

2.2.1 Synthesis

4-(4'-Methyl-benzyloxy)-phthalonitrile (3). 4-nitrophthalonitrile (3g, 17.34 mmol) and 4-methylbenzyl alcohol (2.115 g, 17.34 mmol) were dissolved in 20 ml of dry DMF, 95%, and stirred under N₂. After 5 min, K₂CO₃ (7.189 g, 52.01 mmol) was added and the reaction was

heated 85°C. Reaction was monitored using TLC and it was complete after 7 h. The reaction mixture was poured into cold water. The crude product (1.745 g) was purified further by column chromatography using silica gel 230-400 Mesh (eluent: dichloromethane). FTIR(cm^{-1}): 3044.9 (Ar-CH), 2949.5 (CH), 2235.3 (CN), 1600.3, 1560.0, 15175.5, 1487.3, 1470.0, 1428.9, 1382.5, 1355.4, 1301.6, 1279.9, 1251.7, 1210.9, 1200.4, 1183.9, 1172.5, 1091.1, 997.3, 965.2, 950.9, 920.2, 879.1, 859.0, 834.0, 819.2, 775.7. ^1H NMR (400 MHz, DMSO- d_6): δ 8.02 (dd, J = 8.8 Hz, J = 2.1 Hz, 1H), 7.81 (t, J = 2.3 Hz, 1H), 7.48 (dt, J = 8.8 Hz, J = 2.5 Hz, 1H), 7.35-7.27 (m, 2H), 7.18 (d, J = 6.6 Hz, 2H), 5.19 (s, 2H), 2.28 (s, 3H). Mp=132-134°C. Theoretical 271.08418 [M+Na] $^+$, Experimental 271.08381 [M+Na] $^+$. Elemental composition C₁₆H₁₂N₂O.

2(3), 9(10),16(17), 23(24)-Tetrakis-(4'-methyl-benzyloxy) phthalocyanine zinc(II) (4)

Compound 3 (174mg, 0.7 mmol) was dissolved in 3ml dry DMF and catalytic amount of DBU was added. While stirring reaction under Ar, zinc(OAc)₂ (38.4 mg, 0.175 mmol) was added and the mixture was heated to 150°C and stirred for 18 h. After cooling, the solution was added into cold water (50ml) dropwise. The product was obtained and washed with methanol until the solvent was colorless. Product dried under vacuumed at room temperature prior to weight measurement, 149 mg. M.p. > 200°. FTIR (cm^{-1}): 3044.9 (Ar-CH), 2922.9 (CH), 10607.6, 1516.9, 1487.7, 1455.8, 1397.2, 1377.1, 1338.1, 1277.1, 1223.7, 1180.2, 1119.2, 1093.4, 1050.1, 1019.4, 944.8, 802.4, 744.9, 744.9, 728.7. ^1H NMR (400 MHz, DMSO): δ ppm = 8.78 (dt, J = 26.5 Hz, J = 8.0 Hz, 2H), 8.52-8.31 (m, 2H), 7.73-7.47 (m, 12H), 7.46-7.17 (m, 12H), 5.47 (d, J = 9.8 Hz, 8H), 2.41-2.27 (m, 12H). R_f= 0.87 in 1:1

DCM/THF. ESI-MS (positive ion mode): m/z 1057.31628 [M+H]⁺. C₆₄H₄₈N₈O₄Zn. Ms (MALDI): m/z 1057.31628.

2.2.2 DFT Calculations

Full geometry optimizations for ZnPc and ZnPcBCH3 were carried out using Gaussian 09 software package. Density functional theory at the B3LYP level with dgdzvp and 6-311G+(d,p) basis sets were used for geometry optimization in vacuum. TD-DFT calculation was done in DMF solvent. Optimized structures were verified using vibrational frequency analysis. Calculated bond angles and bond length were compared to the crystal structure that was obtained from literature [155] [156].

2.2.3 Singlet oxygen quantum yield

Singlet oxygen quantum yield (Φ_Δ) was measured using the relative method. This measurement was determined using ZnPc as a standard [157, 158]. Solution of ZnPc and ZnPcBCH3 were prepared in DMF with the maximum absorbance of 0.08 to 0.2 at 699 nm. Both solutions were excited at 699 nm where the excitation count for both standard and the sample are the same. The optical density (OD) of these samples at this wavelength and the area under the typical phosphorescence emission at 1270 nm were used to calculate singlet oxygen quantum yield using equation 7.

$$\Phi_\Delta = \Phi_\Delta (\text{std}) \frac{A_{obs}(x). OD(\text{std})}{A_{obs}(\text{std}). OD(x)} \quad (7)$$

Where OD (std) and OD(x) are the absorbance point of the ZnPc and ZnPcBCH3 respectively.

Band path filter of 675nm was used to measure the emission at 1270 nm.

2.2.4 Steady-State and life-time fluorescence

Fluorescence quantum yield (Φ_f) measurements conducted similar to the procedure that described above for singlet oxygen measurement. ZnPcBCH3 and ZnPc solutions in DMF prepared in DMF within 0.9 to 0.1 absorption units at 608nm. Area of the fluorescence emission and the recorded absorption were used to calculate the fluorescence quantum yield using equation 1. Condition for the sample and standard was the same and this measurement was repeated twice in two different days. ZnPc in DMF was used as a standard for the measurement ($\Phi_f = 0.28$) [159].

$$\Phi_\Delta = \Phi_\Delta (\text{std}) \frac{A_{obs}(x). OD(\text{std})}{A_{obs}(\text{std}). OD(x)} \quad (8)$$

Where A(x) and A (std) are areas under the fluorescence emission curves of the samples and the standard respectively. OD(x) and OD (std) are the optical density of the sample and standard.

Method of choice to measure lifetime is time-correlated single photon counting method that was conducted on the ZnPc and ZnPcBCH3 solutions in DMF. For this measure samples were excited at 625 nm utilizing NanoLED pulse laser. Measurements were repeated twice and performed at repetition rate of 1 MHz and a band pass of 1.5 nm.

2.2.5 Polymeric micelle preparation

Polymeric micelles were prepared by modification of the protocols that was obtained from literature [160]. PLGA-b-PEG polymer (20mg) was dissolved in 2 ml of THF. ZnPcBCH₃ (0.2) mg was added to the THF and the mixture stirred for 10 min. This mixture was added to sterilized water dropwise and let it stir uncovered for 2h. Remaining THF was removed using a vacuum pump at RT. To purify the sample, this mixture was centrifuged at 10000g for 15 min and the precipitate was washed with sterilized water twice followed by centrifugation each time. The precipitate re-suspended in sterilized phosphate buffered saline (PBS) for *in vitro assay*. Similar nanoprecipitation process was repeated using acetonitrile and acetone instead of THF.

2.2.6 TEM measurements

The morphology of the nanoparticles were performed using JEOL 2010F Field Emission transmission electron microscope (TEM) operating at (200 KV). Samples were prepared on carbon grids, examined negative staining and dried at room temperature.

2.2.7 Dynamic light scattering and zeta potential

The diameter, polydispersity index and zeta potential were measured using Malvern Zetasizers S90. Sample were diluted in deionized water for this measurement with no stabilizer.

2.2.8 Sensitizer Drug load and Entrapment Efficiency

Micelle solutions were lyophilized for further analysis. Concentration determination was used by preparing standard curve and UV/VIS in THF at (677 nm). Nanoparticle yield,

sensitizer drug load and drug entrapment efficiency were calculated using the following equations obtained from literature [161].

$$\text{Nanoparticle yields (\%)} = \frac{\text{Weight of nanoparticles}}{\text{Weight of polymer and drug fed initially}} \times 100 \quad (9)$$

$$\text{Drug loading (\%)} = \frac{\text{weight of drug in nanoparticles}}{\text{Weight of nanoparticles}} \times 100 \quad (10)$$

$$\text{Entrapment Efficiency (\%)} = \frac{\text{Weight of the drug in nanoparticle}}{\text{Weight of drug fed initially}} \times 100 \quad (11)$$

2.2.9 Qualitative analysis of hydrophilicity

Each dye solution of ZnPc and ZnPcBCH₃ was prepared with a total concentration of 2 and 4 μM in a DMSO-Media or DMSO-FBS. These solutions were put in a 96-well plate in triplicate for absorption measurement in a plate reader.

2.2.10 Cellular uptake of encapsulated dyes into polymeric micelles

A549 cells were seeded in a 96-well plates at a density of 7500 cells per well. Cells were treated with encapsulated nanoparticles when each well was 99% confluent. Cells were treated with different concentrations of (5, 10, 16, and 24 μl of stock micelle solution that was described in 2.2.5) of encapsulated nanoparticle in triplicate. At each concentration points, cells were harvested after incubation time of (2, 4, 6, and 15 h). To observe the uptake process, cells were washed with PBS and lysed in 100 μl DMSO per well. Each plate was rocked at room temperature in a subdued light for 10 min before fluorescence measurements. Lysed cells in DMSO was excited at 616 nm and emission was recorded at 700 nm.

2.2.11 MTT and CTB Dark toxicity Assays

Cytotoxic effects of free ZnPc and ZnPcBCH₃, and encapsulated ZnPcBCH₃ in PLGA-b-PEG on A549 cells were determined utilizing MTT and CTB assays. For the MTT assay, 7500 cells/well were cultivated in a 96-well plate. Cells were incubated at 37°C overnight and treated with 4μM of ZnPcBCH₃, ZnPc; three wells per condition in 2% DMSO-Media for each dye except that the encapsulated ZnPcBCH₃ in PBS was added in 10 μl. Two controls, one for 2% DMSO in media and one for 10 μl PBS were also set up. After 24 h of incubation, cells were treated with 20 μl of 5mg/ml MTT to each well. One set of wells should be included for the MTT with no cells as a third control. Cells were incubated for another 3.5 h. After incubation media was remove carefully and 150 μl of MTT solvent was added per well. Plate was covered with a Al foil and placed on a shaker for 15 min. Absorbance was read at 570 nm with reference filter of 620 nm.

With a few differences, CTB assay was conducted. The number of cells that was set up for CTB assay was 7000 cells per well and let it grow overnight. Cells were fed with 100 μl of media and after 24 h, 4 μM of ZnPc and ZnPcBCH₃ in DMSO and 20 μl of the nanoparticle solution, described in 2.2.5, were added to the designated wells. These procedures were done in subdued light. After 24 h of incubation, 20 μl of CTB was added to each well and let it incubate for another 3 h. Fluorescence emissions were recorded at 560 nm and 590 nm utilizing the plate reader.

After addition of a sensitize dye 30 μl of nd incubation for 24 h CTB dye was added to were exposed to 1.5 mw/cm² for 4.5 min using a band path filter of 599±25 nm.

2.2.12 MTT and CTB Cytotoxicity Assays

The main difference between the light and dark toxicity for MTT assay can be described as:

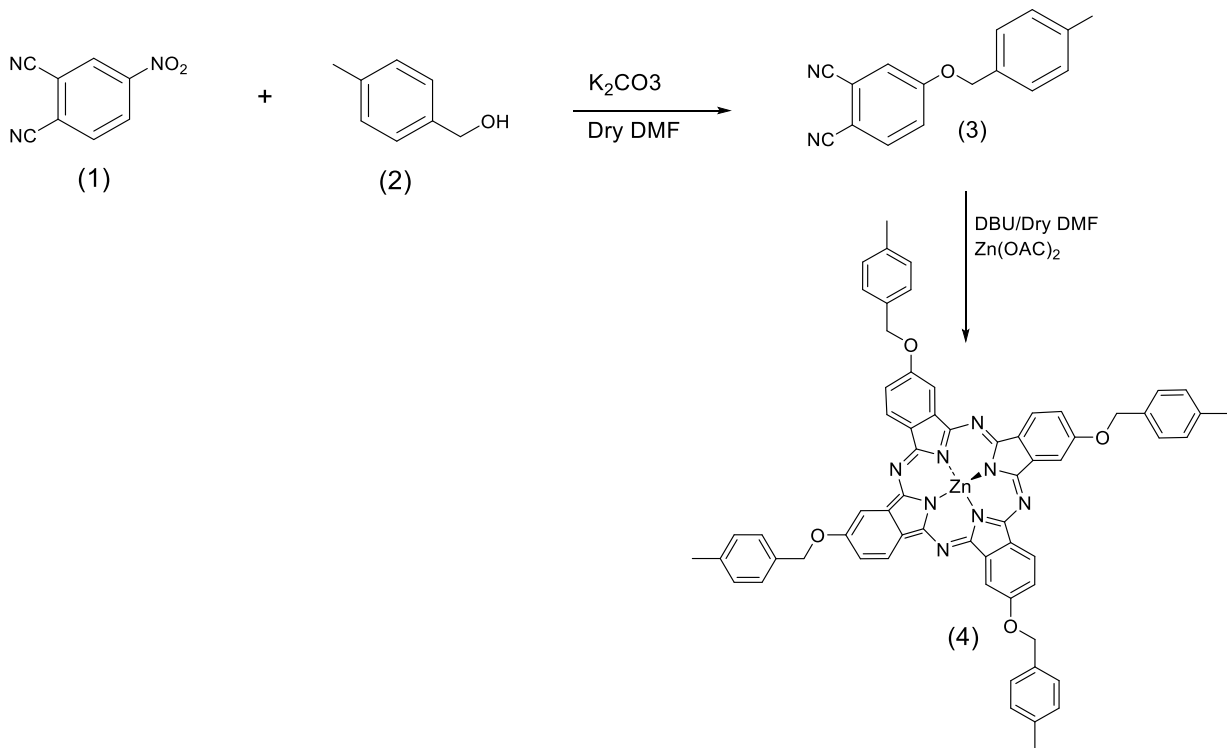
1. For the MTT assay, after 24 h of cell treatment with sensitizer drug, media was removed and 50 μ l of PBS was added. Cells were exposed with 1.5 mw/cm² for 4.5 min using a band path filter of 599±25 nm. To express the light exposure toxicity, cells were incubated for another 24 h after exposure prior to removal of the media and addition of the MTT solution.

2. For CTB assay, For the MTT assay, after 24 h of cell treatment with sensitizer drug, media was removed and 50 μ l of PBS was added. Cells were exposed with 1.5 mw/cm² for 4.5 min using a band path filter of 599±25 nm. To express the light exposure toxicity, cells were incubated for another 24 h after exposure prior to addition of the CTB dye.

2.3 Results and discussion

2.3.1 Synthesis

The synthesis of ZnPcBCH₃ (shown in scheme 1) was conducted in two steps, beginning with the reaction between nitrophthalonitrile (1) and benzyl alcohol, compound 2, in dry DMF. Compound 3 was obtained in 58% yield. The targeted phthalocyanines were obtained in DMF under an inert atmosphere. Characterization of compound 4 was done using ¹H NMR, FTIR, ESI mass spectrometry and MALDI.



Scheme 2-1. Synthesis route for ZnPcBCH_3 .

2.3.2 Computation analysis

The bond angles and distances of the optimized ZnPc structure were compared to the ones that obtained from literature. As it is found in Table 2-1, there is a minor difference between the experimental and the calculated values regardless of changing the basis set, symmetry operation or solvent. Overall these values are in a close agreement with the crystal structure. However, $\text{Zn-N}\alpha$ gives a better bond distance for C1symmetry in DMF. So, we used dgdzvp in DMF for these calculation. The optimized structure of ZnPc and ZnPcBCH_3 are shown in Figure 2-3. For the new compound ZnPcBCH_3 , the optimized structure of ZnPc was used as

the base unit for adding benzyloxy. Different possible geometries for ZnPCBCH₃ can be proposed. To obtain the lowest geometry optimization, energy of all different possible structures were calculated that are shown in Appendix A. Structure 4 in Appendix 4 was chosen as the most stable structure for further calculations.

Table 2-1. Bond angles and lengths that are obtained from crystal structure vs the calculated ones.

Bond length and angle	Experimental	Dgdgvp(C1) vaccum	DFT dgdzvp (D4H)	DFT dgdzvp (C1-DMF)	DFT B3LYP/6-311+gd(D4H)
Zn-N α	1.98	2.006	2.006	2.02	2.008
N α -C α	1.366	1.37	1.37	1.36	1.37
C α -N β	1.332	1.33	1.33	1.33	1.32
C α -C β	1.450	1.46	1.46	1.46	1.46
C β -C β	1.398	1.41	1.41	1.41	1.40
C β -C γ	1.393	1.39	1.39	1.39	1.39
C γ -C δ	1.388	1.39	1.39	1.39	1.39
C δ -C δ	1.399	1.41	1.41	1.41	1.40
Zn-N α -	124.6	125.03	125.04	124.78	125.04
C α	127.5	127.58	127.6	127.54	127.5
N α -C α -	109.4	109.93	109.9	110.38	109.9
N β	108.8	108.42	108.44	108.35	108.45
C α -N α -	106.3	106.60	106.6	106.45	106.59
C α	120.7	121.05	121.08	121.01	121.02
N α -C α -	117.6	117.80	117.80	117.87	117.8
C β	121.5	121.136	121.11	121.10	121.15
C α -C β -					
C β					
C β -C β -					
C γ					
C β -C γ -					
C δ					
C γ -C δ -					
C δ					

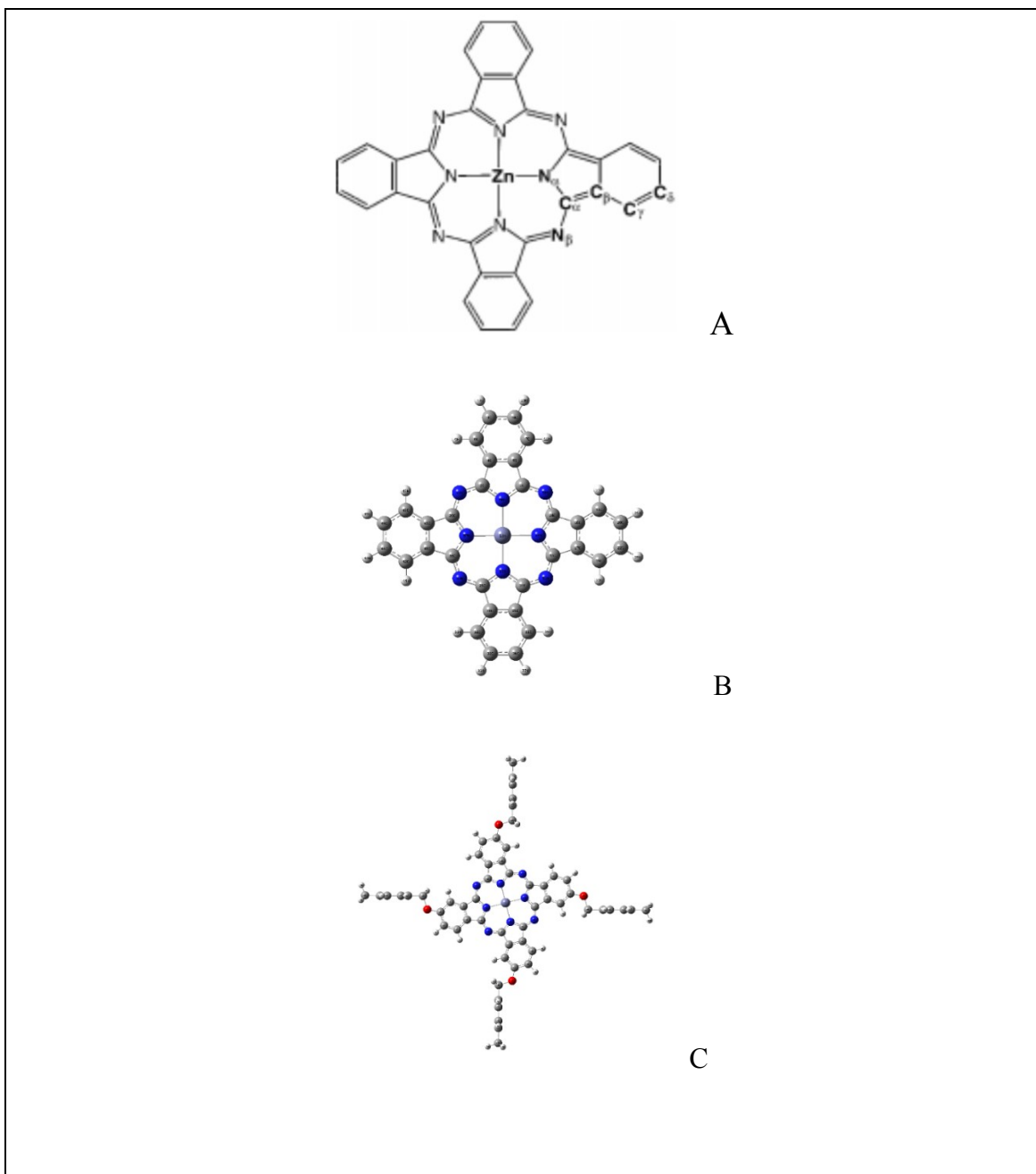


Figure 2-3. A. General structure of ZnPc to demonstrate α , β , γ , and δ positions. B. Optimized structure of ZnPc. C. Optimized structure of ZnPcBCH₃.

Calculations were done once in DMF and once in vacuum in DMF and calculated bond angles and bond lengths were in good agreement with the crystal structure.

Calculated singlet and triplet energies in vacuum are reported in Table 2-1. The energy difference between singlet and triplet of ZnPc and ZnPcBCH₃ are 1.093 and 1.087 eV, respectively. As it is stated before, ($\Delta E_{S0-T1} > 0.98$ eV), as the energy difference increases between singlet and triplet energies, more efficient sensitizer is expected to be obtained. Based on calculated value in Table 2-2, we are not expecting to observe a significant change in terms of efficiency of the sensitizer. This calculation was repeated using double zeta and triple zeta basis sets in the vacuum and the solvent for ZnPc to find out if changing these parameters have effect of the calculated ΔE value. Our results show that there is not a significant change in ΔE values which leads us to choose the smaller basis set to apply on ZnPcBCH₃ to reduce the computer cost.

Finding the relationship between the computation and experimental analysis is useful to develop a calculation model for ZnPc derivatives to predict the sensitizer dyes with highest amount of single oxygen production. This could also indirectly help us to assign a type I or II type reactions.

Table 2-2. Calculated values for the energy gap between the ground state singlet and the first triplet state.

B3LYP/dgdzvp				
Molecule	Singlet Energy	Triplet Energy	ΔE_{s-t} (eV)	Φ_Δ
ZnPc	-3446.448347	-3446.40818	1.093	0.56
ZnPcBCH ₃	-4986.167199	-4986.127119	1.087	0.51 ± 0.056

2.3.3 Singlet oxygen quantum yields

Using the relative method, the author obtained Φ_Δ values in DMF solvent as reported in Table 2-2. In agreement with calculated ΔE_{S0-T1} the rate of change in the singlet oxygen measurements from ZnPC to ZnPcBCH₃ are in the same range. The amount of singlet oxygen that is produced for ZnPc is not significantly higher than the one for ZnPcBCH₃.

It is also important to state that the initial intent was to calculate and measure the singlet oxygen in DMSO because of the biological assay that was done in DMSO. Because of the difficulty to detect singlet oxygen in DMSO experimentally, DMF was chosen for photophysical and photochemical analysis.

2.3.4 Photophysical properties

Photophysical properties of both ZnPC and ZnPcBCH₃ such as fluorescence lifetime decay, fluorescence quantum yield, lambda max, molar absorptivity are reported in Table 2-3 and Table 2-4. The lambda max of the predicted UV-Vis spectrum in DMF are also reported in Figure 2-4. The absorption spectra and fluorescence spectra reflect a bathochromic shift when ZnPc is converted to ZnPcBCH₃. The decay lifetime for ZnPc was 3.166×10^{-9} and was 3.1319×10^{-9} sec for ZnPcBCH₃.

Mirror image absorption and emission spectra imply that the same vibrational levels being involved in absorption and emission. The molar absorptivity slightly dropped down from 677 to 672. We used 96-well plate to measure the lambda max and molar absorptivity.

Repeated UV-VIS measurement in a plate reader in DMSO was necessary since these plates were further used in our biological assays.

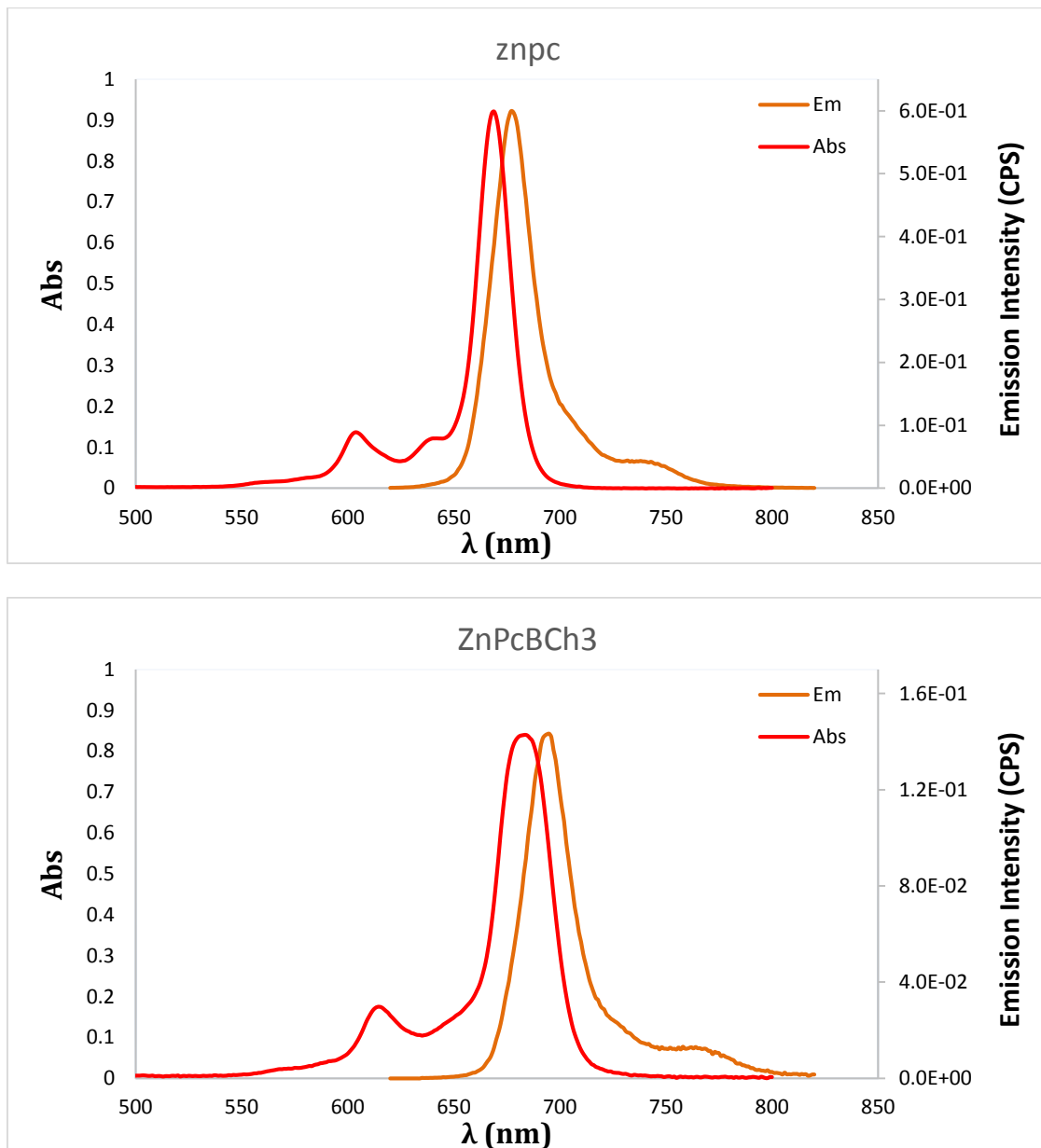


Figure 2-4. Absorption and emission spectra of ZnPc and ZnPcBCh₃ in DMSO.

Table 2-3. Experimental data for photophysical properties of ZnPc and ZnPcBCH₃ in DMSO that was obtained in plate reader with correction factor of 0.32.

Compound	λ_{max} Excitation	ϵ (M ⁻¹ cm ⁻¹)	λ_{max} Excitation	ϵ (M ⁻¹ cm ⁻¹)	Solubility	Φ_f	τ_f
ZnPc	672	1.7E+05	346	8.58E+4	DMF, DMSO(partially), THF(Partially)	0. 28	3.166x 10 ⁻⁹
ZnPcBCH ₃	677	1.6E+05	352	6.4E+04	DMF/DMSO/THF /DCM/Acetonitrile (partially), Acetone(partially)	0. 52	3.1319 x10 ⁻⁹

Table 2-4. Reported molar extinction coefficient in DMF.

Compound	λ Excitation (DMF)	ϵ (M ⁻¹ cm ⁻¹)	λ emission	Stokes shift
ZnPcBCH ₃	681 612	1.60E+05 3.41E+04	697 nm	16

2.3.5 Characterization of nanoparticles

To enhance the selectivity and overcome the low water solubility of ZnPcBCH₃, this dye was encapsulated in PLGA-b-PEG polymeric micelles using nanoprecipitation. Diameter size and shape of the polymeric micelles were determined using dynamic light scattering (DLS) and TEM. Nanoprecipitation was carried out in different solvents to evaluate any change in the diameter size and zeta potential. The average diameter of polymeric micelles

was 112.4 nm using THF and 97.82 nm using acetone. Reported TEM data in Figure 2-5 also confirm that the diameter of the nanoparticle size is a range of 100 nm. Changing solvent for encapsulation did not have a significant impact on the polydispersity index and zeta potential of the micelles. Reported zeta potential for the polymeric micelle using THF or acetone were Zeta -9.74mV and -8.93mV respectively. Representative TEM images showed that the formed micelles from PLGA-b-PEG are spherical. A summary of data obtained is in Table 2-5.

Encapsulation of ZnPc into polymeric micelles such as PLGA or PLC were reported [151, 162]. However, due to the low solubility of ZnPc in volatile organic solvents, nanoprecipitation method could not be the method of choice for encapsulation of this dye. Modification of ZnPc into ZnPcBCH₃ made this dye soluble in a relatively volatile organic solvents such as THF, DCM, and acetone. Therefore, we were able to encapsulate this dye into polymeric micelles using nanoprecipitation methods. As a result we were obtained a smaller size nanoparticles.

Reported dynamic light scattering showed a broader diameter size range for the same dye concentration when THF was used as a solvent for encapsulation instead of acetonitrile or acetone. This is because of higher solubility of ZnPcBCH₃ in THF compared to acetone and acetonitrile and without measurement it can be implied that the efficiency load of ZnPcBCH₃ is higher when THF is used compare to when acetonitrile or acetone is used.

Regardless of the solvent choice, Table 2-5, the zeta potential of the nanoparticle is in ±10 mV. This range of zeta potential indicates that PLGA-b-PEG nanoparticle is a neutral particle [163]. It is known that the nanoparticles with higher surface charge strongly interact

with cell membrane and it facilitates the cell uptake. And, Poly index (PDI) of less than 0.3 indicates a homogeneous particle distribution.

Table 2-5. Reported zeta potential and average diameter values.

Physical characterization data			
Polymeric micelle/solvent	Zeta potential (mV)	Average diameter (nm)	PDI
PEG-b-PLGA (Acetone)	-8.93	97.82	0.209
PEG-b-PLGA (THF)	-9.74	90.09	0.202
PEG-b-PLGA (Acetonitrile)	-6.65	106.7	0.207

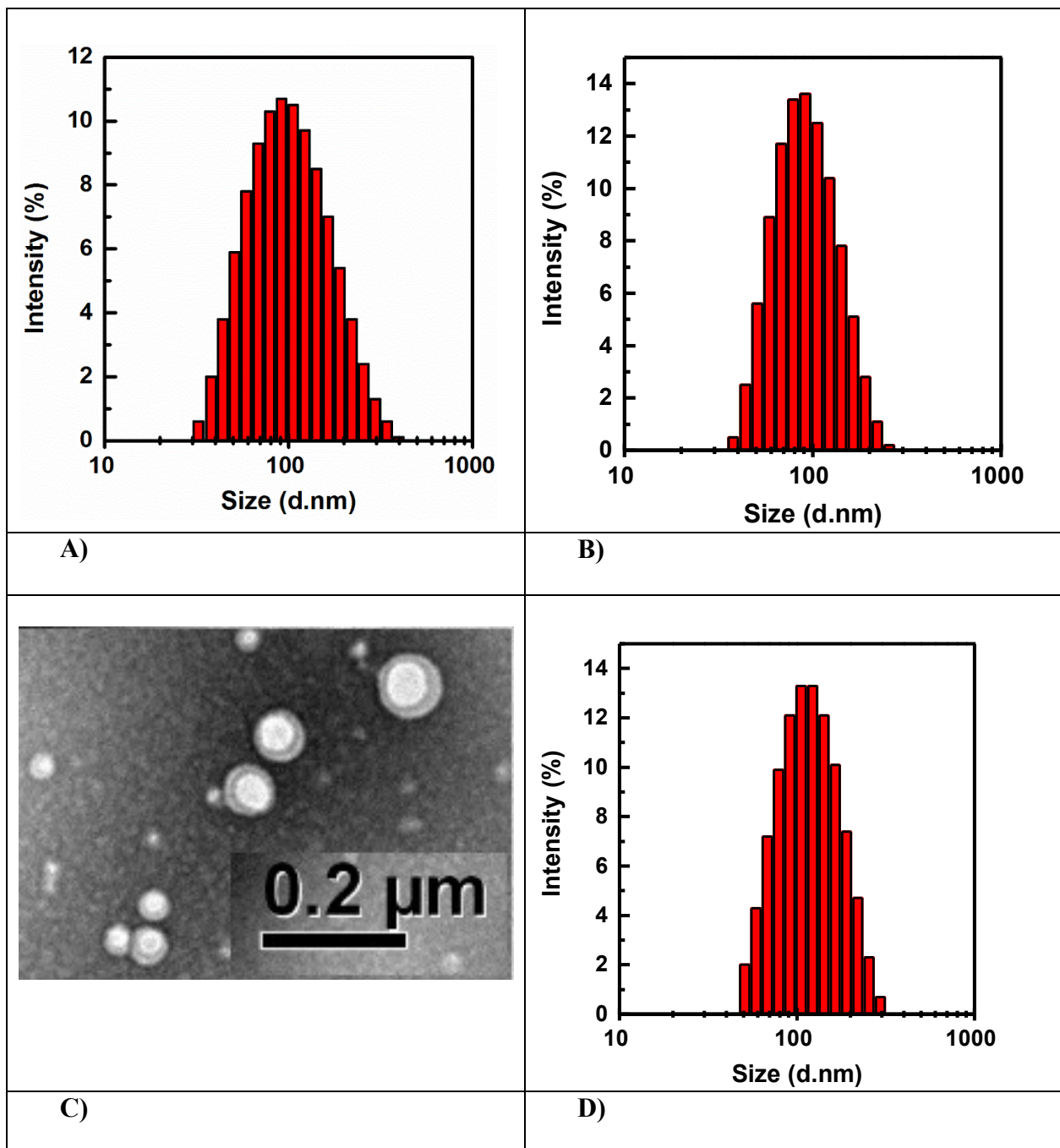


Figure 2-5. A, B and C are the size distribution obtained from DLS using THF(A), acetone (B) and acetonitrile (C, D) in nanoprecipitation process.

Table 2-6. Reported nanoparticle yield, sensitizer drug load and entrapment efficiency obtained from nanoprecipitation with THF.

Sample	ZnPcBCH ₃
Nanoparticle Yield (%)	73.76
Drug Load (%)	0.37
Entrapments Efficiency (%)	28

2.3.6 Study the lipophilicity of ZnPcBCH₃ with ZnPc

Absorption spectra for each concentration of 2 and 4 μM of ZnPc and ZnPcBCH₃ were evaluated in DMEM, DMSO and FBS. As it is previously reported in Table 2-3, the molar extinction coefficient of the ZnPc was reported higher than ZnPcBCH₃. Figure 2-6A showing a spectra with larger absorbance for ZnPc than the one for ZnPcBCH₃ which also confirms that the molar extinction coefficient of ZnPc is higher. Figure 2-6 B represents the interaction of the ZnPc and ZnPcBCH₃ in cell media. Larger absorbance for ZnPcBCH₃ shows a higher interaction of this dye in media compare to ZnPc. Otherwise, at the same concentration it was expected to observe a higher absorbance for ZnPc since it has a higher molar extinction coefficient. Higher absorbance peak reported for ZnPcBCH₃/FBS compare to ZnPc/FBS in Figure 2-6 A confirms the higher interaction and higher lipophilicity of ZnPcBCH₃ with FBS.

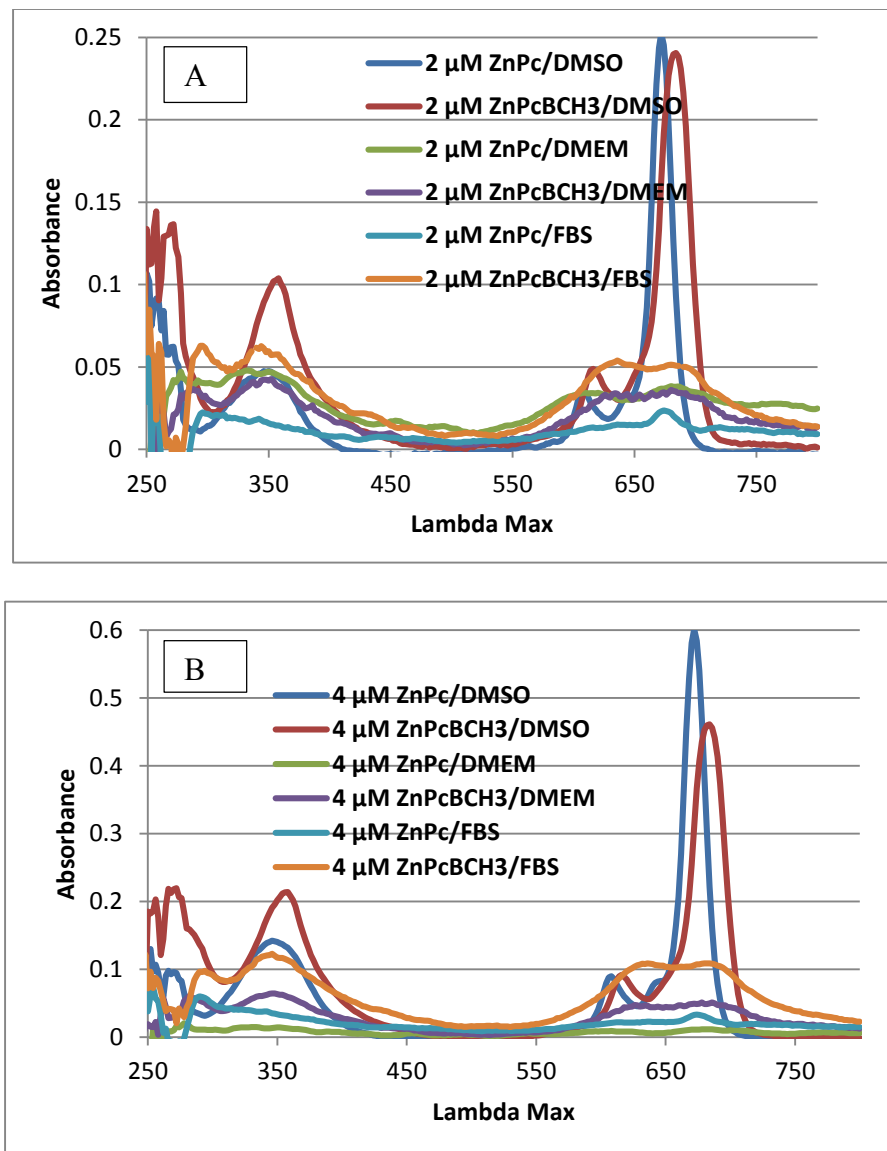


Figure 2-6. Monitoring the lipophilicity of the ZnPc vs ZnPcBCH₃ through absorptivity of the visible spectra in DMSO, DMEM and FBS media.

2.3.7 Cell localization of ZnPc and ZnPcBCH₃ in A549 cells

Live cells were treated with 5 μ l of each dye for 1 min and then it was removed. The dye concentration of each dye was 2 μ M. These cells were also treated with NucBlue as a

reference. As a result of this treatment, localization of ZnPc and ZnPcBCH₃ in A549 cells, shown in Figure 2-7, was determined using fluorescence microscopy (EVOS). The fluorescence associate with ZnPc was green and the one for ZnPcBCH₃ was red. Cell nuclei appear as blue using NuBlue. This results show accumulation of the both ZnPc and ZnPcBCH₃ in cytoplasm of A549 cells. Texas Red light cube was used for ZnPc and Cy5 was used for ZnPcBCH₃. Using different LED light cube also confirms that absorption and emission peak of ZnPc and ZnPcBCH₃ are different.

Looking at Figure 2-7, the images on the left column represent the location where cells are stained because of addition of ZnPc or ZnPcBCH₃. Images in the middle show the nucleus of cells that were stained with NuBlue. Images on the right column show the overlap of the first two columns meaning that the stained cytoplasm also have a related nucleus. This confirms that these images are showing a real cell.

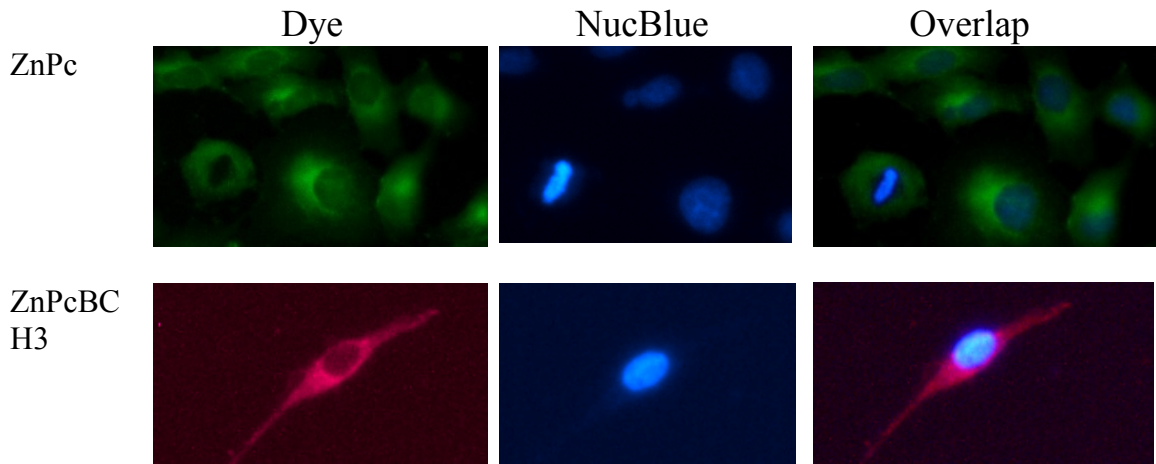


Figure 2-7. Localization of ZnPc and ZnPcBCH₃ in A549 cells were using Texas Red light cube for ZnPc and Cy5 for ZnPcBCH₃.

2.3.8 Cell Uptake:

One important aspect of the PDT study for each individual sensitizer dye is to determine when to expose the cells that were previously treated with sensitizer drug. This time is called “optimized time”. So, the optimized time is the time when dye uptake is maximized. Reaching the maximum cell uptake is important to reach the highest cytotoxicity.

Cell uptake of the encapsulated nanoparticles of ZnPcBCH₃ were studied at different incubation time. Figure 2-8 shows that increasing incubation time, from left to right, have increased the amount of dye uptake. Encapsulated dye was incubated at a range of concentrations to determine the maximum uptake in 24 h prior to the dark and light toxicity assays.

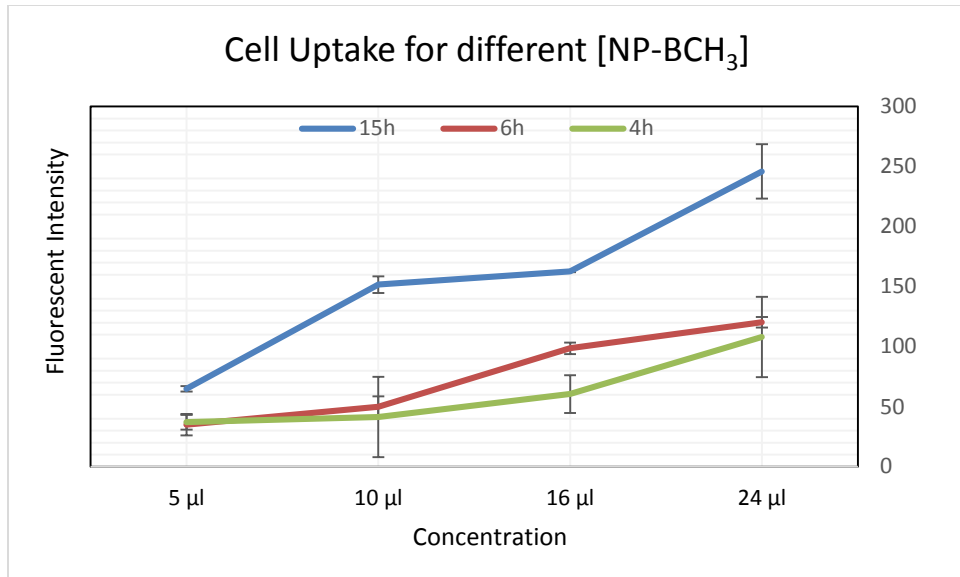


Figure 2-8. Comparing the fluorescence intensity of and cell uptake of encapsulated ZnPcBCH₃ at different incubation time and concentration.

2.3.9 *In vitro* Dark and Cytotoxicity Assay on A549 cells

Dark toxicity of the ZnPc and ZnPcBCH₃ was assessed against A549, Figure 2-9, showing that these dyes were not toxic in the absence of light within 24 h.

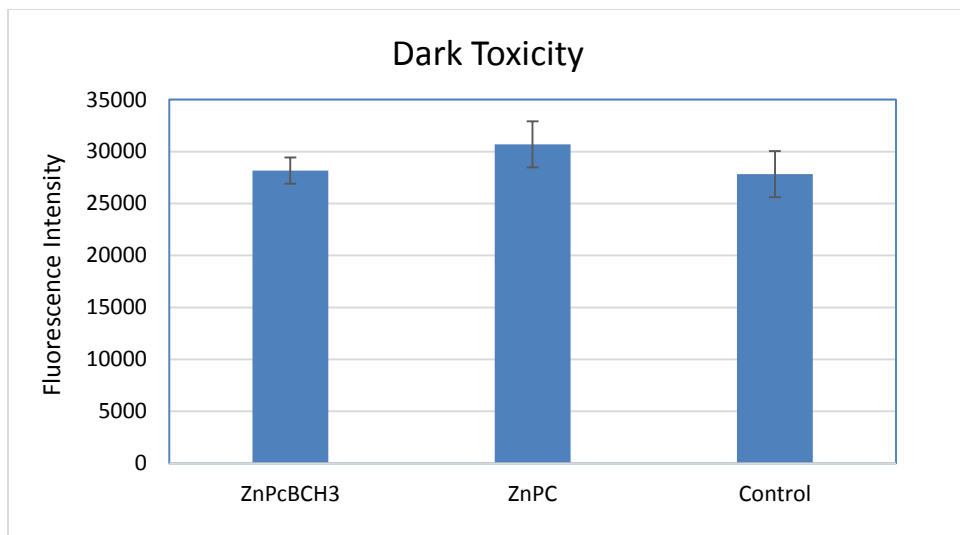


Figure 2-9. Dark toxicity analysis of ZnPC and ZnPcBCH₃.

According to the literature, a significant cell killing effect was expected to be observed for ZnPC with (1.5 mW/cm²) exposure and 1 μM concentration that was tested on A549 cell line. So, for this work, treated cells with sensitizer drug was exposed 1.5 mW/cm².

We did not observe a high cytotoxicity effect for free ZnPC using 1.5 mW/cm² of light exposure for ZnPC on A549 cells. In contrast, encapsulated ZnPcBCH₃ in PLGA-b-PEG showed cytotoxicity in some extent,

Figure 2-10. Although the cytotoxicity of the encapsulated dye was significantly higher than the free dye, a more significant cytotoxicity could have been observed. This result could be due to several reasons.

Regarding encapsulated ZnPcBCH₃, it is possible that ZnPcBCH₃ aggregated once they released from nanoparticle and they did not produce enough singlet oxygen.

Also, the zeta potential of this nanoparticle is defined as neutral. Choosing the cationic nanoparticle with zeta potential of +30 mV may have improved the cell membrane disruption and perhaps cell killing effects.

It is possible that free ZnPc and ZnPcBCH₃ did not show cytotoxicity because these dyes are hydrophobic and they form aggregates in solution. To test this hypothesis, fluorescence measurement was done for ZnPcBCH₃ and ZnPc in a mixture of DMSO-Media with 4 μ M concentration. Obtained results showed a significant drop in the fluorescence intensity but still some signals were observed.

Cell uptake picture, Figure 2-7, also support that in presence of DMSO we can observe the fluorescence emission. The minimum amount of fluorescence that is observed could be because of the present of DMSO that kept some of the dye solubilized in media.

For encapsulated dye in nanoparticle that where no organic solvent involved, the minor toxicity observed may have happened once the drug is still encapsulated. Otherwise, if the drug release in the media it will form aggregate and cannot form singlet oxygen perhaps.

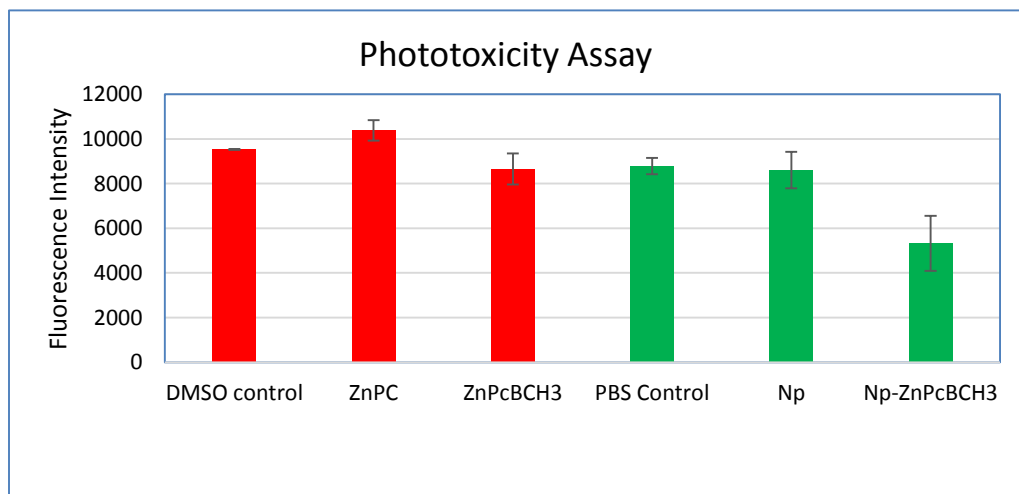


Figure 2-10. CTB toxicity assay for encapsulated vs free dyes.

2.4 Conclusion

A new lipophilic derivative of phthalocyanine, ZnPcBCH₃, with better solubility in organic solvents was synthesized, characterized and its photophysical and phytochemical properties were measured in DMF and DMSO. As expected, both encapsulated and free dyes showed low dark toxicity. Although free ZnPcBCH₃ did not show any cytotoxicity, encapsulated ZnPcBCH₃ in PLGA-b-PEG showed toxicity to some extent. It is possible that the cytotoxicity effect can be improved if sensitizer dyes were covalently bonded to the polymeric micelle.

Density functional theory (DFT) calculation was conducted for ZnPc and ZnPcBCH₃ to calculate the singlet and triplet energy gap to compare it with singlet oxygen quantum yield values. An agreement was observed between ΔE_{S0-T1} of each dye and singlet oxygen production.

2.5 Supporting Documents

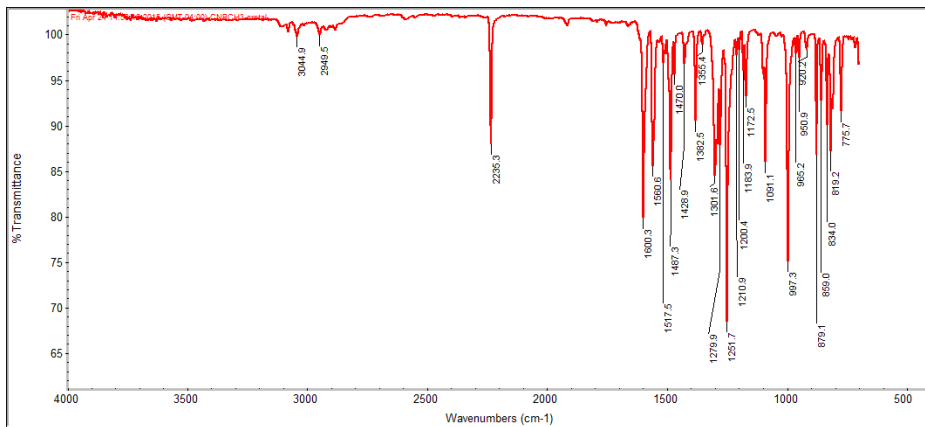


Figure 2-11. FTIR spectrum of compound 3.

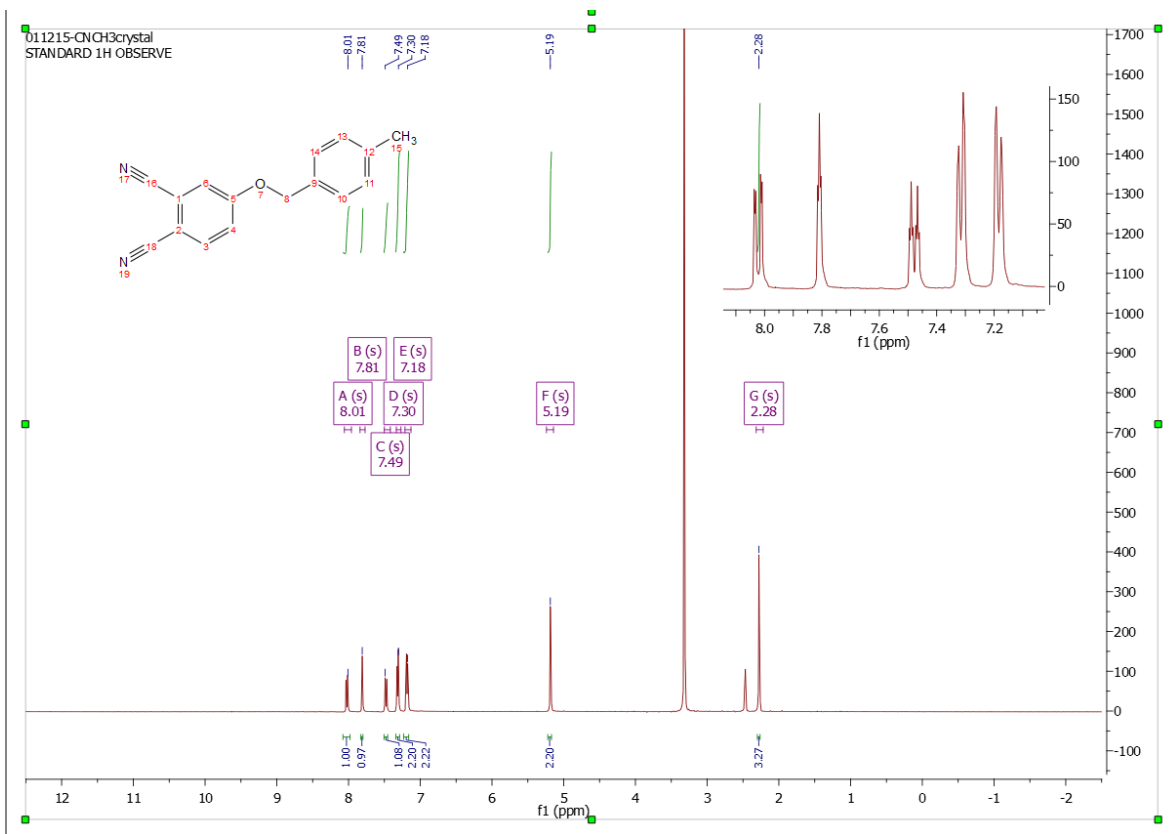


Figure 2-12. ¹H NMR spectrum of compound 3.

141137_Sample1_NM #102-127 RT: 0.55-0.68 AV: 26 NL: 6.20E8
T: FTMS + p ESI Full ms [200.00-1000.00]

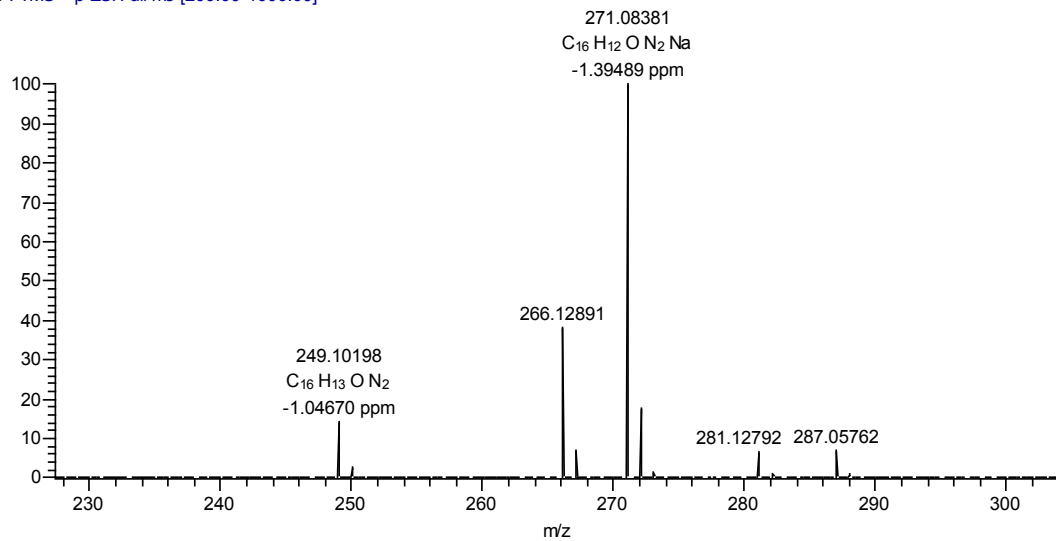


Figure 2-13. ESI mass spectrum of compound 3.

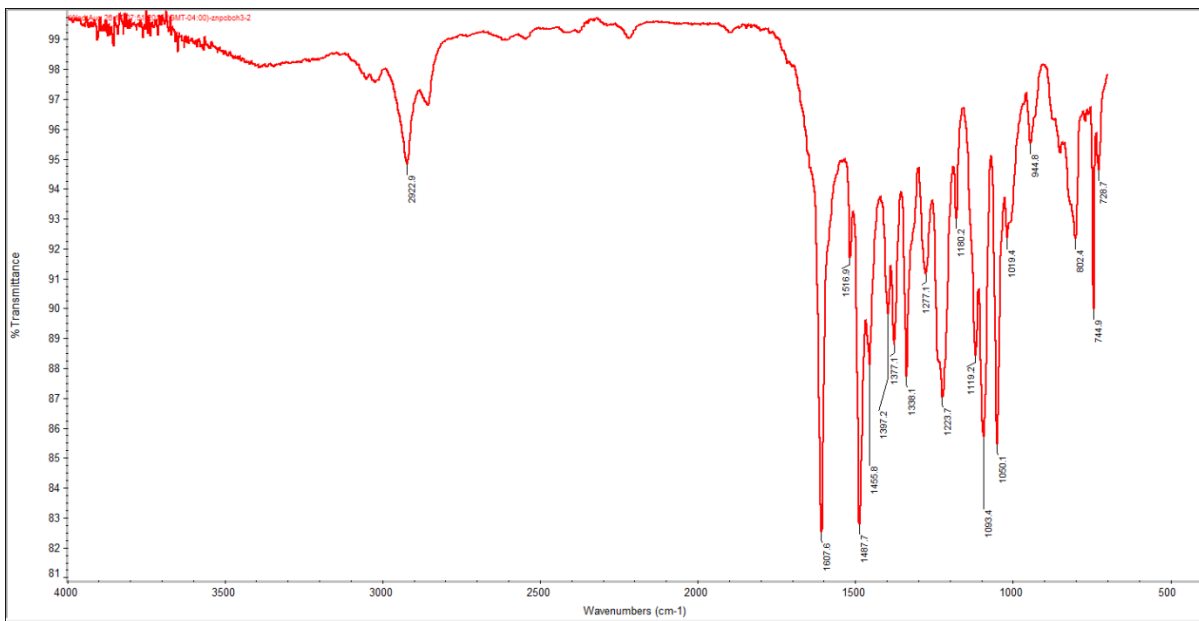


Figure 2-14. FTIR spectrum of compound 4.

141490_PcZnBCH3 #96-341 RT: 0.56-2.01 AV: 246 NI: 6 24F4
T: FTMS + p ESI Full ms [200.00-1200.00]

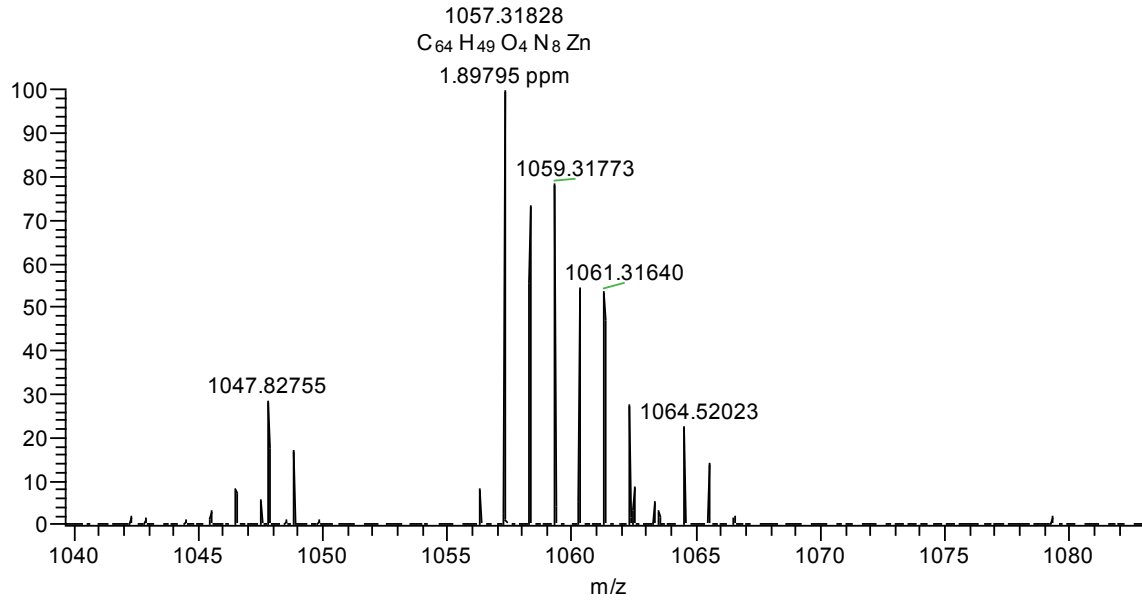


Figure 2-15. ESI mass spectrum of componoud 4.

Chapter 3

SYNTHESIS, CHARACTERIZATION AND EVALUATION OF PHOTOPHYSICAL PROPERTIES OF ZINC PHTHALOCYANINE WITH TETRAZOLE DERIVATIVE

3.1 Introduction

Photodynamic therapy (PDT) is a noninvasive modality that can be used for treatment of cancer, oral disease and infection diseases [143, 144]. PDT involves the action of a photosensitizer, oxygen and light in combination to form reactive oxygen species (ROS) to kill cancer cells. In summary, upon absorption of a photon of light, a PDT sensitizer was promoted to the short-lived first excited state (S_1) and can convert to the first excited triplet state (T_1) through intersystem crossing. It is known that the energy of the first triplet state can be transferred to the surrounding molecular oxygen 3O_2 to form a reactive oxygen species called singlet oxygen (1O_2), and the sensitizer returns to the ground state (S_0). This cycle can be repeated multiple times, depending on the photostability of the sensitizer.

In this work, zinc phthalocyanine as a potent sensitizer was chosen for PDT study. This complex is a photostable sensitizer from the porphyrin family that has a heteroaromatic system comprising 18π bonds. Properties that make this photosensitizer unique are: its low dark toxicity, its resistance to chemical and photochemical degradation, and its relatively

long triplet state lifetime [150]. Compared to other porphyrin-type structures such as protoporphyrin IX, zinc phthalocyanine has a higher molar extinction coefficient which is important to reduce the required drug dose and subsequently their side effects [150]. The main shortcoming of zinc phthalocyanine is its low solubility and selectivity of this compound that can be overcome by suitable modification in the alpha and beta positions.

It is known that the addition of substituents in alpha and beta positions of zinc phthalocyanine has an impact on the photophysical and photochemical properties of this dye. These substituents can introduce additional properties in physiological conditions depending on the type of functional groups that was added.

Addition of tetrazole derivatives in the alpha position and evaluating the photophysical properties of the new dye is the goal of this Chapter.

Tetrazole with more than 20 biological activities is promising in the world pharmaceutical market. Reported biological activities such as antimicrobial, antiviral, and antiallergic activities [164] make this moiety attractive to use it in the alpha position of the zinc phthalocyanine. It was anticipated that addition of this group can introduce new properties into ZnPc that are important in PDT field. To evaluate the characteristics of this dye, the properties of this dye were compared with other ZnPc analogs.

3.2 Material and Method

Chemicals. Zinc phthalocyanine (ZnPc), 4-hydroxybenzoic acid. poly (ethylene glycol) methyl ether-block-poly (lactide-co-glycolide) known as PEG-b-PLGA with PEG average M_n 2000 and PLGA average M_n 11,500 and MTT (3-(4,5-dimethylthiazol-2-yl)-2,5-

diphenyl-2H-tetrazolium bromide) were purchased from Sigma Aldrich. Dimethyl sulfoxide (DMSO) was purchased from Alfa Aesar, while dimethylformamide and acetonitrile were purchased from Fisher Scientific.

Biological supplies. DMEM/High Glucose (SH30243.02) was purchased from Fisher. CellTiter-Blue® Cell Viability Assay (CTB), to measure the cell viability of the cells were purchased from Promega. NucBlue, as a molecular probe was purchased from Thermo-Fisher to stain nucleus. Human A549 lung carcinoma cells cultured in DMEM contain 10% v/v FBS. Cells were incubated at 5% CO₂ at 37°C. Phototoxicity of the encapsulated dye was evaluated using scope light 2000 and a 599±29 long pass filter was used.

Instrumentations. ¹H NMR spectra was recorded on a Varian 400 MHz spectrometer. Fluorescence decay was recorded on a Fluorolog-3 spectrofluorometer (HORIBA Jobin Yvon Inc) and nanoled-625. FTIR spectra were recorded on a Nicolet Nexus 470 FTIR spectrophotometer (Thermos Scientific, USA). UV-VIS measurements were recorded on a Cary 300 spectrophotometer. Plate readers were a Molecular Devices Spectramax Gemini XS fluorescent Plate reader and a Molecular Devices SpectraMax UV/Visible spectrophotometric plate reader. Singlet oxygen quantum yields were measured using an Edinburgh Analytical Instrument (FS920) and NIR PMT from HAMAMATSU (H10330A series).

3.3 Synthesis

5-(4-Hydroxyphenyl)-2-methyltetrazol (4)

4-Hydroxycinnamic acid (1.795, 0.011 mol) was added to the 3 M sodium hydroxide solution under magnetic stirring. A mixture of acetic anhydride (8.9 ml) in ice was added to the mixture and it was stirred vigorously for another 15 min to form a precipitate. Precipitate was isolated through filtration and recrystallized with methanol and water to obtain 5-(4-acetoxyphenyl)tetrazole, compound 2. A solution of compound 2 (0.835 g, 0.004 mol), methyl bromide (0.004 mol), and potassium carbonate (0.55 g, 0.004 mol) was refluxed in acetone for 44 h. This mixture was cooled and filtered to remove the solid. The filtrate was concentrated using a rotary evaporator and the residue was recrystallized from ethanol. Mp 198-200 °C. ^1H NMR (400 MHz, DMSO-d6) δ 9.99 (s, 1H), 7.89 – 7.82 (m, 2H), 6.94 – 6.87 (m, 2H), 4.38 (d, J = 0.9 Hz, 3H). HRMS: Theoretical 177.07709 [M+H] $^+$, Experimental 177.07741 [M+H] $^+$, Elemental composition C₈H₈N₄O, FTIR(cm⁻¹): 3159.6 (Ar-OH), 3026.9 (Ar-CH), 2965.3 (CH).

5-(4-Hydroxyphenyl)-2-butyltetrazol (5)

Following the above solution, a solution of compound 2 (0.835 g, 0.004 mol), and butyl bromide (0.004 mol), and potassium carbonate (0.55g, 0.004 mol) were refluxed in acetone for 44 h. The mixture was cooled and filtered to remove solids. The filterate concentrated using a rotary evaporator and the residue was recrystallized from ethanol.

4-[4-(2-Methyl-tetrazol-5-yl)phenoxy] phthalonitrile (6)

The 4-nitrophthalonitrile (200 mg, 1.156 mmol) and compound 4 (203.67 g, 1.156 mmol) were dissolved in 20 ml of 95% dry DMF and stirred under N₂. After 5 min K₂CO₃ was added (479 mg, 3.468 mmol) and the reaction was heated to 90°C. Reaction was monitored using TLC (silica gel, CH₂Cl₂) and it was complete after 12 h. The reaction mixture was poured into 100 ml of cold water, and 320 mg product was obtained and purified further by recrystallization from H₂O and ethanol. ¹H NMR (400 MHz, DMSO-d6) δ 8.16 (m, J = 8.9, 2.1, 1.1 Hz, 3H), 7.93 (dd, J = 2.7, 1.1 Hz, 1H), 7.53 (m, J = 8.7, 2.5, 1.1 Hz, 1H), 7.41 – 7.32 (m, 2H), 4.75 (m, J = 7.6, 6.5, 1.0 Hz, 2H), 1.96 (pd, J = 7.0, 1.2 Hz, 2H), 1.40 – 1.18 (m, 2H), 0.92 (td, J = 7.4, 1.2 Hz, 3H). FTIR (cm⁻¹): 3085.3, 3046.8, 2236.0 (CN), 1596.6, 1560.9, 1536.4, 1485.0, 1461.5, 1418.3, 1418.3, 1305.5, 1279.2, 1253.0, 1213.0, 1157.5, 1106.6, 1086.7, 1045.4, 1002.7, 954.3, 849.4, 861.7, 841.0, 764.5, 733.8, 720.2. (CH) . Theoretical 303.09889 [M+H]⁺, Experimental 303.09900 [M+H]⁺. Elemental composition C₁₆H₁₀N₆O.

4-[4-(2-Butyl-Tetrazol-5-yl)phenoxy] phthalonitrile (7)

The 4-nitrophthalonitrile (500 mg, 2.89 mmol) and compound 5 (630.809 g, 2.89 mmol) were dissolved in 20 ml of 95% dry DMF and stirred under N₂. After 5 min K₂CO₃ was added (1.198 mg, 8.67 mmol) and the reaction was heated at 90°C. The reaction was monitored using TLC, (silica gel, CH₂Cl₂) and it was complete after 12 h. The reaction mixture was poured into cold water and 320 mg product was obtained and purified further by recrystallization from H₂O and ethanol. ¹H NMR (400 MHz, DMSO-d6) δ 8.16 (ddd, J = 8.9,

2.1, 1.1 Hz, 3H), 7.93 (dd, J = 2.7, 1.1 Hz, 1H), 7.53 (m, J = 8.7, 2.5, 1.1 Hz, 1H), 7.41 – 7.32 (m, 2H), 4.75 (m, J = 7.6, 6.5, 1.0 Hz, 2H), 1.96 (pd, J = 7.0, 1.2 Hz, 2H), 1.40 – 1.18 (m, 2H), 0.92 (td, J = 7.4, 1.2 Hz, 3H). HRMS: Theoretical 345.14584 [M+H]⁺, Experimental 345.14565 [M+H]⁺. Elemental composition C₁₉H₁₆N₆O.

2(3), 9(10), 16(17), 23(24)-Tetrakis [4-(2-methyl-tetrazol-5-yl)phenoxy] phthalocyanine zinc(II) (8)

Compound 4 (250 mg, 0.661 mmol) was dissolved in 3 ml dried DMF and a catalytic amount of DBU was added. While stirring the reaction mixture under argon, zinc acetate (30.34 mg, 0.165 mmol) was added and the mixture was heated to 150°C and stirred for 18 h. After cooling, the solution was added into cold water dropwise. Product was separated and washed with methanol to remove impurities. The product obtained (270 mg) which was washed with methanol several times. M.p. > 200°. ¹H NMR (400 MHz, DMSO-d₆): δ 8.84-8.50 (m, 3H), 8.5-8.6 (m, 1H), 8.32 (s, 2H), 8.25-8.13 (m, 3H), 8.00 (dd, J = 25.9, 16.7 Hz, 6H), 7.91-7.77 (m-2H), 7.68(dt, J =19.0, 10.3 Hz, 5H), 7.55-6.99 (m, 6H), 4.43-4.34 (m, 12H). FTIR(cm⁻¹): 3427.3 (Ar-CH), 2932.8 (CH), 1605.9, 1537.3, 1427.6, 1394.8, 1335.6, 1232.4, 1167.6, 1091.6, 1044.8, 1005.1, 945.0, 842.0, 763.4, 746.7, 733.1. HRMS: Theoretical 1273.30286 [M]⁺, Experimental 1273.30273 [M]⁺, elemental composition C₆₄H₄₀N₂₄O₄Zn.

2(3), 9(10), 16(17), 23(24)-Tetrakis [4-(2-butyl-tetrazol-5-yl)phenoxy] phthalocyanine zinc(II) (9)

Compound 4 (250 mg, 0.661 mmol) was dissolved in 3 ml dried DMF and catalytic amount of DBU was added. While stirring the reaction under argon, zinc acetate (30.34 mg, 0.165 mmol) was added and the mixture was heated to 150°C and stirred for 18 h. After cooling, the solution was added into cold water dropwise. Product in form of precipitate was separated and washed with methanol to remove impurities. 270 mg of product was obtained which was washed with methanol several times to be purified. M.p. > 200°. ¹H NMR (400 MHz, DMSO-d6) δ 8.35 – 8.26 (m, 5H), 8.23 (s, 2H), 8.05 (dd, J = 14.4, 8.0 Hz, 7H), 7.80 – 7.65 (m, 8H), 7.55 (dd, J = 8.3, 4.8 Hz, 3H), 7.49 (t, J = 8.4 Hz, 4H), 4.74 (s, 8H), 1.98 (s, 8H), 1.35 (d, J = 6.5 Hz, 8H), 0.98 – 0.94 (m, 12H).

Zinc (II) tetramethylphthalocyanine (ZnPc4CH₃)

The 4-methylphthalonitrile (1g, 1.577 mmol) was dissolved in 3ml dry DMF and catalytic amount of DBU was added. The reaction mixture was heated at 150° and held under argon for 12 h. After the reaction mixture cooled, it was added to methanol dropwise and filtered to collect dyes in a form of precipitate. Precipitate washed with 200 ml of methanol. HRMS: m/z 302.05361 [M+Na]⁺, C₆₄H₂₄N₈Zn.

Zinc (II) tetranitrophthalocyanine (ZnPc4NO₂)

The 4-nitrophthalonitrile (1g, 757.90 mmol) was dissolved in 3ml dry DMF and a catalytic amount of DBU was added. The reaction mixture was heated at 150° and held

under argon for 12 h. After the reaction mixture cooled, it was added to methanol dropwise and filtered to collect dyes in a form of precipitate. Precipitate washed with 300ml of methanol. Samples washed with 200 ml of methanol. HRMS: m/z 757.02653 [M+H]⁺, C₃₂H₁₂N₁₂O₈Zn.

3.4 Singlet oxygen quantum yield

Singlet oxygen quantum yield (Φ_Δ) measurements was performed using Fluorimeter Edinburgh Analytical Instrument (FS920) and NIR PMT from HAMAMATSU (H10330A series). Data acquisition was controlled by LP900 software program. Separate solution of ZnPc and ZnPcBCH₃, ZnPcNO₂, ZnPcCH₃, ZnPc-M-tet and ZnPc-B-Tet were prepared in DMF with the maximum absorbance of 0.08 to 0.2 at 699 nm. Both solution of ZnPc and ZnPcBCH₃ were excited at 699 nm where the excitation count for both standard and the sample are the same. The OD of these samples at this wavelength and the area under the typical phosphorescence emission at 1270 nm were used to calculate singlet oxygen quantum yield using equation 1.

$$\Phi_\Delta = \Phi_\Delta (\text{std}) \frac{A_{obs}(x).OD(\text{std})}{A_{obs}(\text{std}).OD(x)} \quad (12)$$

Where OD (std) and OD (x) are the absorbance of the ZnPc standard and unknowns respectively.

3.4.1 Steady-State and life-time fluorescence

Steady state fluorescent emission measurement was performed on Hammatsu absolute quantum yield spectrometer (C11347). Fluorescence quantum yield (Φ_f) measurements were conducted similar to the procedure that describe above for singlet oxygen measurement. Except that the excitation point for each sample, ZnPcBCH₃, ZnPcNO₂, ZnPcCH₃, ZnPc-M-Tet and ZnPc-B-Tet are different. Solution of ZnPc in DMF was prepared with OD of 0.9 to 0.1. Absorption Area of the fluorescence emission and the recorded absorption were used to calculate the fluorescence quantum yield using equation 2. Conditions for the samples and the standard were the same and this measurement were repeated twice in two different days. ZnPc in DMF was used as a standard for this measurement ($\Phi_f = 0.28$) [159]

$$(\Phi_f) = (\Phi_f) (\text{std}) \frac{A(x) \cdot OD(\text{std})}{A(\text{std}) \cdot OD(x)} \quad (13)$$

Where A(x) and A (std) are areas under the fluorescent emission curves of the samples and the standard respectively. OD(x) and OD (std) are the absorbance of the samples and standards.

Method of choice to measure lifetime was time-correlated single photon counting method that was conducted on the ZnPc and ZnPcBCH₃ solutions in DMF. For this measure samples were excited at 625 nm utilizing NanoLED pulse laser. Measurements were repeated twice and performed at repetition rate of 1MHz and a band pass of 1.5 nm.

3.4.2 MTT and CTB Dark toxicity Assays

Cytotoxic effects of free ZnPc vs other dyes, ZnPc-M-Tet, ZnPc-B-Tet, ZnPcCH₃, ZnPcNO₂ and ZnPcBCH₃, and encapsulated ZnPcBCH₃ in PLGA-b-PEG on A549 cells were determined utilizing CTB assays. For the MTT assay, 7500 cells/well were cultivated in a 96-well plate. Cells were incubated at 37°C overnight and treated with 4μM of ZnPcBCH₃, ZnPc; three wells per condition in 2% DMSO-Media for each dye except that the encapsulated ZnPcBCH₃ in PBS was added in 10 μl. Two controls, one for 2% DMSO in media and one for 10 μl PBS were also set up. After 24 h of incubation, cells were treated with 20 μl of 5mg/ml MTT to each well. One set of wells should be included for the MTT with no cells as a third control. Cells were incubated for another 3.5 h. After incubation media was remove carefully and 150 μl of MTT solvent was added per well. Plate was covered with Al foil and placed on a shaker for 15 min. Absorbance was read at 570 nm with reference filter of 620 nm.

With a few differences, CTB assay was conducted. The number of cells that was set up for CTB assay was 7000 cells per well and let it grow overnight. Cells were fed with 100 μl of media and after 24 h, 4 μM of ZnPc and ZnPcBCH₃ in DMSO and 20 μl of the nanoparticle solution, described in 2.2.5, were added to the designated wells. These procedures were done in subdued light. After 24 h of incubation, 20 μl of CTB was added to each well and let it incubate for another 3 h. Fluorescence emissions were recorded at 560 nm and 590 nm utilizing the plate reader.

After addition of a sensitize dye 30 μl and incubation for 24 h CTB dye was added to were exposed to 1.5 mw/cm² for 4.5 min using a band path filter of 599±25 nm.

3.4.3 MTT and CTB Cytotoxicity Assays

The main difference between the light and dark toxicity for MTT assay can be described as:

1. For the MTT assay, after 24 h of cell treatment with sensitizer drug, media was removed and 50 μ l of PBS was added. Cells were exposed with 1.5 mw/cm² for 4.5 min using a band path filter of 599 \pm 25 nm. To express the light exposure toxicity, cells were incubated for another 24 h after exposure prior to removal of the media and addition of the MTT solution.

2. For CTB assay, For the MTT assay, after 24 h of cell treatment with sensitizer drug, media was removed and 50 μ l of PBS was added. Cells were exposed with 1.5 mw/cm² for 4.5 min using a band path filter of 599 \pm 25 nm. To express the light exposure toxicity, cells were incubated for another 24 h after exposure prior to addition of the CTB dye.

3.4.4 Cell Uptake Assay

Cell uptake of each dye was tested on A549 cells. For uptake measurements, 5000-10000 cells per well were seeded in a 96-well plate. From stock solution (2 mM) of each dye in DMSO, 0.5 μ l of each dye was added to each well. After 24 h of incubation at 37°C media was removed and cells washed with PBS. Cells were lysed with DMSO to measure the fluorescence intensity using a plate reader.

3.5 Results

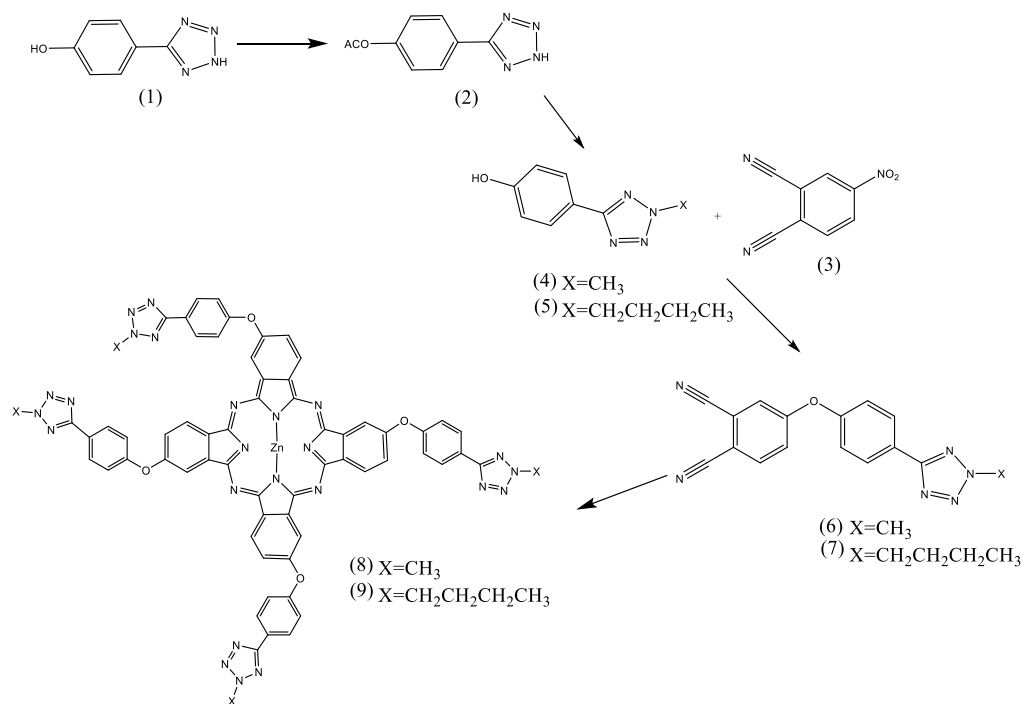
3.5.1 Synthesis

The synthesis of 2(3), 9(10), 16(17), 23(24)-Tetrakis [4-(2-methyl-tetrazol-5-yl)phenoxy] phthalocyanine zinc(II), (ZnPc-M-Tett) and 2(3), 9(10), 16(17), 23(24)-Tetrakis

[4-(2-butyl-tetrazol-5-yl)phenoxy] phthalocyanine zinc(II),ZnPc-B-Tet (shown in Scheme 3-1) were conducted in three steps, beginning with the reaction of 4-acetoxyphenyl tetrazole and methyl bromide or butyl bromide to obtain compounds 4 and 5, respectively. Similar reaction conditions are found in literature [165].

Compound 4 and 5 and nitrophthalonitrile were reacted in dry DMF to obtain compound 6 in 100% yield and compound 7 in about 80% yield. The targeted phthalocyanine were obtained in DMF under an inert atmosphere. Characterization of compound 6 and 7 were done using ^1H NMR, FTIR, ESI mass spectrometry.

The low solubility of the ZnPc was increased through addition of methyl-tetrazole group.



Scheme 3-1. Synthesis route for compound 8 (ZnPc-M-Tet) and compound 9 (ZnPc-B-Tet).

3.5.2 Singlet oxygen quantum yield

The singlet oxygen quantum yield of all dyes were measured in DMF. Since aggregation has an effect in quantum yield measurement, these measurements must be conducted in non-coordinating solvents in which sensitizers form the monomeric band [166]. Comparing the singlet oxygen quantum yield measurements listed in Table 3-1, ZnPc-M-tetr and ZnPc-B-Tet produce higher amount of singlet oxygen compare to other dyes.

Table 3-1. Measured singlet oxygen and fluorescence quantum yields in DMF.

Compound	Excitation point	Φ_{Δ}	Excitation point	Φ_f
ZnPc	---	0.56	---	0.28
ZnPcCH ₃	669	0.48±0.020	608	0.69

Table 3-1 Continued

ZnPcBCH ₃	669	0.51±0.056	607	0.52
ZnPc-M-tet	669	0.58±0.093	608	0.47
ZnPcNO ₂	669	0.43±0.048	625	0.06
ZnPc-B-tet	669	0.57±0.099	608	0.16

Time-correlated single-photon counting method (TCSPC) was used to measure the fluorescence lifetime. To excite the phthalocyanine at the Q-band peak in DMF, a 625 nm Nano LED was used and the lifetime was measured at the most intense fluorescence emission peak. The scattering solution, Ludox, was used to measure the prompt for instrument response. Lifetime measurements for all peaks listed in Table 3-2, are in the same range of 2 to 3 nanosecond. The exponential fittings of fluorescence lifetime is shown shown in Figure 3-1 .

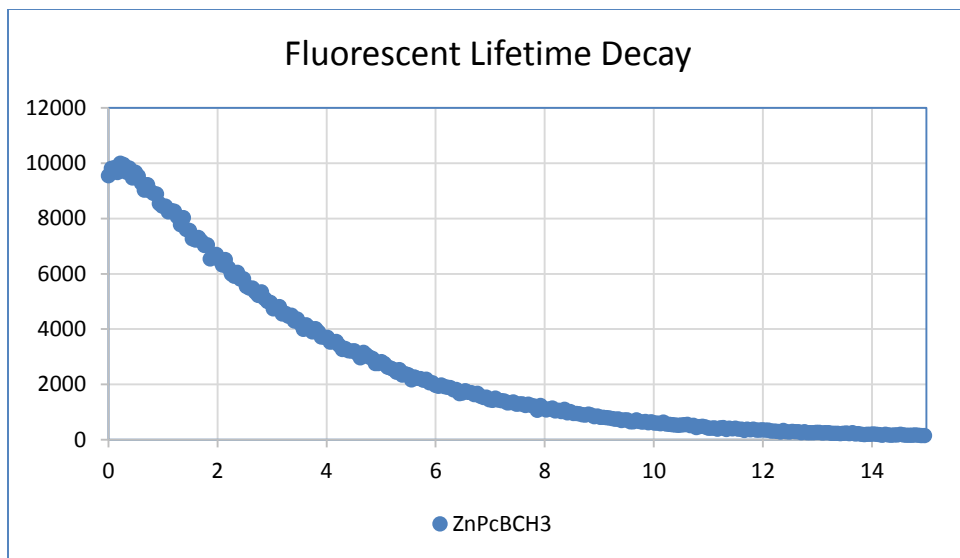


Figure 3-1. Profile decay of ZnPcBCH₃ which is the same as the one for ZnPc, ZnPcCH₃, ZnPcNO₂, ZnPc-M-Tet, ZnPc-B-Tet.

Fluorescence quantum yield of all sensitizers as a parameter to determine the efficiency of the absorbed photon into an emitted photons are reported in Table 3-1 and Table 3-2. Also, this quantity is needed to determine the fluorescence energy transfer process. Samples were all prepared close to 0.1 absorbance at the lambda max to avoid the reabsorption effect. Zinc phthalocyanine is chosen as a standard since it has similar wavelength in accordance to other samples.

Molar extinction coefficients, a parameter to determine the number of light photon that absorb in dye solution, are listed in Table 3-2, Table 3-3 and Table 3-4.

Table 3-2. Measured absorption lambda max λ_{max} , fluorescence emission f_e , excited state lifetime τ , fluorescence quantum yield Φ_f and Stokes shift in DMF.

Compound	λ_{max} (Q band)	f_e	τ (ns)	Φ_f	Stokes shift
ZnPc	669	675	3.29	0.28	6
ZnPcCH ₃	674	681	2.98	0.69	7
ZnPcNO ₂	684	708	2.35	0.12	24
ZnPcBCH ₃	681	689	2.72	0.52	8
ZnPc-M-Tet	676	684	2.98	0.47	8
ZnPc-B-Tet	676	683	3.19	0.35	7

Table 3-3. Measure molar extinction coefficient DMF using a Cary 300.

Compound	$\lambda(\text{max})$	ϵ ($M^{-1}cm^{-1}$)	$\lambda(\text{max})$	ϵ ($M^{-1}cm^{-1}$)	$\lambda(\text{max})$	ϵ ($M^{-1}cm^{-1}$)	Φ_f
ZnPc	669	1.42E+05	604	2.10E+04	345	3.46E+04	0.28
ZnPcCH ₃	674	1.92E+05	608	3.05E+04	349	5.99E+04	0.69
ZnPcNO ₂	686	4.39E+04	644	2.80E+04	349	3.31E+04	0.06
ZnPcBCH ₃	681	1.57E+05	612	3.30E+04	353	0.375	0.52
ZnPc-M-Tet	677	1.36E+05	610	2.65E+04	355	6.03E+04	0.47
ZnPc-B-Tet	677	2.23E+05	609	4.03E+04	356	8.63E+04	0.45

Table 3-4. Molar absorptivity measured in 96-well plate with correction factor of 0.32 in DMSO.

Compound	λ Excitation	ϵ ($M^{-1}cm^{-1}$)	λ Excitation	ϵ ($M^{-1}cm^{-1}$)
ZnPc	672	1.7E+05	346	85.8E+4
ZnPcCH ₃	684	1.2E+05	358	7.5E+04
ZnPcNO ₂	---	---	---	---
ZnPcBCH ₃	677	1.6E+05	352	6.4E+04

Fluorescence emission of all dyes, shown in Figure 3-2, shows a shift to the higher wavelength regardless of the addition of electron donating or withdrawing group. This shift to the higher wavelength is more significant for ZnPcNO₂ with four electron withdrawing groups.

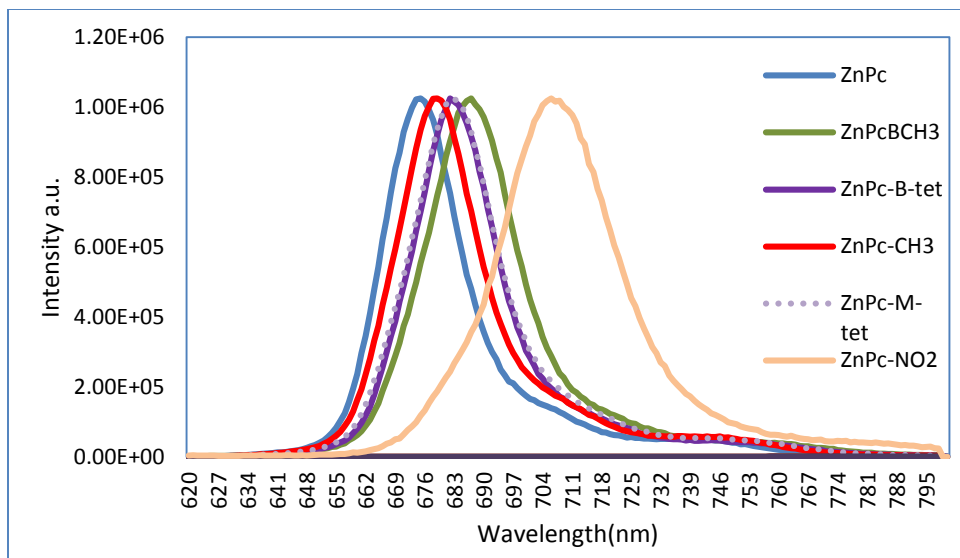


Figure 3-2. Normalized emission spectrum of ZnPc, ZnPcBCH₃, ZnPc-M-Tet, ZnPc-B-Tet, ZnPcCH₃, and ZnPcNO₂.

The UV-Vis absorption spectra of all dyes were recorded in DMF. The normalized UV-Vis absorption spectra of ZnPcNO₂, ZnPcCH₃, ZnPcM-Tet, ZnPc-B-Tet, Figure 3-3 , shows a bathochromic shift at the Q band, and hyperchromic shift at the solet band bands compare to ZnPc.

Comparing the ground state electronic absorption spectra of all dyes in DMF, the nature of these dyes are monomeric at the Q band except ZnPcNO₂. The higher energy band Qx in ZnPcNO₂ is due to the monomer and the lower energy band is due to the aggregation. Similar absorption peak behavior was observed for sulfonated metallophthalocyanine complexes in water where the sulfonate is the electron withdrawing group at the alpha position [167].

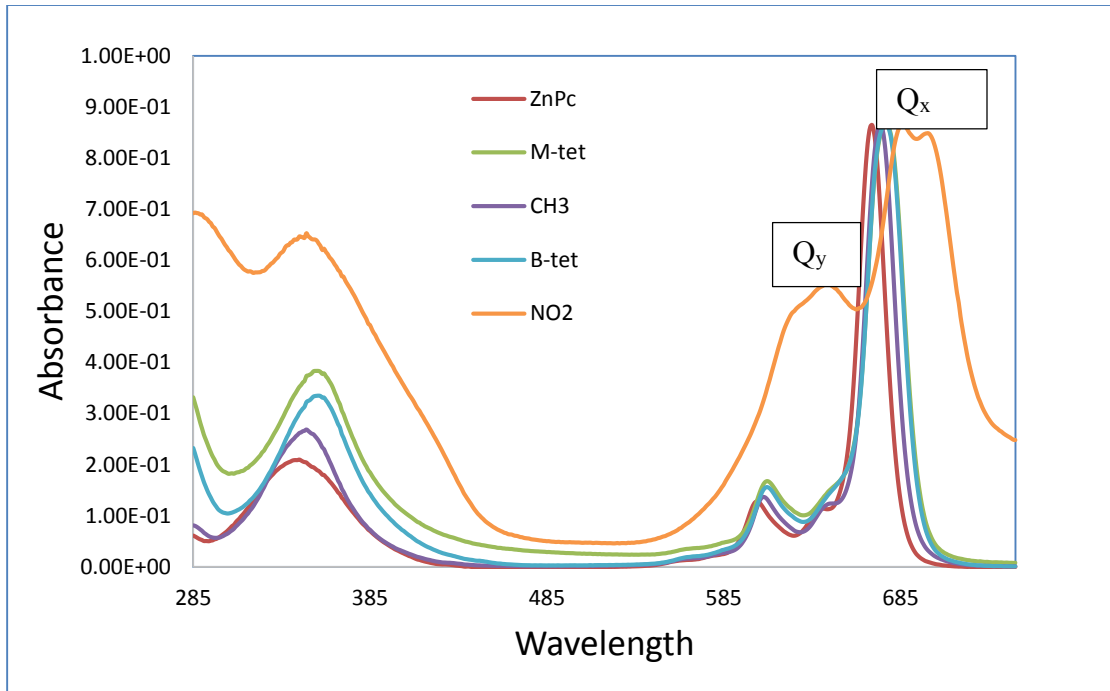


Figure 3-3. Normalized visible spectra for ZnPc, ZnPc-M-Tet, ZnPcCH₃, ZnPc-B-Tet, ZnPcNO₂.

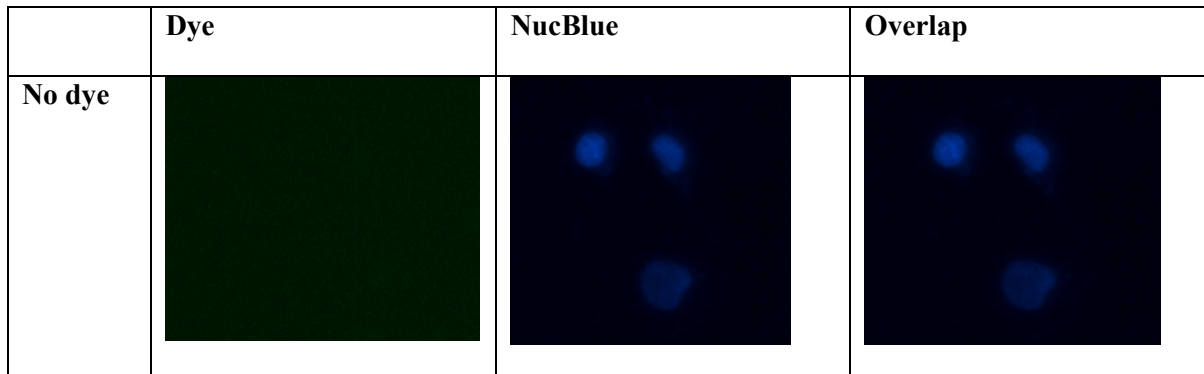


Figure 3-4. Fluorescence imaging of A549 cells showing the main localization of ZnPc, ZnPcBCH₃, and ZnPcCH₃ in cytoplasm. ZnPc-M-Tet and ZnPc-B-Tet are localized both in the cytoplasm and in the nucleus.

Figure 2-19 Continued

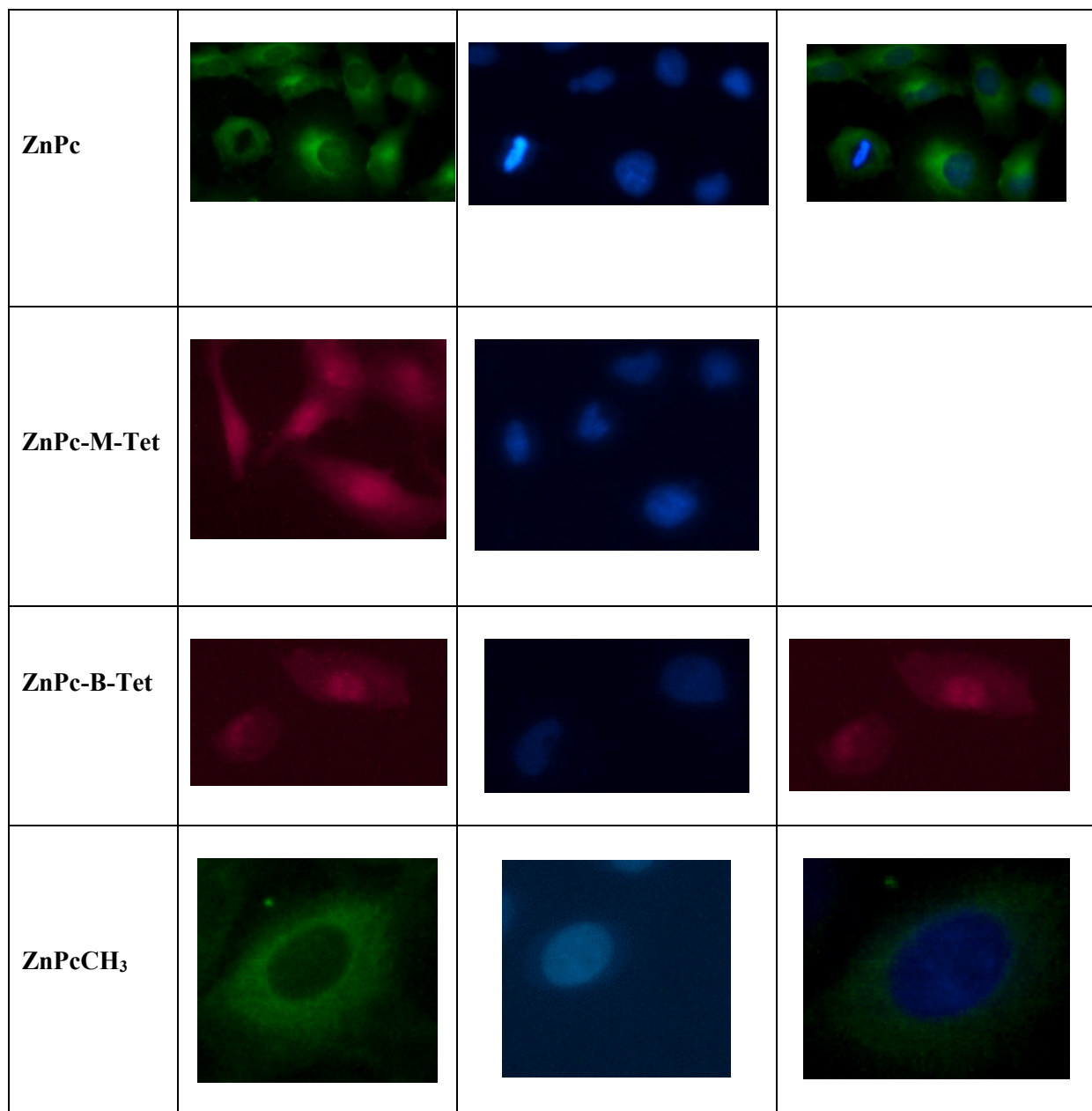
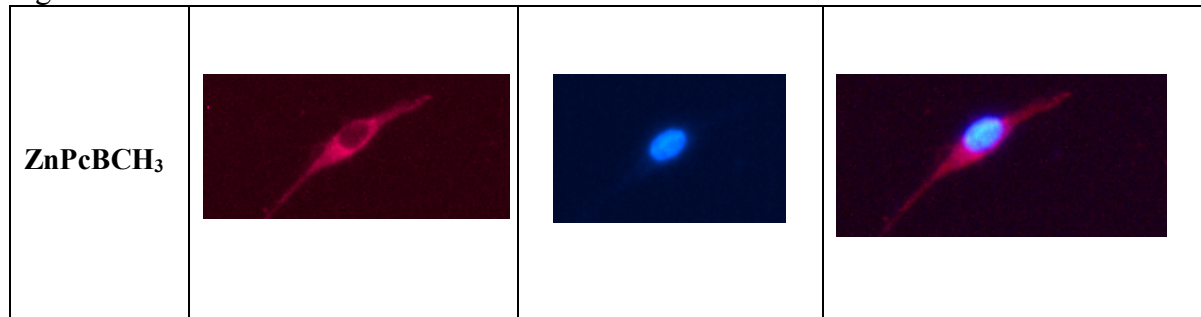


Figure 2-19 Continued



Dark toxicity of all dyes was tested using CTB assay, Figure 3-5. In this assay cells were treated with dyes for 24 h and incubated in absence of light. Result showed no dark toxicity for these dyes.

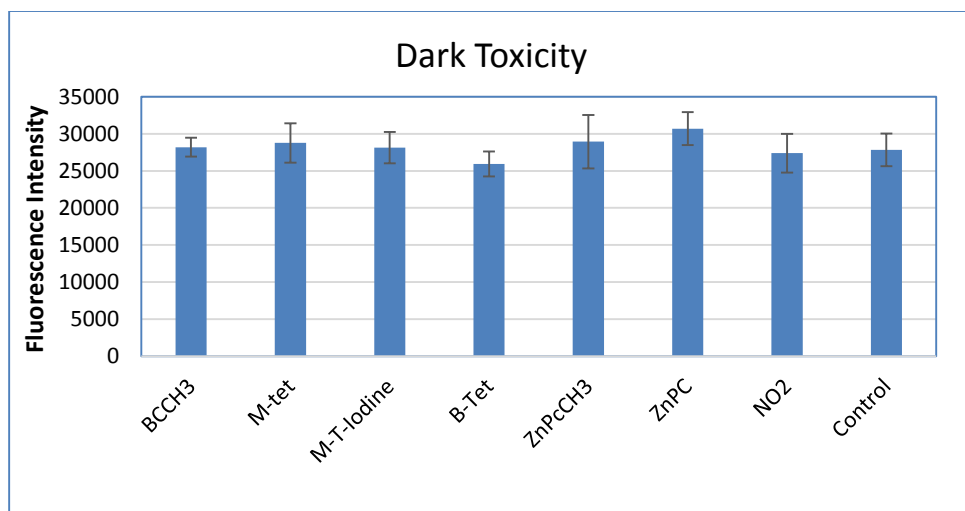


Figure 3-5. Dark toxicity results for tested dyes.

The idea of developing hydrophobic sensitizer drugs for PDT derived from the literature where a high cytotoxicity of ZnPc on mammalian cell culture was reported. Therefore, the dark and light toxicity of ZnPcBCH₃, ZnPc-B-Tet, ZnPc-M-Tet, ZnPcCH₃ and ZnPcNO₂

were tested against ZnPc on A549 cells. As shown in Figure 3-8, no dark toxicity was observed for any dyes including ZnPc. It is not quite clear why we did not observe a significant cytotoxicity effect.

It is important to note that generating a false positive result in PDT studies can happen easily for MTT assay and a few critical points are needed to be considered. Most of previous work did not report the amount of DMSO-DMEM that was used per well. We observed that addition of DMSO reduce down the fluorescence intensity in MTT assay, Figure 3-6. And it is critical to add the same amount of DMSO that was fed to other cells to the control. Otherwise, treated cells with dye will show higher toxicity because of addition of DMSO compare to control cells. This issue is not very critical for CTB assay because addition of DMSO does not show a significant impact on the fluorescence intensity, Figure 3-7.

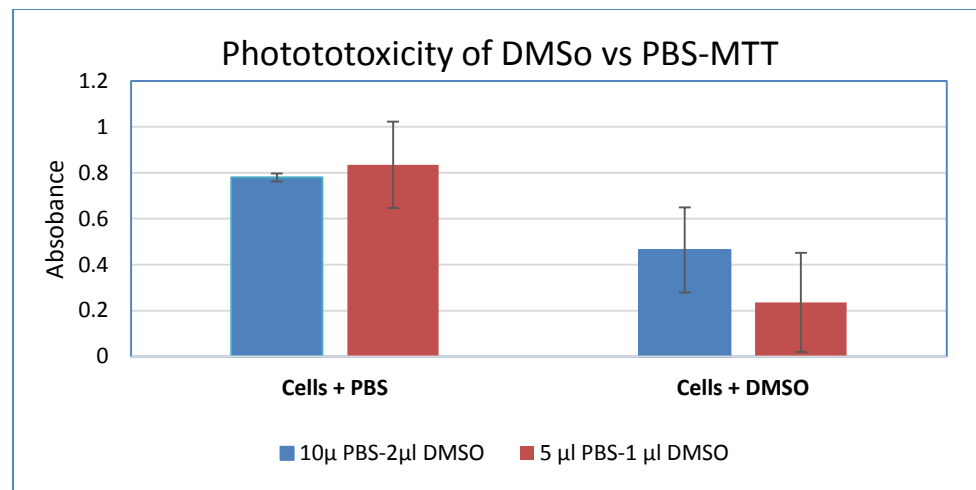


Figure 3-6. Addition of DMSO has impact on absorbance.

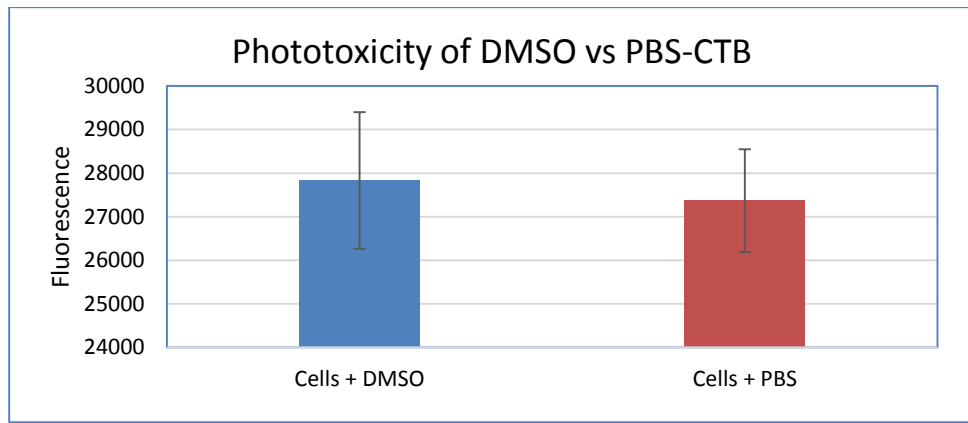


Figure 3-7. Addition of DMSO has no impact on fluorescence measurement.

To make it clear whether the cytotoxicity effect is because of the dye and not DMSO, setting up a control treated with the same amount of DMSO-MEDIA that was used to treat cells with dyes is necessary.

There are also studies in which the cytotoxic effects of the sensitized dye were evaluated based on the concentration of the dye that was used to treat the cells. This way, the

minimum amount of the sensitizer dye needed to increase cytotoxicity will be defined. While studying the dye concentration can easily be done for water soluble dyes, testing hydrophobic dyes needs to be done more carefully. Addition of more hydrophobic dyes means to add more DMSO on the cells. So, it is important to add the same amount of DMSO into other samples too.

Absence of cell toxicity could be because of aggregation of these dyes in aqueous media. In some papers FBS was not used in the media in the tests because FBS might quench singlet oxygen formation.

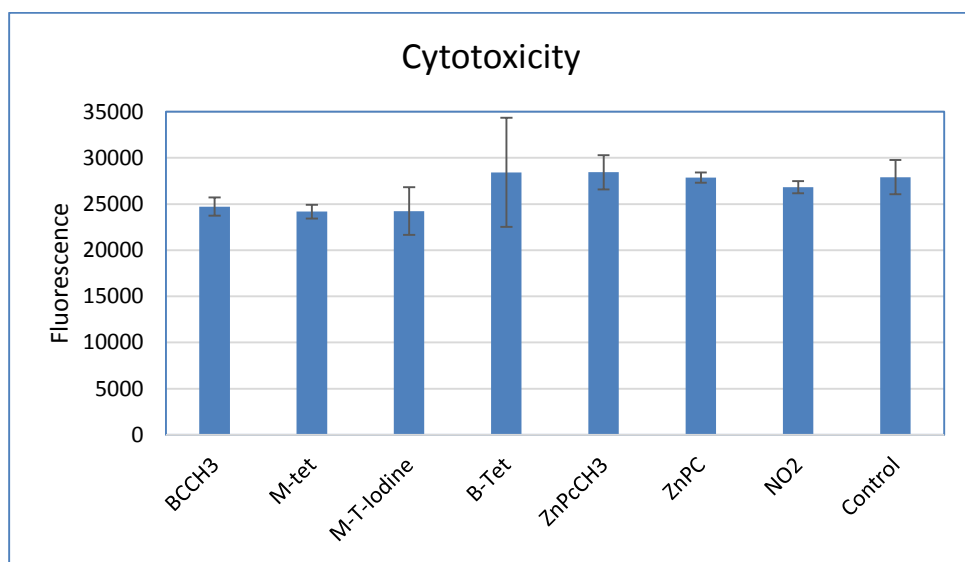


Figure 3-8. Measured cytotoxicity of ZnPc, ZnPc-M-Tet, ZnPc-NO₂, ZnPcCH₃ and ZnPcBCH₃ using CTB assay.

Cell uptake of all dyes against A549 cell was compared for 24 hr, Figure 3-9. Although the bathochromic shift of the ZnPc derivatives compared to the ZnPc are not very large, excitation at different wavelengths give emission intensities. What can be implied from

this experiment is that the comparison of the cell uptake of different dyes at the same wavelength is not a very reliable comparison. It is more accurate if the dye uptake of each dye is studied individually.

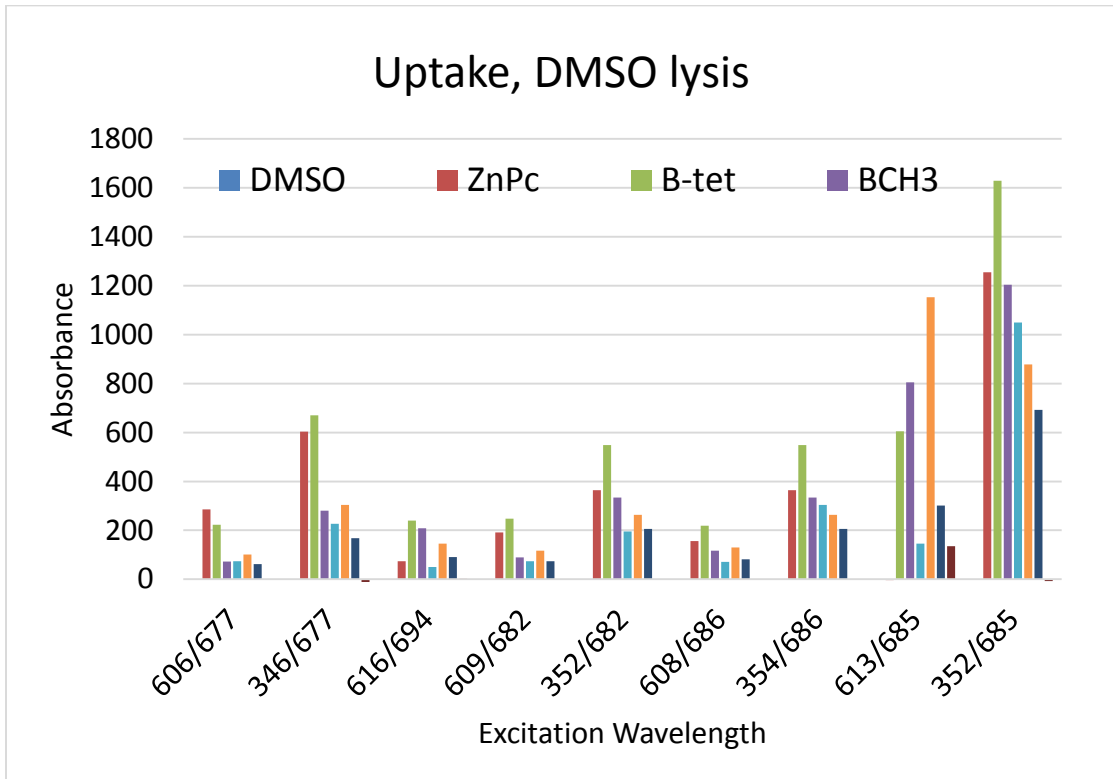


Figure 3-9. Measured cell uptake of all dyes against A549 cells.

For the encapsulation procedure, ZnPc-Me-Tet were encapsulated in PEG-b-PLGA. In contrast to cell uptake results for ZnPcBCH₃ in chapter 2, the cell uptake did not increase through increasing the concentration or incubation time. Or, it is better to say that a significant fluoresce intensity was not detected for this dye Figure 3-10. The difference between the ZnPcBCH₃ and ZnPc-M-tet is the polarity of these dyes, which is higher in

ZnPc-M-tet. This data is also consistent with the cell uptake study of the non-encapsulated dye. Cell uptake of the free ZnPc-M-tet is significantly lower than the uptake of ZnPcBCH₃. Interestingly, incorporation of nanoparticles did not increase the cell uptake. So, one may conclude that the nature of the dye can effect drug release. Prior to measuring cell uptake, media was removed and cells washed with PBS. So, it is possible that encapsulated dye washed off.

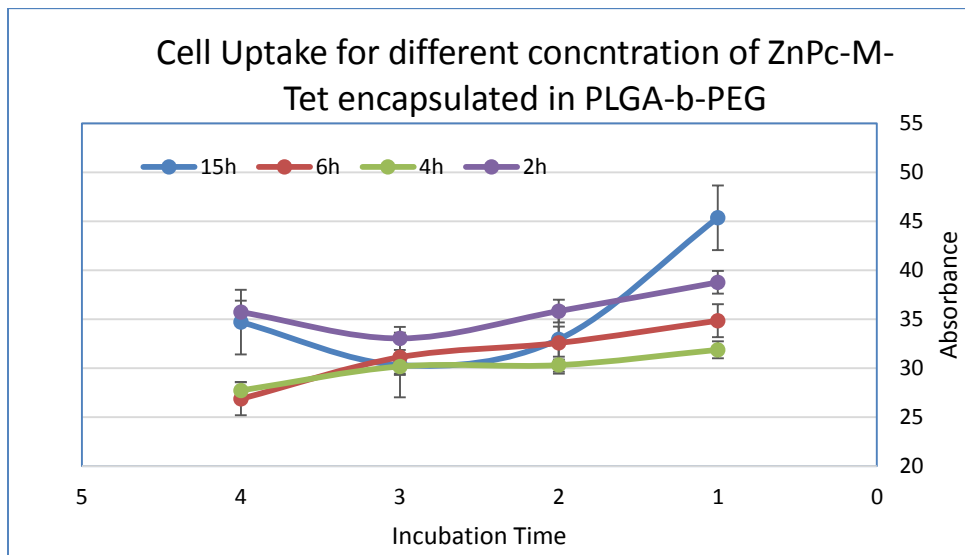


Figure 3-10. Measured cell uptake of encapsulated ZnPc-M-tetrazole.

3.6 Conclusion

ZnPc with a tertrazole moiety showed different physiological properties compared to ZnPc, ZnPcCH₃, ZnPcBCH₃, ZnPcNO₂. The singlet oxygen production of this derivative is higher than other tested dyes. Also ZnPc-tet localizes both in the nucleus and the cytoplasm, while other ZnPc dyes only localize in the cytoplasm.

Although no significant light and dark toxicity were observed for any dyes, it is not logical to conclude that hydrophobic dyes cannot be used for PDT, because enzymatic chemical reactions can happen in the cells that convert hydrophobic dyes to a hydrophilic form. This is reason *in vivo* studies are necessary as a follow-up to *in vitro* testing as part of the FDA regulation process.

3.7 Supporting Documents

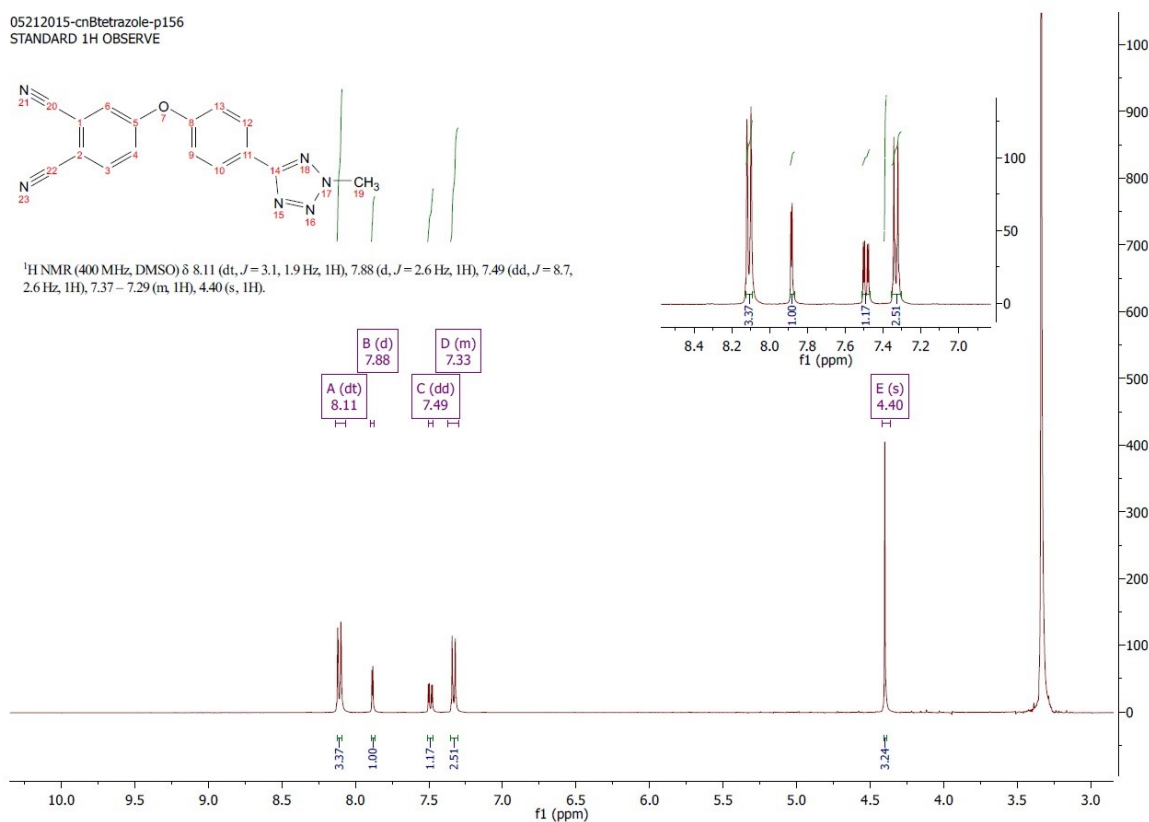


Figure 3-11. ¹H NMR spectrum for compound 3.

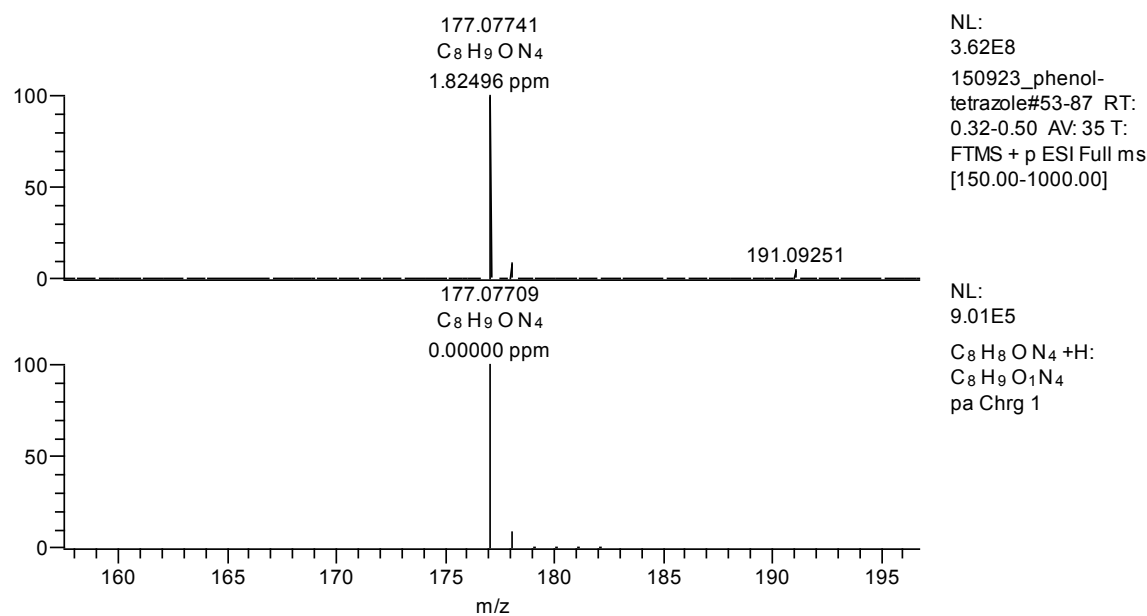


Figure 3-12. ESI mass spectrum of compound 3.

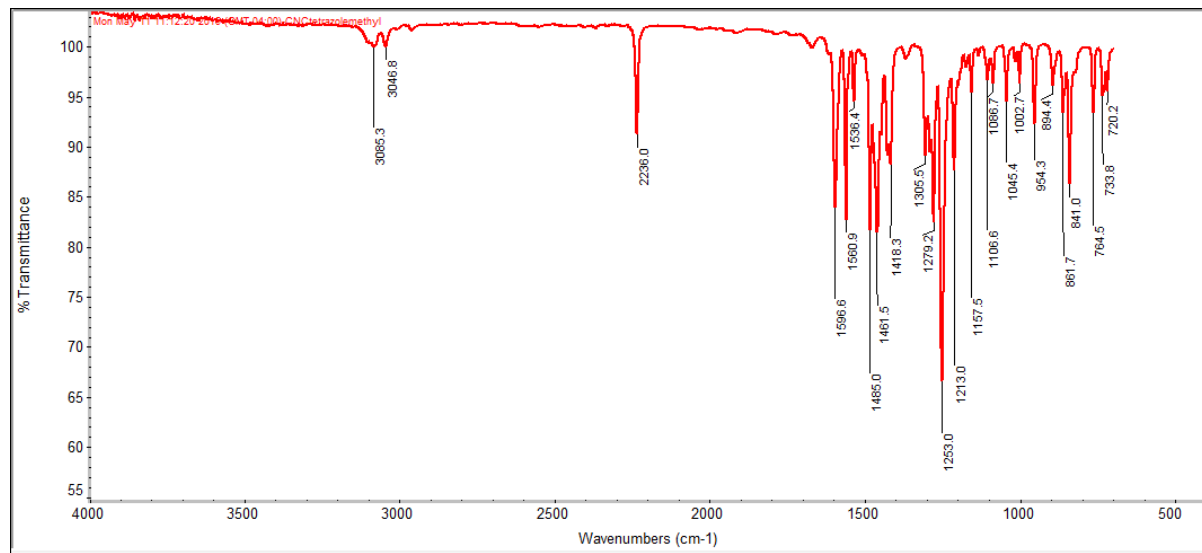


Figure 3-13. FTIR spectrum of compound 3.

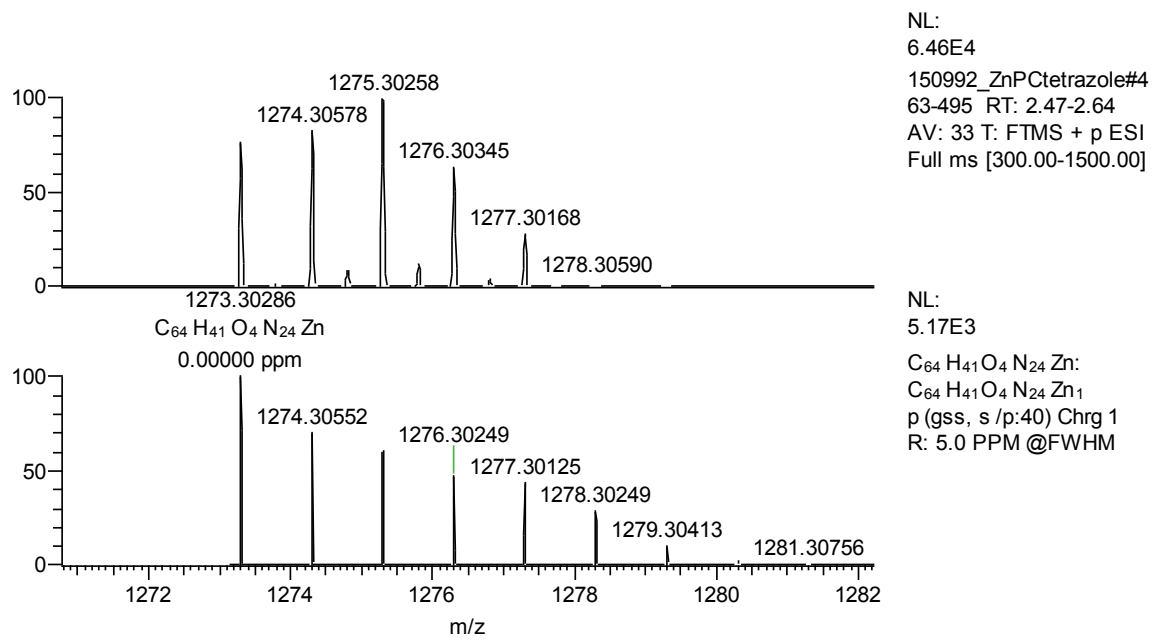


Figure 3-14. mass spectrum of compound 4.

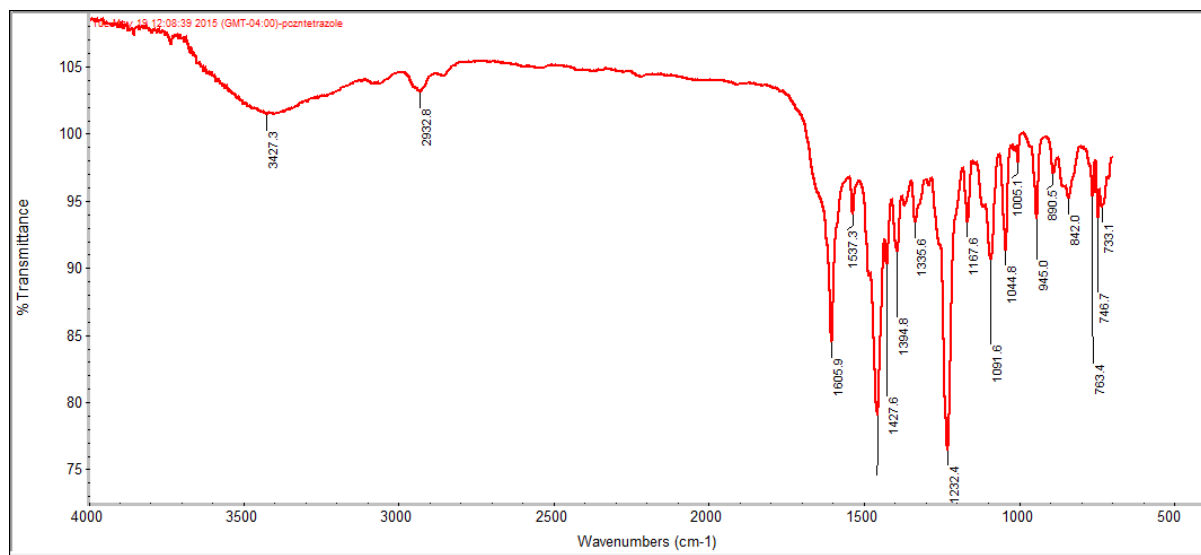


Figure 3-15. FTIR of compound 4.

Chapter 4

DFT CALCULATIONS TO DEVELOP A MODEL TO PREDICT SINGLET OXYGEN PRODUCTION FOR BRANCHED PHTHALOCYANINE

4.1 Introduction

Formation of singlet oxygen (${}^1\text{O}_2$) has an important role in applications such as photodynamic therapy (PDT), photodegradation, and photo-oxidative damage [168]. In PDT, ${}^1\text{O}_2$ formation is critical in killing malignant cells and designing sensitizers that can produce high levels of ${}^1\text{O}_2$ is in high interests for this field. Based on the mechanism of formation of ${}^1\text{O}_2$ that was described in previous chapters, it is known that the energy difference between T_1 and S_0 , $\Delta_{\text{S}0-\text{T}1}$, impacts the efficiency of the photosensitizer in PDT. The higher the energy difference between the ground state singlet (S_0) and first triplet state (T_1), the more efficient sensitizer will be obtained as this energy difference passes the minimum threshold of 0.98 eV.

Formation of ${}^1\text{O}_2$ is mainly influenced by increasing the intersystem crossing from the singlet excited to the triplet state. The higher rate intersystem crossing, the higher triplet state lifetime is expected [169]. Some possible methods to increase the intersystem crossing rate is by addition of a metal, heavy metal or changing the symmetry of the structure.

Based on what is stated above, formation of a high amount of singlet oxygen is one important criteria that must be considered in design of a high efficient sensitizer for PDT. Other parameters that also needed to be considered are: 1) Ability to absorb light in therapeutic windows of at least 600 to 900 nm, to increase the depth of tissue penetration; 2) Low dark toxicity, meaning that these dyes should not be intrinsically toxic unless it is excited with light to produce singlet oxygen; 3) High molar extinction coefficient, to reduce the amount of dye that is needed for treatment; and 4) High photostability or low photo bleaching.

The main goal of this work was to find the smallest and most efficient phthalocyanine for PDT. To achieve this goal a few questions were need to be addressed. 1) Is there a correlation between the experimental singlet oxygen production and calculated ΔE_{S0-T1} ? 2) What is the impact of the electron donating and withdrawing groups on the ΔE_{S0-T1} , and the Q-band of the visible spectrum? 3) How does changing the number of substituents in molecular geometry change ΔE_{S0-T1} and lambda max? 4) What is the impact of placing a metal in the cavity of phthalocyanine on changing the optimized geometry, ΔE_{S0-T1} and lambda max? 5) How does ΔE_{S0-T1} and lambda max change through addition or subtraction of a fused ring? 6) Does addition of a substituent that can do energy transfer to the compound has impact on the ΔE_{S0-T1} ?

Phthalocyanine (Pc) was chosen as the base structure to study because of its potential to give dyes with low dark toxicity, high molar extinction coefficient, and a relatively high lambda max. This dye can be substituted very differently and also more than 40 metals can be introduced into the cavity of the Pc. So, there are were lots of possible modifications that

could be evaluated to find the best phthalocyanine for PDT. It was deemed more cost effective and faster to compare the effect of modifications using calculation than going through the actual syntheses one by one.

4.2 Material and Methods:

Zinc phthalocyanine (ZnPc) was purchased from Sigma Aldrich. Dimethyl sulfoxide (DMSO) was obtained from Alfa Aesar, dimethylformamide and acetonitrile were obtained from Fisher Scientific. Steady state fluorescence emission measurement was performed on Hammatsu absolute quantum yield spectrometer (C11347). FTIR spectra were recorded on a Nicolet Nexus 470 FTIR spectrophotometer (Thermo Scientific, USA). UV-VIS measurement was recorded on a Cary 300 spectrophotometer. Singlet oxygen quantum yields were measured using Edinburgh Analytical Instrument (FS920) and NIR PMT from HAMAMATSU (H10330A series).

4.2.1 Modeling:

4.2.1.1 Density Functional Theory (DFT) Calculation

DFT calculations were carried out using Gaussian 09 software package. Geometry optimization for both the ground state and the lowest energy triplet state were performed using the density functional theory at the B3LYP level with the dgdzvp basis set. Optimized structures were verified using vibrational frequency analysis. Calculated bond angles and bond lengths were compared to the published crystal structure of ZnPc [156].

4.2.1.2 Time-Dependent Density Functional Theory (TD-DFT)

Time dependent calculations on optimized ground state geometries were performed using Gaussian 09. Symmetry was restricted to C1 and polarizable continuum model (PCM) was used to simulate DMF solvent effects. Density functional theory at the CAM-B3LYP level function with 6-311G+(d,p) was used for TD-DFT calculation.

4.2.2 Singlet oxygen quantum yield

Singlet oxygen quantum yield (Φ_Δ) measurements were performed using Fluorimeter Edinburgh Analytical Instrument (FS920) and NIR PMT from HAMAMATSU (H10330A series). Data acquisition was controlled by LP900 software program. Solution of ZnPc, ZnPcBCH₃, ZnPcNO₂ and ZnPcCH₃ were prepared in DMF with the maximum absorbance of 0.08 to 0.2 at 699 nm. All samples and standards were excited at 699 nm where the excitation count for both standard and the sample are the same. The OD of these samples at this wavelength and the area under the typical phosphorescence emission at 1270 nm were used to calculate singlet oxygen quantum yield using equation 1.

$$(\Phi_f) = (\Phi_f) (std) \frac{A(x).OD(std)}{A(std).OD(x)} \quad (14)$$

Where OD (std) and OD(x) are the absorbance of the ZnPc and the samples respectively.

4.2.3 Steady-State and life-time fluorescence

Steady state fluorescence emission measurement was performed on Hammatsu absolute quantum yield spectrometer (C11347). Fluorescence quantum yield (Φ_f) measurements conducted similar to the procedure described above for singlet oxygen

measurement. Except that each of the samples, ZnPcBCH₃, ZnPcNO₂, ZnPcCH₃, were prepared to reach the absorption unit of 0.9 to 0.1 at the excitation point. The absorption area of the fluorescence emission and the recorded absorption was used to calculate the fluorescence quantum yield using equation 2. Conditions for the samples and the standard were the same and these measurement were repeated twice in two different days. ZnPc in DMF was used as a standard for this measurement ($\Phi_f = 0.28$) [159]

$$(\Phi_f) = (\Phi_f) (\text{std}) \frac{A(x) \cdot OD(\text{std})}{A(\text{std}) \cdot OD(x)} \quad (15)$$

Where A(x) and A (std) are areas under the fluorescent emission curves of the samples and the standard respectively. And OD(x) and OD (std) are the absorbance of the samples and standard.

Method of choice to measure lifetime was time-correlated single photon counting method that was conducted on the ZnPc and ZnPcBCH₃ solutions in DMF. For this measure samples were excited at 625 nm using NanoLED pulse laser. Measurements were repeated twice and performed at repetition rate of 1MHz and a band pass of 1.5 nm.

4.3 Results and discussion

4.3.1 Evaluation of energy efficiency (ΔE_{s0-t1})

We have synthesized and/or purchased a series of known and new zinc phthlaocyanines, ZnPc, ZnPc4CH₃, ZnPc4BCH₃ and ZnPc4NO₂, to evaluate the absorption and ¹O₂ properties of these compounds in DMF. Synthesis of ZnPcBCH₃, ZnPcCH₃, and ZnPcNO₂ were described in chapter 2 and 3. Since the crystal structure of most of the

synthesized dyes are not available, the optimized ZnPc structure was used as an initial structure to draw other dyes.

Calculated ΔE_{S-T} (eV) and measured singlet oxygen quantum yield (Φ_Δ) were reported in Table 4-1. Although the ΔE_{S-T} and (Φ_Δ) are not exactly match, a reasonable agreement was observed in the range of formation of singlet oxygen and calculated ΔE_{S-T} . The minor difference between the calculated and experimental result can be because of quenching or aggregation behavior of some of the dyes in DMF. Also, it is important to note that the singlet oxygen measurement was not measured in a degassed condition that will also can impact on the result.

Table 4-1. Comparing the singlet oxygen production with energy difference between singlet and triplet states.

Molecule	Singlet Energy	Triplet Energy	ΔE_{S-T} (eV)	Φ_Δ (exp)
ZnPc	-3446.448347	-3446.40818	1.093	0.56
ZnPc4BCH ₃	-4986.167199	-4986.127119	1.087	0.51±0.056
ZnPc4CH ₃ (1)	-3603.731328	-3603.691211	1.09	0.48±0.020
ZnPc4CH ₃ (2)	-3603.691483	-3603.691483	1.09	0.48±0.020
ZnPc4NO ₂ (1)	-4264.595671	-4264.555405	1.09	0.43±0.048
ZnPc4NO ₂ (2)	-4264.59480469	-4264.555356	1.07	0.43±0.048

Φ_Δ is singlet oxygen quantum yield

4.3.2 Impact of the presence of metal and the number of substituents

To obtain the best structure in terms of ΔE_{S-T} difference and lambda max, several proposed ZnPc derivatives in and Figure 4-2 and phthalocyanine with and without some metals shown in Figure 4-3 were evaluated.

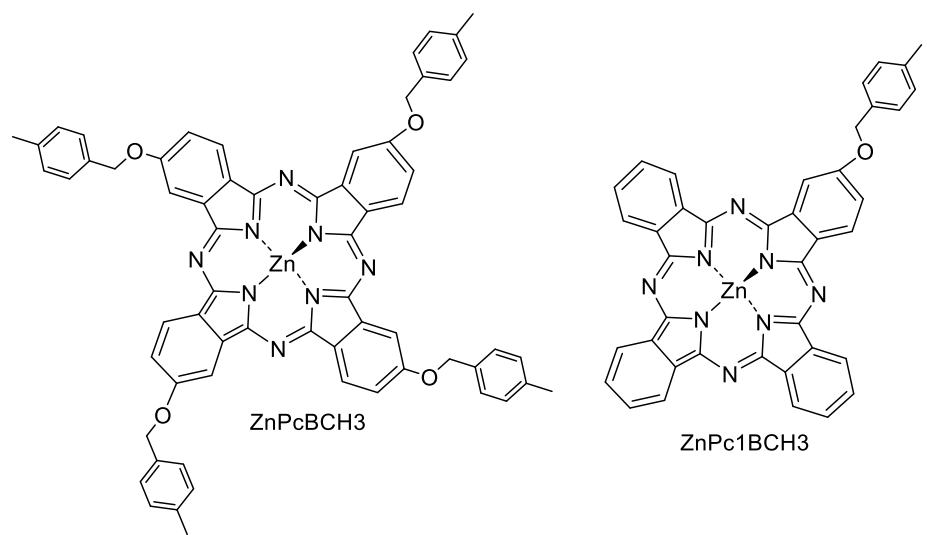


Figure 4-1. ZnPc4BCH_3 and ZnPc1BCH_3 structures.

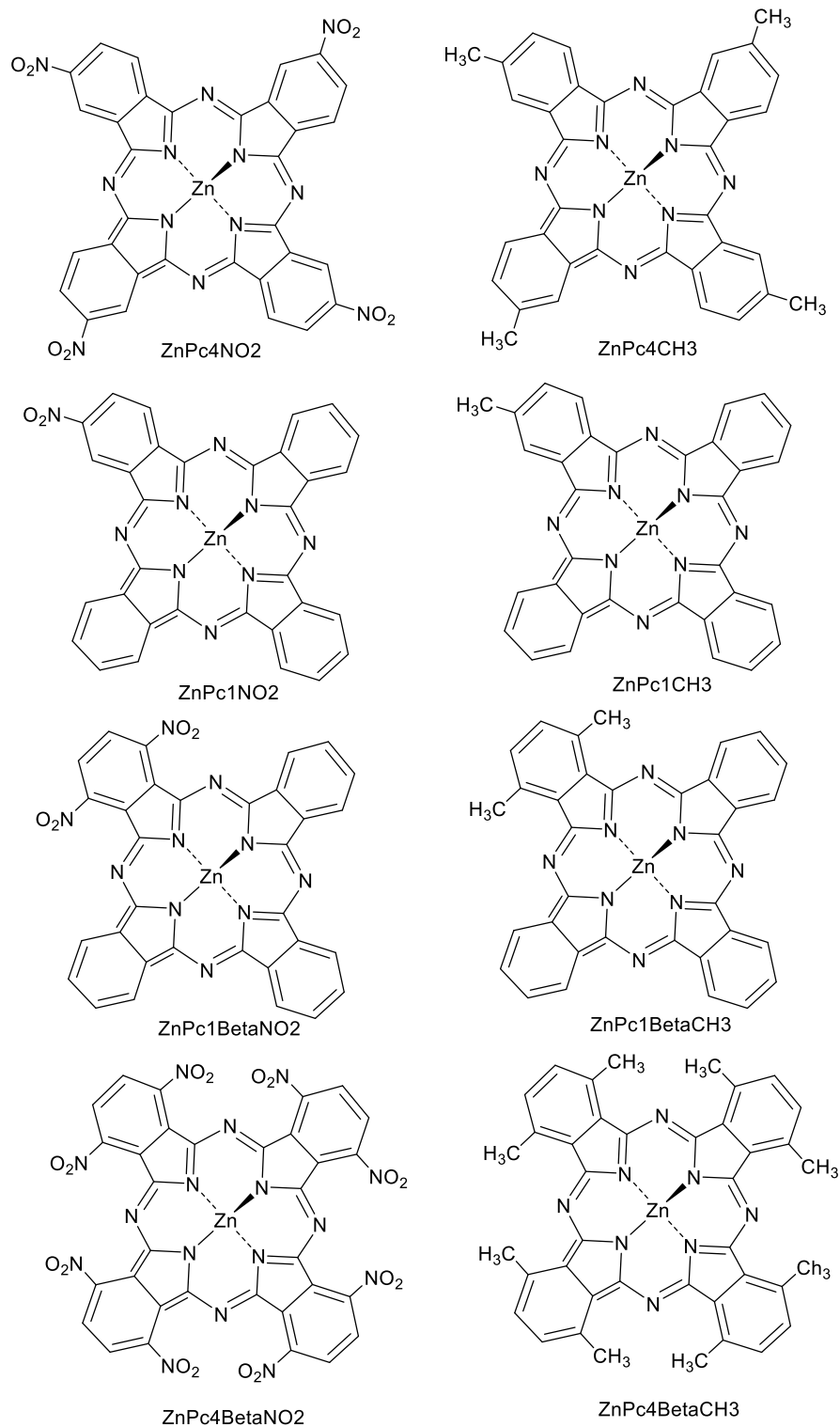


Figure 4-2. Phthalocyanines with one to four substituent in the peripheral position.

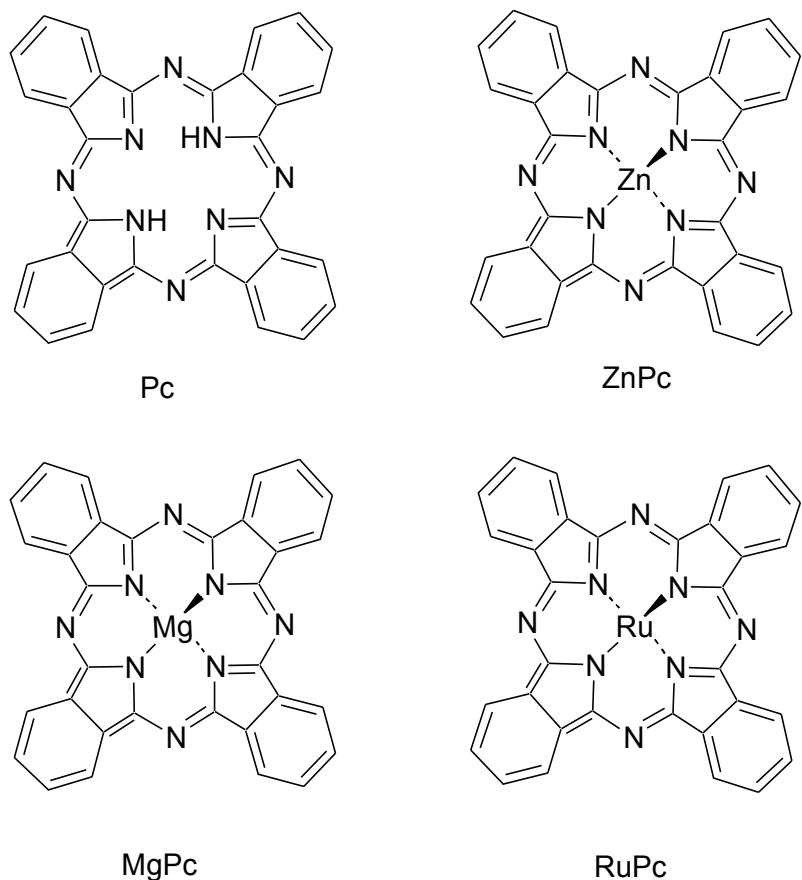


Figure 4-3. Phthalocyanine with a Zn, Mg and Ru metal.

Calculated ΔE_{s-t} values for ZnPc derivatives with either one or four electron donating and withdrawing groups did not change significantly. Results for these structures are listed in Table 4-1, Table 4-2.

Reported results are collected in Table 4-3, showed that changing the metal from Zn to Mg did not change the ΔE_{s-t} significantly. Although this energy difference is not very significant for ZnPc or MgPc, a very small ΔE_{s-t} was calculated for RuPc that means that production of singlet oxygen is not expected. This result is in agreement with the literature. No singlet oxygen was detected for RuPC[170].

Calculation was not repeated further for all metals because of the limitation in using metals for PDT studies.

Table 4-2. Calculated ΔE_{s-t} (eV) value for the phthalocyanines with one substituents.

Molecule	Singlet Energy	Triplet Energy	ΔE_{s-t} (eV)
1BCH3	-3831.378221	-3831.338109	1.09
1NO2	-3650.987142	-3650.948302	1.06
1CH3	-3485.769217	-3485.729015	1.09
1BetaCH3	-3525.089315	-3525.049337	1.09
1BetaNO2	-3855.499312	-3855.46031	1.06
4BetaNO2	-5082.624855	-5082.52694914	
4BetaCH3	-3761.003576	-3760.964267	

Table 4-3. Calculated ΔE_{s-t} (eV) value for the free phthalocyanine vs ZnPc, MgPc and RuPc.

Molecule	Singlet Energy	Triplet Energy	ΔE_{s-t} (eV)
Pc	-1668.45985	-1668.422876	1.01
PcZn	-3446.448347	-3446.40818	1.09
PcMg	-1867.482129	-1867.442897	1.07
PcRu	-6110.106779	-6110.141858	-0.95

4.3.3 Impact of the addition of substituents that can do energy transfer with ZnPc

Since addition of small electron donating and withdrawing groups did not show any change in energy difference between the singlet and triplet states, to find a desired ZnPc derivative, calculations were repeated for other groups such as a carbazole with an ether and triple bond or the best case with another ZnPc as a substituent to see how the singlet oxygen formation changes, Figure 4-4. This calculation was only conducted for the alpha position where the lowest steric hindrance for such big molecules are allowed. Obtained results did not show a significant change in ΔE_{s-t} calculation of these molecules, Table 4-4. ZnPc-carbazole calculations were repeated for a rigid triplet bond as well as flexible ether bond. Some increase in ΔE_{s-t} was seen for ZnPc and carbazole that were covalently bonded together through triplet bond compare to an ether bond.

In case of forming a dimer where with two ZnPc bonded through a triple bond the ΔE_{s-t} decreased and got closer to the 0.98 eV threshold value.

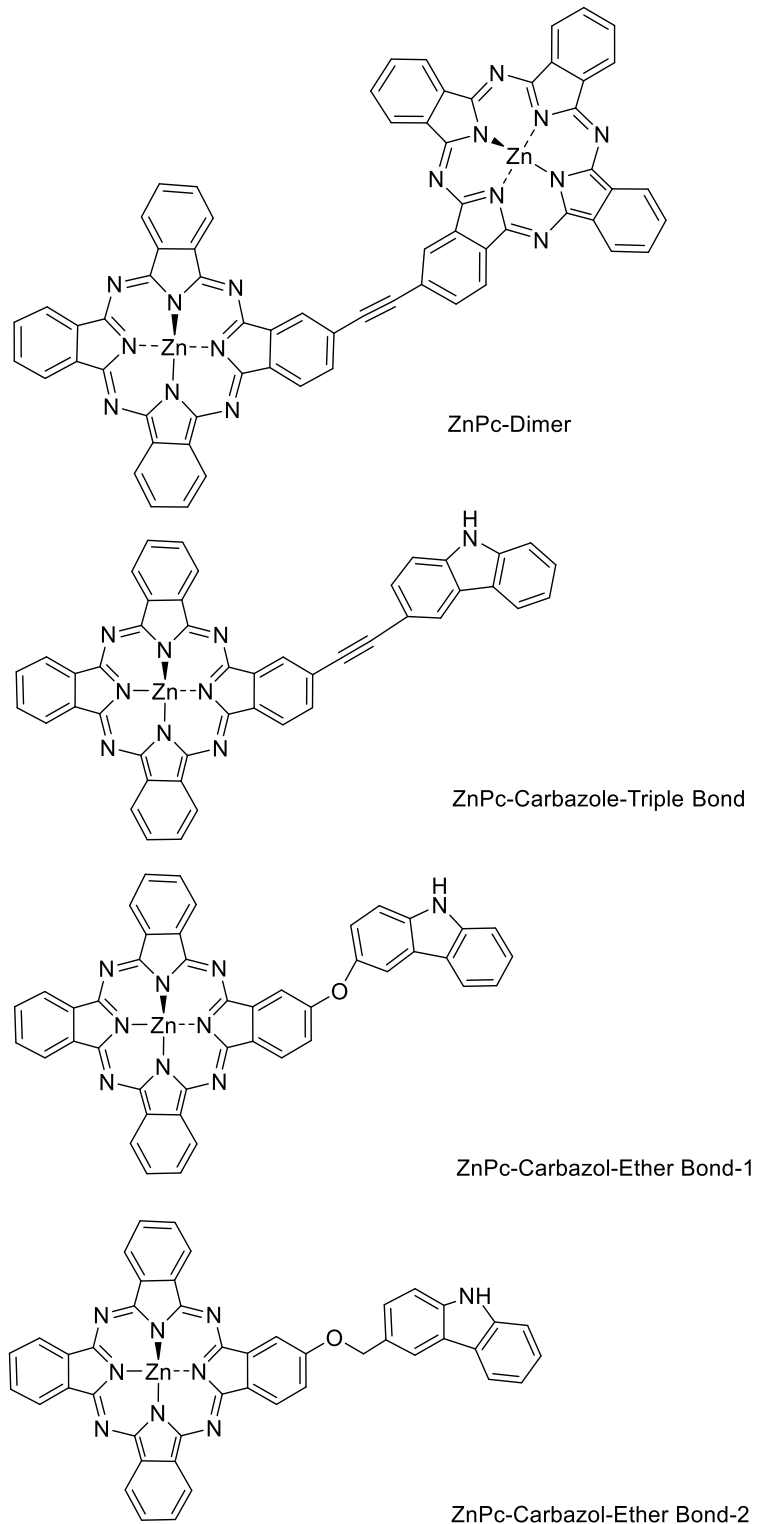


Figure 4-4. Proposed ZnPc derivatives with carbazole and another ZnPc as a substituents.

Table 4-4. Calculated ΔE_{s-t} (eV) value for ZnPc dimer and ZnPccarbazole.

Molecule	Singlet Energy	Triplet Energy	ΔE_{s-t} (eV)
ZnPc-1Dimer (triplet bond)	-6967.856763	-6967.820434	0.99
ZnPc-1Carbazole(triple bond)	-4038.856188	-4038.813396	1.16
ZnPc-1Carbazole-ether-1	-4037.982734	-4037.942648	1.09
ZnPc-1Carbazole-ether-2	-4077.297851	-4077.258411	1.07

4.3.4 Impact of the addition and subtraction of the number of fused rings on ΔE_{s-t}

ZnPc structure was evaluated through addition or subtraction of a fused ring to the phthalocyanine structure, Figure 4-5. Reported data in Table 4-5 shown subtraction of 4 benzene ring from the structure significantly increase the singlet oxygen production. Addition of four benzene rings or deletion of 1 fused ring decreases the singlet and triplet energy. Addition of only one fused ring increases the efficiency but this is not as effective as subtraction of four fused rings.

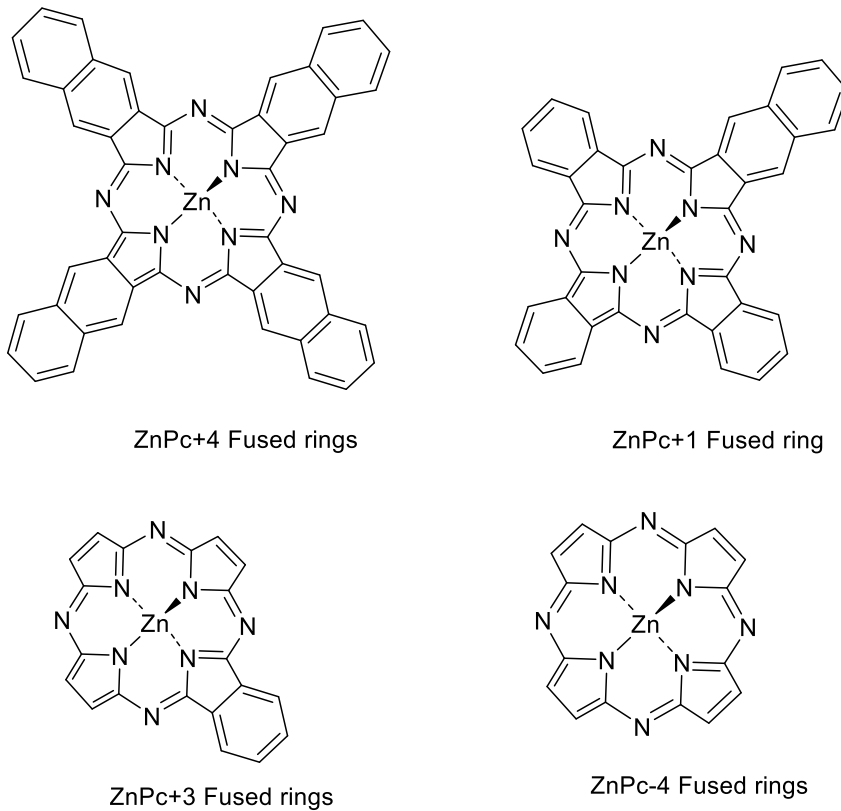


Figure 4-5. Changing the Symmetry of the phthalocyanine through changing the number of fused rings.

Table 4-5. Calculated ΔE_{s-t} (eV) value for ZnPc with plus and minus fused rings.

Molecule	Singlet Energy	Triplet Energy	ΔE_{s-t} (eV)
ZnPc Plus 1 fused ring (ZnPc+1 Fused rings)	-3600.08133	-3600.04	1.11
ZnPc Plus 4 fused ring (ZnPc+4 Fused rings)	-4061.011756	-4060.98	0.99
ZnPc minus 1 fused ring (ZnPc-3 Fused rings)	-3292.700575	-3292.664555	0.98
ZnPc minus 4 fused ring (ZnPc-4 fused rings)	-2831.779393	-2831.720516	1.60

4.3.5 Evaluation of UV/VIS Spectra

Evaluation of UV/VIS spectrum is important in design of sensitizers for PDT. Higher wavelengths closer to infrared region are desired. Calculated lambda max for the synthesized dyes are listed in Table 4-6. This table showed the HOMO to LUMO and HUMO to LUMO+1 molecular orbital contributions in the Q band lambda max. The lambda max of the UV/VIS spectrum are in agreement with 10 nm difference. Calculated and experimental singlet energies reported in Table 4-7 shown that the calculated lambda max is in a good agreement with the experimental data. Therefore, we use the same optimized basis set for the rest of the calculations.

Table 4-6. Calculated and experimental lambda max values.

Compound	λ_{max} (DMF) Calculated	F		Configurations	λ Expe	Dif (nm)
ZnPc	659.49	0.7031	State 1 State 2	H-2 → L (3.5%)+H → L+1 (95.3%) H-2 → L+1 (3.5%) H → L (95.3%)	669	10
ZnPcBCH ₃	670.64	0.774	State 1 State 2	H-10 → L+1 (2.48%)+ H → L (82.48%) H-10 → L (2.48%)+ H → L+1 (82.48%)	681	10
ZnPcNO ₂ (1)	680.14	0.7977	State 1 State 2	H-1 → L (3.68%)+ H → L (94.56%) H-1 → L (3.68%)+ H → L+1 (94.56%)	686	6
ZnPcNO ₂ (2)	708.61	0.7673 0.8338	State 1 State 2	H-1 → L (3.35%)+ H → L (95.21%) H-1 → L (4.30%)+ H → L+1 (93.80%)	686	22

Table 4-6 Continued

ZnPcCH ₃ (1)	668.09	0.7317	State 1 State 2	H-4 → L+1 (2.20%)+ H → L (95.94%) H-4 → L (2.20%)+H → L+1(95.94%)	674	6
ZnPcCH ₃ (2)	672.61 664.01	0.7375 0.7235	State 1 State 2	H-6 → L+2 (2.27%)+H → L(96.04%) H-4 → L (2.16%)+H → L+1 (95.86%)	674	10

λ_{\max} is the lambda max, F is molar extinction coefficient, Dif is the difference between the calculated and measured lambda max

Table 4-7. Comparing the calculated and experimental differences between the singlet energies.

	Cal(singlet energy-eV)	Exp singlet energy
ZnPc	1.88	1.82062
ZnPc4BCH ₃	1.8508	1.82062
ZnPc4CH ₃	1.8388	1.812634
ZnPc4NO ₂		

(Cal) is calculated and (Exp) is experimental

Referring to Table 4-6, ZnPcNO₂ and ZnPcCH₃ are labeled as 1 and 2. This is because of the different isomers that can form during synthesis. Two of the most possible isomers are shown in Figure 4-6. Comparing the singlet state energy of the isomer 1 is close to the experimental value. Therefore, we considered isomer 1 for the rest of calculations when there are four alpha substituents. Also, based on HUMO-LUMO images, it can be interpreted that structure 1 is more plausible because the HUMO and LUMO are mostly distributed on the 18 π .

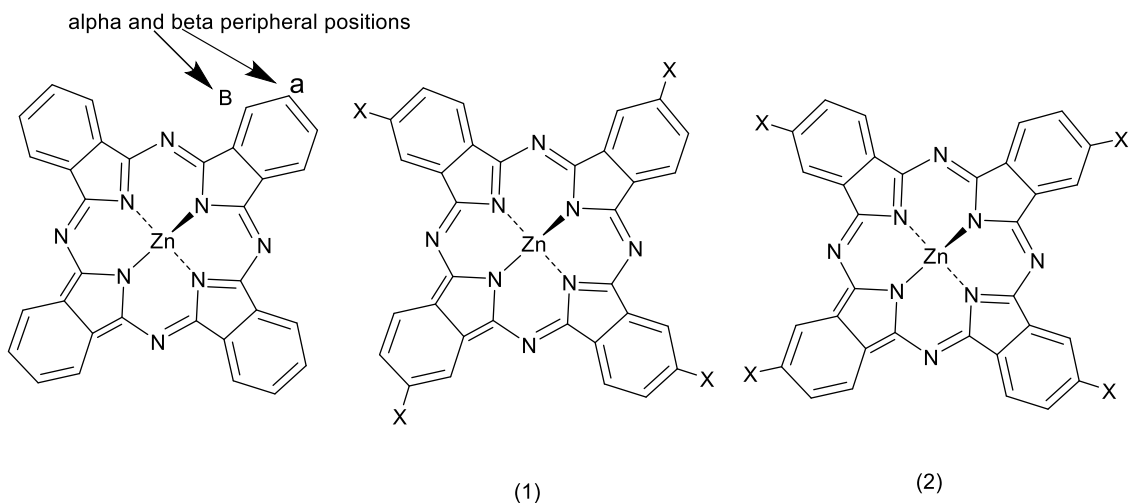


Figure 4-6. Two possible structures for ZnPc with a substituent in the alpha positions.

Calculated lambda max at the Q band is reported for all proposed dyes in Table 4-8. Based on information that is obtained by comparison of the experimental vs calculated data in Table 4-6, it is expected to observe a same range of shift for the lambda max of the proposed molecules. Comparing the ZnPc and MgPc, the difference between the singlet and triplet energy are almost the same. However, the lambda max of the MgPc is higher than the ZnPc lambda max.

Although, almost the same efficiency calculated for all phthalocyanine with either four or one electron donating and withdrawing substituents, dyes with one peripheral substituents give a higher lambda max in about 20 nm.

Table 4-8. Reported calculated and experimental lambda max.

Compound	$\lambda_{\text{max}} (\text{DMF})$ cal	f	
1BCH ₃	669.88	0.7209	H-3 → L+1 (2.17%) + H → L (94.69%) H-3 → L (2.11%) + H → L+1 (94.57%)
1NO ₂	690.66 670.6	0.7855 0.6706	H → L (95.24%) H → L+1 (95.40%)
1CH ₃	667.3	0.7033	H-2 → L+1 (2.38%) + H → L (94.73%) H-2 → L (2.25%) + H → L+1 (94.69%)
1BetaCH ₃	668.89 667.28	0.6884 0.7278	H-3 → L+1 (2.32%) + H → L (95.92%) H-3 → L (2.09%) + H → L+1 (95.94%)
1BetaNO ₂	667.72 631.51	0.7111 0.6422	H → L (96.23%) H-1 → L (2.35%) + H → L+1 (94.90%)
4BetaNO ₂	646.27 645.56	0.6229 0.6283	H-1 → L+1 (5.58%) + H → L (94.12%) H-1 → L (5.63%) + H → L+1 (94.08%)
4BetaCH ₃	684.56 684.56	0.7288 0.7288	H-4 → L+1 (3.38%) + H → L (95.83%) H-4 → L (3.38 %) + H → L+1 (95.83%)
Pc	678.24 675.27	0.6653 0.7119	H-1 → L (2.82%) + H → L+1 (94.56%) H → L (96.69%)
PcZn	659.49	0.7031	H-2 → L (3.5%) + H → L+1 (95.3%) H-2 → L+1 (3.5%) H → L (95.3%)
PcMg	676.69 676.34	0.6935 0.6931	H-1 → L+1 (4.07%) + H → L (95.70 %) H → L (4.08%) + H → L+1 (95.69%)

4.3.6 HUMO-LUMO gap

It is expected to observe a relation between the π bond conjugation and the HUMO-LUMO energy gap. Lower energy gap is expected for higher conjugated structures and therefore higher lambda max is expected to be observed. Based on the HOMO and LUMO images that can be seen in Figure 4-7, Figure 4-8, Figure 4-9 , addition of electron donating or withdrawing substituents does not have impact on changing the localization of the HOMO and LUMO from the ring. Also, these additions have no impact on increasing the number of conjugation so does the band gap.

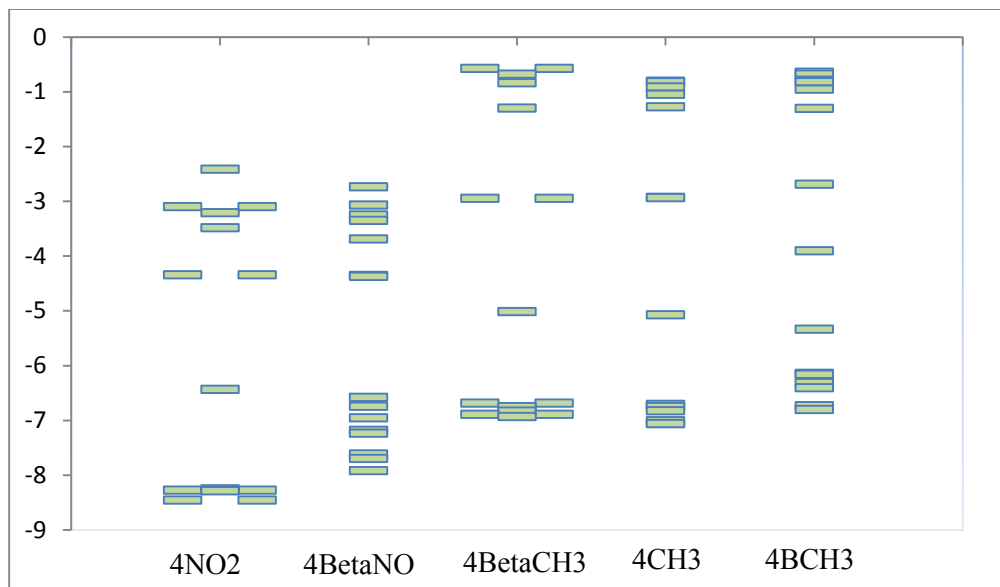


Figure 4-7. Electron configuration of ZnPc with four electron donating and withdrawing substituents.

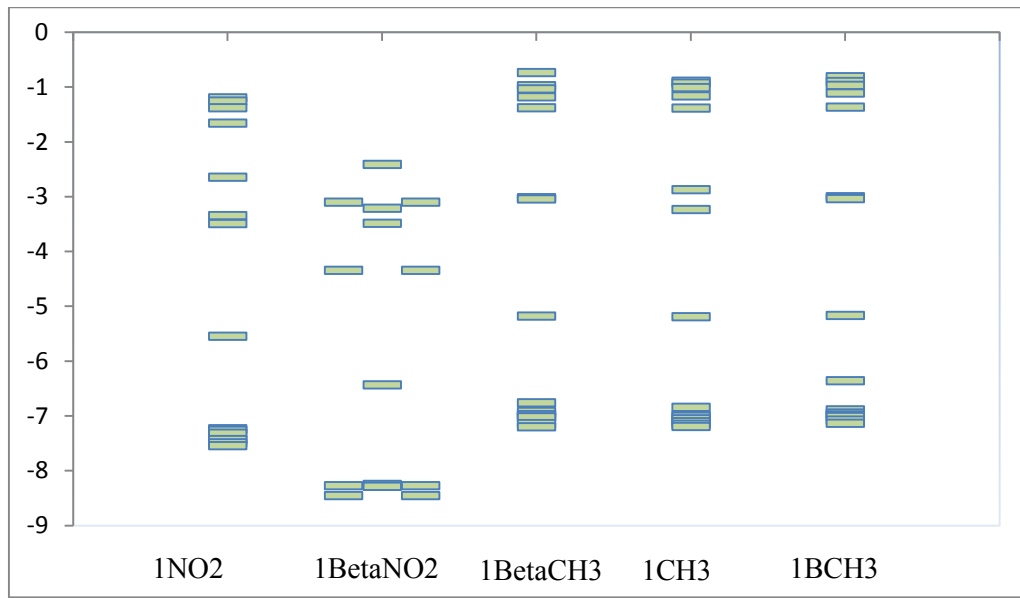


Figure 4-8. Electron configuration of ZnPc with an electron donating or an electron withdrawing substituent.

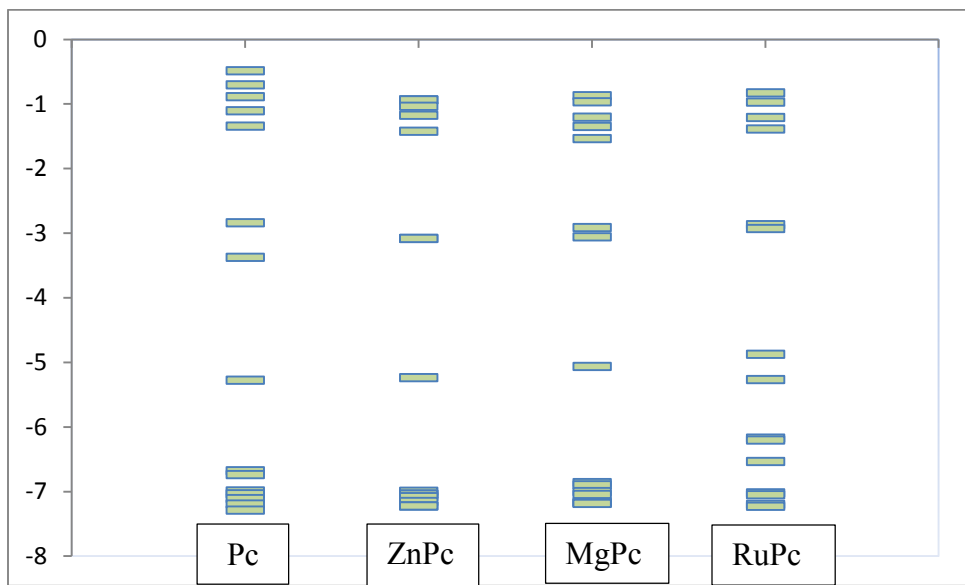


Figure 4-9. Electron configuration of phthalocyanine with and without metals.

Comparing the HUMO-LUMO gap, and the degeneracy of the molecular orbitals show that addition of electron donating and withdrawing groups on the peripheral substituent has a minor effect on HUMO and LUMO gap.

Table 4-9. Calculated HOMO and LUMO gap values for phthalocyanine with different metals.

	HOMO-LUMO
Pc	1.90
ZnPc	2.15
MgPc	2.01
RuPc	0.39

Addition of either electron donating or withdrawing group mainly has effects on stabilization and destabilization of the HUMO and LUMO gap. This impact is not very noticeable for a small electron donating or withdrawing group. As an example, while addition of four CH₃ groups has no impact to decrease the HOMO-LUMO gap, this gap has stabilized by 0.93 when BCH₃ is used as an electron donating group. The impact of this decrease in HUMO-LUMO gap is on increasing the Q band to the higher lambda max.

Addition of four NO₂ groups, stabilized the H-L gap, not as much as BCH₃ did. But, the lambda max increased

Table 4-10. Measured HOMO –LUMO gap values for ZnPc derivative with 4 substituents.

	HUMO-LUMO gap
ZnPc	2.15
4NO ₂	2.09
4BetaNO ₂	2.20
4BetaCH ₃	2.07
4CH ₃	2.14
4BCH ₃	1.22

In their UV/Vis spectra these complexes represent an intense vibronic-structure absorption band at $\lambda > 660$

Table 4-11. HOMO-LUMO gap values for ZnPc derivatives with one substituents.

	HUMO-LUMO gap
ZnPc	2.15
1NO ₂	2.06
1BetaNO ₂	2.09
1BetaCH ₃	2.13
1CH ₃	1.95
1BCH ₃	2.13

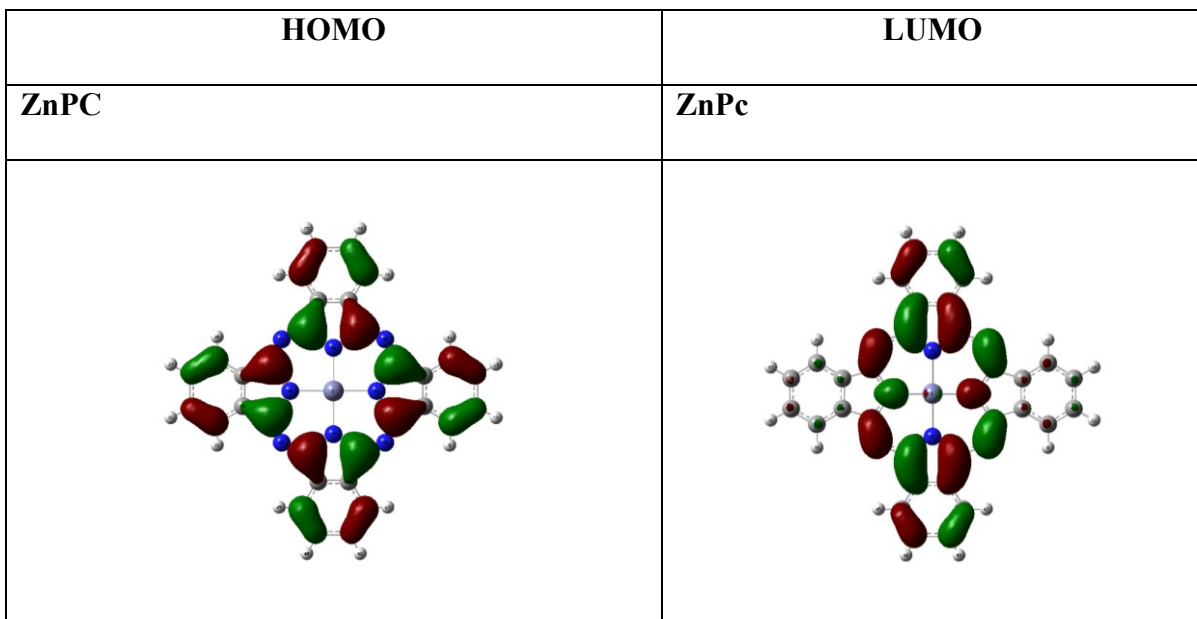


Figure 4-10. Localization of HOMO and LUMO of ZnPc derivatives studied in chapter 4.

Figure 4-10 Continued

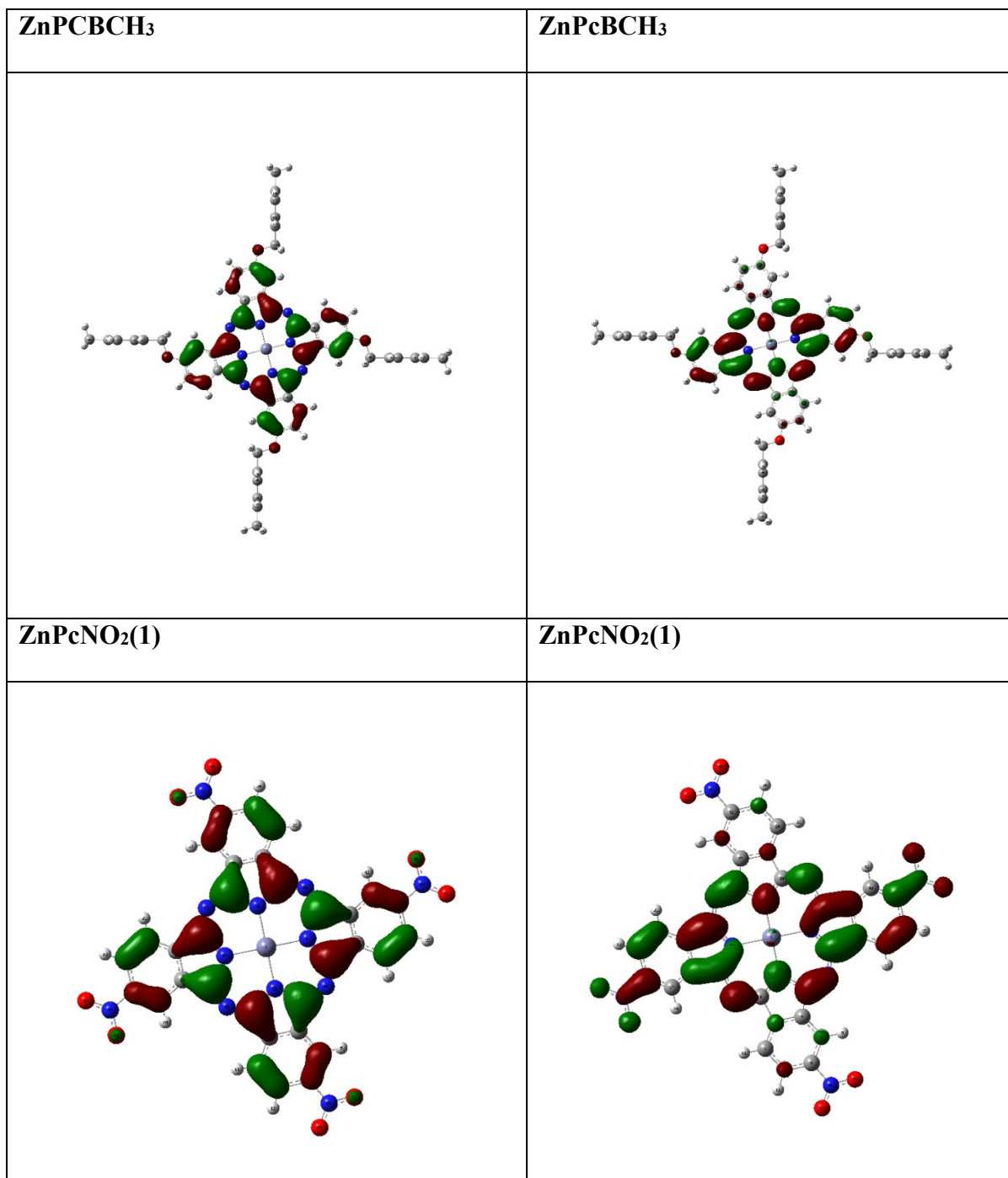


Figure 4-10 Continued

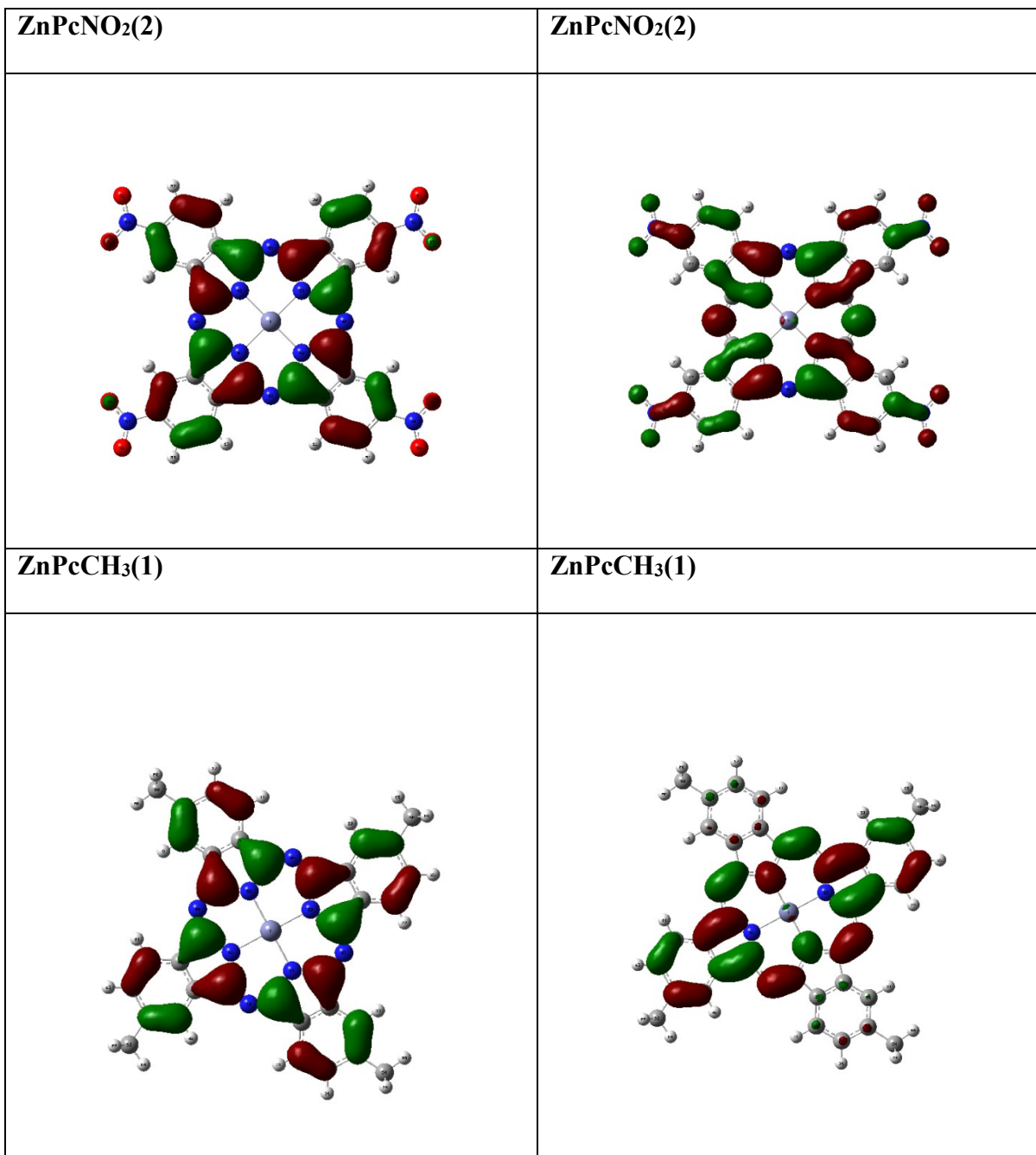


Figure 4-10 Continued

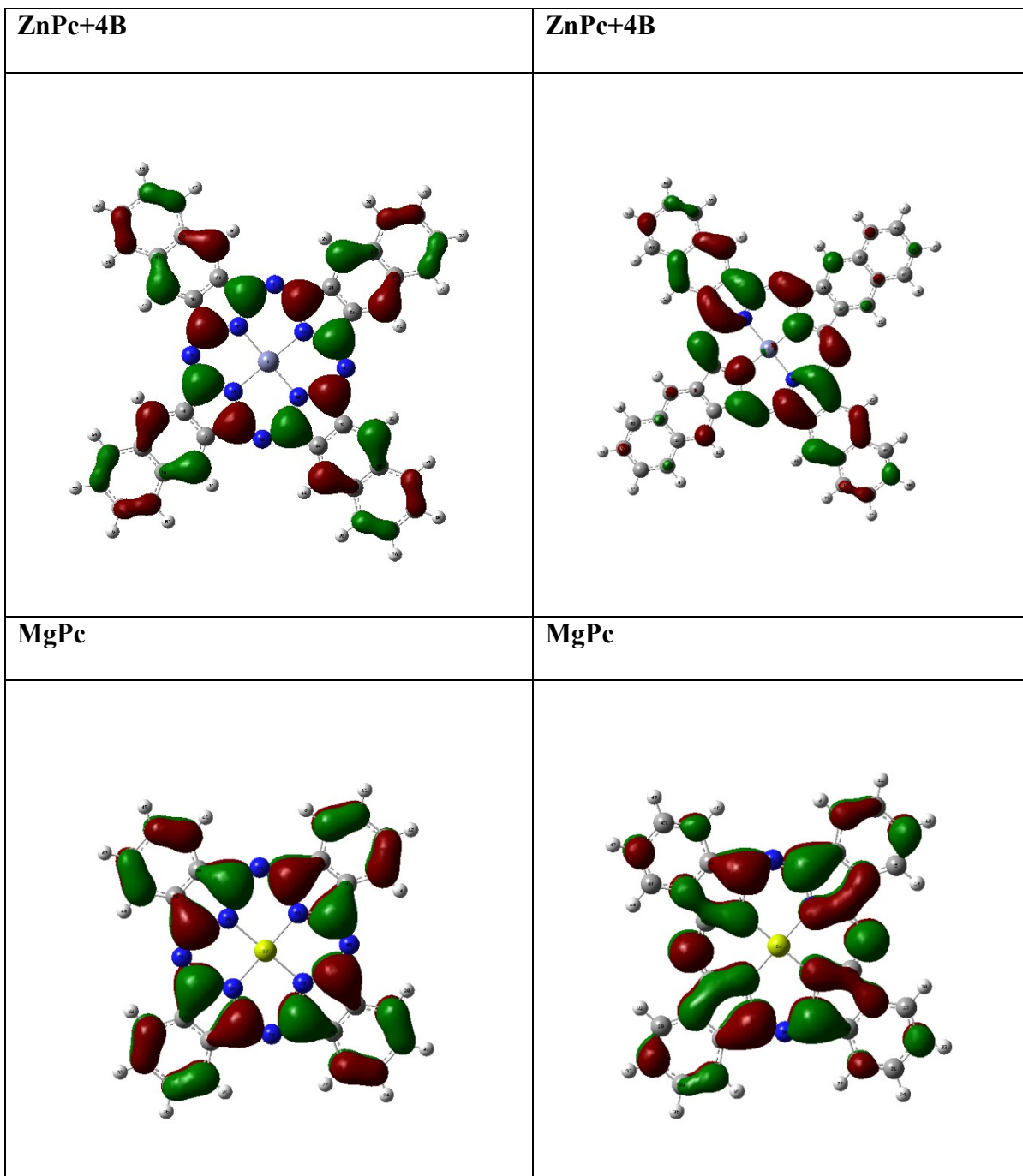


Figure 4-10 Continued

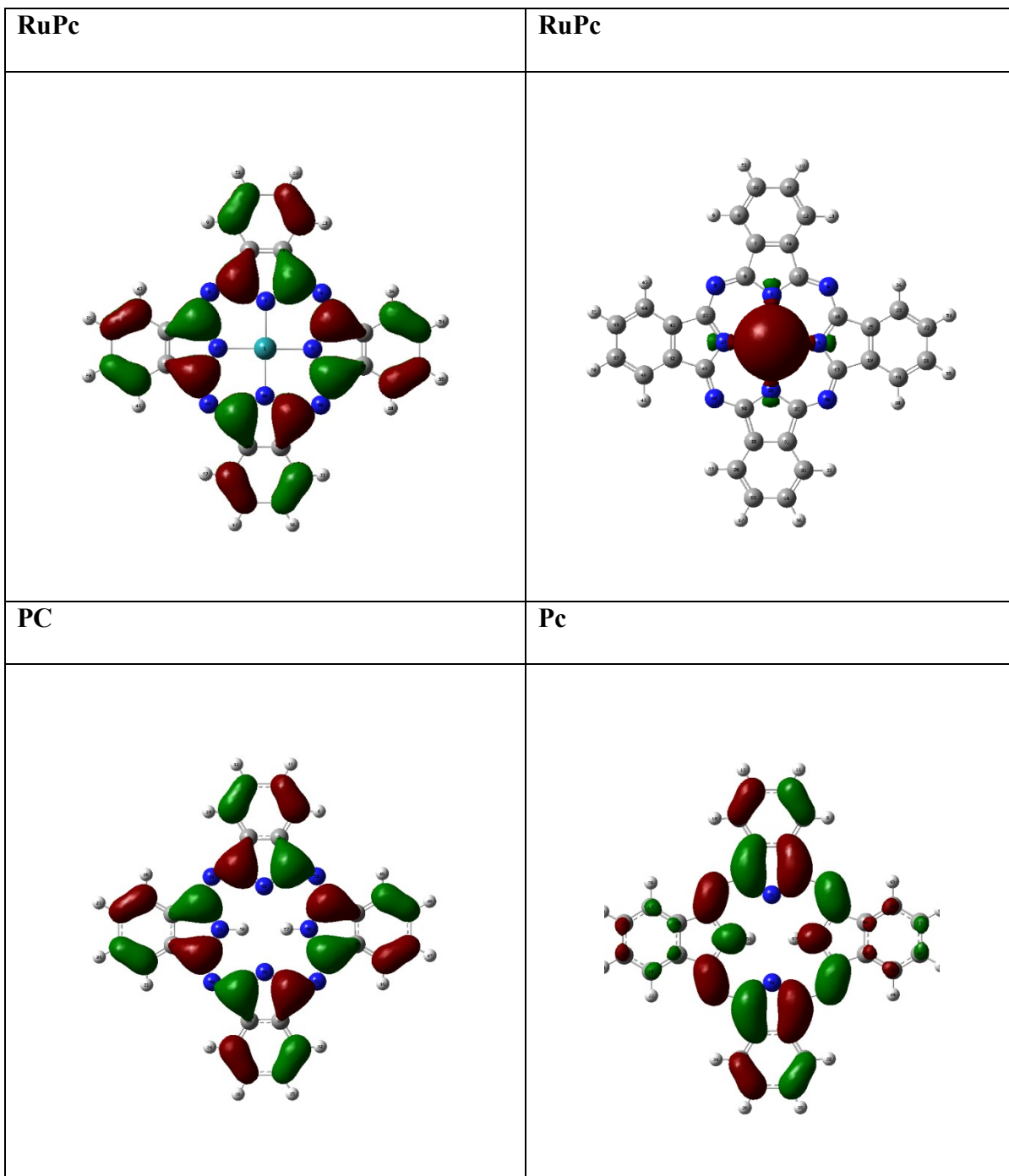


Figure 4-10 Continued

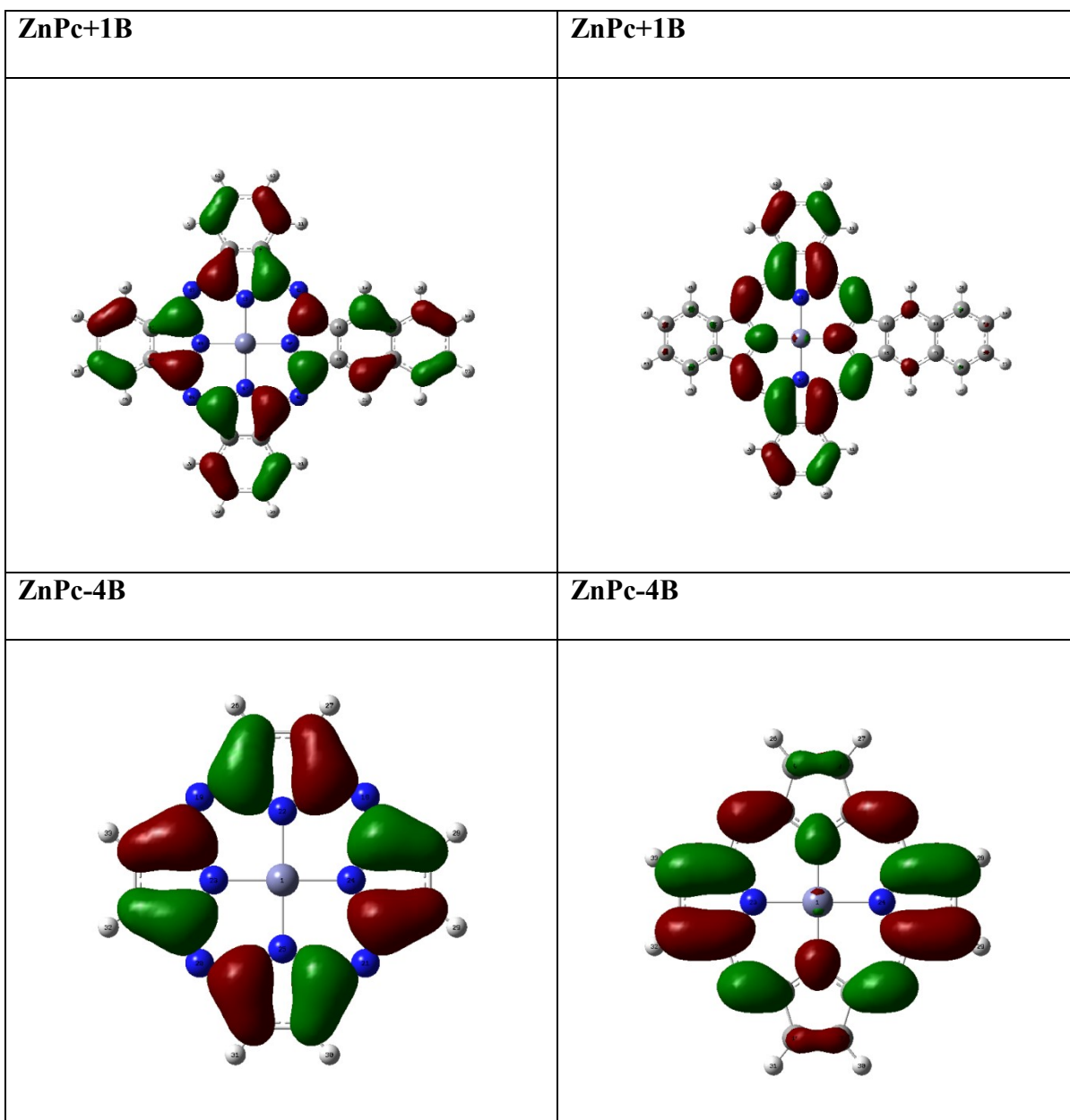


Figure 4-10 Continued

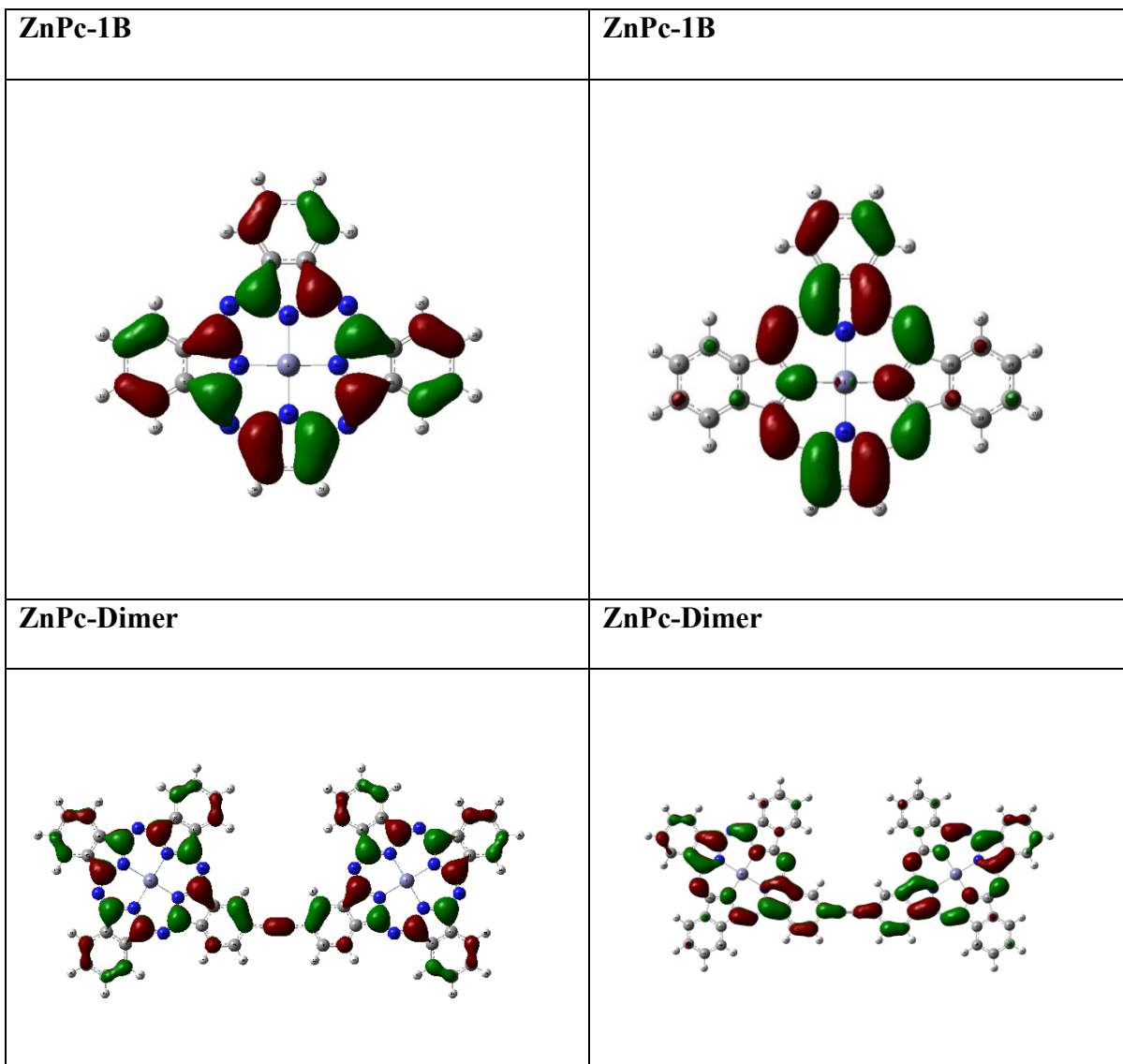
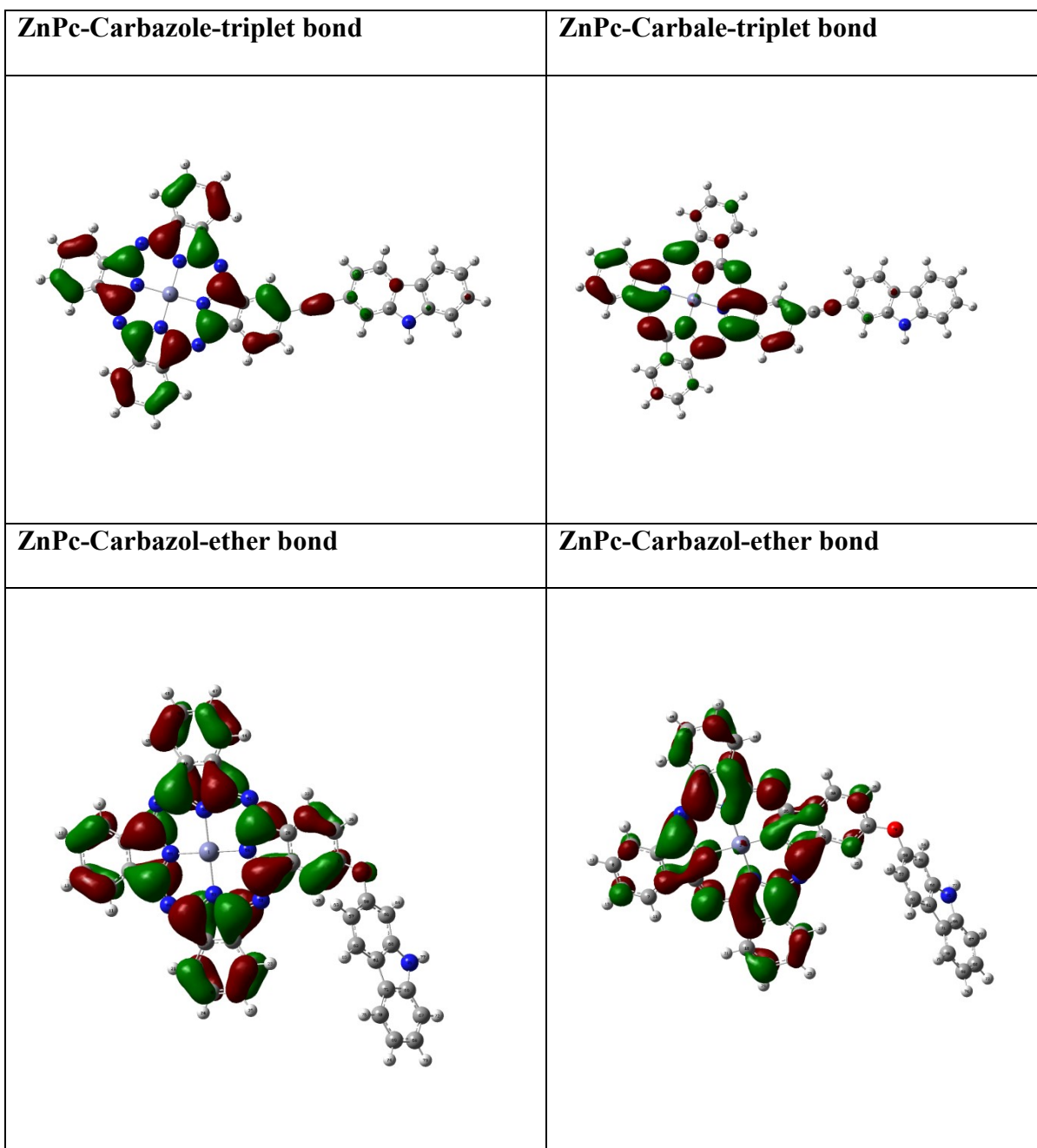


Figure 4-10 Continued



4.4 Conclusion

The aim of this study was to develop the idea of finding a correlation between singlet oxygen production and energy difference between the singlet and triplet states. Finding this correlation is helpful in generating the best structures for predicting singlet oxygen formation and higher lambda max for target compounds. According to the literature, the number and position of the substituents in alpha or beta peripheral positions impact singlet oxygen production. Also, non-substituted phthalocyanines with and without metals were compared in this study. Results show that changing the number of substituents through addition of electron donating or withdrawing groups mainly impacts the lambda max. Singlet oxygen production does not change significantly. The impact of singlet oxygen production for various metals was more noticeable.

4.5 Supporting Documents

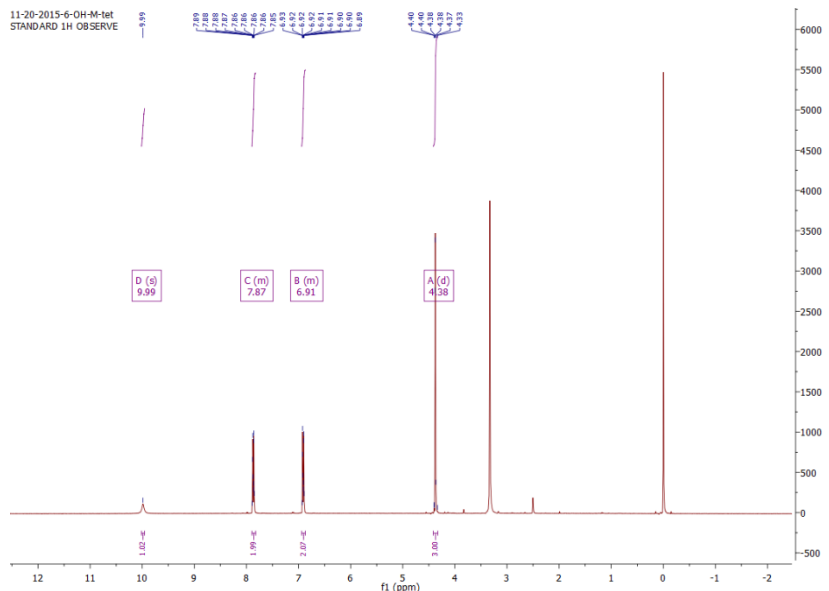


Figure 4-11. ^1H NMR spectrum of compound 1.

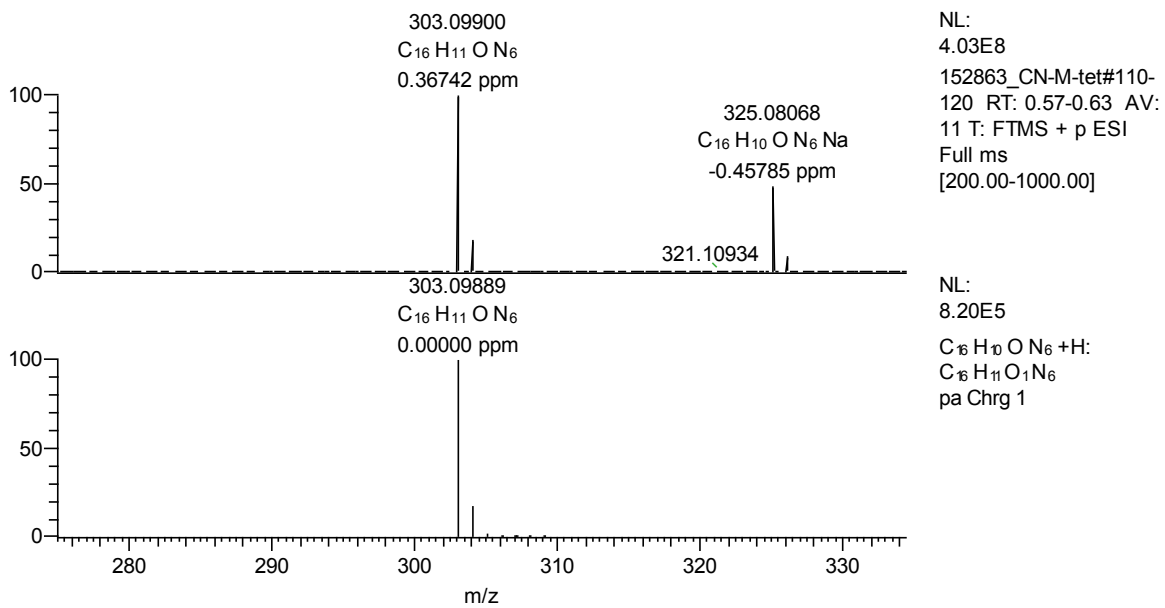


Figure 4-12. ESI mass spectrum of compound 6.

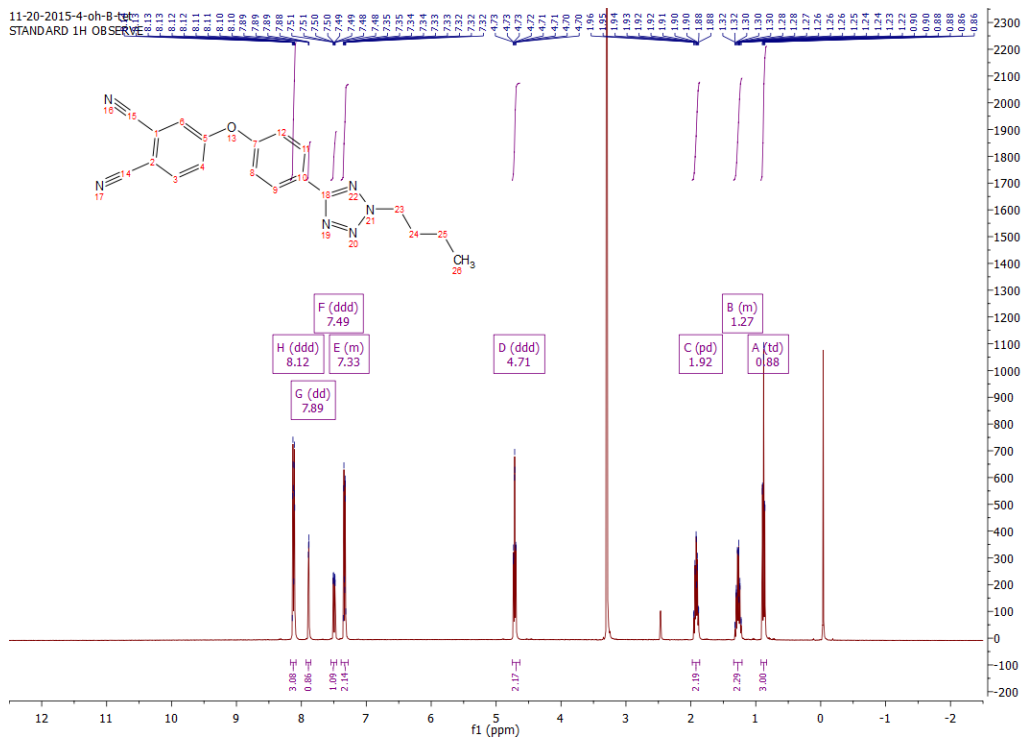


Figure 4-13. ^1H NMR spectrum of compound 7.

140906_PcNO₂ #818-858 RT: 4.47-4.68 AV: 41 NI: 2 08F6
T: FTMS + p ESI Full ms [180.00-1000.00]

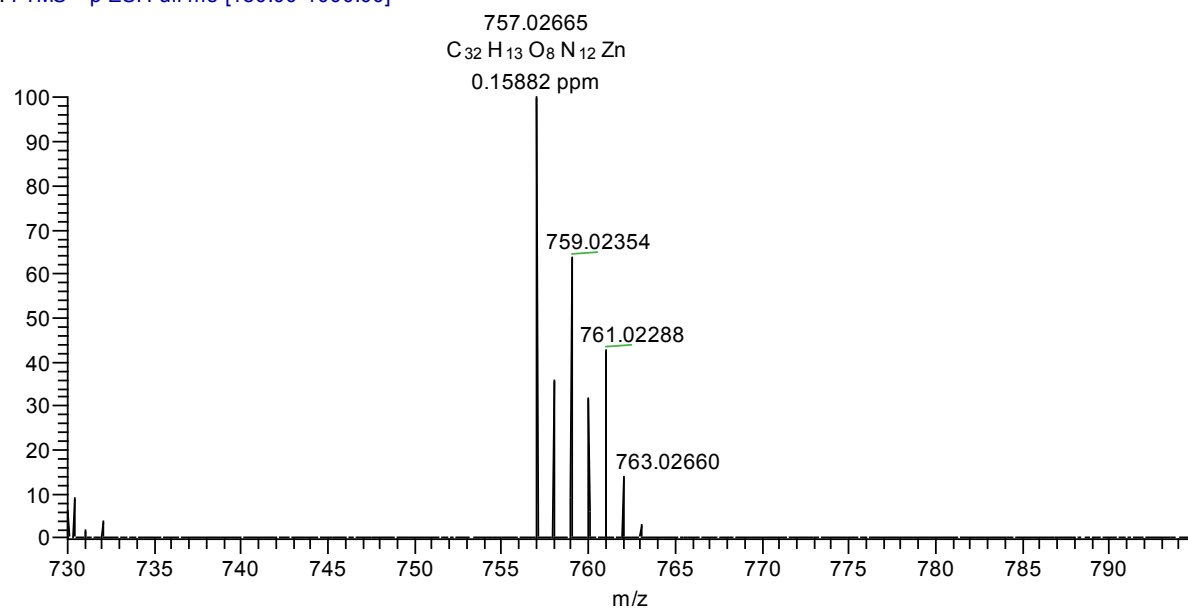


Figure 4-14. ESI mass spectrum of ZnPcNO₂.

140950_PcCH₃ #67-78 RT: 0.37-0.42 AV: 12 NL: 5.69E7
T: FTMS + p ESI Full ms [280.00-1000.00]

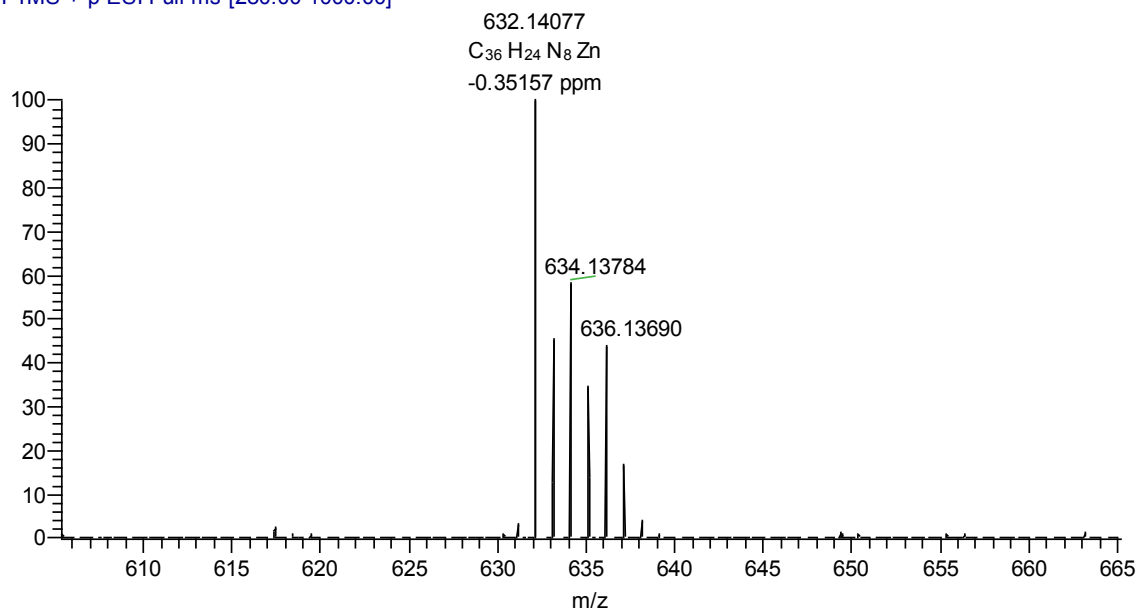


Figure 4-15. ESI mass spectrum of ZnPcCH₃.

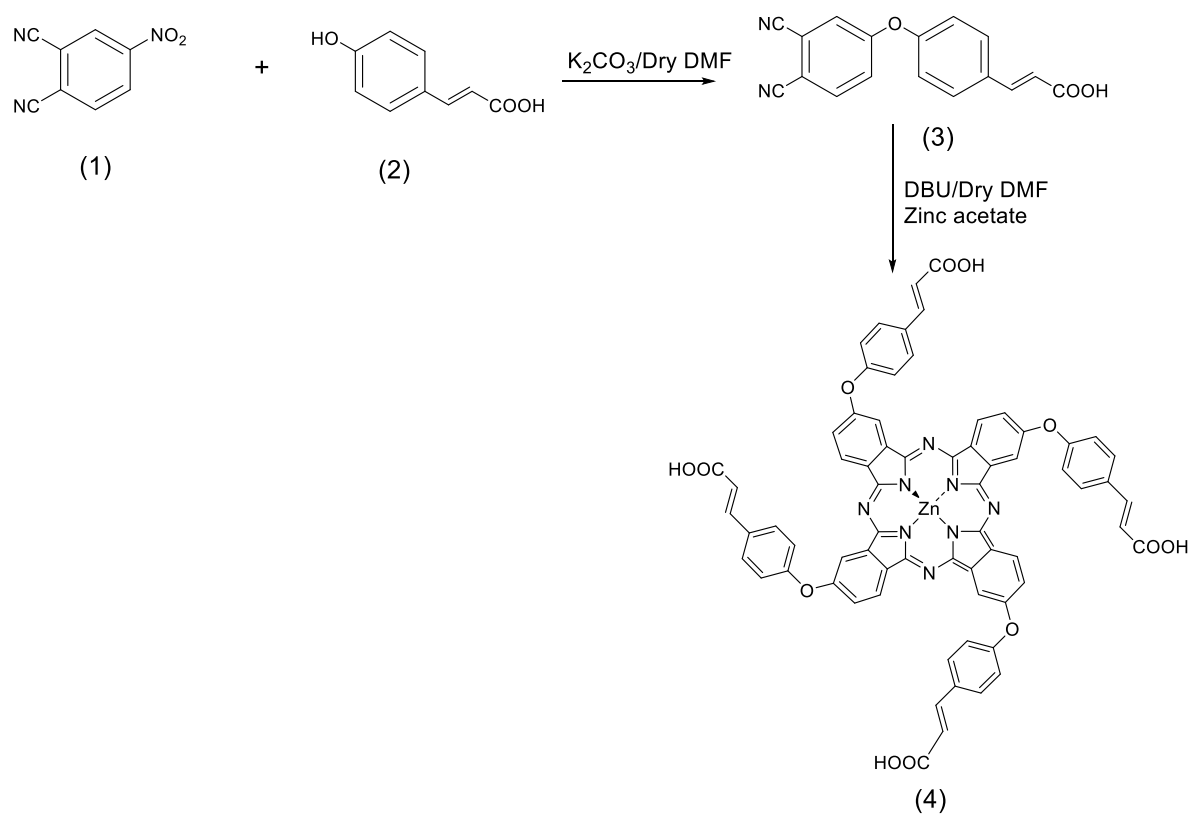
Chapter 5

FUTURE WORK

General statement: Based on the literature survey, amphiphilic sensitizer dyes and hydrophilic sensitizer dyes can be encapsulated into polymeric micelles more efficiently. For this reason, a new amphiphilic phthalocyanine with four carboxylic acid group has been synthesized. The goal was to covalently conjugate this dye with gamma cyclodextrin. First attempt to covalently bond gamma cyclodextrin and the dye failed. Optimizing the best condition to covalently bond this dye to gamma cyclodextrin is part of the future work.

4-[4-2-(-Carboxyl-ethylene)phenoxy)]phthalonitrile (3)****

4-Nitrophthalonitrile (1g, 5.76 mmol) and 4-hydroxycinnamic acid (0.947 g, 164.16 mmol) were dissolved in 20 ml of 95% dry DMF and stirred under N₂. After 5 min, K₂CO₃ (2.388 g, 17.28 mmol) was added and the reaction was heated to 85°C. The reaction was monitored using TLC (silicagel, CH₂Cl₂) and it was complete after 7 h. The reaction mixture was poured into cold water and 550 mg product was obtained and purified by crystallization from methanol and water. ¹H NMR (400 MHz, DMSO-d₆) δ 8.04 (d, J = 8.8 Hz, 1H), 7.80 – 7.67 (m, 3H), 7.54 (d, J = 16.0 Hz, 1H), 7.38 (dd, J = 8.7, 2.6 Hz, 1H), 7.18 – 7.05 (m, 2H), 6.45 (d, J = 16.0 Hz, 1H).



Scheme 5-1. Synthesis route for compound 4.

5.1 Supporting Document

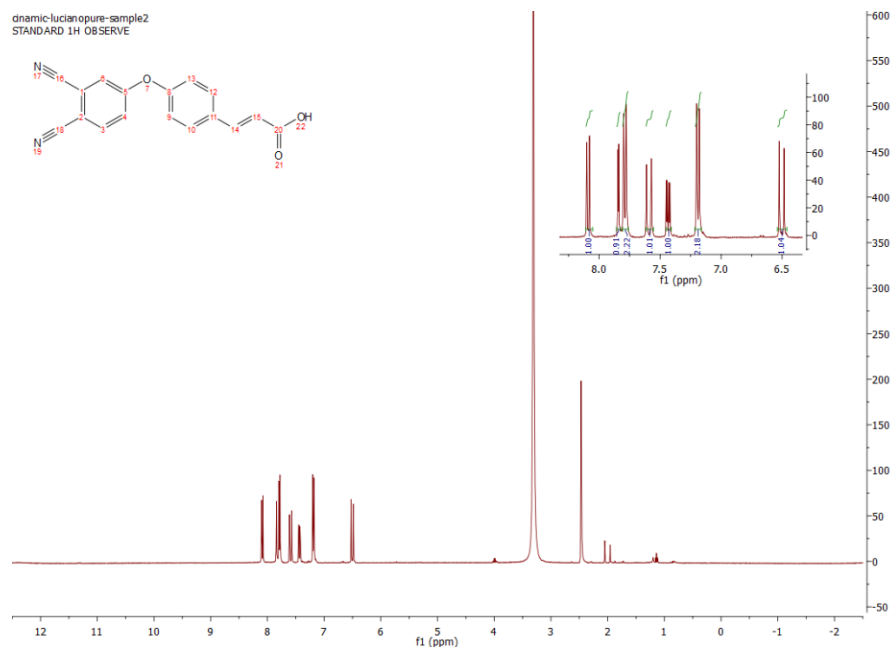


Figure 5-1. ^1H NMR spectrum of compound 3.

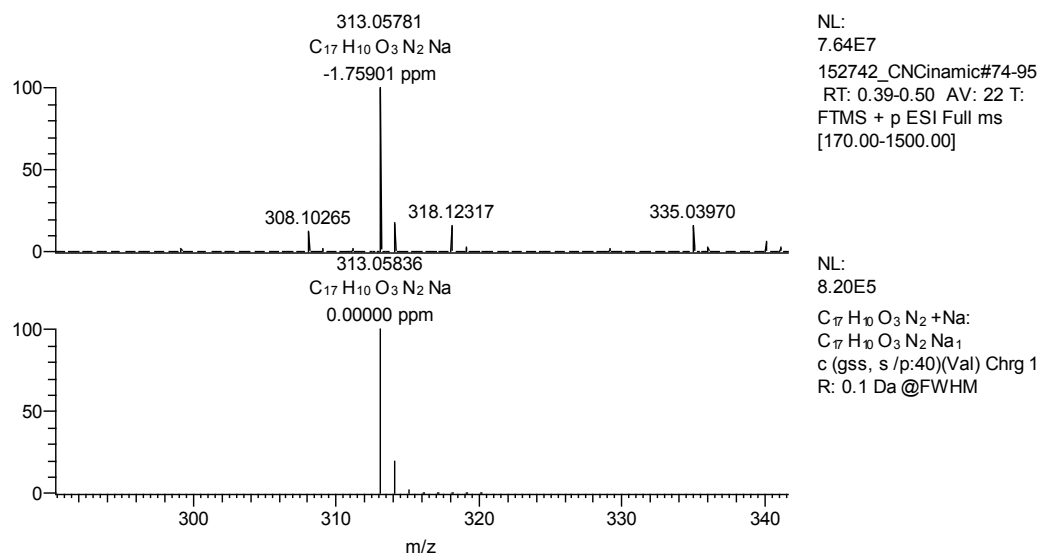


Figure 5-2. ESI mass spectrum of compound 3.

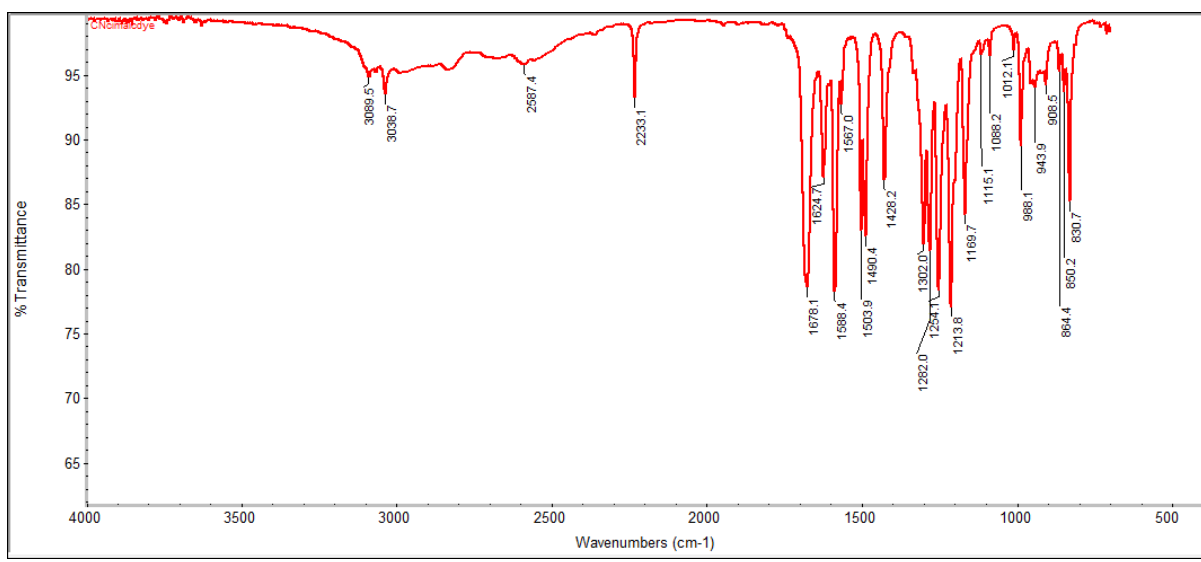


Figure 5-3. FTIR spectrum of compound 3.

Chapter 6

SUMMARY AND CONCLUSIONS

6.1 PDT Dye Design

Development of improved PDT methods for cancer treatment is important. One method involves the design of more efficient sensitizer dyes for PDT. Two key factors to consider in this design are increasing the production of singlet oxygen and increasing the lambda max of target dyes, both of which can be predicted using DFT calculations. Another method involves increasing the selectivity of the sensitizer dye for the targeted cancer cells. Increasing dye selectivity can be performed through either modification of the sensitizer dye or by using a suitable drug delivery system. A third method for improving PDT effectiveness is to develop a standard protocol for *in vitro* assays prior to *in vivo* evaluations.

In the present work, three different studies were conducted to address a few specific questions. The first question was related to the enormous number of potential sensitizer dyes that have been synthesized but only a few of them are FDA approved. Since many of these potential dyes are hydrophobic, our question was whether the current drug delivery systems providing sufficient water solubility for PDT. To answer this question, in the second chapter a new hydrophobic zinc phthalocyanine derivative with better solubility and higher lambda max than zinc phthalocyanine itself was synthesized as a model compound. This sensitizer dye was encapsulated into a polymeric micelle and evaluated using A549 cancer cell line. No

dark toxicity was observed for the free and encapsulated dyes in the absence of light but some cytotoxicity was measured for the encapsulated dye, as expected. It is possible that this happened because inadequate photoexcitation was applied.

The second question was whether there is a method to design a better phthalocyanine for PDT without going through the synthesis. The goal of Chapter 4 was to find an answer for this question. For this purpose, DFT calculations were used to predict the lambda max and singlet oxygen production efficiency of phthalocyanines by modifying this system in four different ways: 1) Through addition of electron donating and withdrawing groups in the alpha and beta positions of the ZnPc; 2) Through addition and subtraction of a fused ring on the ZnPc; 3) Through addition of substituents with the ability to have energy transfer to ZnPc; 4) Through changing the type of metals in the cavity of the phthalocyanine moiety. Results showed that an increase in the number of fused ring and changing the metal had the most impact on the singlet oxygen production of this system. Changing the substituents either through addition of electron donating or withdrawing group or groups that facilitate energy transfer with ZnPc does not change the efficiency of these dyes significantly.

In Chapter 3, the synthesis of two new dyes were reported. Based on the results in Chapter 2, addition of new substituents on phthalocyanine mostly impacts the lambda max with almost no effect on singlet oxygen production efficiency. It was interesting to know if incorporation of a new substituent with unique biological activities can change the phototoxicity of these dyes. For this reason, tetrazole derivatives with antimicrobial properties were chosen as a substituent on ZnPc. Testing these dyes on A549 cells indicated accumulation of this dye both in cytoplasm and the nucleus, which was different from ZnPc

which only accumulated in cytoplasm. We also attempted to encapsulate this dye into a polymeric micelle to increase the selectivity and cell uptake of these dyes. Our results showed no increase in the cell uptake for this dye specifically. This result implies that PLGA-b-PEG with a longer PLGA side is not the right choice as a nanoparticle for highly polar dyes such as this dye and a different drug delivery method is essential to achieve the desired goal.

6.2 *In vitro* studies

Based on *in vitro* experiments against A549 cells, a few points need to be considered to improve the *in vitro* assay protocols for PDT. First, it is not appropriate to compare the cell uptake of a newly synthesized dye, for example ZnPcBCH₃, with the dye that is derived from ZnPc. These dyes have different absorption profiles and excitation at different wavelengths impact the fluorescence intensity that is required in the analysis of the cell uptake. So, it is recommended to evaluate the uptake of each dye separately.

Based on the present study, the best standard protocol for an *in vitro* assay to evaluate a new dye is:

First: Find the minimum dye concentration that is required to show cytotoxicity on a cancer cell line. If the dye is not water soluble and it needs to be dissolved in DMSO, it is critical to add the same amount of the DMSO to the blank cell line. Results showed that DMSO decreased the intensity of the absorbance and this can produce a false positive result if it is not considered.

The amount of DMSO used should not exceed more than 2% of the medium that will be used to feed a cell line. Extra DMSO keeps the dye soluble in the medium but the behavior of the dye needs to be evaluated under conditions similar to the subsequent assay.

Second, to test the selectivity of the free dye toward cancer cells, the above procedure should be repeated on a normal cell line. Dye with high selectivity to the cancer cells should not show a high cytotoxicity on a normal cell line. Then, repeating this experiment after using an encapsulated dye in a nanoparticle can clearly show how much the selectivity has improved.

Third, once the minimum concentration is optimized, the next step is to find the best light dose to obtain the highest cytotoxicity. In this case the light dose (usually fixed light intensity and different exposure time) that previously was used to find the minimum concentration is the standard and based on this higher and lower exposure time can be evaluated to find the highest cytotoxicity.

Fourth, after optimizing the minimum concentration with a suitable light exposure time, finding the maximum uptake is necessary. The best method to optimize the cell uptake is to use the fixed dye concentration and test it on the cell line at different time points. A few time points for the first 8 h and one for 16, 24, 48 and 72 h can be used to obtain an exponential growth rate curve.

Following the above protocol, the new PDT dye is ready to be tested in an *in vivo* study as part of the sequential evaluation of dye for PDT utility.

References

1. Wainwright, M. Photodynamic therapy—from dyestuffs to high-tech clinical practice. *Review of Progress in Coloration and Related Topics* **2004**, *34*, 95-109.
2. Ormond, A. B.; Freeman, H. S. Dye sensitizers for photodynamic therapy. *Materials* **2013**, *6*, 817-840.
3. de Melo, L. S.; Gomes, A. S.; Saska, S.; Nigoghossian, K.; Messaddeq, Y.; Ribeiro, S. J.; de Araujo, R. E. Singlet oxygen generation enhanced by silver-pectin nanoparticles. *J. Fluoresc.* **2012**, *22*, 1633-1638.
4. Zhu, T. C.; Finlay, J. C. The role of photodynamic therapy (PDT) physics. *Med. Phys.* **2008**, *35*, 3127-3136.
5. Wainwright, M. Non-porphyrin photosensitizers in biomedicine. *Chem. Soc. Rev.* **1996**, *25*, 351-359.
6. Kamkaew, A.; Lim, S. H.; Lee, H. B.; Kiew, L. V.; Chung, L. Y.; Burgess, K. BODIPY dyes in photodynamic therapy. *Chem. Soc. Rev.* **2013**, *42*, 77-88.
7. Avirah, R. R.; Jayaram, D. T.; Adarsh, N.; Ramaiah, D. Squaraine dyes in PDT: from basic design to in vivo demonstration. *Organic & biomolecular chemistry* **2012**, *10*, 911-920.
8. Dąbrowski, J. M.; Urbanska, K.; Arnaut, L. G.; Pereira, M. M.; Abreu, A. R.; Simões, S.; Stochel, G. Biodistribution and Photodynamic Efficacy of a Water- Soluble, Stable, Halogenated Bacteriochlorin against Melanoma. *ChemMedChem* **2011**, *6*, 465-475.
9. Maggioni, D.; Galli, M.; D’Alfonso, L.; Inverso, D.; Dozzi, M. V.; Sironi, L.; Iannacone, M.; Collini, M.; Ferruti, P.; Ranucci, E. A Luminescent Poly (amidoamine)-Iridium Complex as a New Singlet-Oxygen Sensitizer for Photodynamic Therapy. *Inorg. Chem.* **2015**.
10. Ogilby, P. R. Singlet oxygen: there is indeed something new under the sun. *Chem. Soc. Rev.* **2010**, *39*, 3181-3209.
11. Sharpless, C. M.; Blough, N. V. The importance of charge-transfer interactions in determining chromophoric dissolved organic matter (CDOM) optical and photochemical properties. *Environmental Science: Processes & Impacts* **2014**, *16*, 654-671.

12. Salice, P.; Arnbjerg, J.; Pedersen, B. W.; Toftegaard, R.; Beverina, L.; Pagani, G. A.; Ogilby, P. R. Photophysics of squaraine dyes: role of charge-transfer in singlet oxygen production and removal. *The Journal of Physical Chemistry A* **2010**, *114*, 2518-2525.
13. Weyergang, A.; Berg, K.; Kaalhus, O.; Peng, Q.; Selbo, P. K. Photodynamic therapy targets the mTOR signaling network in vitro and in vivo. *Molecular pharmaceutics* **2008**, *6*, 255-264.
14. Agostinis, P.; Berg, K.; Cengel, K. A.; Foster, T. H.; Girotti, A. W.; Gollnick, S. O.; Hahn, S. M.; Hamblin, M. R.; Juzeniene, A.; Kessel, D. Photodynamic therapy of cancer: an update. *CA: a cancer journal for clinicians* **2011**, *61*, 250-281.
15. da Silva, E. F.; Pedersen, B. W.; Breitenbach, T.; Toftegaard, R.; Kuimova, M. K.; Arnaut, L. G.; Ogilby, P. R. Irradiation-and sensitizer-dependent changes in the lifetime of intracellular singlet oxygen produced in a photosensitized process. *The Journal of Physical Chemistry B* **2011**, *116*, 445-461.
16. Wilkinson, F.; Helman, W. P.; Ross, A. B. Rate constants for the decay and reactions of the lowest electronically excited singlet state of molecular oxygen in solution. An expanded and revised compilation. *Journal of Physical and Chemical Reference Data* **1995**, *24*, 663-677.
17. Schweitzer, C.; Schmidt, R. Physical mechanisms of generation and deactivation of singlet oxygen. *Chem. Rev.* **2003**, *103*, 1685-1758.
18. Robertson, C.; Evans, D. H.; Abrahamse, H. Photodynamic therapy (PDT): a short review on cellular mechanisms and cancer research applications for PDT. *Journal of Photochemistry and Photobiology B: Biology* **2009**, *96*, 1-8.
19. Wei, M.; Chen, M.; Chen, K.; Lou, P.; Lin, S. Y.; Hung, S.; Hsiao, M.; Yao, C.; Shieh, M. Autophagy promotes resistance to photodynamic therapy-induced apoptosis selectively in colorectal cancer stem-like cells. *Autophagy* **2014**, *10*, 1179-1192.
20. Dewaele, M.; Maes, H.; Agostinis, P. ROS-mediated mechanisms of autophagy stimulation and their relevance in cancer therapy. *Autophagy* **2010**, *6*, 838-854.
21. Xu, J.; Gattaccea, F.; Amiji, M. Biodistribution and Pharmacokinetics of EGFR-Targeted Thiolated Gelatin Nanoparticles Following Systemic Administration in Pancreatic Tumor-Bearing Mice. *Molecular pharmaceutics* **2013**, *10*, 2031-2044.
22. Castano, A. P.; Demidova, T. N.; Hamblin, M. R. Mechanisms in photodynamic therapy: part three—photosensitizer pharmacokinetics, biodistribution, tumor localization and

- modes of tumor destruction. *Photodiagnosis and Photodynamic Therapy* **2005**, *2*, 91-106.
23. Dumoulin, F. Design and Conception of Photosensitisers. *Photosensitizers in Medicine, Environment, and Security* **2012**, *1*.
 24. Silva, E. F.; Serpa, C.; Dąbrowski, J. M.; Monteiro, C. J.; Formosinho, S. J.; Stochel, G.; Urbanska, K.; Simões, S.; Pereira, M. M.; Arnaut, L. G. Mechanisms of Singlet-Oxygen and Superoxide-Ion Generation by Porphyrins and Bacteriochlorins and their Implications in Photodynamic Therapy. *Chemistry-A European Journal* **2010**, *16*, 9273-9286.
 25. Castano, A. P.; Demidova, T. N.; Hamblin, M. R. Mechanisms in photodynamic therapy: part one—photosensitizers, photochemistry and cellular localization. *Photodiagnosis and photodynamic therapy* **2004**, *1*, 279-293.
 26. Rubio, N.; Fleury, S. P.; Redmond, R. W. Spatial and temporal dynamics of in vitro photodynamic cell killing: extracellular hydrogen peroxide mediates neighbouring cell death. *Photochemical & Photobiological Sciences* **2009**, *8*, 457-464.
 27. Kessel, D.; Reiners, J. J. Promotion of Proapoptotic Signals by Lysosomal Photodamage. *Photochem. Photobiol.* **2015**.
 28. Rajaputra, P.; Nkepang, G.; Watley, R.; You, Y. Synthesis and in vitro biological evaluation of lipophilic cation conjugated photosensitizers for targeting mitochondria. *Bioorg. Med. Chem.* **2013**, *21*, 379-387.
 29. Balaji, B.; Balakrishnan, B.; Perumalla, S.; Karande, A. A.; Chakravarty, A. R. Mitochondria-Targeting Photocytotoxic Ferrocenyl Conjugates of N-Alkylpyridinium Salts. *European Journal of Inorganic Chemistry* **2015**, *2015*, 1398-1407.
 30. Odeh, A. M.; Craik, J. D.; Ezzeddine, R.; Tovmasyan, A.; Batinic-Haberle, I.; Benov, L. T. Targeting mitochondria by Zn (II) N-Alkylpyridylporphyrins: the impact of Compound sub-mitochondrial partition on cell respiration and overall photodynamic efficacy. **2014**.
 31. Rancan, F.; Wiehe, A.; Nöbel, M.; Senge, M. O.; Omari, S. A.; Böhm, F.; John, M.; Röder, B. Influence of substituents on asymmetric dihydroxychlorins with regard to intracellular uptake, subcellular localization and photosensitization of Jurkat cells. *Journal of Photochemistry and Photobiology B: Biology* **2005**, *78*, 17-28.
 32. Reiners, J. J.; Agostinis, P.; Berg, K.; Oleinick, N. L.; Kessel, D. H. Assessing autophagy in the context of photodynamic therapy. *Autophagy* **2010**, *6*, 7-18.

33. Liu, L.; Zhang, Z.; Xing, D. Cell death via mitochondrial apoptotic pathway due to activation of Bax by lysosomal photodamage. *Free Radical Biology and Medicine* **2011**, *51*, 53-68.
34. Xie, H.; Svenmarker, P.; Axelsson, J.; Gräfe, S.; Kyriazi, M.; Bendsoe, N.; Andersson-Engels, S.; Svanberg, K. Pharmacokinetic and biodistribution study following systemic administration of Fospeg®—a Pegylated liposomal mTHPC formulation in a murine model. *Journal of biophotonics* **2015**, *8*, 142-152.
35. Pandey, R. K. Recent advances in photodynamic therapy. *Journal of Porphyrins and Phthalocyanines* **2000**, *4*, 368-373.
36. Pavani, C.; Uchoa, A. F.; Oliveira, C. S.; Iamamoto, Y.; Baptista, M. S. Effect of zinc insertion and hydrophobicity on the membrane interactions and PDT activity of porphyrin photosensitizers. *Photochemical & Photobiological Sciences* **2009**, *8*, 233-240.
37. Zhang, X.; Xu, H. Influence of halogenation and aggregation on photosensitizing properties of zinc phthalocyanine (ZnPC). *J. Chem. Soc., Faraday Trans.* **1993**, *89*, 3347-3351.
38. Sakamoto, K.; Kato, T.; Kawaguchi, T.; Ohno-Okumura, E.; Urano, T.; Yamaoka, T.; Suzuki, S.; Cook, M. J. Photosensitizer efficacy of non-peripheral substituted alkylbenzopyridoporphyrazines for photodynamic therapy of cancer. *J. Photochem. Photobiol. A* **2002**, *153*, 245-253.
39. Baek, S.; Na, K. A nano complex of hydrophilic phthalocyanine and polyethylenimine for improved cellular internalization efficiency and phototoxicity. *Colloids and Surfaces B: Biointerfaces* **2013**, *101*, 493-500.
40. Lee, Y.; Cho, H.; Choi, M.; Park, H.; Bang, J.; Lee, S.; Kwon, I. C.; Kim, S. Directed molecular assembly into a biocompatible photosensitizing nanocomplex for locoregional photodynamic therapy. *J. Controlled Release* **2015**, *209*, 12-19.
41. Çakır, D.; Göksel, M.; Çakır, V.; Durmus, M.; Biyiklioglu, Z.; Kantekin, H. Amphiphilic Zinc Phthalocyanine Photosensitizers: Synthesis, Photophysicochemical Properties and in vitro Studies for Photodynamic Therapy. *Dalton Transactions* **2015**.
42. Jin, Y.; Zhang, X.; Zhang, B.; Kang, H.; Du, L.; Li, M. Nanostructures of an amphiphilic zinc phthalocyanine polymer conjugate for photodynamic therapy of psoriasis. *Colloids and Surfaces B: Biointerfaces* **2015**, *128*, 405-409.

43. Doshi, M.; Krienke, M.; Khederzadeh, S.; Sanchez, H.; Copik, A.; Oyer, J.; Gesquiere, A. J. Conducting Polymer Nanoparticles for Targeted Cancer Therapy. *RSC Advances* **2015**.
44. Lo, P. C.; Huang, J. D.; Cheng, D. Y. Y.; Chan, E. Y. M.; Fong, W. P.; Ko, W. H.; Ng, D. K. P. New amphiphilic silicon (IV) phthalocyanines as efficient photosensitizers for photodynamic therapy: synthesis, photophysical properties, and in vitro photodynamic activities. *Chemistry-A European Journal* **2004**, *10*, 4831-4838.
45. Theodossiou, T. A.; Gonçalves, A. R.; Yannakopoulou, K.; Skarpen, E.; Berg, K. Photochemical Internalization of Tamoxifens Transported by a “Trojan-Horse” Nanoconjugate into Breast-Cancer Cell Lines. *Angewandte Chemie International Edition* **2015**, *54*, 4885-4889.
46. Moromizato, S.; Hisamatsu, Y.; Suzuki, T.; Matsuo, Y.; Abe, R.; Aoki, S. Design and synthesis of a luminescent cyclometalated iridium (III) complex having N, N-diethylamino group that stains acidic intracellular organelles and induces cell death by photoirradiation. *Inorg. Chem.* **2012**, *51*, 12697-12706.
47. Nakagawa, A.; Hisamatsu, Y.; Moromizato, S.; Kohno, M.; Aoki, S. Synthesis and Photochemical Properties of pH Responsive Tris-Cyclometalated Iridium (III) Complexes That Contain a Pyridine Ring on the 2-Phenylpyridine Ligand. *Inorg. Chem.* **2013**, *53*, 409-422.
48. Huang, P.; Xu, C.; Lin, J.; Wang, C.; Wang, X.; Zhang, C.; Zhou, X.; Guo, S.; Cui, D. Folic Acid-conjugated Graphene Oxide loaded with Photosensitizers for Targeting Photodynamic Therapy. *Theranostics* **2011**, *1*, 240-250.
49. Schneider, R.; Schmitt, F.; Frochot, C.; Fort, Y.; Lourette, N.; Guillemin, F.; Müller, J.; Barberi-Heyob, M. Design, synthesis, and biological evaluation of folic acid targeted tetraphenylporphyrin as novel photosensitizers for selective photodynamic therapy. *Bioorg. Med. Chem.* **2005**, *13*, 2799-2808.
50. van Dongen, G. A. M. S.; Visser, G. W. M.; Vrouenraets, M. B. Photosensitizer-antibody conjugates for detection and therapy of cancer. *Adv. Drug Deliv. Rev.* **2004**, *56*, 31-52.
51. Yoon, I.; Li, J. Z.; Shim, Y. K. Advance in photosensitizers and light delivery for photodynamic therapy. *Clinical endoscopy* **2013**, *46*, 7-23.
52. Josefson, L.; Boyle, R. Photodynamic therapy: novel third-generation photosensitizers one step closer? *Br. J. Pharmacol.* **2008**, *154*, 1-3.

53. Wöhrle, D.; Hirth, A.; Bogdahn-Rai, T.; Schnurpeil, G.; Shopova, M. Photodynamic therapy of cancer: second and third generations of photosensitizers. *Russian chemical bulletin* **1998**, *47*, 807-816.
54. van Nostrum, C. F. Polymeric micelles to deliver photosensitizers for photodynamic therapy. *Adv. Drug Deliv. Rev.* **2004**, *56*, 9-16.
55. Komeda, C.; Ikeda, A.; Kikuchi, J.; Ishida-Kitagawa, N.; Tatebe, H.; Shiozaki, K.; Akiyama, M. A photo-triggerable drug carrier based on cleavage of PEG lipids by photosensitiser-generated reactive singlet oxygen. *Organic & biomolecular chemistry* **2013**, *11*, 2567-2570.
56. Bovis, M. J.; Woodhams, J. H.; Loizidou, M.; Scheglmann, D.; Bown, S. G.; MacRobert, A. J. Improved in vivo delivery of m-THPC via pegylated liposomes for use in photodynamic therapy. *J. Controlled Release* **2012**, *157*, 196-205.
57. Choi, Y.; Kim, S.; Choi, M.; Ryoo, S.; Park, J.; Min, D.; Kim, B. Highly Biocompatible Carbon Nanodots for Simultaneous Bioimaging and Targeted Photodynamic Therapy In Vitro and In Vivo. *Advanced Functional Materials* **2014**.
58. Castagnos, P.; Siqueira-Moura, M.; Goto, P. L.; Perez, E.; Franceschi, S.; Rico-Lattes, I.; Tedesco, A.; Blanzat, M. Catanionic vesicles charged with chloroaluminium phthalocyanine for topical photodynamic therapy. In vitro phototoxicity towards human carcinoma and melanoma cell lines. *RSC Advances* **2014**, *4*, 39372-39377.
59. Wang, N.; Zhao, Z.; Lv, Y.; Fan, H.; Bai, H.; Meng, H.; Long, Y.; Fu, T.; Zhang, X.; Tan, W. Gold nanorod-photosensitizer conjugate with extracellular pH-driven tumor targeting ability for photothermal/photodynamic therapy. **2014**.
60. Cheng, Y.; Doane, T. L.; Chuang, C.; Ziady, A.; Burda, C. Near Infrared Light-Triggered Drug Generation and Release from Gold Nanoparticle Carriers for Photodynamic Therapy. *Small* **2014**, *10*, 1799-1804.
61. Fraix, A.; Gref, R.; Sortino, S. A multi-photoresponsive supramolecular hydrogel with dual-color fluorescence and dual-modal photodynamic action. *Journal of Materials Chemistry B* **2014**, *2*, 3443-3449.
62. Kesharwani, P.; Jain, K.; Jain, N. K. Dendrimer as nanocarrier for drug delivery. *Progress in Polymer Science* **2014**, *39*, 268-307.
63. Yin, M.; Ju, E.; Chen, Z.; Li, Z.; Ren, J.; Qu, X. Upconverting Nanoparticles with a Mesoporous TiO₂ Shell for Near-Infrared-Triggered Drug Delivery and Synergistic Targeted Cancer Therapy. *Chemistry-A European Journal* **2014**.

64. García Vior, M. C.; Marino, J.; Roguin, L. P.; Sosnik, A.; Awruch, J. Photodynamic Effects of Zinc (II) Phthalocyanine-Loaded Polymeric Micelles in Human Nasopharynx KB Carcinoma Cells. *Photochem. Photobiol.* **2013**, *89*, 492-500.
65. Chen, Y.; Lo, C.; Hsieue, G. Multifunctional nanomicellar systems for delivering anticancer drugs. *Journal of Biomedical Materials Research Part A* **2014**, *102*, 2024-2038.
66. Kataoka, K.; Harada, A.; Nagasaki, Y. Block copolymer micelles for drug delivery: design, characterization and biological significance. *Adv. Drug Deliv. Rev.* **2001**, *47*, 113-131.
67. Peng, C.; Shieh, M.; Tsai, M.; Chang, C.; Lai, P. Self-assembled star-shaped chlorin-core poly(ϵ -caprolactone)-poly(ethylene glycol) diblock copolymer micelles for dual chemo-photodynamic therapies. *Biomaterials* **2008**, *29*, 3599-3608.
68. Wu, D.; Li, Z.; Li, C.; Fan, J.; Lu, B.; Chang, C.; Cheng, S.; Zhang, X.; Zhuo, R. Porphyrin and galactosyl conjugated micelles for targeting photodynamic therapy. *Pharm. Res.* **2010**, *27*, 187-199.
69. Knop, K.; Mingaud, A.; El-Akra, N.; Violeau, F.; Souchard, J. Monomeric pheophorbide (a)-containing poly (ethyleneglycol-b- ϵ -caprolactone) micelles for photodynamic therapy. *Photochemical & Photobiological Sciences* **2009**, *8*, 396-404.
70. Synatschke, C. V.; Nomoto, T.; Cabral, H.; Förtsch, M.; Toh, K.; Matsumoto, Y.; Miyazaki, K.; Hanisch, A.; Schacher, F. H.; Kishimura, A. Multicompartment Micelles with Adjustable Poly (ethylene glycol) Shell for Efficient In Vivo Photodynamic Therapy. *ACS nano* **2014**, *8*, 1161-1172.
71. Ma, D.; Liu, Z.; Zheng, Q.; Zhou, X.; Zhang, Y.; Shi, Y.; Lin, J.; Xue, W. Star-Shaped Polymer Consisting of a Porphyrin Core and Poly (L-lysine) Dendron Arms: Synthesis, Drug Delivery, and In Vitro Chemo/Photodynamic Therapy. *Macromolecular rapid communications* **2013**, *34*, 548-552.
72. Lee, S. U.; Min, K. H.; Jeong, S. Y.; Bae, H.; Lee, S. C. Calcium phosphate-reinforced photosensitizer-loaded polymer nanoparticles for photodynamic therapy. *Chem. Asian J.* **2013**, *8*, 3222-3229.
73. Li, S. P.; Lau, C. T.; Louie, M.; Lam, Y.; Cheng, S. H.; Lo, K. K. Mitochondria-targeting cyclometalated iridium (III)-PEG complexes with tunable photodynamic activity. *Biomaterials* **2013**, *34*, 7519-7532.

74. Verma, S.; Watt, G. M.; Mai, Z.; Hasan, T. Strategies for Enhanced Photodynamic Therapy Effects†. *Photochem. Photobiol.* **2007**, *83*, 996-1005.
75. Master, A.; Malamas, A.; Solanki, R.; Clausen, D. M.; Eiseman, J. L.; Sen Gupta, A. A cell-targeted photodynamic nanomedicine strategy for head and neck cancers. *Molecular pharmaceutics* **2013**, *10*, 1988-1997.
76. Peng, C.; Lai, P.; Lin, F.; Yueh-Hsiu Wu, S.; Shieh, M. Dual chemotherapy and photodynamic therapy in an HT-29 human colon cancer xenograft model using SN-38-loaded chlorin-core star block copolymer micelles. *Biomaterials* **2009**, *30*, 3614-3625.
77. Koo, H.; Lee, H.; Lee, S.; Min, K. H.; Kim, M. S.; Lee, D. S.; Choi, Y.; Kwon, I. C.; Kim, K.; Jeong, S. Y. In vivo tumor diagnosis and photodynamic therapy via tumoral pH-responsive polymeric micelles. *Chemical communications* **2010**, *46*, 5668-5670.
78. Lau, J. T.; Lo, P.; Jiang, X.; Wang, Q.; Ng, D. K. A Dual Activatable Photosensitizer Toward Targeted Photodynamic Therapy. *J. Med. Chem.* **2014**.
79. Liang, J.; Wu, W.; Xu, X.; Zhuo, R.; Zhang, X. pH Responsive micelle self-assembled from a new amphiphilic peptide as anti-tumor drug carrier. *Colloids and Surfaces B: Biointerfaces* **2014**, *114*, 398-403.
80. Master, A. M.; Qi, Y.; Oleinick, N. L.; Gupta, A. S. EGFR-mediated intracellular delivery of Pc 4 nanoformulation for targeted photodynamic therapy of cancer: in vitro studies. *Nanomedicine: Nanotechnology, Biology and Medicine* **2012**, *8*, 655-664.
81. Li, L.; Cho, H.; Yoon, K. H.; Kang, H. C.; Huh, K. M. Antioxidant-photosensitizer dual-loaded polymeric micelles with controllable production of reactive oxygen species. *Int. J. Pharm.* **2014**, *471*, 339-348.
82. Hofman, J.; Carstens, M. G.; van Zeeland, F.; Helwig, C.; Flesch, F. M.; Hennink, W. E.; Van Nostrum, C. F. Photocytotoxicity of mTHPC (temoporfin) loaded polymeric micelles mediated by lipase catalyzed degradation. *Pharm. Res.* **2008**, *25*, 2065-2073.
83. Chen, J.; Wang, H.; Li, C.; Han, K.; Zhang, X.; Zhuo, R. Construction of surfactant-like tetra-tail amphiphilic peptide with RGD ligand for encapsulation of porphyrin for photodynamic therapy. *Biomaterials* **2011**, *32*, 1678-1684.
84. Ding, H.; Sumer, B. D.; Kessinger, C. W.; Dong, Y.; Huang, G.; Boothman, D. A.; Gao, J. Nanoscopic micelle delivery improves the photophysical properties and efficacy of photodynamic therapy of protoporphyrin IX. *J. Controlled Release* **2011**, *151*, 271-277.

85. Yuan, A.; Yang, B.; Wu, J.; Hu, Y.; Ming, X. Dendritic nanoconjugates of photosensitizer for targeted photodynamic therapy. *Acta Biomaterialia* **2015**.
86. Dong, H.; Li, Y.; Wen, H.; Xu, M.; Liu, L.; Li, Z.; Guo, F.; Shi, D. Highly Efficient Drug Delivery Nanosystem via L-Phenylalanine Triggering Based on Supramolecular Polymer Micelles. *Macromolecular rapid communications* **2011**, *32*, 540-545.
87. Mojzisova, H.; Bonneau, S.; Vever-Bizet, C.; Brault, D. The pH-dependent distribution of the photosensitizer chlorin e6 among plasma proteins and membranes: A physico-chemical approach. *Biochimica et Biophysica Acta (BBA) - Biomembranes* **2007**, *1768*, 366-374.
88. Chong, K.; Ku, T.; Saw, P. E.; Jon, S.; Park, J.; Choi, C. Enhancement of the photocytotoxic efficiency of sub-12 nm therapeutic polymeric micelles with increased co-localisation in mitochondria. *Chemical Communications* **2013**, *49*, 11476-11478.
89. Nishiyama, N.; Nakagishi, Y.; Morimoto, Y.; Lai, P.; Miyazaki, K.; Urano, K.; Horie, S.; Kumagai, M.; Fukushima, S.; Cheng, Y. Enhanced photodynamic cancer treatment by supramolecular nanocarriers charged with dendrimer phthalocyanine. *J. Controlled Release* **2009**, *133*, 245-251.
90. Master, A. M.; Livingston, M.; Oleinick, N. L.; Sen Gupta, A. Optimization of a nanomedicine-based silicon Phthalocyanine 4 Photodynamic Therapy (Pc 4-PDT) strategy for targeted treatment of EGFR-overexpressing cancers. *Molecular pharmaceutics* **2012**, *9*, 2331-2338.
91. Syu, W.; Yu, H.; Hsu, C.; Rajan, Y. C.; Hsu, Y.; Chang, Y.; Hsieh, W.; Wang, C.; Lai, P. Improved Photodynamic Cancer Treatment by Folate-Conjugated Polymeric Micelles in a KB Xenografted Animal Model. *Small* **2012**, *8*, 2060-2069.
92. Gong, H.; Dong, Z.; Liu, Y.; Yin, S.; Cheng, L.; Xi, W.; Xiang, J.; Liu, K.; Li, Y.; Liu, Z. Engineering of Multifunctional Nano-Micelles for Combined Photothermal and Photodynamic Therapy Under the Guidance of Multimodal Imaging. *Advanced Functional Materials* **2014**.
93. Lee, U. Y.; Oh, Y. T.; Kim, D.; Lee, E. S. Multimeric grain-marked micelles for highly efficient photodynamic therapy and magnetic resonance imaging of tumors. *Int. J. Pharm.* **2014**, *471*, 166-172.
94. Pelosi, D. S.; Estevão, B. M.; Freitas, C. F.; Tsubone, T. M.; Caetano, W.; Hioka, N. Photophysical properties of erythrosin ester derivatives in ionic and non-ionic micelles. *Dyes and Pigments* **2013**, *99*, 705-712.

95. Chen, K.; Yu, M.; Zhang, H.; Ma, D.; Pang, S.; Huang, W.; Peng, Y. In *In Polyion complex micelles incorporating poly (aryl benzyl ether) dendritic phthalocyanine: effective photosensitizers for enhanced photodynamic therapy*; Photonics Asia; International Society for Optics and Photonics: 2012; , pp 85532C-85532C-5.
96. Gibot, L.; Lemelle, A.; Till, U.; Moukarzel, B.; Mingotaud, A.; Pimienta, V.; Saint-Aguet, P.; Rols, M.; Gaucher, M.; Violleau, F. Polymeric micelles encapsulating photosensitizer: structure/photodynamic therapy efficiency relation. *Biomacromolecules* **2014**, *15*, 1443-1455.
97. Shao, W.; Wang, H.; He, S.; Shi, L.; Peng, K.; Lin, Y.; Zhang, L.; Ji, L.; Liu, H. Photophysical properties and singlet oxygen generation of three sets of halogenated corroles. *The Journal of Physical Chemistry B* **2012**, *116*, 14228-14234.
98. Lo, P.; Wang, S.; Zeug, A.; Meyer, M.; Röder, B.; Ng, D. K. P. Preparation and photophysical properties of halogenated silicon(IV) phthalocyanines substituted axially with poly(ethylene glycol) chains. *Tetrahedron Lett.* **2003**, *44*, 1967-1970.
99. Tanielian, C.; Wolff, C. Determination of the parameters controlling singlet oxygen production via oxygen and heavy-atom enhancement of triplet yields. *J. Phys. Chem.* **1995**, *99*, 9831-9837.
100. de Melo, J.; Rondão, R.; Burrows, H. D.; Melo, M. J.; Navaratnam, S.; Edge, R.; Voss, G. Spectral and photophysical studies of substituted indigo derivatives in their keto forms. *ChemPhysChem* **2006**, *7*, 2303-2311.
101. Louis Gaboury, Richard Giasson, Ajay Kumar Gupta, Li Tiechao, Luc Villeneuve WO1996007431 A1, Mar 14, 1996.
102. Araki, K.; Engelmann, F. M.; Mayer, I.; Toma, H. E.; Baptista, M. S.; Maeda, H.; Osuka, A.; Furuta, H. Doubly N-Confused Porphyrins as Efficient Sensitizers for Singlet Oxygen Generation. *Chem. Lett.* **2003**, *32*, 244-245.
103. Obata, M.; Hirohara, S.; Tanaka, R.; Kinoshita, I.; Ohkubo, K.; Fukuzumi, S.; Tanihara, M.; Yano, S. In vitro heavy-atom effect of palladium (II) and platinum (II) complexes of pyrrolidine-fused chlorin in photodynamic therapy. *J. Med. Chem.* **2009**, *52*, 2747-2753.
104. Weitman, H.; Shatz, S.; Ehrenberg, B. Complexation of Mg-tetrabenzoporphyrin with pyridine enhances singlet oxygen generation and affects its partitioning into apolar microenvironments. *J. Photochem. Photobiol. A*. **2009**, *203*, 7-12.

105. Marydasan, B.; Nair, A. K.; Ramaiah, D. Optimization of Triplet Excited State and Singlet Oxygen Quantum Yields of Picolylamine–Porphyrin Conjugates through Zinc Insertion. *The Journal of Physical Chemistry B* **2013**, *117*, 13515-13522.
106. Peceli, D.; Hu, H.; Fishman, D. A.; Webster, S.; Przhonska, O. V.; Kurdyukov, V. V.; Slominsky, Y. L.; Tolmachev, A. I.; Kachkovski, A. D.; Gerasov, A. O. Enhanced Intersystem Crossing Rate in Polymethine-Like Molecules: Sulfur-Containing Squaraines versus Oxygen-Containing Analogues. *The Journal of Physical Chemistry A* **2013**, *117*, 2333-2346.
107. Webster, S.; Peceli, D.; Hu, H.; Padilha, L. A.; Przhonska, O. V.; Masunov, A. E.; Gerasov, A. O.; Kachkovski, A. D.; Slominsky, Y. L.; Tolmachev, A. I. Near-unity quantum yields for intersystem crossing and singlet oxygen generation in polymethine-like molecules: design and experimental realization. *The Journal of Physical Chemistry Letters* **2010**, *1*, 2354-2360.
108. Sagun, E.; Zenkevich, E.; Knyukshto, V.; Panarin, A. Y.; Semeikin, A.; Lyubimova, T. Relaxation processes with participation of excited S 1 and T 1 states of spatially distorted meso-phenyl-substituted octamethylporphyrins. *Optics and Spectroscopy* **2012**, *113*, 388-400.
109. Röder, B.; Büchner, M.; Rückmann, I.; Senge, M. O. Correlation of photophysical parameters with macrocycle distortion in porphyrins with graded degree of saddle distortion. *Photochemical & Photobiological Sciences* **2010**, *9*, 1152-1158.
110. Shimakoshi, H.; Baba, T.; Iseki, Y.; Aritome, I.; Endo, A.; Adachi, C.; Hisaeda, Y. Photophysical and photosensitizing properties of brominated porphycenes. *Chemical Communications* **2008**, 2882-2884.
111. Luo, C.; Zhou, Q.; Jiang, G.; He, L.; Zhang, B.; Wang, X. The synthesis and 1 O 2 photosensitization of halogenated asymmetric aniline-based squaraines. *New Journal of Chemistry* **2011**, *35*, 1128-1132.
112. Zhou, L.; Wei, S.; Ge, X.; Zhou, J.; Yu, B.; Shen, J. External heavy-atomic construction of photosensitizer nanoparticles for enhanced in vitro photodynamic therapy of cancer. *The Journal of Physical Chemistry B* **2012**, *116*, 12744-12749.
113. Maeda, D.; Shimakoshi, H.; Abe, M.; Hisaeda, Y. Syntheses and photophysical behavior of porphyrin isomer Sn (IV) complexes. *Inorg. Chem.* **2009**, *48*, 9853-9860.
114. Kim, O.; Lee, K.; Woo, H. Y.; Kim, K.; He, G. S.; Swiatkiewicz, J.; Prasad, P. N. New class of two-photon-absorbing chromophores based on dithienothiophene. *Chemistry of materials* **2000**, *12*, 284-286.

115. Das, S.; Nag, A.; Goswami, D.; Bharadwaj, P. K. Zinc (II)-and copper (I)-mediated large two-photon absorption cross sections in a bis-cinnamaldiminato Schiff base. *J. Am. Chem. Soc.* **2006**, *128*, 402-403.
116. Oar, M. A.; Dichtel, W. R.; Serin, J. M.; Fréchet, J. M.; Rogers, J. E.; Slagle, J. E.; Fleitz, P. A.; Tan, L.; Ohulchanskyy, T. Y.; Prasad, P. N. Light-harvesting chromophores with metalated porphyrin cores for tuned photosensitization of singlet oxygen via two-photon excited FRET. *Chemistry of materials* **2006**, *18*, 3682-3692.
117. Luo, T.; Wilson, B. C.; Lu, Q. Evaluation of one- and two-photon activated photodynamic therapy with pyropheophorbide-a methyl ester in human cervical, lung and ovarian cancer cells. *Journal of Photochemistry and Photobiology B: Biology* **2014**, *132*, 102-110.
118. Pefkianakis, E. K.; Christodouleas, D.; Giokas, D. L.; Papadopoulos, K.; Vougioukalakis, G. C. A Family of RuII Photosensitizers with High Singlet Oxygen Quantum Yield: Synthesis, Characterization, and Evaluation. *European Journal of Inorganic Chemistry* **2013**, *2013*, 4628-4635.
119. Zhao, J.; Wu, W.; Sun, J.; Guo, S. Triplet photosensitizers: from molecular design to applications. *Chem. Soc. Rev.* **2013**, *42*, 5323-5351.
120. Zhao, Q.; Liu, S.; Shi, M.; Li, F.; Jing, H.; Yi, T.; Huang, C. Tuning photophysical and electrochemical properties of cationic iridium (III) complex salts with imidazolyl substituents by proton and anions. *Organometallics* **2007**, *26*, 5922-5930.
121. Majumdar, P.; Yuan, X.; Li, S.; Le Guennic, B.; Ma, J.; Zhang, C.; Jacquemin, D.; Zhao, J. Cyclometalated Ir (III) complexes with styryl-BODIPY ligands showing near IR absorption/emission: preparation, study of photophysical properties and application as photodynamic/luminescence imaging materials. *Journal of Materials Chemistry B* **2014**, *2*, 2838-2854.
122. Guo, S.; Ma, L.; Zhao, J.; Küçüköz, B.; Karatay, A.; Hayvali, M.; Yaglioglu, H. G.; Elmali, A. BODIPY triads triplet photosensitizers enhanced with intramolecular resonance energy transfer (RET): broadband visible light absorption and application in photooxidation. *Chemical Science* **2014**, *5*, 489-500.
123. Armaroli, N. Electronic Excited-State Engineering. *ChemPhysChem* **2008**, *9*, 371-373.
124. Tyson, D. S.; Luman, C. R.; Zhou, X.; Castellano, F. N. New Ru (II) chromophores with extended excited-state lifetimes. *Inorg. Chem.* **2001**, *40*, 4063-4071.

125. Vachova, L.; Novakova, V.; Kopecky, K.; Miletin, M.; Zimcik, P. Effect of intramolecular charge transfer on fluorescence and singlet oxygen production of phthalocyanine analogues. *Dalton Transactions* **2012**, *41*, 11651-11656.
126. Abdel-Shafi, A. A.; Hassanin, H. A.; Al-Shihry, S. S. Partial charge transfer contribution to the solvent isotope effect and photosensitized generation of singlet oxygen, O₂ (1 Δg), by substituted ruthenium (ii) bipyridyl complexes in aqueous media. *Photochemical & Photobiological Sciences* **2014**, *13*, 1330-1337.
127. Kasuga, K.; Tsutsuo, M. Some new developments in the chemistry of metallophthalocyanines. *Coord. Chem. Rev.* **1980**, *32*, 67-95.
128. Pass, H. I. Photodynamic therapy in oncology: mechanisms and clinical use. *J. Natl. Cancer Inst.* **1993**, *85*, 443-456.
129. Leznoff, C. C.; Lever, A. B. P. *Phthalocyanines Properties and Applications*, ; VCH: 1989; .
130. Çakır, V.; Çakır, D.; Pişkin, M.; Durmuş, M.; Büyüklioğlu, Z. Water soluble peripheral and non-peripheral tetrasubstituted zinc phthalocyanines: Synthesis, photochemistry and bovine serum albumin binding behavior. *J Lumin* **2014**, *154*, 274-284.
131. AliáErmeydan, M. Glycerol and galactose substituted zinc phthalocyanines. Synthesis and photodynamic activity. *Photochemical & Photobiological Sciences* **2009**, *8*, 312-318.
132. Sakamoto, K.; Yoshino, S.; Takemoto, M.; Furuya, N. Syntheses of near infrared absorbed phthalocyanines to utilize photosensitizers. *J. Porphyrins Phthalocyanines* **2013**, *17*, 605-627.
133. North Carolina State University Office of Research and Graduate Studies North Carolina State University, Office of Research and Graduate Studies, Expired Project Files, 1966-1997 manuscript].
134. Herbst, W.; Hunger, K. *Industrial organic pigments: production, properties, applications*; John Wiley & Sons: 2006; .
135. Moussaron, A.; Arnoux, P.; Vanderesse, R.; Sibille, E.; Chaimbault, P.; Frochot, C. Lipophilic phthalocyanines for their potential interest in photodynamic therapy: synthesis and photo-physical properties. *Tetrahedron* **2013**, *69*, 10116-10122.

136. Sevim, A. M.; Yenilmez, H. Y.; Bayır, Z. A. Synthesis and photophysical properties of novel (trifluoromethyl) phenylethynyl-substituted metallophthalocyanines. *Polyhedron* **2013**, *62*, 120-125.
137. Ishii, K. Functional singlet oxygen generators based on phthalocyanines. *Coord. Chem. Rev.* **2012**, *256*, 1556-1568.
138. Ricci-Júnior, E.; Marchetti, J. M. Zinc (II) phthalocyanine loaded PLGA nanoparticles for photodynamic therapy use. *Int. J. Pharm.* **2006**, *310*, 187-195.
139. Agostinis, P.; Berg, K.; Cengel, K. A.; Foster, T. H.; Girotti, A. W.; Gollnick, S. O.; Hahn, S. M.; Hamblin, M. R.; Juzeniene, A.; Kessel, D. Photodynamic therapy of cancer: an update. *CA: a cancer journal for clinicians* **2011**, *61*, 250-281.
140. Mang, T. S. Lasers and light sources for PDT: past, present and future. *Photodiagnosis and Photodynamic Therapy* **2004**, *1*, 43-48.
141. Wilson, B.; Patterson, M. The physics of photodynamic therapy. *Phys. Med. Biol.* **1986**, *31*, 327.
142. Foster, T. H.; Murant, R. S.; Bryant, R. G.; Knox, R. S.; Gibson, S. L.; Hilf, R. Oxygen consumption and diffusion effects in photodynamic therapy. *Radiat. Res.* **1991**, *126*, 296-303.
143. Hamblin, M. R.; Hasan, T. Photodynamic therapy: a new antimicrobial approach to infectious disease? *Photochemical & Photobiological Sciences* **2004**, *3*, 436-450.
144. Gursoy, H.; Ozcakir-Tomruk, C.; Tanalp, J.; Yilmaz, S. Photodynamic therapy in dentistry: a literature review. *Clin. Oral Investig.* **2013**, *17*, 1113-1125.
145. Yang, E.; Diers, J. R.; Huang, Y.; Hamblin, M. R.; Lindsey, J. S.; Bocian, D. F.; Holten, D. Molecular electronic tuning of photosensitizers to enhance photodynamic therapy: synthetic dicyanobacteriochlorins as a case study. *Photochem. Photobiol.* **2013**, *89*, 605-618.
146. Kanner, R. C.; Foote, C. S. Singlet oxygen production from singlet and triplet states of 9, 10-dicyanoanthracene. *J. Am. Chem. Soc.* **1992**, *114*, 678-681.
147. Macdonald, I. J.; Dougherty, T. J. Basic principles of photodynamic therapy. *Journal of Porphyrins and Phthalocyanines* **2001**, *5*, 105-129.

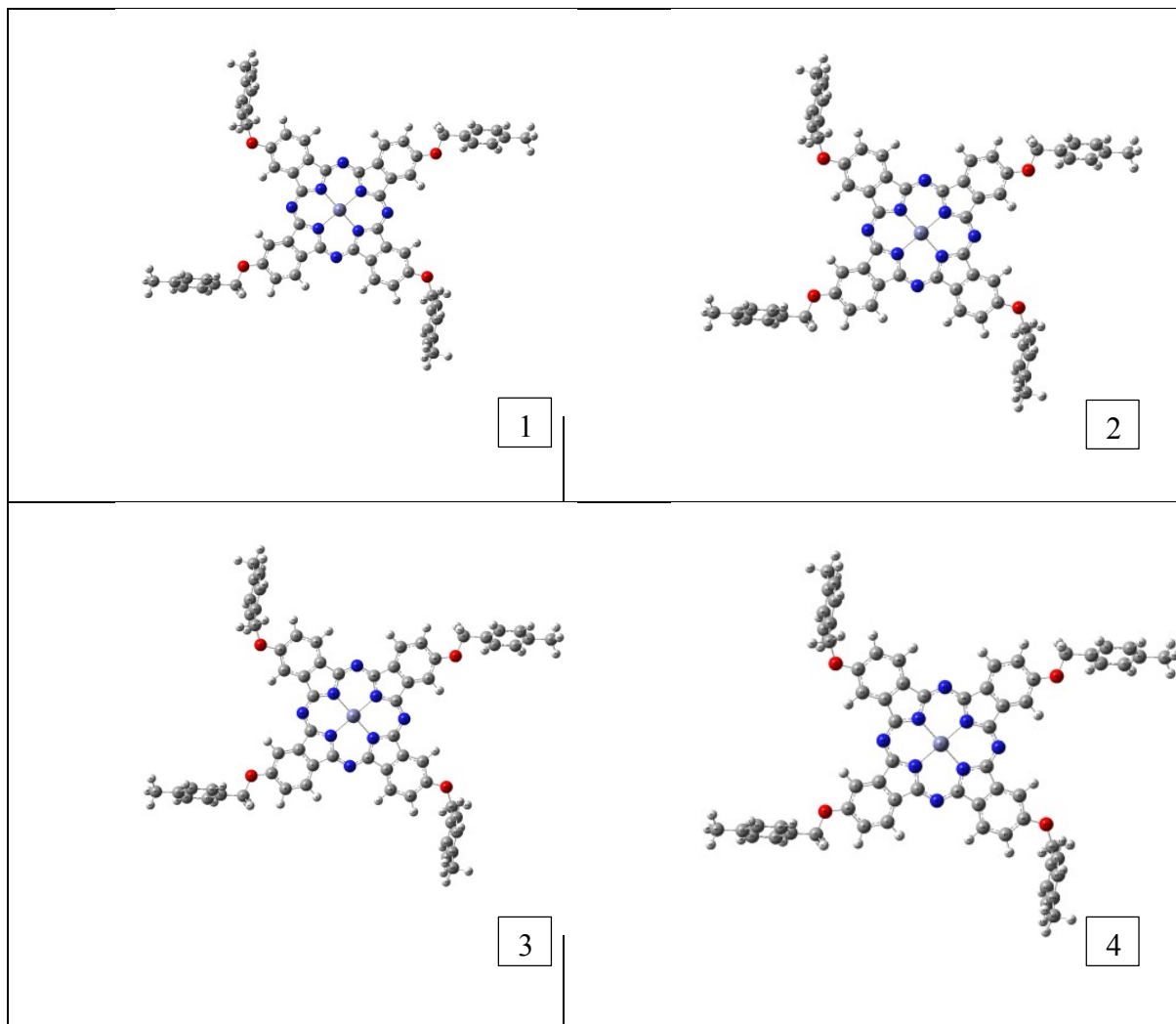
148. Plaetzer, K.; Krammer, B.; Berlanda, J.; Berr, F.; Kiesslich, T. Photophysics and photochemistry of photodynamic therapy: fundamental aspects. *Lasers in medical science* **2009**, *24*, 259-268.
149. Klán, P. *Photochemistry of organic compounds : from concepts to practice*; Wiley: Chichester, U.K., 2009; .
150. Rossetti, F. C.; Lopes, L. B.; Carollo, A. R. H.; Thomazini, J. A.; Tedesco, A. C.; Bentley, M. V. L. B. A delivery system to avoid self-aggregation and to improve in vitro and in vivo skin delivery of a phthalocyanine derivative used in the photodynamic therapy. *J. Controlled Release* **2011**, *155*, 400-408.
151. Fadel, M.; Kassab, K.; Fadeel, D. A. Zinc phthalocyanine-loaded PLGA biodegradable nanoparticles for photodynamic therapy in tumor-bearing mice. *Lasers in medical science* **2010**, *25*, 283-292.
152. da Volta Soares, M.; Oliveira, M.; Dos Santos, E.; de Brito Gitirana, L.; Barbosa, G.; Quaresma, C.; Ricci-Júnior, E. Nanostructured delivery system for zinc phthalocyanine: preparation, characterization, and phototoxicity study against human lung adenocarcinoma A549 cells. *Int J Nanomedicine* **2011**, *6*, 227-238.
153. Dumoulin, F.; Durmuş, M.; Ahsen, V.; Nyokong, T. Synthetic pathways to water-soluble phthalocyanines and close analogs. *Coord. Chem. Rev.* **2010**, *254*, 2792-2847.
154. Dörwald, F. Z. *Lead optimization for medicinal chemists : pharmacokinetic properties of functional groups and organic compounds*; Wiley-VCH: Weinheim, 2012; .
155. Ueno, L. T.; Jayme, C. C.; Silva, L. R.; Pereira, E. B.; Oliveira, S. M. d.; Machado, A. E. Photophysics and spectroscopic properties of zinc phthalocyanine revisited using quantum chemistry. *Journal of the Brazilian Chemical Society* **2012**, *23*, 2237-2247.
156. Tackley, D. R.; Dent, G.; Smith, W. E. IR and Raman assignments for zinc phthalocyanine from DFT calculations. *Physical Chemistry Chemical Physics* **2000**, *2*, 3949-3955.
157. Tyson, D. S.; Henbest, K. B.; Bialecki, J.; Castellano, F. N. Excited state processes in ruthenium (II)/pyrenyl complexes displaying extended lifetimes. *The Journal of Physical Chemistry A* **2001**, *105*, 8154-8161.
158. Ogunsipe, A.; Maree, D.; Nyokong, T. Solvent effects on the photochemical and fluorescence properties of zinc phthalocyanine derivatives. *J. Mol. Struct.* **2003**, *650*, 131-140.

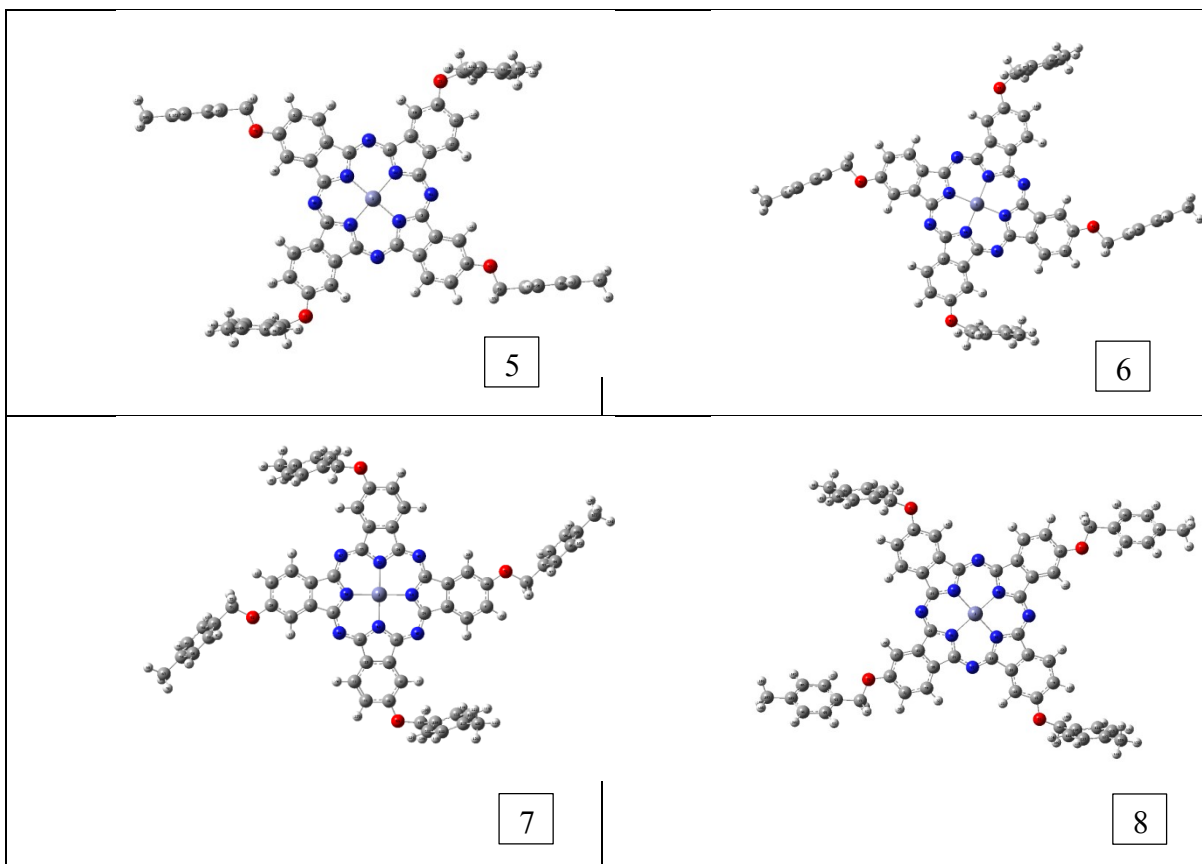
159. Scalise, I.; Durantini, E. N. Synthesis, properties, and photodynamic inactivation of *Escherichia coli* using a cationic and a noncharged Zn (II) pyridyloxyphthalocyanine derivatives. *Bioorg. Med. Chem.* **2005**, *13*, 3037-3045.
160. Ferrari, M. Cancer nanotechnology: opportunities and challenges. *Nature Reviews Cancer* **2005**, *5*, 161-171.
161. Papadimitriou, S.; Bikaris, D. Novel self-assembled core–shell nanoparticles based on crystalline amorphous moieties of aliphatic copolyesters for efficient controlled drug release. *J. Controlled Release* **2009**, *138*, 177-184.
162. Ricci-Júnior, E.; Marchetti, J. M. Zinc (II) phthalocyanine loaded PLGA nanoparticles for photodynamic therapy use. *Int. J. Pharm.* **2006**, *310*, 187-195.
163. Clogston, J. D.; Patri, A. K. In *Zeta potential measurement*; Characterization of nanoparticles intended for drug delivery; Springer: 2011; pp 63-70.
164. Ostrovskii, V.; Trifonov, R.; Popova, E. Medicinal chemistry of tetrazoles. *Russian Chemical Bulletin* **2012**, *61*, 768-780.
165. dos Santos, D. R.; Silva de Oliveira, Ana Gabriela; Coelho, R. L.; Begnini, I. M.; Magnago, R. F.; Da Silvac, L. Synthesis of liquid crystals materials derived from oxadiazole, isoxazole and tetrazole heterocycles. *Arkivoc* **2008**, *17*, 157-166.
166. Kuznetsova, N. A.; Okunchikov, V. V.; Derkacheva, V. M.; Kaliya, O. L.; Lukyanets, E. A. Photooxidation of metallophthalocyanines: the effects of singlet oxygen and Pcm-O₂ complex formation. *Journal of Porphyrins and Phthalocyanines* **2005**, *9*, 393-397.
167. Ogunsipe, A.; Nyokong, T. Photophysical consequences of bovine serum albumin binding to non-transition metal phthalocyanine sulfonates. *Photochemical & Photobiological Sciences* **2005**, *4*, 510-516.
168. Krieger-Liszka, A.; Fufezan, C.; Trebst, A. Singlet oxygen production in photosystem II and related protection mechanism. *Photosynthesis Res.* **2008**, *98*, 551-564.
169. Freyer, W.; Mueller, S.; Teuchner, K. Photophysical properties of benzoannelated metal-free phthalocyanines. *J. Photochem. Photobiol. A* **2004**, *163*, 231-240.
170. Charlesworth, P.; Truscott, T.; Brooks, R.; Wilson, B. The photophysical properties of a ruthenium-substituted phthalocyanine. *Journal of Photochemistry and Photobiology B: Biology* **1994**, *26*, 277-282.

APPENDICES

Appendix A

Lowest possible structure of ZnPcBCH₃





Structure	Energy
1	-4986.79
2	-4986.79
3	-4986.79
4	-4986.79
5	-4986.79
6	-4986.79
7	-4986.79
8	-4986.79

Appendix B

Crystallographic data and structure refinement for compound 3 of Chapter 2

Identification code	rds435
Chemical formula	C16H12N2O
Formula weight	248.28 g/mol
Temperature	100(2) K
Wavelength	0.71073 Å
	0.202 x 0.226 x 0.727
Crystal size	mm
Crystal habit	colorless block
Crystal system	monoclinic
Space group	P 1 21/c 1
Unit cell dimensions	$a = 9.7343(2)$ Å $\alpha = 90^\circ$ $b = 7.8188(2)$ Å $\beta = 92.3170(10)^\circ$ $c = 16.5444(3)$ Å $\gamma = 90^\circ$
Volume	1258.17(5) Å ³
Z	4
Density (calculated)	1.311 g/cm ³
Absorption coefficient	0.084 mm ⁻¹
F(000)	520

Atomic coordinates and equivalent isotopic displacement parameters (\AA^2) for rds435

	x/a	y/b	z/c	U(eq)
O1	0.39781(5)	0.51335(6)	0.18356(3)	0.01484(9)
N1	0.58287(6)	0.91446(8)	0.91615(4)	0.01822(11)
N2	0.93312(6)	0.66247(9)	0.94814(4)	0.02007(12)
C1	0.51089(6)	0.53326(7)	0.13960(4)	0.01129(10)
C2	0.49840(6)	0.65767(7)	0.07887(4)	0.01126(10)
C3	0.60803(6)	0.68792(7)	0.02990(3)	0.01069(9)
C4	0.73168(6)	0.59537(8)	0.04044(4)	0.01172(10)
C5	0.74307(6)	0.47250(8)	0.10133(4)	0.01359(10)
C6	0.63328(6)	0.44116(8)	0.15085(4)	0.01338(10)
C7	0.59443(6)	0.81455(8)	0.96722(4)	0.01292(10)
C8	0.84392(6)	0.63107(8)	0.98968(4)	0.01439(11)
C9	0.40270(6)	0.38449(8)	0.24676(4)	0.01391(10)
C10	0.26306(6)	0.37546(8)	0.28136(4)	0.01226(10)
C11	0.16385(7)	0.26493(9)	0.24778(4)	0.01644(11)
C12	0.03511(7)	0.25229(10)	0.28083(4)	0.01812(12)
C13	0.00207(6)	0.35029(9)	0.34767(4)	0.01527(11)
C14	0.10082(7)	0.46284(8)	0.38036(4)	0.01483(11)
C15	0.23021(6)	0.47481(8)	0.34784(4)	0.01324(10)
C16	0.86398(7)	0.33198(11)	0.38426(5)	0.02372(15)

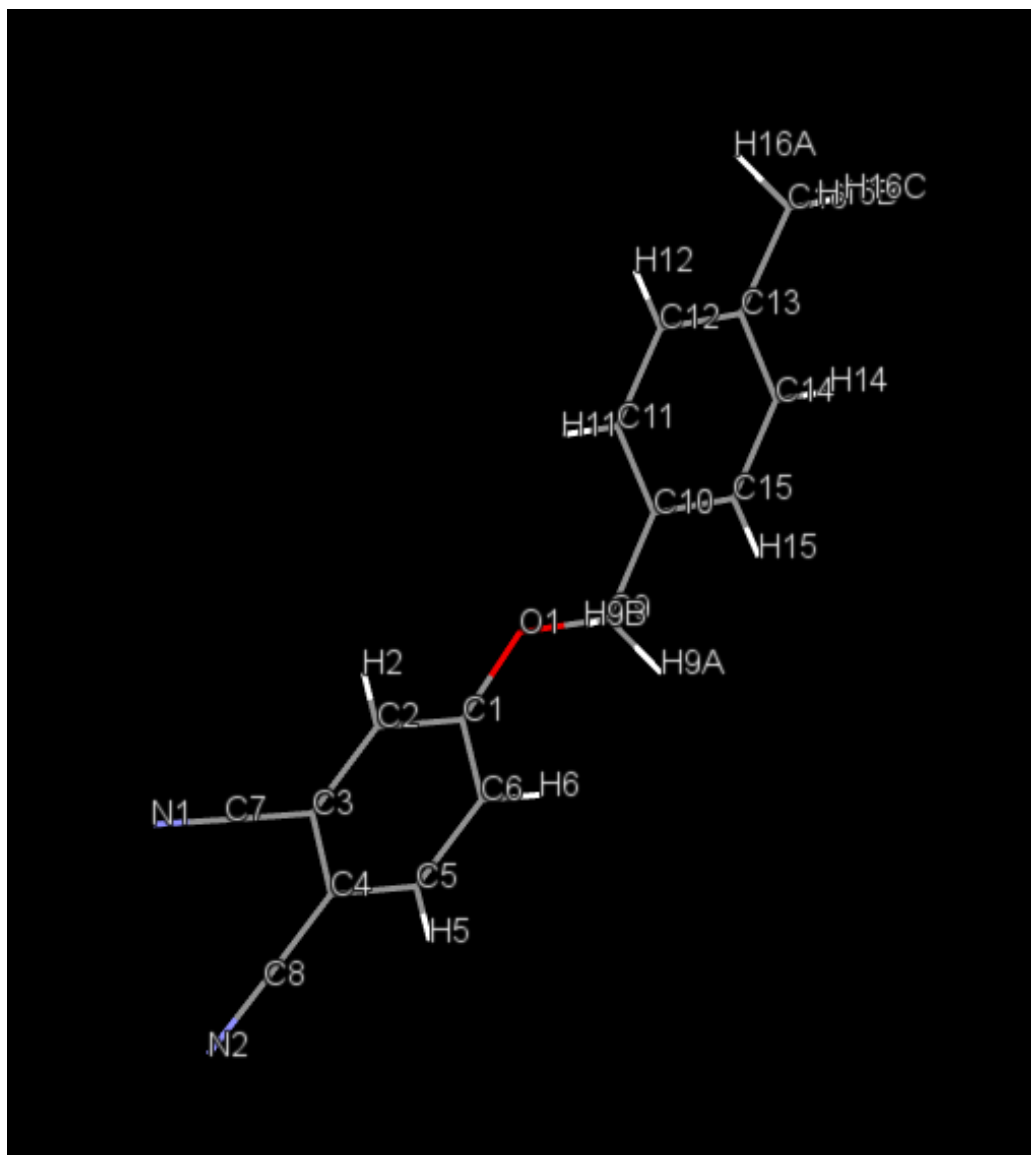
Bond Length [Å°] for rds435

O1-C1	1.3526(7)	O1-C9	1.4514(8)
N1-C7	1.1529(8)	N2-C8	1.1553(8)
C1-C6	1.3980(8)	C1-C2	1.4003(8)
C2-C3	1.3860(8)	C2-H2	0.95
C3-C4	1.4092(8)	C3-C7	1.4360(9)
C4-C5	1.3933(9)	C4-C8	1.4322(8)
C5-C6	1.3944(8)	C5-H5	0.95
C6-H6	0.95	C9-C10	1.4978(8)
C9-H9A	0.99	C9-H9B	0.99
C10-C15	1.3941(9)	C10-C11	1.3946(9)
C11-C12	1.3909(9)	C11-H11	0.95
C12-C13	1.3936(10)	C12-H12	0.95
C13-C14	1.3961(10)	C13-C16	1.5032(9)
C14-C15	1.3926(8)	C14-H14	0.95
C15-H15	0.95	C16- H16A	0.98
C16-H16B	0.98	C16- H16C	0.98

Bond angle [°] for rds435

C1-O1-C9	117.61(5)	O1-C1-C6	125.22(5)
O1-C1-C2	114.63(5)	C6-C1-C2	120.14(5)
C3-C2-C1	119.43(5)	C3-C2-H2	120.3
C1-C2-H2	120.3	C2-C3-C4	120.93(5)
C2-C3-C7	119.28(5)	C4-C3-C7	119.79(5)
C5-C4-C3	119.09(5)	C5-C4-C8	121.20(5)
C3-C4-C8	119.70(5)	C4-C5-C6	120.37(5)
C4-C5-H5	119.8	C6-C5-H5	119.8
C5-C6-C1	120.04(6)	C5-C6-H6	120.0
C1-C6-H6	120.0	N1-C7-C3	179.04(7)
N2-C8-C4	178.71(7)	O1-C9-C10	107.71(5)
O1-C9-H9A	110.2	C10-C9-H9A	110.2
O1-C9-H9B	110.2	C10-C9-H9B	110.2
H9A-C9-H9B	108.5	C15-C10-C11	118.84(6)
C15-C10-C9	121.06(6)	C11-C10-C9	120.10(6)
C12-C11-C10	120.52(6)	C12-C11-H11	119.7
C10-C11-H11	119.7	C11-C12-C13	120.89(6)
C11-C12-H12	119.6	C13-C12-H12	119.6
C12-C13-C14	118.46(6)	C12-C13-C16	120.40(6)
C14-C13-C16	121.13(6)	C15-C14-C13	120.80(6)
C15-C14-H14	119.6	C13-C14-H14	119.6
C14-C15-C10	120.48(6)	C14-C15-H15	119.8
C10-C15-H15	119.8	C13-C16- H16A	109.5
C13-C16-H16B	109.5	H16A-C16- H16B	109.5
C13-C16-H16C	109.5	H16A-C16- H16C	109.5
H16B-C16- H16C	109.5		

Crystal Structure of 4-(4'-Methyl-benzyloxy)-phthalonitrile



Crystal structure

4-(4'-Methyl-benzyloxy)-phthalonitrile

